University of Alberta

Towards Bioactive Rosette Nanotubes for Biomedical Applications

by

Alaaeddin Alsbaiee

A thesis submitted to the Faculty of Graduate Studies and Research
in partial fulfillment of the requirements for the degree of

Doctor of Philosophy

Department of Chemistry

Fall 2013
Edmonton, Alberta

Abstract

Rosette nanotubes (RNTs) are bio-inspired nanomaterials generated from the self-assembly of a guanine-cytosine motif called the "G∧C" base. These nanotubular architectures are promising 2-D coating materials for bone tissue engineering applications, and delivery scaffolds for hydrophobic drug molecules in physiological media. For successful biomedical applications of RNTs however, it is necessary to: 1) explore the extent to which peptides on their outer surface can be tolerated, 2) develop radiolabeling methods to facilitate *in vivo* studies, and 3) extend the RNT inner diameter for enhanced drug encapsulation capability. This thesis aims to provide physical and synthetic tools in which to expand the scope of the RNTs for biomedical applications, particularly within the areas of bone tissue engineering and drug delivery.

Chapter 1 provides a literature review of self-assembled nanomaterials that are based on bio-inspired building blocks including peptides and nucleic acids and are currently being investigated for biomedical applications. Given the importance of functionalizing such nanomaterials with peptides, Chapter 2 aims to demonstrate that RNTs can act as a scaffold to express three bioactive 11-amino acid-long peptides named A, B and C. Specifically, the synthesis and self-assembly of peptides (A-C)-functionalized twin G∧C motifs, (pA-TB, pB-TB and pC-TB) and a lysine-functionalized motif K1-TB, are presented. Next, three co-assembled

RNT-constructs consisting of 90% of K1-TB and 10% of each of the peptide-TB conjugates are prepared. Circular dichroism in combination with microscopy techniques, provide evidence for the first time of the formation of bi-functionalized RNTs having a random mixed configuration.

Chapter 3 introduces two radiolabeling strategies of RNTs for single photon emission computed tomography (SPECT) and positron emission tomography (PET) imaging techniques. In these strategies, the synthesis and self-assembly of RNTs, which are functionalized with an oxo-rhenium complex (for SPECT) and *p*-fluorobenzoate (for PET) are presented. Next, Chapter 4 describes a 13-step synthetic strategy to obtain an organic-soluble tetracyclic yG∧C motif for self-assembly into RNTs with a *ca.* 1.7 nm inner diameter for drug delivery applications. The self-assembly of this motif is then investigated using microscopy techniques. Finally, Chapter 5 highlights the significance and future directions of this work.

Dedication

To my Parents……who I love the most

"Your prayers, wishes, hopes, and dreams for my success came true… You deserve a special "thank you" from your little son, who is nothing without you"

Acknowledgments

First and foremost, I thank Almighty God for giving me the power, passion, and patience to complete this work. I thank him for illuminating my path and lighting my way to achieve my goals. Thank you God for everything.

I am very thankful to my supervisor Professor Hicham Fenniri for his support, feedback, and directions throughout my studies. The freedom that he gave me in my research and projects was essential to build my independence and creativity during the past four years.

I am so grateful to Alberta Innovates Technology Futures (AITF) for the generous doctoral fellowship in nanotechnology during the period of May 2010-May 2013. The generous stipend and annual research allowance allowed me to focus on my research and to participate in 5 international conferences in the US and Canada. I would also like to thank the department of chemistry for their support and help throughout my studies. Especially, Professor Todd Lowary and my co-supervisor Professor Frederick West for their support and guidance. I also thank my supervisory committee members; Professor Nils Petersen and Professor Robert Campbell for their feedback during my studies.

I deeply thank all SNAG group members for the wonderful time that we spent at NINT, and their continuous support. I especially express my gratitude to Dr.

Rachel Beingessner for the valuable scientific discussions that we had, for teaching me precious scientific writing and communication skills, and for her patience and unconditional support. I am so grateful to my wonderful friends Dr. Mounir El Bakkari and Mr. Mohammad Rokib Hassan, with whom I spent a wonderful and unforgettable time. I thank Dr. Jae-Young Cho for microscopy imaging studies, and Dr. Takeshi Yamazaki for the modeling studies.

Finally, I thank my wife for her patience and unconditional love, which has been a continuous stream of support and strength during my studies. I thank my little daughter (Dana), who provided me with her sweet love that was the source of my greatest joy over the past three years. I am so grateful to my beloved parents for their sacrifices and for being the main source of moral support and encouragement in my life. I am so indebted to my sister and best friend Ola, who strived to see my success; to my brother Ammar, who guided me throughout my studies; and to my brother and friend Obada for his continuous advise and emotional support.

Table of Contents

Chapter 2. Peptide-Functionalized Rosette Nanotubes for Bone Tissue Engineering

List of Figures

List of Tables

List of Abbreviations

1,2-DCE	1,2-dichloroethane
2-D	Two-dimensional
3-D	Three-dimensional
ACN	Acetonitrile solvent
AFM	Atomic force microscopy
BMP-7	Bone morphogenic proteins-7
BMP-2	Bone morphogenic proteins-2
Bn	Benzyl group
Boc	Di-tert-butyl dicarbonate protecting group
CD	Circular dichroism
CNS	Central nervous system
DABCO	1,4-diazabicyclo[2.2.2]octane
DCM	Dichloromethane solvent
DEX	Dexamethasone
DIC	N,N'-diisopropylcarbodiimide
DIPEA	Diisopropyl ethylamine
DMAP	4-dimethylaminopyridine
DMF	Dimethylformamide
DMSO	Dimethyl sulfoxide
DSC	N,N`-Disuccinimide carbonate

DTT	Dithiothreitol
ECM	Extracellular matrix
FGF	Fibroblast growth factor
Fmoc	Fluorenylmethyloxycarbonyl chloride
G∧C	Guanine-cytosine motif
HA	Hydroxyapitite
HBPA	Heparin-peptide amphiphile
HBTU	O-benzotriazole-N,N,N',N'-tetramethyl-uronium-hexafluoro-phosphate
HPLC	High performance liquid chromatography
K1-TB	Lysine functionalized twin G∧C motif
MAG_3	Mercaptoacetyl triglycine ligand
MAG_3-ReO	Mercaptoacetyl triglycine-oxo rhenium complex
MALDI	Matrix-assisted laser desorption ionization
MeOH	Methanol
MVEC	Human microvascular endothelial cells
NGF	Nerve growth factor
NMR	Nuclear magnetic resonance
OB	Osteoblast cells
pA	Peptide A (SNVILKKYRN)
pA-TB	Peptide A - twin G∧C motif
pB	Peptide B (KPSSAPTQLN)
pB-TB	Peptide B - twin G∧C motif

pC	Peptide C (KAISVLYFDDS)
pC-TB	Peptide C - twin G∧C motif
PET	Positron emission tomography
pHEMA	poly(2-hydroxyethyl methacrylate)
PHP	polyHIPE
Re	Rhenium metal
RNTs	Rosette nanotubes
SEM	Scanning electron microscopy
SFB	4-[^{18}F]fluorobenzoate
S_N2	Nucleophilic substitution
S_NAr	Nucleophilic aromatic substitution
SPECT	Single photon emission computed tomography
TAM	Tamoxifen
TB-BA	Twin G∧C-butylamine
TB-MAG_3-Bz	Twin G∧C motif functionalized with Marcaptoacetyl triglycine-benzoyl ligand
TB-MAG_3-ReO	Twin G∧C motif functionalized with Marcaptoacetyl triglycine-oxo rheium complex
TB-PEG_3-NH_2	Twin-G∧C functionalized with PEG_3-propylamine chain
Tc	Technetium metal
TEA	Triethylamine
TEM	Transmission electron microscoppy
TFA	Triflouroacetic acid

TGF-β	Transforming growth factor-β
THF	Tetrahydrofuran solvent
Ti	Titanium metal
TIS	Triisopropyl silane
TLC	Thin layer chromatography
UV-Vis	Ultraviolet-visible spectroscopy
VEGF	Vascular endothelial growth factor
xG∧C	Tricyclic guanine-cytosine motif
yG∧C	Tetracyclic guanine-cytosine motif

Chapter 1

Bioinspired Self-Assembled Nanomaterials for Biomedical Applications*

1.1 Introduction

The natural drive of complementary molecular building blocks to organize or self-assemble in solution using intermolecular interactions can lead to well-defined supramolecular architectures with immense complexities and functions.[1] Being that these interactions are reversible[2], there is tremendous opportunity to control the properties and stabilities of these materials, by changing the solution parameters including temperature, concentration or pH.[3]

Nature uses this principle of self-assembly to create a vast array of functional systems that work in tandem to create and sustain life. Among the classic examples of self-assembled systems are proteins, which rely mainly on H-bonding, electrostatic interactions, and the hydrophobic effect to create the secondary and tertiary structures. Double-stranded DNA, which is maintained by stacking interactions and hydrogen bonding between cytosine-guanine and adenine-thymine is another example. Using these examples as inspiration, scientists have designed and studied a myriad of self-assembled peptide- and nucleic acid-based nanostructured materials. Included in these are β-sheet fibrous hydrogels[4,5] and rosette nanotubes[6], which are derived from naturally occurring amino acids and synthetic nucleic acid building blocks, respectively.

---

* This chapter is part of a book chapter published by: Alsbaiee, A.; Beingessner, R. L.; and Fenniri, H.; 'Self-Assembled Nanomaterials for Tissue Engineering'; in 'Nanomedicine: Technologies and Applications'; Webster, T. J. (Ed); Woodhead Publishing Ltd, Cambridge, UK, **2012**, *Ch. 17*, pp. 490-533.

This chapter aims to capture the most recent developments in the synthesis of these two types of nanomaterials and focus on the conditions and properties of the molecular building blocks (e.g. peptides and nucleic acids) in controlling the 3D matrix properties. A description of the state-of-the-art biomedical applications of these materials as scaffolds in tissue engineering[7,8] is also provided, which serves to highlight their biocompatibility, tunability and structural similarity to natural tissues.

1.2 Peptide-Based Self-Assembled Nanomaterials

Many natural proteins and peptides form fibrous architectures with nano- and micrometer dimensions that provide important mechanical properties in living organisms.[9] Cytoskeleton proteins, such as actin filaments and microtubules for instance, are fibrous proteins that provide the platform for the transport of cargos and movement of protein motors inside cells.[10] Fibrous proteins such as collagens and elastic fibers in extracellular matrices, also provide the scaffold that supports cell growth and allows for nutrients to access the cells.[11]

Given these complex functions, researchers have strived to isolate and identify domains within various proteins that are responsible for the fibrous architectures. Included in this are proteins that self-assemble into β-sheet based fibers. Many studies in this area have included amyloid and amyloid-like proteins, which have been linked to several diseases[12-15], involving the conversion of soluble functional proteins into insoluble β-sheet fibrillar aggregates.[16,17] The discovery of such peptide sequences have been instrumental in the *de novo* design and synthesis of artificial oligopeptide-based materials that have similar self-assembling properties.[18] Depending on the hydrophilic and hydrophobic amino acid sequences, these synthetic oligopeptides can be classified into two categories; ionic self-complementary and surfactant-like. Although several reviews are available on each[4,5,7,11,19-22], the most recent advances of these oligopeptide

nanomaterials are discussed in Sections 1.2.1 and 1.2.2, followed by applications in tissue engineering in Section 1.3.

1.2.1 Ionic Self-Complementary Peptides

Ionic self-complementary oligopeptides consist of repeat units of positively charged (K, R) and negatively charged (D, E) amino acids separated by hydrophobic/neutral amino acids (A, F, L, I, G). The complementarity is a result of having both charges in the same peptide sequence. Depending on the number of charged residues in every repeat unit, the peptides can be classified into four modules (I-IV), having the charge arrangements "– + – + – + – +", "– – + + – – + +", "– – – + + +", and "– – – – + + + +", respectively.[20]

The first discovery of a self-complementary ionic peptide was made by Zhang *et al.* in 1992.[23] While working on yeast proteins, a naturally occurring 16-mer self-complementary oligopeptide sequence called EAK16-II, was identified in a Z-DNA binding yeast protein called "Zuotin". This EAK16-II protein, which belongs within the modulus II category, was determined to have the sequence n-AEAEAKAKAEAEAKAK-c. Upon dissolution in water, it adopts a β-sheet conformation in which each side chain is rotated 180˚ with respect to the adjacent side chain (stretched or staggered conformation). In this arrangement, the hydrophobic alanine residues lying on one side of the peptide form a hydrophobic phase, while the positive lysine and negative glutamic acid residues are positioned on the other side to form a hydrophilic phase. In salt-free solution, EAK16-II forms a soluble 2D β-sheet using backbone hydrogen bonding. When monovalent metal cations such as Na^+ or Li^+ are added, the peptide self-assembles into a hydrogel made up of a network of filaments 10-20 nm in diameter with 50-80 nm pores in-between. Interestingly, and quite unusual for a β-sheet structure, EAK16-II is stable at high temperatures (90°C) and in the presence of denaturing agents (Figure 1.1).[18,24]

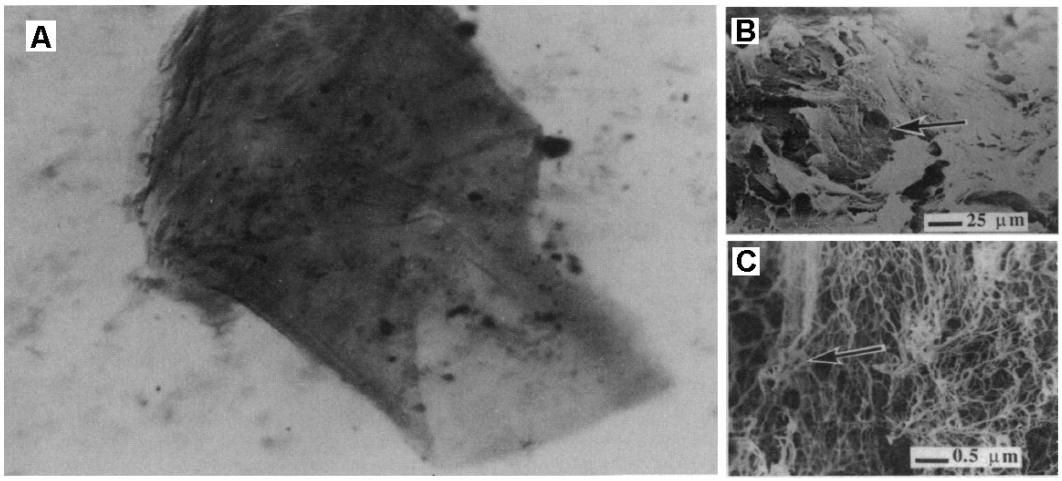

Figure 1.1. Self-assembling peptide EAK 16-II filamentous 3-D scaffold. (A) A photograph of the membrane scaffold, ~2x3 mm (x20); and (B,C) scanning electron microscopy (SEM) images. (Used with permission. Copyright (1993) National Academy of Sciences, USA).

This work by Zhang was instrumental in introducing and providing significant insight into the design, properties and self-assembling behavior of self-complementary ionic peptides and inspired the synthesis of many artificial analogues. Holmes *et al.*, for example, synthesized RAD16 I ("RADARADARADARADA") and II ("RARADADARARADADA"), in which the lysine and glutamic residues of EAK16 are replaced with arginine and aspartic acid.[25] Similar to EAK16-II, RAD16 I and II form a macroscopic matrix of β-sheet based fibers 10-20 nm in diameter in aqueous solution and in the presence of millimolar concentrations of monovalent metal ions such as Na^+ or K^+ (Figure 1.2).

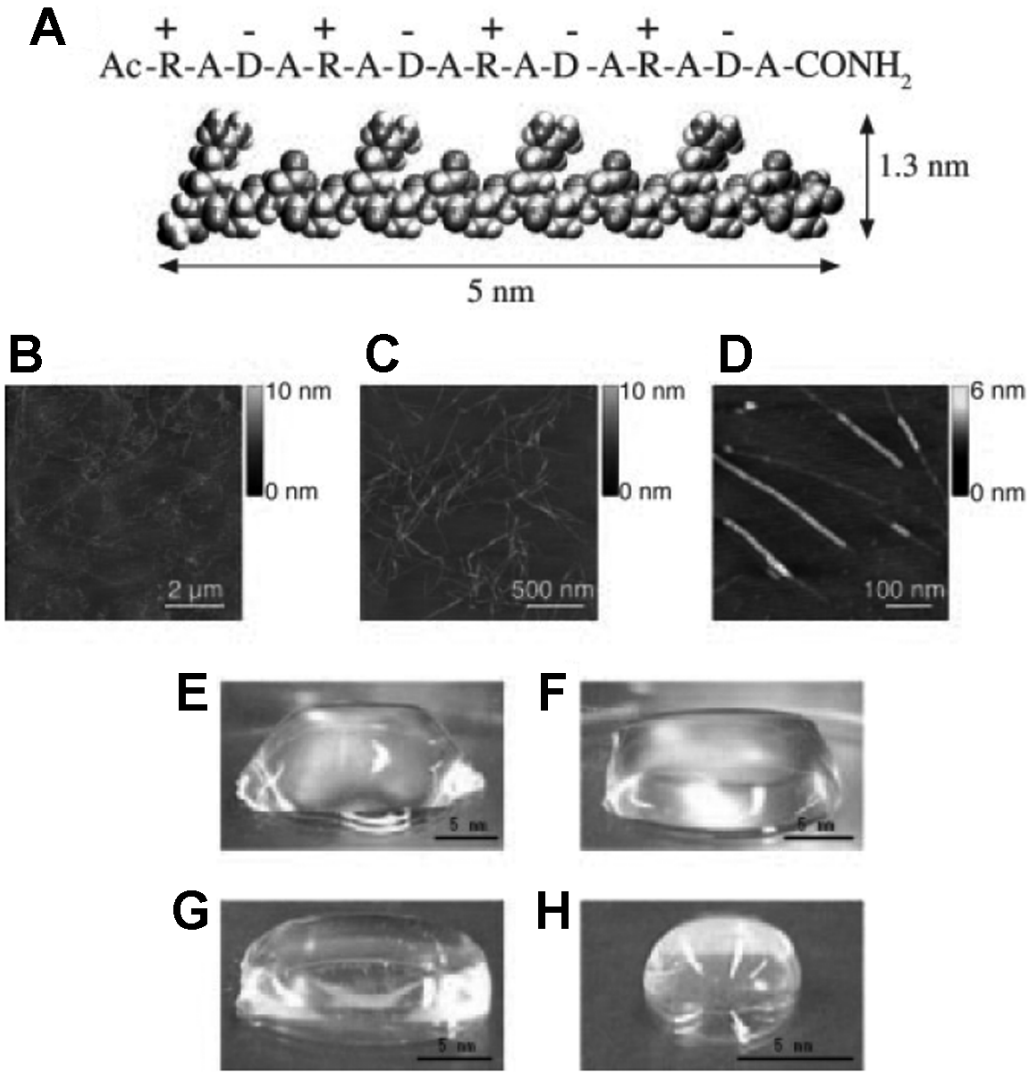

Figure 1.2. Peptide RAD16-I. (A) 3-D molecular model, dimensions 5 nm long, 1.3 nm wide, and 0.8 nm thick; (B–D) atomic force microscopy (AFM) images; Photographs of the hydrogel scaffold at (E) 0.5 wt% (pH 7.5); (F) 0.1 wt% (pH 7.5, Tris-HCl); (G) 0.1 wt% (pH 7.5, phosphate buffered saline (PBS)) before sonication; (H) reassembled hydrogel after four rounds of sonication. (Used with permission. Copyright (2005) National Academy of Sciences, USA).

In addition to RAD16 I and II, other peptides have also been synthesized and studied which are more structurally diverse to EAK16-II.[3,26-28] An analysis of these peptide designs and self-organization behavior, suggests that there are four

main considerations for establishing a stable β-sheet fibrous structure. These considerations, which include the length of the peptide, the amino acid sequence and hydrophobicity as well as the presence of salts, are illustrated in the following discussion, using specific examples described in the literature.

Length of the ionic self-complementary peptide: Shorter peptide analogues of EAK16-II[18,24] such as EAK12-II and EAK8-II for example, do not form a stable β-sheet-based 3D matrix, but rather proceed through a transition between an α-helix and β-sheet respectively, or adopt a random coil conformation even in the presence of salts. Since the amino acid sequences are the same among these three peptides, it is likely that EAK8-II and EAK12-II cannot adopt the necessary staggered or stretched conformation, because of the shorter lengths.

Amino acid sequence: This is considered one of the most important aspects of the peptide design, which affects the nanostructure formation and stability. EAK16-II has been shown in the literature for example, to form a stable β-sheet fibrous structure at all pH values.[3] This is because the staggered conformation of the peptide is readily adopted and not disrupted by unfavorable electrostatic interactions. EAK16-IV (module IV) in contrast, has the same amino acid composition as EAK16-II, but the residues are in a different sequence (AEAEAEAEAKAKAKA). In water, this peptide forms a globular assembly at neutral pH and a fibrillar structure only when the pH is below 6.5 or above 7.5. Under these latter conditions, neutralization of the glutamic acid or lysine ionizable side groups respectively, minimizes repulsive electrostatic interactions within the peptide chain and enables the staggered conformation to be adopted (Figure 1.3).

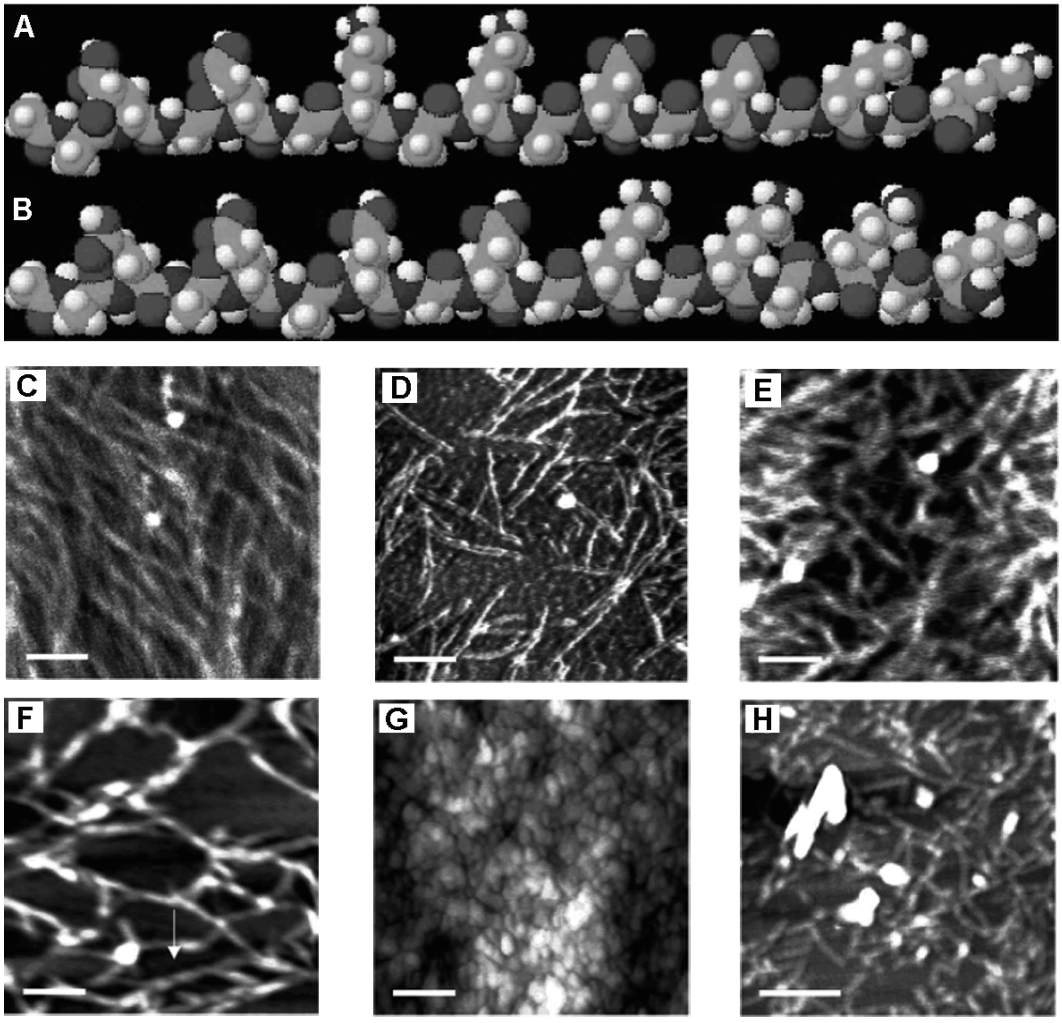

Figure 1.3. (A,B) Three-dimensional schematic presentation models of EAK16-II and EAK16-IV respectively; (C-E) AFM images of EAK16-II at pH values 4, 7.15, 11 respectively; (F-H) AFM images of EAK16-IV at pH values, 4, 7.15, 11, respectively. Scale bars 200 nm. (Used with permission. Copyright (2003) American Chemical Society, USA).

In a second reported example illustrating the importance of the amino acid sequence, both Group 1 peptides A and B shown in Figure 1.4, contain the amino acids Glu, Leu and Lys, but in different sequences.[26] Although these three particular residues have an α-helical intrinsic propensity as predicted by the Chou-Fasman statistical compilation[29-31], 1A forms an α-helix whereas 1B forms

a β-sheet. In a similar manner, both an α-helix and β-sheet were observed for Group 2 peptides also shown in Figure 1.4, despite both consisting of amino acids (Ile, Asp, Arg) predicted to have β-sheet forming propensity. These examples therefore demonstrate the importance of the amino acid sequence and not merely their presence alone, in determining the secondary structure adopted in solution.

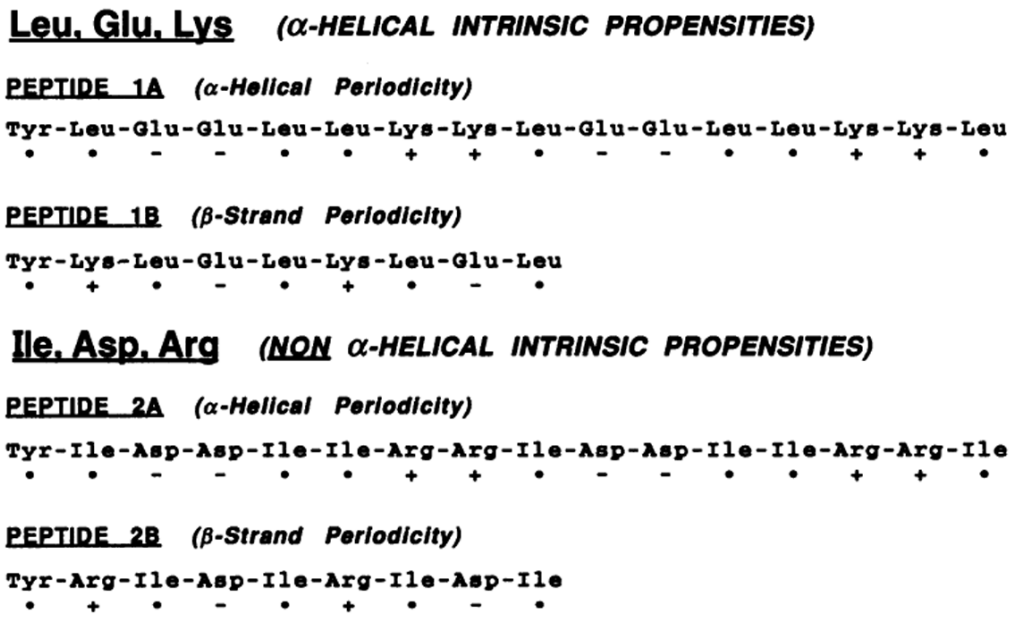

Figure 1.4. Schematic representation of the two sets of oligopeptides; peptides 1A and 1B are composed of residues with α-helical intrinsic propensity. 1A adopts α-helical conformation in solution, while 1B adopts β-sheet conformation. Peptides 2A and 2B alternatively, are composed of residues with non α-helical intrinsic propensity. 2A adopts α-helical conformation, while 2B adopts β-sheet conformation. (Used with permission. Copyright (1995) National Academy of Sciences, USA).

Hydrophobicity of the hydrophobic amino acid residues: Increasing the hydrophobicity of the hydrophobic residues can improve hydrogel formation from ionic self-complementary peptides.[26-28] EAK peptides containing alanine for example, require at least sixteen amino acids to form a stable macroscopic

structure.[26] Replacing the alanine with more hydrophobic residues such as leucine (ELK8) or phenylalanine (EFK12), requires only 8-mer and 12-mer peptides respectively, to form a stable 3D matrix.

For peptides of the same length, substituting hydrophobic amino acids with those which are more hydrophobic, can decrease the critical coagulation concentrations (CCC) (the critical concentration of the peptide at which it can form a stable macroscopic structure).[32] For peptides EIK12 (IKIEIKIEIKIE), EFK12 (FKFEFKFEFKFE) and EVK12 (VKVEVKVEVKVE) for example, the CCC values are in the order EIK12 < EFK12 < EVK12, which is consistent with the hydrohobicity of the amino acids, isoleucine > phenylalanine > valine.

Salt effects: Self-assembling peptides which are soluble at low millimolar concentrations in a salt-free aqueous environment, can form ordered 3D fibrous hydrogels with a water content of >99%, when exposed to physiological conditions or sufficient monovalent cations to screen the charged residues.[4,32]

Mechanism of Self-Assembly: Based on studies investigating the formation of β-sheet fibrous materials from different ionic self-complementary peptides, the mechanism of self-assembly was proposed to involve the initial formation of a β-sheet 2D layer.[4] This involves peptide backbone H-bonding, along with hydrophobic interactions between the hydrophobic residues on one side and electrostatic interactions between ion pairs on the adjacent side. In the presence of monovalent cations which function by screening the charged peptide residues thereby decreasing the repulsive intermolecular interactions[32], the hydrophobic phases then stack together to form a double β-sheet structure. The outer surface of this double layer contains the positive and negative residues packed together through intermolecular ionic bonds in a checkerboard manner. Every double β-sheet is an individual fiber with a diameter of 10-20 nm and a length up to several

hundred nanometers. These nanofibers further self-assemble into a fibrillar hydrogel having pores 5-200 nm in size.

Reversibility of Self-Assembly: In a study involving the RAD16-I peptide, it has been demonstrated that this self-assembly process is reversible.[2] RAD16-I nanofibers several hundred nanometers in length for instance, can be mechanically broken down with sonication to generate shorter fibers 20-100 nm in length. These nanofibers then undergo reassembly within a 2 h time-frame to their original dimensions. During this self-healing process[2], the hydrophobic ends re-associate to minimize their exposure to water and then diffusively slide along the nanofiber until they are completely hidden from the water (Figure 1.5). This is also assisted by the formation of electrostatic interactions between oppositely charged residues on the charged side of the fibers.[2,22] Unlike polymer fibers that cannot undergo reversible re-assembly, this self-assembly/re-assembly process in peptide assemblies is a very important property for the fabrication of novel materials for biological applications.

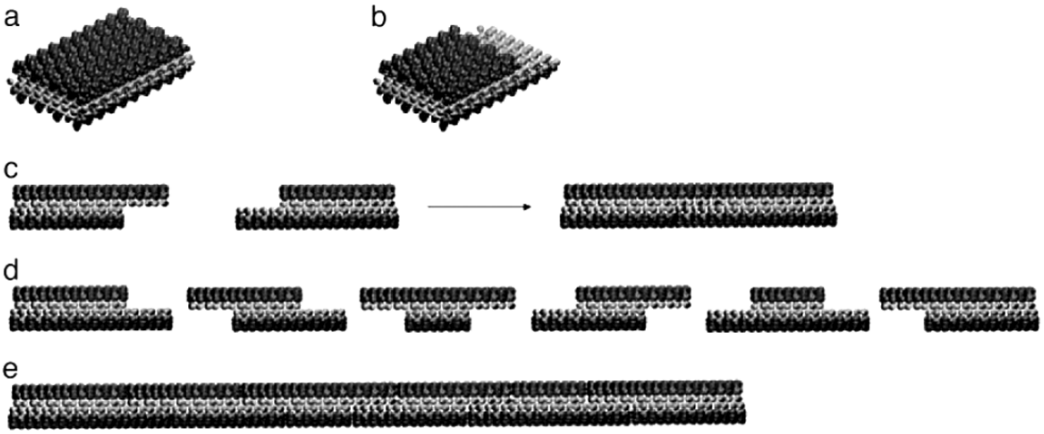

Figure 1.5. The proposed sliding diffusion mechanism for the dynamic reassembly of RAD16-I. The light sides represent the hydrophobic phases of the β-sheets and the dark sides represent the hydrophilic phases. The nanofiber fragments formed during self-assembly having (a) Blunt ends, or (b) Semiprotruding ends. (c) The self-assembly of the fragments with protruding ends

via hydrophobic interactions. (d) The self-assembly of the fragments with semiprotruding and protruding ends. (e) The formation of nanofibers with blunt ends through self-assembly. (Used with permission. Copyright (2005) National Academy of Sciences, USA).

1.2.2 Surfactant-Like Peptide Amphiphiles

Amphiphilic molecules, such as the phospholipids in cell membranes, consist of a distinct hydrophilic head and hydrophobic tail segment. When self-assembled in solution, phospholipids are known to generate unique nano-architectures such as micelles and tubules.[20,22] In an attempt to emulate the properties and self-assembling behaviour of these naturally occurring molecules, researchers have synthesized short peptide amphiphiles (PA) and studied their self-organization behaviour in solution.[20,22] Two types of PAs in particular have received considerable attention in the literature and will be the focus of this Section. These are PAs consisting of natural amino acids with negatively charged head groups, positively charged head groups and mixed hydrophobic tails as well as amphiphiles derived from hybrid building blocks.

1.2.2.1 PAs from Natural Amino Acids

PAs with negatively charged head group: In early 2000, Vauthey *et al.*, designed PAs made exclusively from natural L-amino acids containing a negatively charged head group.[33] Four unique PAs were synthesized that contained a hydrophilic head consisting of one or two aspartic acid residues at the C-terminus. The hydrophobic tail was comprised of six alanine, valine or leucine amino acids, which have increasing hydrophobicity. The end of each hydrophobic tail group was then capped by acetylation to mask the positive charge of the terminal amino acid. In total, four peptides with the following sequences were generated: A_6D_1 (Ac-AAAAAAD), V_6D_1 (Ac-VVVVVVD), V_6D_2 (Ac-VVVVVVDD), and L_6D_2

(Ac-LLLLLLDD). Each had a length of ~ 2 nm and properties and dimensions very similar to phospholipids. Upon self-assembly in water at neutral pH, DLS measurements and quick-freeze/deep-etch TEM images of peptides A_6D_1, V_6D_1, and V_6D_2, revealed a similar network of nanotubes ~ 30-50 nm in diameter (Figure 1.6 A-C). Although Peptide L_6D_2, having the most hydrophobic leucine residue also self-assembled, the material in the TEM image was much less defined suggesting that the hydrophobic tail packing is different from the other three peptides (Figure 1.6 D). Yang and Zhang further demonstrated using a similar system, that the critical aggregate concentration (CAC) at which the PA peptides form the nanofibers decreases when the tail hydrophobicity is increased.[34]

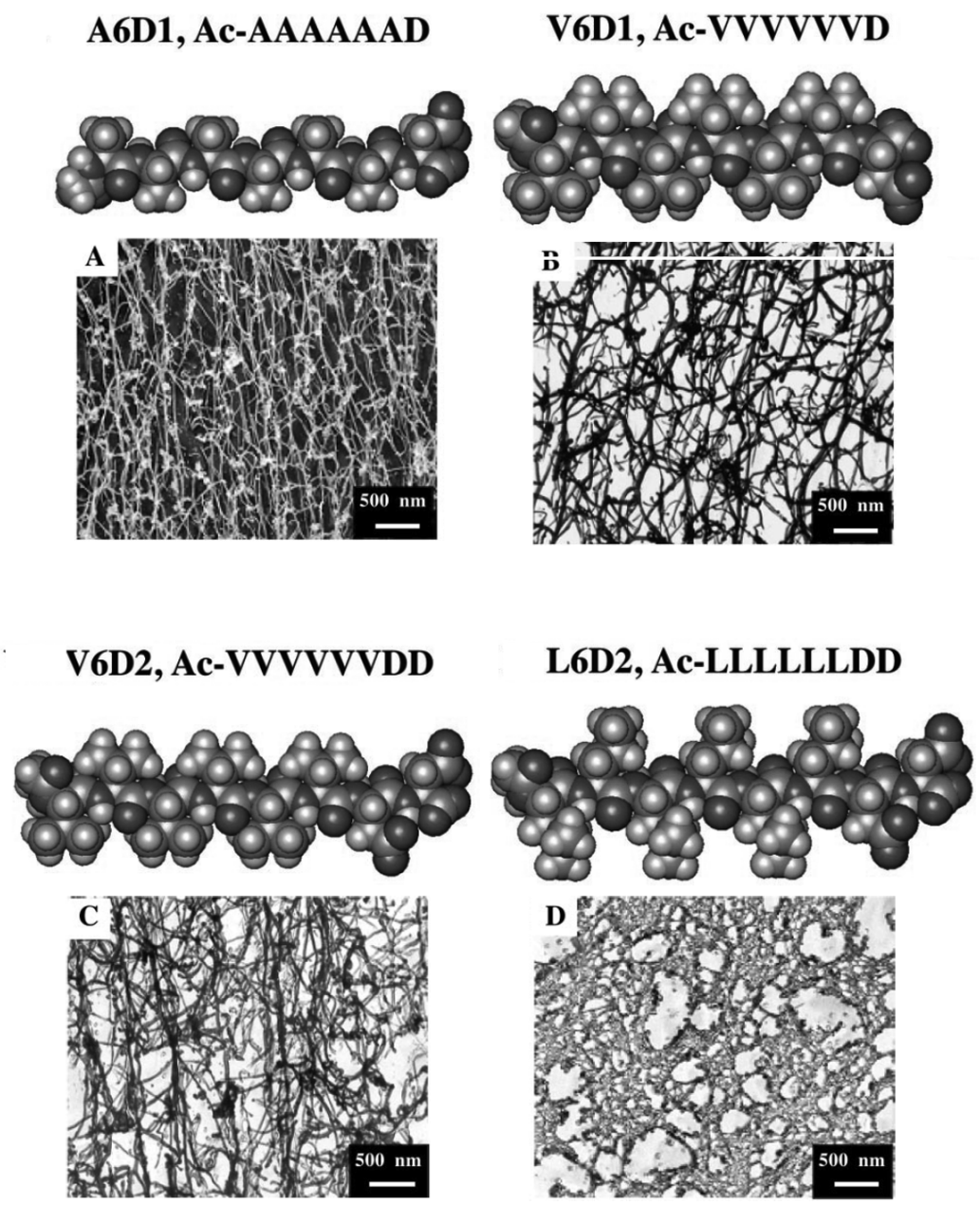

Figure 1.6. Molecular models and quick-freeze/deep-etch TEM images of (A) A_6D; (B) V_6D; (C) V_6D_2; and (D) L_6D_2 in water. (Used with permission. Copyright (2002) National Academy of Sciences, USA).

In addition to exploring the effects of tail hydrophobicity on the self-assembly process of PAs with negatively charged head groups, scientists have also

examined the effect of extending the tail length. Santoso *et al*., for example, prepared four negatively charged PAs (G_4D_2, G_6D_2, G_8D_2, $G_{10}D_2$) containing 4, 6, 8, or 10 glycine residues in the hydrophobic tails and two asparatic acid residues in the hydrophilic head.[35] As illustrated in Figure 1.7, after self-assembly, the TEM images revealed a more entangled network of nanotubes with greater polydipersity as the number of glycine residues increased.

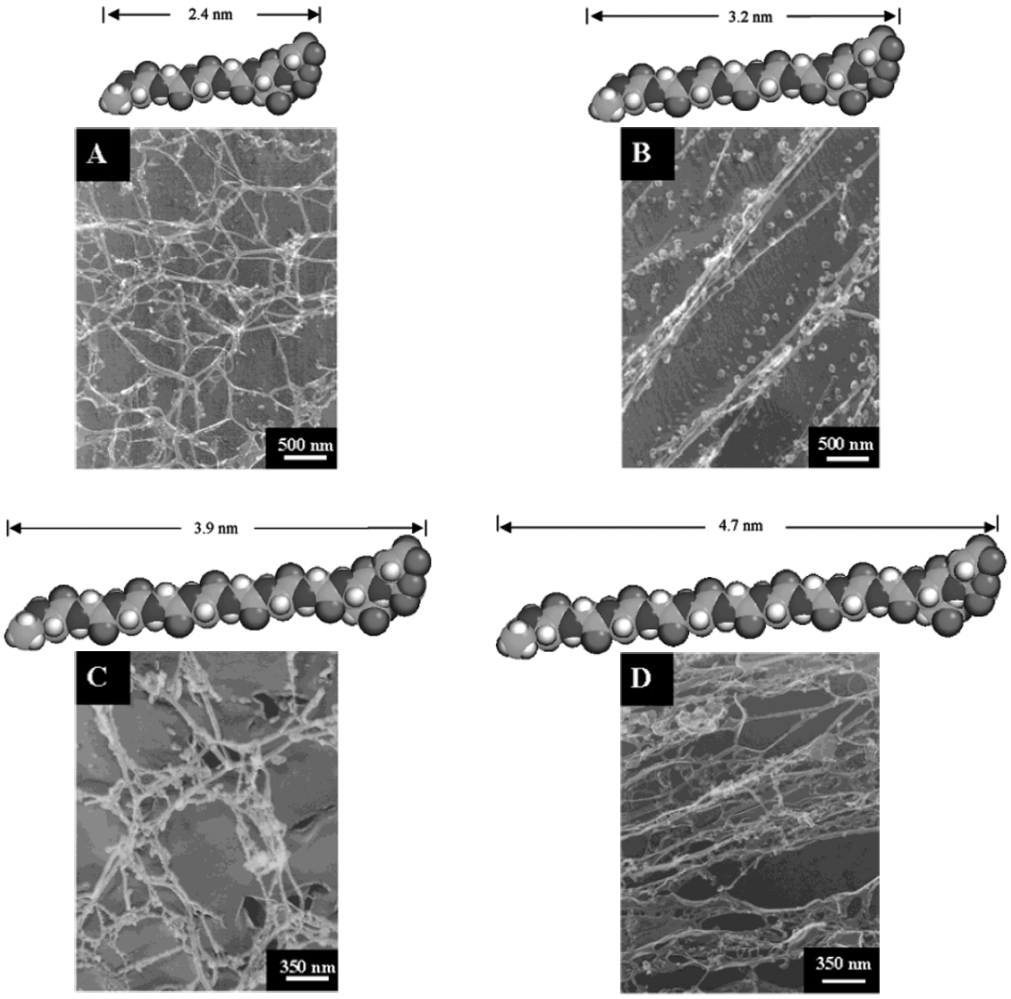

Figure 1.7. Molecular models and quick-freeze/deep-etch TEM images of (A) G_4D_2; (B) G_6D_2; (C) G_8D_2; and (D) $G_{10}D_2$ in water. (Used with permission. Copyright (2002) American Chemical Society, USA).

PAs with positively charged head group: In addition to negatively charged PAs, positively charged PAs have also been described that contain lysine or histidine amino acids as the head group.[36] The TEM analysis of the aqueous solutions of these peptides revealed a network of nanotubes and vesicles very similar in morphology and dimensions to the nanostructures obtained from the negatively charged peptide lipids.

PAs with mixed hydrophobic tail group: Recently, Khoe *et al.*, in 2009 have reported the synthesis of a positively charged cone-shaped peptide amphiphile Ac-GAVILRR-NH_2, that contains a hydrophilic head group comprised of two arginine residues and a hydrophobic tail group derived from a mixture of 5 hydrophobic amino acids with decreasing size towards the N-terminus (cone-shape) (Figure 1.8, A and B).[37] Interestingly, this peptide was found to self-assemble into a nanodonut structure having an outer diameter of approximately 105 nm (Figure 1.8, C and D).

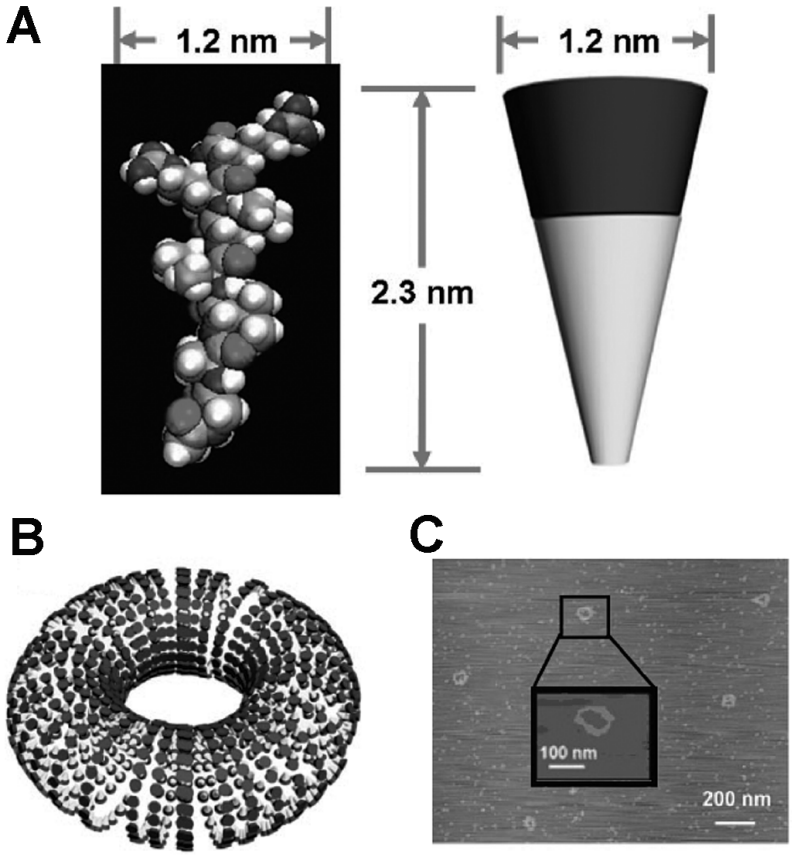

Figure 1.8. Peptide Ac-GAVILRR-NH_2. (A) 3-D molecular model; (B) depiction of the cone-shape of the peptide; (C) model of the nanodonut; (D) AFM image in water at a concentration of 1 μM. (Used with permission. Copyright (2009) American Chemical Society, USA).

1.2.2.2 Amphiphiles from Hybrid Building Blocks

Stupp and colleagues have developed novel hybrid PAs comprised of four key elements, which embody the structural features of surfactants and the function of bioactive peptides.[38] As illustrated in Figure 1.9 A, region (1) of these PAs contains a hydrocarbon tail consisting of a long fatty acid chain such as palmitic acid, linked via an amide bond to the N-terminus of the peptide chain. Region (2) contains a short sequence of hydrophobic amino acids which have a strong

tendency to form β-sheet hydrogen bonds. Region (3) consists of one or two charged amino acids incorporated to improve the solubility of the molecule. Finally, region (4) features a bioactive peptide sequence that is incorporated for a targeted application. Under physiological conditions, the PA shown in Figure 1.9 B for example, self-assembles into a nanofiber scaffold, whereby each nanofiber is an individual cylindrical micelle with a diameter of approximately 8 nm. In this manner, the hydrocarbon tail groups point inward and the bioactive peptide sequence is expressed on the outer surface.[38]

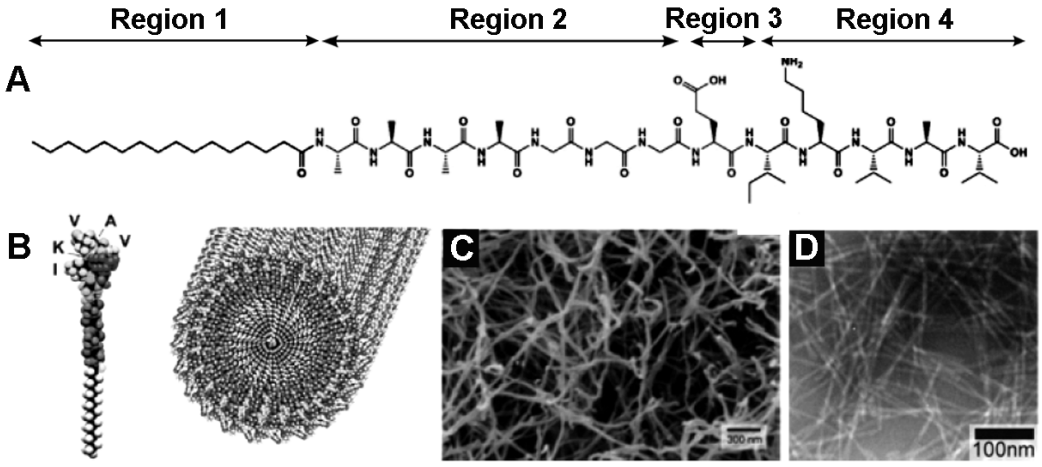

Figure 1.9. (A) Molecular structure of a representative PA showing the four rationally designed regions; (B) molecular model illustrating the PA and its subsequent self-assembly into nanofibers; (C) SEM image of the nanofiber network under physiological conditions; (D) TEM image of the nanofibers. (Used with permission. Copyright (2010) John Wiley & Sons, Inc).

In order to design PAs that self-assemble into nanostructures with desirable dimensions and physical properties for biomedical applications, variations in the PA molecular structure have been explored, along with the coassembly of different PAs, as described in the following section.

Variations in the molecular structure:

Variation in Region 1 (Figure 1.9): The effect of hydrophobicity on the self-organization of hybrid PAs was investigated by Hartgerink *et al.*, using various hydrophobic tail lengths.[39] During the course of their studies, they determined that alkyl chains of at least 10 carbons are required for the PAs to self-assemble into fibrous hydrogels, in order to have a sufficient hydrophobic effect that can counteract the repulsive intermolecular electrostatic interactions in region 3. For PAs with alkyl chains longer than 10 carbons, the cylindrical morphology of the nanofibers and the gelation properties of the PAs remains the same regardless of the length.

The alkyl chain region has also been demonstrated to serve as a handle in which to covalently link other PAs. Several studies for instance, have described PAs with diacetylene functional groups in these alkyl chains (Figure 1.10).[40-42] Upon irradiation with UV light, the diacetylene polymerizes in the core of the nanofibers to form highly conjugated polydiacetylene backbones. Since the shape and size of the nanofibers are not disrupted by this process, such materials may have improved stability and exhibit interesting electronic properties in addition to bioactivity.[41]

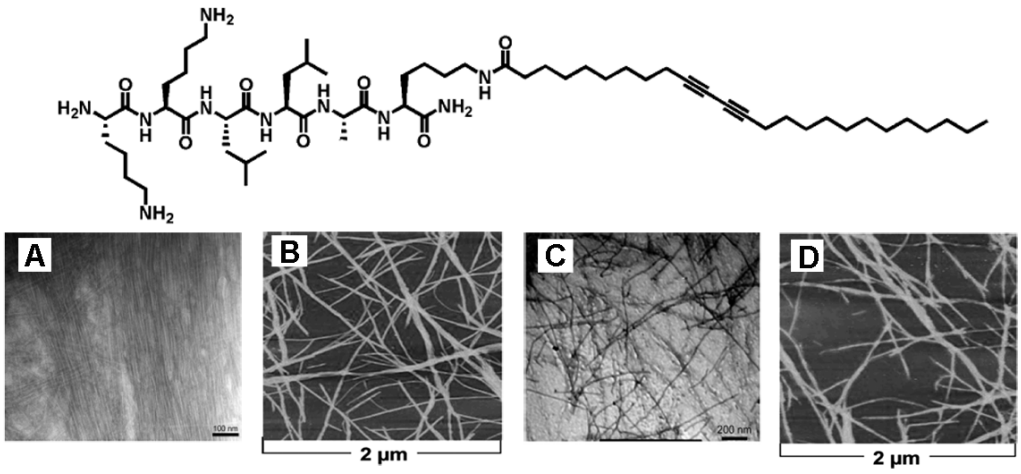

Figure 1.10. (A) Chemical structure of KKLLAK-OC 25 H 40 peptide; (B,C) TEM and AFM images, respectively, before irradiation; (D,E) TEM and AFM

images, respectively, after exposure to λ = 256 nm for 2 min. (Used with permission. Copyright (2008) American Chemical Society, USA).

Variation within Region 2: This region is made of short peptide sequences consisting of hydrophobic amino acids that have a strong propensity for β-sheet H-bonding among the middle peptide segments in the nanofibers. A recent study by Jiang *et al.*, showed that these H-bonds are oriented parallel to the axis of the fiber (Figure 1.11).[43] These interactions not only provide additional stability and organization to the molecular packing of the PAs, but also improve the nanofiber mechanical properties.[38] That being said, Niece and coworkers found that replacing glycine residues with bulky hydrophobic (alanine or isoleucine) or hydrophilic (serine) amino acids in this region, can increase the gelation time (i.e. suppress the formation) of the PAs.[44]

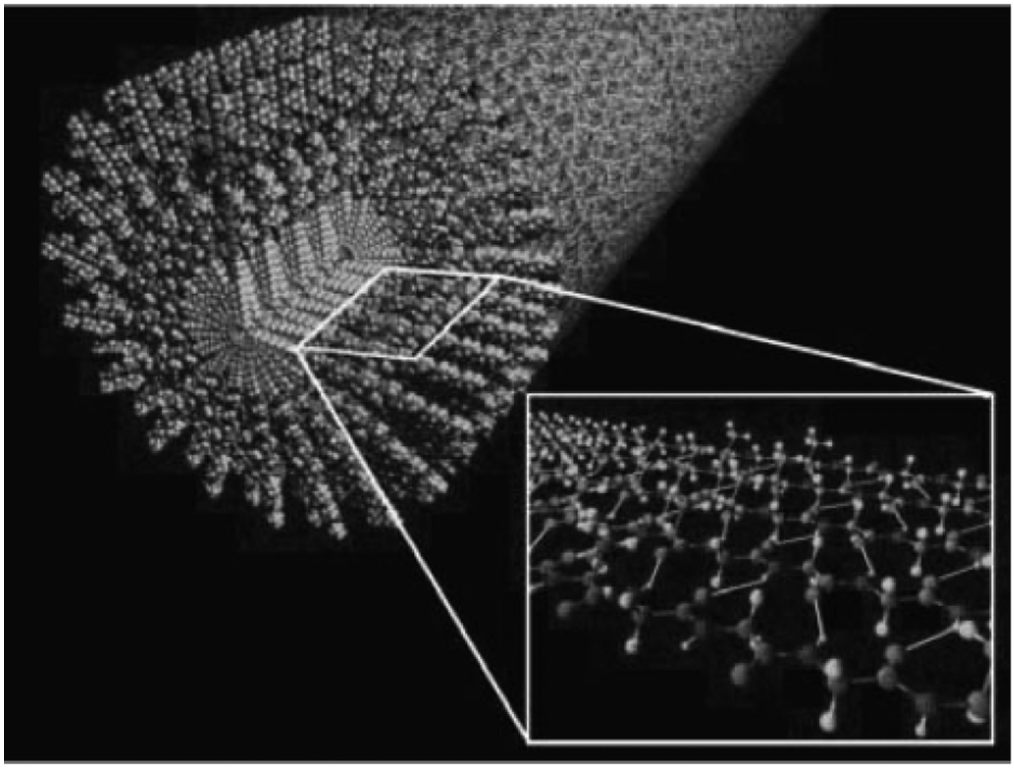

Figure 1.11. Schematic representation of β-sheets within PA nanofibers. (Used with permission. Copyright (2007) Royal Society of Chemistry, UK).

Interestingly, Hartgerink and coworkers also demonstrated the incorportation of amino acids capable of forming covalent bonds in region 3.[39,45] The PAs were designed to have four consecutive cysteine residues, which upon oxidation, form disulfide bonds with the adjacent nanofibers. By adding a mild reducing agent such as dithiothreitol (DTT), the supramolecular structure can once again be "unlocked." This reversible cross-linking strategy enables the rigidity of the nanofiber and the mechanical properties to be altered when desired (Figure 1.12).

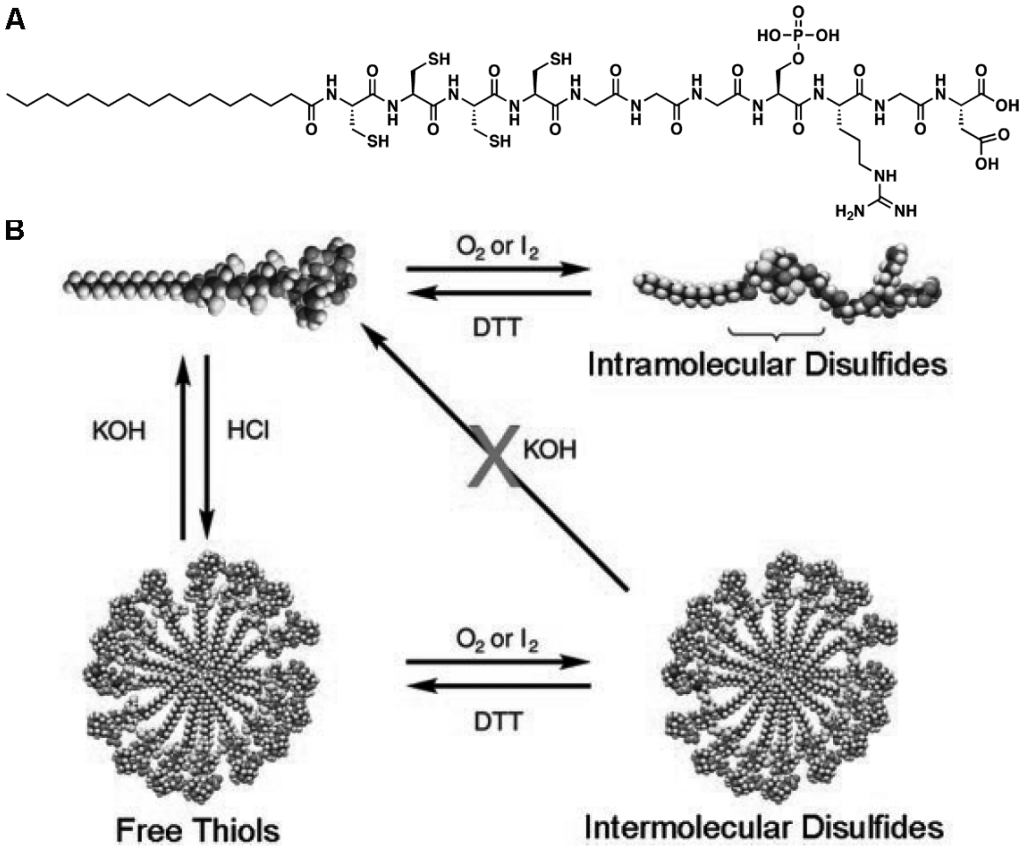

Figure 1.12. (A) Chemical structure of a representative PA showing the four consecutive cysteine residues in Region 2; (B) schematic representation of the self-assembly under acidic conditions and cross-linking upon oxidation. (Used with permission. Copyright (2002) National Academy of Sciences, USA).

Variation within Region 3: This region generally has only one or two positively (lysine, histidine) or negatively (glutamic acid, aspartic acid) charged amino acid residues to increase the solubility of the peptide in water and assist in the purification.[38] Stendahl *et al*., established, that by adjusting the protonation state of the carboxylate or ammonium groups of these resides through pH changes in the solution, the assembled or disassembled states of the PAs can be promoted.[46] Adding an inorganic salt such as $CaCl_2$ also screens the charges on the PAs to trigger self-assembly.

Variation within Region 4: The last segment of the PA is the bioactive peptide sequence, which is incorporated for biomedical applications. Two commonly used peptides are RGDS and IKVAV.[38] RGDS is found in many extracellular matrix (ECM) proteins such as fibronectin, vitronectin, type I collagen, osteopontin and bone sialoprotein and acts as a key mediator of cell adhesion.[47] This short peptide is thus used to mimic ECM components for PAs applications in bone tissue engineering.[48] IKVAV alternatively, is critical for cell attachment, migration, and neurite outgrowth and is incorporated into PAs for neural applications.[38] Details pertaining to the applications of both RGDS and IKVAV conjugated PAs are described in Section 1.3.2.

Coassembly of PAs: Coassembling more than one PA presenting different bioactive sequences is a novel method to construct nanofibers that display multiple bioactive signals at the surface for a synergetic effect. This can be achieved by mixing two PAs that contain oppositely charged amino acids. Niece *et al*., demonstrated this concept with the coassembly of a PA containing glutamic acid in region 3 followed by the IKVAV bioactive sequence at the C-terminus, with a second PA that featured lysine followed by YIGSR (Figure 1.13).[49]

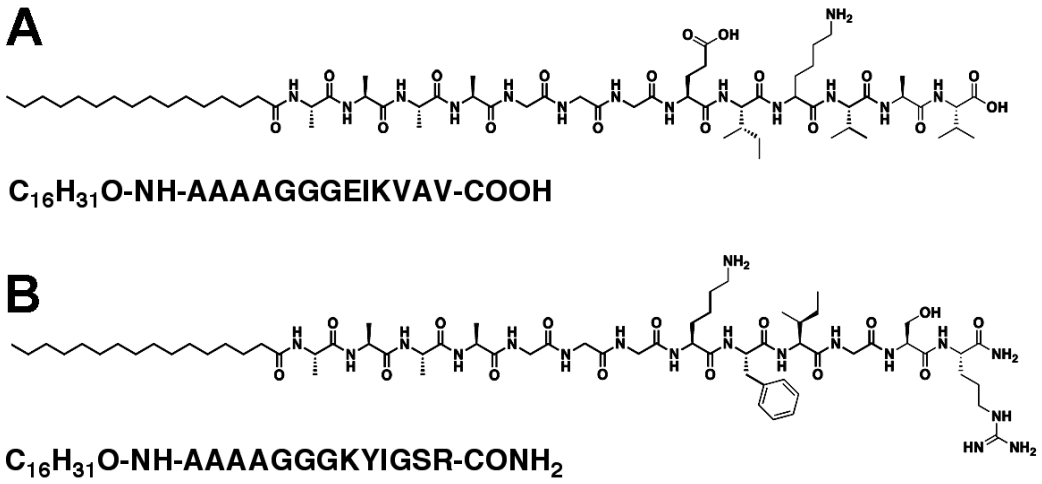

Figure 1.13. Chemical structure of the two oppositely charged PAs containing (A) negatively charged glutamic acid in Region 3; (B) positively charged lysine in Region 3. (Used with permission. Copyright (2003) American Chemical Society, USA).

Behanna *et al*., also demonstrated that two PAs with opposite charges in region 3 could form mixed nanofibers.[50] Specifically, they designed complementary PAs in which the last three amino acids in the peptide sequence were positively (lysine) and negatively (glutamic acid) charged, while maintaining the same structure in the rest of the molecule (Figure 1.14). They found that the PAs had a very strong tendency to coassemble together to generate an unusually stable nanostructure compared to the self-assembly of the individual components.

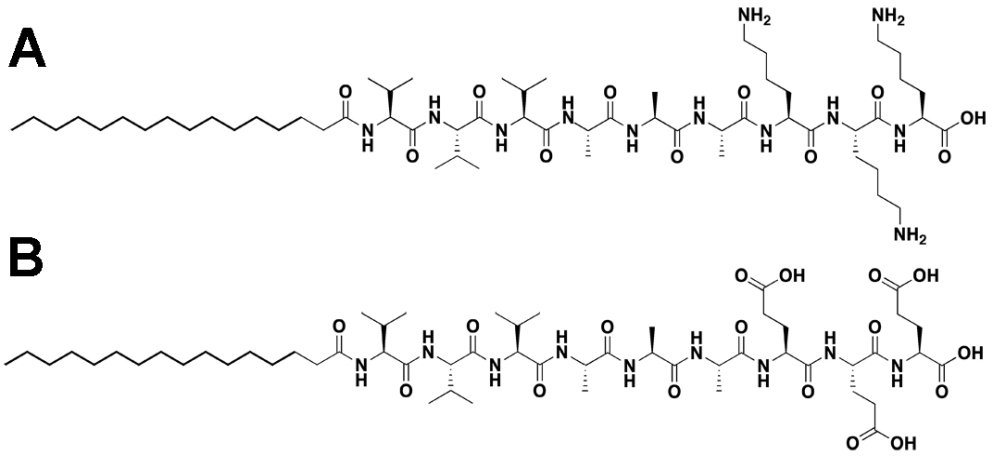

Figure 1.14. Chemical structure of two PAs with complementary charges containing (A) three positively charged lysine residues at the C-terminus; (B) three negatively charged glutamic acid residues at the C-terminus. (Used with permission. Copyright (2005) American Chemical Society, USA).

1.3 Biomedical Applications of Peptide-Based Materials

The damage or failure of an organ or tissue is one of the most costly problems in human healthcare.[51] Recent advances in the field of tissue engineering however, have aimed to develop functional artificial tissues that can replace, restore or repair the organ or tissue including that of bone, cartilage, skin, bladder, liver, heart, and spine among others.

The most effective method for fabricating artificial tissues involves seeding living cells (usually stem cells) in a pre-made biocompatible scaffold *in vitro*, while maintaining the medium requirements for cell growth and differentiation such as oxygen, pH, humidity, ambient temperature and nutrients. As artificial scaffolds, ionic self-complementary and surfactant-like peptide hydrogels are biocompatible and biodegradable and can be designed with varying mechanical properties depending on the peptide concentration or the amino acid sequence.[7] As this concentration can be as low as ~ 1%, this poses no barriers for the cells to access

the required nutrients. The following sections describe a variety of studies that have used ionic self-complementary and surfactant-like peptide hydrogels as scaffolds for neural engineering, angiogenesis and bone tissue engineering applications.

1.3.1 Applications of Ionic Self-Complementary Peptides

As described in Section 1.2.1, ionic self-complementary peptides form fibrous hydrogel scaffolds with a 50-100 nm porosity and a very high water content (>99%). These scaffolds therefore closely mimic the extracellular matrix, which allow cells to attach and grow in a biocompatible 3D environment, in the presence of nutrients that can diffuse in and out very slowly.[20] Several *in vitro* studies, involving cells seeded or attached on these peptide scaffolds, indicated that cells were well maintained and viable during the time frame of the studies. Semino *et al*., for example, demonstrated that adult rat hepatocyte progenitor cell (Lig-8) viability was close to 90% in RAD16-I peptide scaffolds (1% wt) over a period of 4 days.[52] Another example by Narmoneva *et al*., showed that microvascular endothelial cells embedded in the RAD16-II (1% wt) scaffold were viable for up to 2 weeks.[53] Along with demonstrating the *in vitro* biocompatibility, several *in vivo* studies showed that the injection of ionic self-complementary peptides in animals did not cause any immune response or toxic effects.[20] For instance, RAD16 or EAK16 peptides (1 mg/ml) injections (20 μl each) in rat legs did not show muscle necrosis or inflammation at the site of injection 5 weeks after treatment.[25] This biocompatibility and lack of immunogenicity is important to reduce immune rejection upon application in tissue engineering.

Zhang has been a leader in demonstrating the interesting cellular behaviors that ionic self-complementary peptide hydrogels can induce, including cell attachment, growth, migration, differentiation and production of their own ECM.[20] For example, RAD16-I having four repeating units of RADA (see Section

1.2.1), has an amino acid sequence and cell-attachment activity that is similar to the well-known cell adhesion receptor integrin RGD.[54,55] This particular peptide was the first commercially available peptide matrix and has been marketed under the name "PuraMatrix" (3DM, Inc., Cambridge, MA, USA).[56]

Applications in neural tissue engineering: One of the prominent application areas that ionic self-complementary peptide hydrogels have been used in is neural tissue engineering. These 3D scaffolds promote neural cell differentiation by functioning in a similar manner to extracellular matrix proteins.[5] Holmes *et al*., demonstrated this quite well by showing that RAD16-II could support extensive neurite outgrowth, and that most importantly, had a permissive environment for the formation of functioning synapse connections (Figure 1.15).[25] This is a very interesting observation because very few new neurons are produced in the adult central nervous system, and neurons that lack an appropriate substrate cannot re-grow.[57] Moreover, this neuron-hydrogel matrix can be readily transported from one medium to another, making it suitable for transplantation into patients.[4]

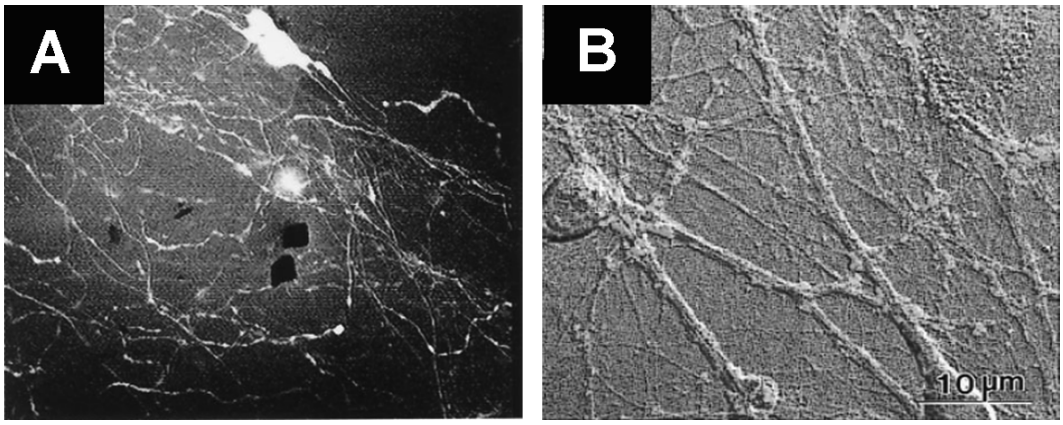

Figure 1.15. Confocal images of (A) nerve growth factor (NGF) preprimed PC12 rat pheochromocytoma cells attached to RAD16-II and showing extensive neurite outgrowth; (B) primary rat hippocampal neurons with active synapses on the RAD16-II scaffold. (Used with permission. Copyright (2000) National Academy of Science, USA).

Recently, Gelain *et al.*, demonstrated that neural stem cell differentiation and survival can be supported by RAD16-I hydrogels functionalized with the marrow homing motifs BMHP1 and BMHP2, in the absence of extra soluble growth factors.[58] The observed neural stem survival and differentiation was very similar to that observed when using the Matrigel scaffold, which is a natural extract considered the most effective and standard cell-free substrate for stem cell cultures.

RAD16-I scaffolds can also promote *in vitro* cellular migration. To this end, Semino *et al.*, have presented a report describing the migration of neural cells from postnatal hippocampal brain slices successfully entrapped on a layer (~500 μm) of a RAD16-I hydrogel and new tissue was observed after 3 days at the interface between the slice and the peptide hydrogel.[59]

Along with their use *in vitro*, ionic self-complementary peptide hydrogels have served as excellent scaffolds *in vivo*. Ellis-Behnke *et al*., for instance, applied RAD16-I in the repair of injured brain tissue in the central nervous system (CNS) of Syrian hamsters.[60] In their study, a knife cut of 1.5 mm deep and 2.0 mm wide was created in the midbrain (optic tract within the CNS) of a young and adult Syrian hamster, which caused the vision function of the animals to collapse. A solution of the RAD16-I peptide was then injected in these gaps to promote neural cell growth. After 72 h, the gaps had completely closed and more significantly, 75% of the vision function in the animals was restored. This observation is in stark contrast with control animals treated with saline solutions, in which the gaps did not close and no restoration of the vision was obtained. Although the mechanism of this neural gap closure is not well understood, it is likely that the hydrogel works at the nanoscale level with the ECM on both sides of the sliced area, to provide a permissive environment that allows for the migration of the generated cells through the hydrogel onto the other side (Figure 1.16).[60]

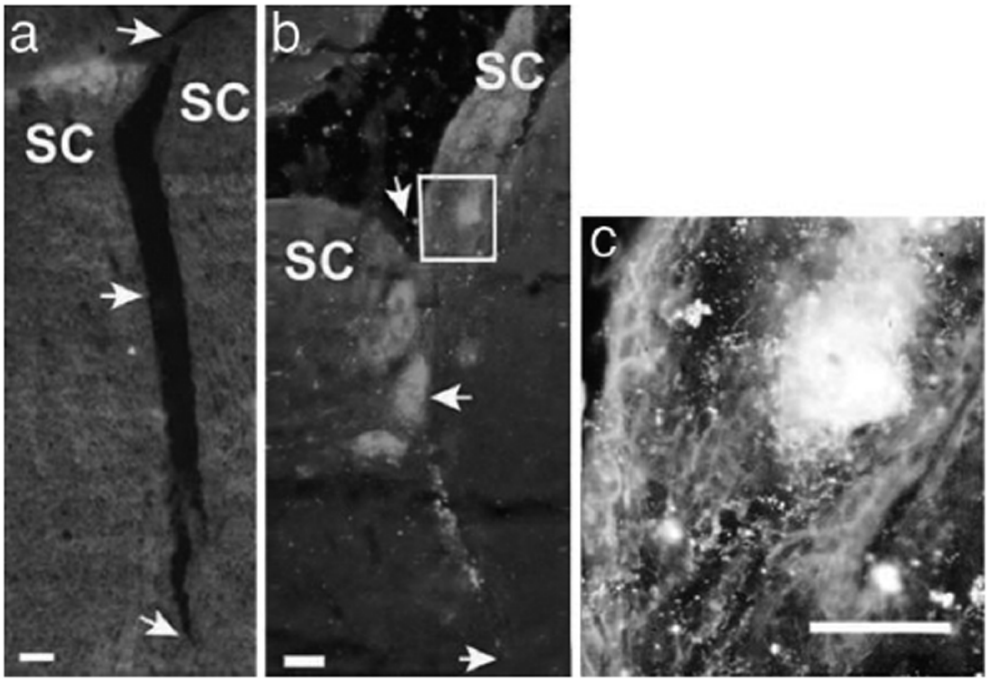

Figure 1.16. Dark-field composite photos of parasagittal sections from animals 30 days after treatment. (a) Section from the brain after 30 days of treatment with saline solution shows the failure of the tissue healing; (b) a similar section from the brain treated with self-assembled peptide hydrogels after 30 days; (c) enlarged view of the boxed area in b. (Used with permission. Copyright (2006) National Academy of Science, USA).

Applications in angiogenesis and vascularization: Establishing a sufficient blood supply for oxygen and nutrients to reach cells is critical for the *in vitro* generation of an artificial tissue or the *in vivo* healing of a damaged tissue.[61,62] In this regard, ionic self-complementary peptide hydrogels are promising scaffolds to support angiogenesis; the formation of new blood vessels from existing vessels.[53,63-67] As an example of this, Narmoneva *et al*., have shown that human microvascular endothelial cells (MVEC) seeded on the surface of RAD16-II, undergo rapid spatial organization to form interconnected vascular networks within 16 h (Figure 1.17 A-C).[53] The peptide scaffold also inhibits endothelial cell apoptosis without the addition of angiogenic factors. In contrast, MVEC seeded on the surface of collagen type I gels, remain attached and randomly distributed (Figure 1.17 D-F).

As an alternative *in vivo* example, RAD16-II has been used to create an injectable microenvironment within the myocardium of beating mice hearts, in order to promote angiogenesis and the formation of a microvascular network. After 28 days of the injection, endothelial cells were spread and vascular network was observed within the injected hydrogel area.[68]

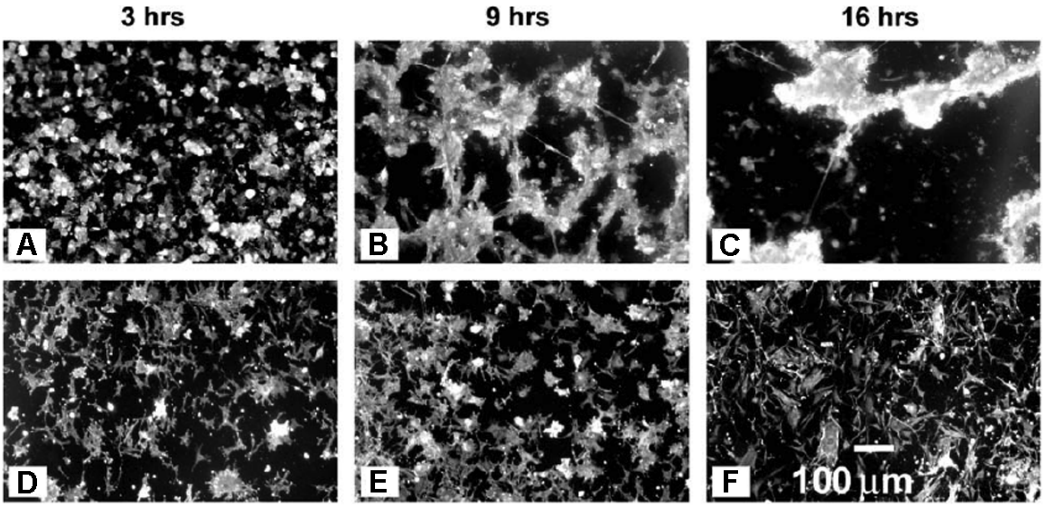

Figure 1.17. (A-C) Capillary-like network formation by MVEC seeded on the surface of a RAD16-II peptide hydrogel; (D-F) MVEC seeded on the collagen gel maintained their initial random distribution. (Used with permission. Copyright (2005) Elsevier Ltd).

Functionalization of the peptide scaffold is a further strategy that can be used to enhance angiogenesis and vascularization. Wang *et al*., recently reported two RAD16 peptide scaffolds functionalized with KLT (KLTWQELYQLKYRGDS-$CONH_2$) and PRG (PRGDSGYRGDS-$CONH_2$), that have enhanced angiogenic activities and endothelial cell survival, proliferation, migration, and capillary network formation, compared to the unfunctionalized peptide scaffold.[67]

Applications in bone tissue engineering and cartilage repair: Bone and cartilage defects resulting from traumatic injuries or deterioration from aging, severely impact the functioning of the skeletal system and joints. Cell seeded

biocompatible scaffolds have the potential to become the treatment of choice to initiate *de novo* tissue regeneration on the defect site.[69] Ionic self-complementary peptide scaffolds have demonstrated excellent potential for the repair of these tissues because they are able to stimulate cell adhesion and division and provide the appropriate environment for the accumulation of ECM produced by the seeded cells. Kisiday *et al.*, have shown for example, that the hydrogel made from the self-complementary ionic peptide KLD16-I (Ac-KLDLKLDLKLDLKLDL-NH_2), provides an appropriate environment for the retention and maintenance of chondrocyte (cartilage forming cells) morphology during the culture period (4 weeks) and also promotes the synthesis of functional cartilage ECM. This leads to the deposition of mechanically functional neo-tissue.[70]

In regards to bone tissue regeneration, *in vitro* studies on animal and human osteoblast cells seeded in multi-functional RAD16-I peptide hydrogels, exhibit enhanced osteoblast adhesion, proliferation and migration into the hydrogel, as well as function in producing ECM proteins without the need for additional growth factors. These studies have included RAD16-I conjugated to polyHIPE (PHP) (formed by high internal phase emulsion polymerization) polymers[71], the osteogenic growth peptide ALK (ALKRQGRTLYGF), osteopontin cell adhesion motifs DGR (DGRGDSVAYG) and PGR (PRGDSGYRGDS)[72], as well as the laminin cell adhesion motif PDS (PDSGR).[73]

1.3.2 Applications of Surfactant-Like Peptide Amphiphiles

The linear PAs described in Section 1.2.2, are made of hybrid building blocks and have great promise for tissue engineering applications.[44] This is because the peptides form pH and ionic strength responsive β-sheet fibrous hydrogels containing >99% water and also have controllable gelation kinetics and properties. Furthermore, these materials can be covalently functionalized with

bioactive motifs in region 4 (Figure 1.9), as well form co-assemblies to generate multifunctional fibers expressing more than one biological signal at the surface.

Similar to ionic self-complementary peptides, PA nanofibers resemble the filamentous structures in natural ECM, which results in a highly biomimetic and biocompatible matrix in which embedded cells can survive and function normally.[38,44,74] Silva *et al*., for example, demonstrated that neural progenitor cells encapsulated *in vitro* within IKVAV functionalized PA matrix (1% wt) remained viable and active for three weeks.[75] More importantly, *in vivo* studies involving several PAs indicated that these materials are biocompatible and nontoxic. Guler *et al*., for instance showed that RGDS functionalized PAs (10 mg/ml) injected (10 μl) subcutaneously in mice did not cause any inflammatory response in the site of injection during 4 days.[48] This indicates that these peptides are too the short to elicit an immune response and that their self-assembly into nanofibers does not induce a significant foreign-body response.

To further enhance the biocompatibility and performance of the PAs, several branched PAs (b-PA) and branched double PAs (b-d-PA) shown in Figure 1.18, have been developed that use a lysine dendron in region 3 functionalized with the RGDS adhesion motifs in region 4.[76,77] These b-PAs also self-assemble into nanofibers, but exhibit a lower bioactive motif packing density at the surface. As a result, they have improved cell adhesion, spreading and migration compared to their linear counterpart.

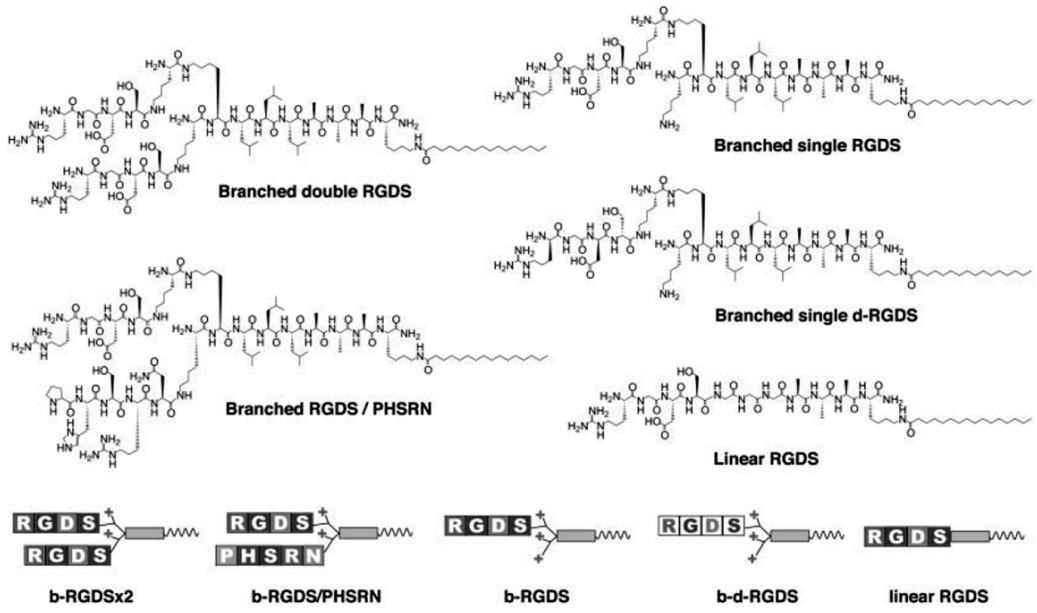

Figure 1.18. The chemical structure of linear, branched (b-PA), and double branched (b-d-PA). PAs functionalized with the RGDS bioactive peptide. (Used with permission. Copyright (2006) John Wiley & Sons, Inc).

Applications in neural engineering: Several studies have demonstrated the potential of the PA scaffold for neural tissue engineering applications when functionalized with the sequence IKVAV. This peptide is found in the laminin protein and is crucial for neurite cell attachment, migration and outgrowth.[78]

The first of these studies was reported by Silva *et al.*, in 2004.[75] They demonstrated that progenitor neural cells seeded in the IKVAV functionalized PAs, display neurite outgrowth and undergo rapid and selective differentiation into neurons compared to cells cultured in laminin or unfunctionalized PAs. This has been attributed to the high density of the bioactive motifs at the surface of the nanofibers, relative to motif density in laminin in solution.

This *in vitro* observation later inspired the use of PAs for the treatment of mouse spinal cord injuries *in vivo*. More specifically, Tysseling-Mattiace *et al.*, investigated the incorporation of the IKVAV-PA hydrogel into an injured section

of a mouse spinal cord.[79] After 10 days, they observed reduced cell death and astrogliosis and increased the number of oligodendroglia at the injured site. The treatment also enhanced the density of serotonergic fibers caudal to the lesion and promoted the regeneration and/or sparing of descending motor fibers and ascending sensory fibers. This resulted in significant behavioral improvements in the animals after only 5 weeks.[79,80]

Applications in angiogenesis: Several studies have also reported the use of PAs in promoting angiogenesis. For these studies, the PA (HBPA) containing the positively charged binding sequence LRKKLGKA in region 4 is used to form an electrostatic complex with negatively charged heparin molecules. Heparin is a natural highly sulfated polysaccharide that binds angiogenic growth factors such as the vascular endothelial growth factor (VEGF) and fibroblast growth factor 2 (FGF-2). This complex formation is required to boost cell signaling for new blood vessel formation.[81-83] Because of the charge screening that results upon forming the heparin-PA (HBPA), self-assembly occurs without the need for inorganic salts.

Rajangam *et al*., have demonstrated that PA-heparin hydrogels containing VEGF/FGF-2 growth factors promote significant neovascularization in damaged rat cornea *in vivo*, compared to that observed with collagen gels containing heparin and/or growth factors (Figure 1.19).[83] In a subsequent study, they determined that this heparin binding sequence is essential for the observed angiogenesis.[84] PAs containing a scrambled heparin-binding sequence for example, had less angiogenic activity due to a weaker (less stable) interaction with the heparin in the hydrogel.

PA-heparin hydrogels containing VEGF/FGF-2 growth factors have also been used to facilitate the transplantation of islet cells from a donor mice pancreas into host mice omentum with type I diabetes.[85] This treatment led to enhanced blood vessel density in the omentum as a result of better signaling due to the larger

surface area presentation of heparin (bound to the nanofibers) to the added growth factors. Compared to the control mice, the treated mice exhibited higher incidences of normoglycemia or a normal sugar content in blood.

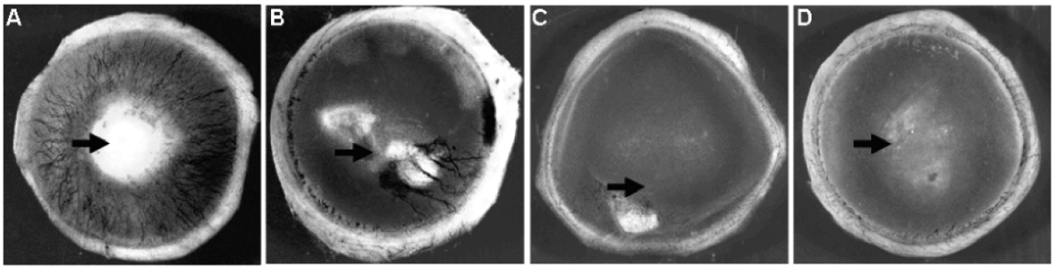

Figure 1.19. Rat cornea photographs 10 days after treatment with (A) Heparin-PA hydrogel plus growth factors. Extensive neovascularization can be seen; (B) control of collagen plus heparin and growth factors; (C) collagen plus growth factors; and (D) Heparin and growth factors. (Used with permission. Copyright (2006) American Chemical Society, USA).

As a further example of the use of PA's for angiogenesis applications, Webber and colleagues described a PA that features the VEGF mimetic oligopeptide sequence, KLTWQELYQLKYKGI in region 4.[86,87] This particular PA was found to promote the *in vitro* proangiogenesis in endothelial cells and enhance the *in vivo* angiogenic response in the host vasculature during the chicken chorioallantoic membrane assay. This scaffold also increased tissue perfusion, functional recovery, and treadmill endurance in mouse ischemic hind-limb tissue repair.[87]

Applications in bone tissue engineering: The NiTi alloy is one of the implant materials currently used for restoring the function of an injury in the human skeleton. In order to increase the biocompatibility and bioactivity of the NiTi alloy surface for bone cells, several inorganic and organic coatings, including growth factors containing the cell adhesive RGD peptide[88], have been introduced to the surface by physical deposition. This coating approach however, has limited

long-term success because of the dissolution of this functional layer.[47] One approach to overcoming this obstacle has been to covalently attach the functional motifs directly onto the surface of the alloy. Typically, aminosilanes are used to bind to the hydroxy groups on the TiO_2 surface, leaving the exposed amino functionalities to covalently attach to peptides or proteins using coupling reactions (Figure 1.20).[89,90] Sargeant *et al*., demonstrated this TiNi functionalization strategy using RGD-PA nanofibers, and found that there was significant osteoblast cell adhesion, compared to the unmodified alloy surface.[91]

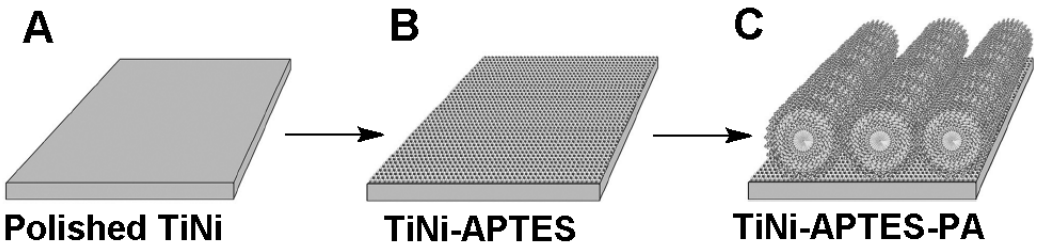

Figure 1.20. Schematic presentation of the covalent functionalization of TiNi surface; (A) polished TiNi surface; (B) TiNi coated with aminopropyltriethoxysilane (APTES); and (C) PA nanofibers covalently attached to the APTES layer on the TiNi surface. (Used with permission. Copyright (2008) Elsevier Ltd).

An alternative functionalization strategy was also reported by Sargeant *et al.*, in the same year.[92] In this study, they prepared a Ti-6Al-4V alloy foam having a 52% porosity. This foam was then filled with the RGDS-PA nanofiber solution, which self-assembed into a hydrogel that fully occupied the pores. The resulting scaffold was found to induce *in vitro* mineralization and osteogenic differentiation as well as enhance *in vivo* bone formation around and inside the foam.

PA hydrogels have also been used for inducing and supporting enzyme-mediated hydroxyapatite crystallization for *in vitro* bone regeneration. For this purpose, the PA has been designed to feature a phosphorylated serine residue in region 3, in order to template hydroxyapatite in mineralized tissue using the acidic phosphates

as nucleation sites.[93] As described by Spoerke *et al.*, after incubating this PA in a mixture of culture and mineralization medium, the formation of hydroxyapatite crystals in the hydrogel could be observed that exhibit a morphology and orientation closely resembling the biological hydroxyapatite crystals in bone (Figure 1.21).

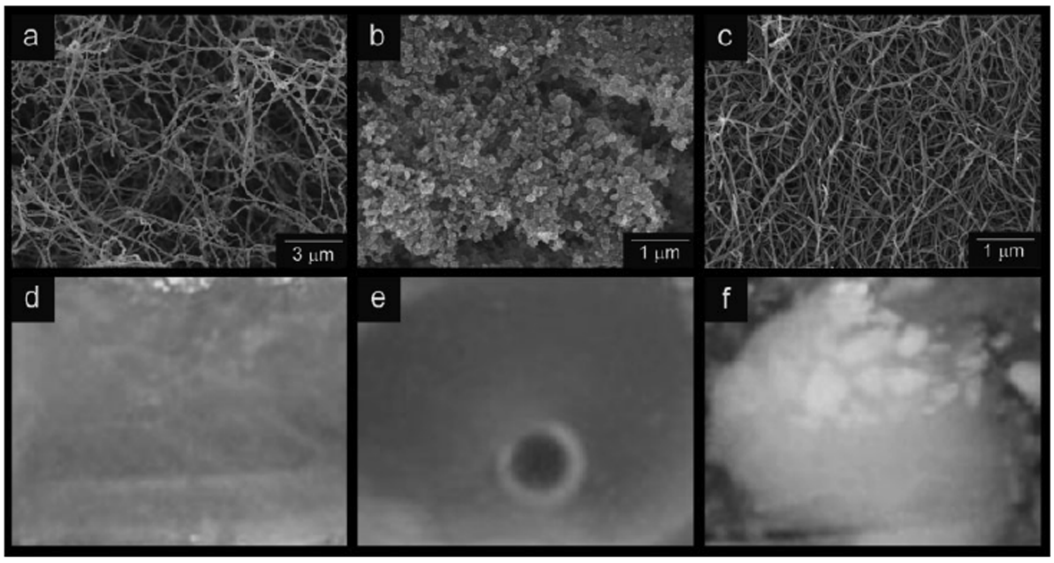

Figure 1.21. Top: SEM images of unmineralized gels of (a) collagen control; (b) alginate control; and (c) PA nanofibers. Bottom: Photographs of mineralized scaffolds after 14 days; (d) collagen gel; (e) alginate gel; and (f) PA gel, showing much higher hydroxyapatite mineralization in PA compared with the two controls. (Used with permission. Copyright (2009) John Wiley & Sons, Inc).

In addition to bone tissue applications, PAs have also been used for dental enamel regeneration. Enamel is the outermost layer of the vertebrate teeth, which is formed by ameloblast cells.[94] Reforming this tissue is challenging because ameloblasts undergo apoptosis with age, thereby preventing enamel regeneration during adulthood.[44] Huang *et al*., have demonstrated that ameloblast-like cells and primary enamel organ epithelial cells cultured within the RGD-PA hydrogel, exhibit enhanced proliferation and greater ECM protein production *in vitro*.[95] When injected *in vivo* into the enamel epithelia of mouse embryonic incisors, the

RGD-PA hydrogel induces cell proliferation and differentiation into ameloblasts at the site of injection.

1.3.3 Conclusion and Prospects

In Section 1.2, two types of peptide-based nanomaterials were described: ionic self-complementary and surfactant-like peptides, which self-assemble into β-sheet based fibrous hydrogels. These biologically inspired materials are promising scaffolds for biomedical tissue engineering applications for several reasons: (1) they are biocompatible and biodegradable; (2) economically viable for large scale synthesis; (3) they self-assemble into a network of fibers having 5-20 nm diameters and lengths up to several micrometers, thereby mimicking the dimensions of the natural biomolecules for better interactions with cells; (4) the scaffold pores can range in size from a few nanometers to a few hundred nanometers, which is appropriate for encapsulating biomolecules and slowly releasing them; (5) they can be functionalized with bioactive peptide sequences for specific applications, and finally; (6) they can express more than one biological signal through a coassembly process.

The formation of these supramolecular materials is not limited to these two types of peptides however, as there is extensive literature on other peptide systems that form β-sheet fibrillar structures not covered in this chapter. For example, several peptide sequences have been developed that contain only lysine and leucine amino acids (KLK, LKL, KL sequences), which self-assemble into β-sheet hydrogels in response to external stimuli such as enzymes or pH changes.[21,96-98] Twenty-residue self-assembling β-hairpin peptides have also been synthesized, that consist of alternating valine and lysine amino acids with two proline residues in the middle of the peptide.[99-102] These β-hairpin peptides form β-sheet hydrogels in response to changes in pH, light, heat, or inorganic salts.

In Section 1.3 however, the applications of ionic self-complementary peptides and surfactant-like peptide amphiphiles were explored in soft and hard tissue engineering including neural, vascular, bone, and cartilage tissue engineering. In addition to being biocompatible and biodegradable, these nanofibers resemble the structure and dimensions of natural ECM and were found to induce important cellular functions *in vitro* and *in vivo* including cell adhesion, proliferation, and differentiation.

Although the applications of the peptides in these three areas in tissue engineering were discussed, there are other *in vitro* and *in vivo* biological studies that have not been mentioned. For example, the RAD16-I hydrogel has been used in the *in vivo* treatment of rat kidney injuries[103] and deep second degree burns[104] as well as the inhibition of human breast cancer growth and leukemia.[105,106] Additional studies that have used RAD16 hydrogels include the work on hepatocyte cells[107] and embryonic fibroblasts[108,109] and spinal cord injury treatment.[110,111] For PAs, there are also other excellent studies, including that on cardiovascular disease treatment.[112,113] Although these scaffolds have proven to be biocompatible and bioactive both *in vitro* and *in vivo*, the mechanism by which they interact with cells remains unclear. Understanding this interaction will likely be one of the focuses in the future, as this is necessary to further increase the scaffolds bioactivity and to mimic the ECM in inducing multi-cellular functions.

1.4 Nucleic Acid Based Nanomaterials

1.4.1 Introduction

Inspired by the Watson-Crick hydrogen bonding arrays of adenine-thymine and guanine-cytosine pairs, several nucleic acid based supramolecular nanostructures have been designed over the past decade, including DNA nanotubes, G-quartets and rosette nanotubes (RNTs). Whereas DNA nanotubes are based on the self-assembly of complementary oligonucleotide chains, G-quartets are a tetracyclic

hydrogen bonded array of four guanine nucleosides. Both of these architectures have been well-explored and reviewed[114-117] and have found applications as therapeutic agents or as drug delivery vehicles.[8,115] As these applications do not coincide with the focus of this chapter in tissue engineering applications, they will not be described herein.

RNTs alternatively, are self-assembled from a synthetically-derived DNA hybrid molecule called the G∧C motif, which features the Watson-Crick donor-donor-acceptor hydrogen bonding arrays of guanine and acceptor-acceptor-donor hydrogen bonding arrays of cytosine.[118,119] Because of their tunable design features and biocompatibility, they have been studied as scaffolds for bone tissue engineering and cartilage repair as presented below.

1.4.2 Rosette Nanotubes: Design and Properties

The first reported synthesis of the G∧C motif was made by Marsh *et al*., and Mascal *et al*., in 1996. Possessing the complementary hydrogen-bonding array of both guanine and cytosine in the same molecule, the G∧C motif was found to form a hexameric rosette in solution maintained by 18 hydrogen bonds.[118,119] Fenniri *et al*., later demonstrated that these rosettes undergo a second level of organization in solution by π-π stacking, to form RNTs which have an inner channel diameter of 1.1 nm and a length of up to several micrometers (Figure 1.22).[6,120,121] In aqueous solution, this self-assembly process is entropically driven by the release of water molecules from the surface of the hydrophobic rosettes into the bulk solvent during the π-π stacking.[120] This leads to the formation of a viscous gel, which as described in Section 1.4.3, is an interesting and important feature of the RNTs for their use as injectable therapeutic agents for *in situ* tissue repair applications.

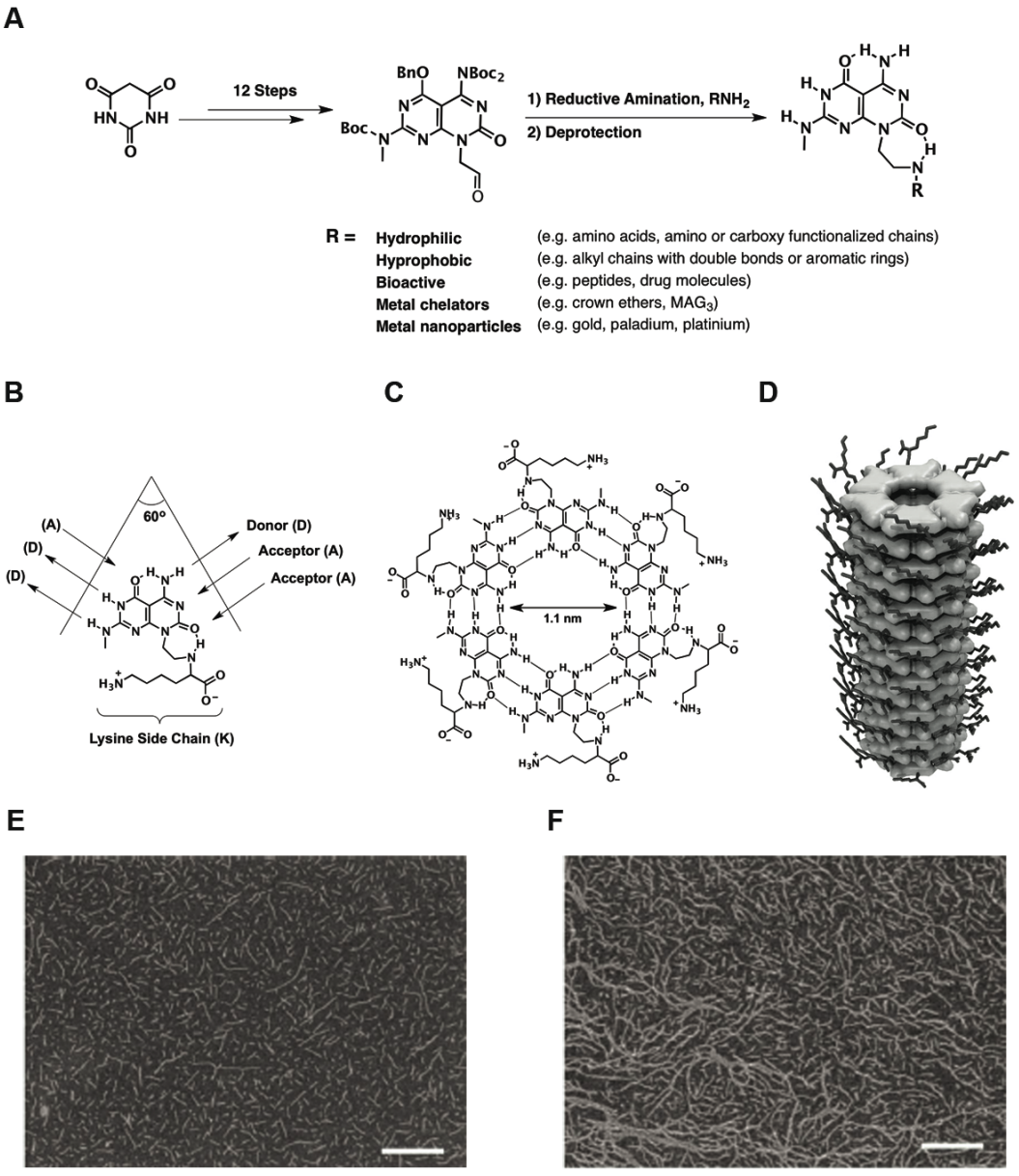

Figure 1.22. (A) The general strategy of the synthesis of the protected G∧C base aldehyde in 12 steps from the commercially available barbituric acid, followed by reductive amination reaction with R-NH_2 for the outer functionalization of RNTs. (B) Lysine functionalized G∧C motif showing the Watson-Crick hydrogen-bonding array of guanine and cytosine. (C) Hexameric rosette from lysine functionalized G∧C motif maintained by 18 hydrogen bonds showing the inner diameter of 1.1 nm. (D) RNTs obtained by π-π stacking of rosettes in

physiological medium. (E and F) SEM images of unheated (E) and heated (F) 0.05 mg/ ml solution of RNTs-K in water.

Among the other interesting features of the RNTs is their high thermal (>90°C) and pH range (5-10) stability and their ability to tolerate a variety of functional groups on their outer surface for unique and highly tailored physical and chemical RNTs properties. As illustrated in Figure 1.22, this is achieved by functionalizing the aldehyde moiety of the protected G∧C motif using a reductive amination strategy.[120,121] In using this synthetic approach, many different bioactive groups have been expressed on the outer RNT surface including lysine (RNTs-K), RGD, RGDSK and KRSR peptides. These individual G∧C motifs can also be co-assembled to obtain multi-functional RNTs that express more than one biological functional group on the same scaffold. This creates a synergetic effect of the bioactive components on the outer surface.

Beside their outer surface functionalization, RNTs can also encapsulate hydrophobic molecules and slowly release them into the medium. In order to examine the encapsulation of therapeutic agents into RNTs with larger inner diameters of 1.4 nm and 1.7 nm, the tricyclic and tetracyclic G∧C motifs were developed, respectively (Figure 1.23).[122-124] This extended π system of the tricyclic G∧C motif also leads to J-type RNT properties as a result of the through-space intermolecular electronic communication along the nanotubes.[124]

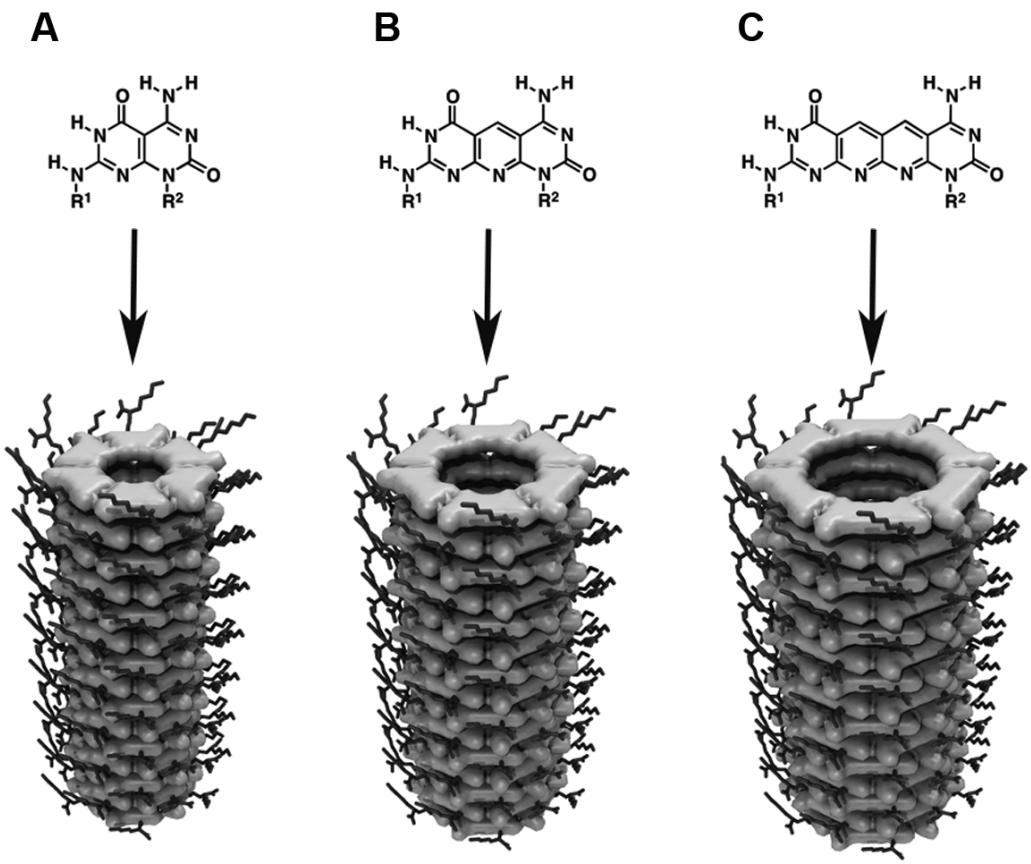

Figure 1.23. (A, B, and C) The G∧C, tricyclic xG∧C, and tetracyclic yG∧C motifs (upper) and the corresponding RNTs (lower), respectively.

1.4.3 Toxicity and Biocompatibility of RNTs

Similar to the peptide-based nanomaterials described earlier, RNTs are biologically inspired scaffolds, possessing dimensions that mimic the organic components of the natural ECM. *In vitro* and *in vivo* studies have also demonstrated that RNTs are biocompatible and non-toxic, which makes them well-suited for biomedical applications. Human Calu-3 pulmonary epithelial cells for example, which are the first defense lines against inhaled environmental pollutants[125], do not exhibit an inflammatory response and remain viable upon *in vitro* exposure to a 50 μg mL^{-1} solution of lysine functionalized RNTs (RNT-K).[126] These same RNTs also do not induce a robust inflammatory response and

are non-cytotoxic in human macrophage white cells at 1 and 5 μg mL^{-1} concentrations. When the pulmonary system of mice is exposed to a 5 μg of RNTs-K *in vivo,* there is also no inflammatory response after 24 h and 7 days.[127] At a higher dose of 25 or 50 μg however, a response is observed after 24 h, but is resolved within 7 days, which indicated that these materials have only modest acute toxicity at high concentrations.

1.4.4 Biomedical Applications of RNTs

RNTs as 2D coatings on Ti implant materials: RNTs represent a new class of soft organic nanomaterials that possess structural and chemical similarities with naturally-occurring nanostructured constituent components in bone such as collagen and hydroxyapatite. Over the past few years, several reports have demonstrated that RNTs are a biocompatible coating for Ti implants, and most importantly, are able to enhance osteoblast (OB, bone cell) attachment and function. RNTs-K and RNTs-Arg coated on Ti for instance, increase OB adhesion by approximately 50% at concentrations as low as 5 μg mL^{-1} compared to an uncoated surface.[128] The dimensions and nanostructured topography of the RNTs are a key element to this OB activity, as poly-lysine (Poly-K) coated Ti is not nearly as effective.[129]

Along with OB cell adhesion, adequate endothelial cell interactions with a Ti implant are detrimental to its success. Ti vascular stents for example, are inserted into partially clogged arteries to promote blood flow and prevent myocardial infractions. Unfortunately, these stents often trigger an inflammatory response because of the lack of endothelial cell interactions, which leads to implant loosening and dislodging.[130] When a Ti surface is coated with RNTs-K however, *in vitro* endothelial cell attachment increases by 52% after only 4 days, compared to the uncoated Ti surface. Cell proliferation likewise increases. This highlights

the promise that biocompatible coatings such as RNTs-K have for improving vascular stent performance.[131]

Cell adhesion can be further enhanced with RNTs-K, by heating the solution to promote the formation of longer and more dense RNT networks along with adding serum proteins, which are known to induce cell signaling and proliferation upon interaction with cells.[132,133] Interestingly, these RNTs-K which have been heated, exhibit the same level of OB adhesion as uncoated Ti under serum conditions, thereby suggesting that these materials may act as substitutes for serum proteins.[132]

Another approach to enhancing the *in vitro* bioactivity is to functionalize the RNTs with different bioactive peptide sequences and co-assemble them.[134] RNTs-RGD and RNTs-KRSR for instance, both show a 124% increase in OB adhesion compared to uncoated Ti. Whereas RNTs-KRSR alone selectively improves OB adhesion relative to fibroblast cell (soft-tissue forming cells) and endothelial cell adhesion, RNTs-RGD co-assembled with RNTs-K, significantly enhance fibroblast cell, endothelial cell and OB adhesion. This is a significant observation, which may have implications in the *in vivo* vascularization of newly formed bone tissue.[134]

As mentioned previously, nanocrystalline hydroxyapatite (HA; $Ca_{10}(PO4)_6(OH)_2$) is an essential inorganic component of natural bone ECM. When coated on Ti implants alone, it was found to induce *in vivo* osteointegration.[135] Combining HA with RNTs-K increased the OB adhesion by 36%.[136] Although this enhancement is similar to that observed with RNTs-K alone, creating a better biomimetic coating on Ti by adding HA is an excellent approach to promoting long-term bone tissue formation and lower implant failure rate.

RNTs embedded in or coated on pHEMA hydrogels: RNTs undergo a phase transition from a liquid to a viscous gel when heated to 60ºC or when added directly to a serum-supplemented or serum-free media at body temperature.[132] Because of this gelation property and nanoscale biologically inspired features, RNTs are well suited as an injectable therapeutic material for the treatment of bone fractures *in situ*. In this regard, RNTs can be combined with the biocompatible hydrogel poly(2-hydroxyethyl methacrylate) (pHEMA) in order to increase the mechanical strength of the scaffold.[137] Compared to pHEMA alone, coating or embedding the hydrogel with RNTs-K increases OB cell viability and improves adhesion up to 129.5%. This is also substantially more than observed with lysine coated pHEMA at the same (lysine) concentration. To further increase OB adhesion, pHEMA can be coated with a co-assembled mixture of 90% RNTs-K and 10% RNTs-RGDSK.[138] This results in a 209% increase in OB adhesion compared to the hydrogel alone, an 81% increase compared to the RNTs-K coated hydrogel and a 72% increase compared to poly-lysine and collagen coated hydrogels.[138] Moreover, 2 wt% HA can be added to the RNTs-K pHEMA scaffold, in order to create a composite material which contains the organic as well as the inorganic biomimetic components in bone ECM. This increases the mechanical properties of RNTs-K/pHEMA composite by 38% and improves OB adhesion by 236% and 99% compared to the pHEMA hydrogel alone and 2 wt% HA embedded in the hydrogel, respectively.[137]

RNTs for cartilage repair: Articular cartilage defects are very common and widespread diseases that result from sport injuries and genetic disorders. One of the key steps to repairing these cartilage defects involves seeding chondrocyte cells onto synthetic or naturally derived scaffold matrices in order to repair the ECM.[139-141] The major challenge of this approach however, is the lack of tissue bonding between engineered cartilage and natural tissue.[142] Very recently, a novel RNTs/hydrogel composite prepared by an *in situ* electrospinning method has demonstrated promise for treating cartilage damage.[143] The nanostructured roughness created by the RNTs on submicron hydrogel fibers, enhances synovial

fibroblast (SFB) cell and chondrocyte viability and adhesion. When present in the hydrogel as a composite, the RNTs also induce SFB chondrogenic differentiation and increase the hydrogel adhesive strength to the level of collagen sheets, thereby improving the hydrogel properties as a tissue sealant.[143]

1.4.5 Conclusions

RNTs are a novel organic nanomaterial which are self-assembled from a G∧C motif under physiological conditions. These scaffolds are biocompatible and nontoxic *in vivo* and *in vitro* due to their metal-free and biomimetic design. They also have many other desirable properties for tissue engineering applications including spontaneous self-assembly in body fluids, tailorable surface chemistry for specific implant applications, nanoscale dimensions similar to those of the natural extracellular matrix, and the possibility to present multiple biological signals through coassembly. As a result, these materials induce several cellular functions such as adhesion and proliferation when coated on Ti implants or when embedded in 3D hydrogels.

Along with tissue engineering applications, RNTs are also promising materials for other biomedical applications such as cancer treatment. Suri *et al*., for example, showed that coassembled RNTs-K/RNTs-RGDSK induce inflammation and apoptosis in human adenocarcinoma (Calu-3) cells, which suggests that these materials may have potential as a cancer therapy.[144] RNTs also encapsulate hydrophobic drug molecules and slowly release these bioactive molecules in a physiological medium.[145,146]

1.5 Summary, Perspective, and Thesis Objectives

Summary: This chapter describes the synthesis and biomedical tissue engineering applications of self-assembled nano/biomaterials that are based on biomimetic

peptide- and nucleic acids-based building blocks. Due to their biocompatibility, biodegradability, and their structural similarity with the natural components of the extracellular matrix, these materials show promising potential in soft and hard tissue engineering applications. These applications are still in the cell or animal model stage and the next focus will be to test these materials as injectable therapeutic agents for soft and hard tissues repair in humans. Upon achieving this ultimate goal, these *in situ* therapeutic agents will hopefully avoid the need for surgical tissue repair, thereby reducing the suffering of patients as well as minimizing the financial burden on the healthcare system.

Perspective: From a structural and properties points of view, peptide-based building blocks form β-sheet fibers, which self-assemble into 3-D hydrogel scaffolds upon adding external stimuli such as monovalent or divalent metal cations or adjusting the pH of the medium. As described in Section 1.3, these materials are mainly used as injectable hydrogels or 3-D scaffolds for soft tissue engineering applications such as neural, and vascular tissue engineering. This is due to their soft mechanical properties and porous structure, which allow for cell migration, proliferation and differentiation within the hydrogel scaffold. Although few studies showed that surfactant-like peptide amphiphiles can be covalently linked on Ti implants or embedded in Ti-Al alloy foam, these materials have limited applications in bone tissue engineering because of the lack of stability and sustainability of the peptide fibers on the surface of Ti implants.

RNTs on the other hand show great potential for hard tissue engineering applications such as bone and cartilage when used as 2-D coating materials on the current state-of-the-art Ti implants (Section 1.4.4). This is partly due to their strong adsorption and stability on the Ti surface, and their ability to display cell adhesive peptides such as RGD and KRSR. Moreover, RNTs are biomimetic, biocompatible, and have nanotopographic features that resemble the organic components (mainly collagen fibers) in the ECM of natural tissues.

Thesis Objectives: This PhD thesis aims to develop bioactive RNTs for bone tissue engineering and drug delivery applications. In chapter 2, RNTs, which are functionalized with osteogenic peptide sequences for bone tissue engineering applications, are described. As demonstrated in Section 1.4.4, RGDSK and KRSR peptides-functionalized RNTs were found to cause a 124% increase in OB cells adhesion when coated on Ti implant materials. However, for successful long term treatment and enhanced life-time of the Ti implant materials, it is necessary to develop RNTs which can promote OB cells functions such as proliferation and differentiation on Ti surface. In Chapter 2, RNTs that are functionalized with three 11 amino acids long peptide sequences that mimic the bioactivity of bone morphogenic proteins-7 (BMP-7) in promoting OB cells functions, are developed. Since the longest peptide sequences that were previously displayed on RNTs included 5-amino acids, I initially aim to demonstrate that RNTs can bear multi-charged 11-amino acids long peptide sequences on their outer surface through self-assembly. In the second half of the chapter, co-assembled RNTs consisting of 90% lysine functionalized twin-G∧C and 10% of each of the peptide-functionalized twin G∧C motifs are described. In addition to creating multi-functionalized RNTs that promote bone cells adhesion and functions at the same time, this part aims to provide evidence of the formation of co-assembled RNTs from two different G∧C motifs as proof of principle.

In Chapter 3 however, two radiolabeling strategies of RNTs for positron emission tomography (PET) and single photon emission computed tomography (SPECT) techniques are described. These radiolabeling strategies are developed in order to facilitate the *in vitro* and *in vivo* studies of RNTs and to determine their biodistribution in the biological systems. For PET imaging technique, twin-G∧C motifs functionalized with terminal primary amino groups are considered, and their coupling with *p*-fluorobenzoate is investigated. For SPECT imaging technique however, two twin-G∧C motifs are considered: the first is functionalized with marcaptoacetyl triglycine (MAG_3) ligand, and the second is

functionalized with LGGGC penta-peptide. The chelation studies of the two motifs with cold rhenium are presented, and the self-assembly of the resulting complexes is then investigated.

Finally, Chapter 4 presents the synthesis and self-assembly of an organic-soluble di-allyl tetracyclic yG∧C motif, which has the same G and C face H-bonding array but juxtaposed between naphthyridine core, for sustained drug delivery applications. This motif is an extended version of the tricyclic xG∧C motif that was previously developed, and is intended to form RNTs with an extended inner diameter of *ca* 1.7 nm. The resulting yG∧C-RNTs have potential to be loaded with larger drug molecules compared with the G∧C- and xG∧C-RNTs. In addition, the formation of yG∧C-RNTs demonstrates the tunability of the inner diameter of the RNT scaffold and its tolerance for further expansion in the G∧C core.

1.6 References

(1) Parak, W. J.; Simmel, F. C.; Holleitner, A. W. *Top-Down Versus Bottom-Up*; Wiley-VCH Verlag GmbH & Co. KGaA: Weinheim, Germany, **2010**.

(2) Yokoi, H.; Kinoshita, T.; Zhang, S. *Proc. Natl. Acad. Sci. U.S.A.* **2005**, *102*, 8414–8419.

(3) Hong, Y.; Legge, R. L.; Zhang, S.; Chen, P. *Biomacromolecules* **2003**, *4*, 1433–1442.

(4) Holmes, T. C. *Trends Biotechnol* **2002**, *20*, 16–21.

(5) Zhao, X.; Zhang, S. In *Advances in Polymer Science*; Advances in Polymer Science; Springer-Verlag: Berlin/Heidelberg, **2006**; Vol. 203, pp. 145–170.

(6) Fenniri, H.; Mathivanan, P.; Vidale, K. L.; Sherman, D. M.; Hallenga, K.; Wood, K. V.; Stowell, J. G. *J. Am. Chem. Soc.* **2001**, *123*, 3854–3855.

(7) Ramachandran, S.; Yu, Y. B. *BioDrugs* **2006**, *20*, 263–269.

(8) Lo, P. K.; Karam, P.; Aldaye, F. A.; McLaughlin, C. K.; Hamblin, G. D.;

Cosa, G.; Sleiman, H. F. *Nat. Chem.* **2010**, *2*, 319–328.

(9) Brändén, C.-I.; Tooze, J. *Introduction to Protein Structure*; Garland Pub, **1999**.

(10) Schliwa, M.; Woehlke, G. *Nature* **2003**, *422*, 759–765.

(11) MacPhee, C. E.; Woolfson, D. N. *Curr. Opin. Solid. State. Mater. Sci.* **2004**, *8*, 141–149.

(12) Taylor, J. P. *Science* **2002**, *296*, 1991–1995.

(13) Fraser, P. E.; McLachlan, D. R.; Surewicz, W. K.; Mizzen, C. A.; Snow, A. D.; Nguyen, J. T.; Kirschner, D. A. *J. Mol. Biol.* **1994**, *244*, 64–73.

(14) Trojanowski, J. Q.; Lee, V. M. Y. *NeuroToxicology* **2002**, *23*, 457–460.

(15) Wyss-Coray, T.; Mucke, L. *Neuron* **2002**, *35*, 419–432.

(16) Carrell, R. W.; Lomas, D. A. *The Lancet* **1997**, *350*, 134–138.

(17) Pan, K. M.; Baldwin, M.; Nguyen, J.; Gasset, M.; Serban, A.; Groth, D.; Mehlhorn, I.; Huang, Z.; Fletterick, R. J.; Cohen, F. E. *Proc. Natl. Acad. Sci. U.S.A.* **1993**, *90*, 10962–10966.

(18) Zhang, S.; Holmes, T.; Lockshin, C.; Rich, A. *Proc. Natl. Acad. Sci. U.S.A.* **1993**, *90*, 3334–3338.

(19) Zhang, S.; Marini, D. M.; Hwang, W.; Santoso, S. *Curr. Opin. Chem. Biol.* **2002**, *6*, 865–871.

(20) Zhang, S. *Nat. Biotechnol.* **2003**, *21*, 1171–1178.

(21) Higashi, N.; Koga, T. *Adv. Polym. Sci.* **2008**, *219*, 27–68.

(22) Yanlian, Y.; Ulung, K.; Xiumei, W.; Horii, A.; Yokoi, H.; Shuguang, Z. *Nano Today* **2009**, *4*, 193–210.

(23) Zhang, S.; Lockshin, C.; Herbert, A.; Winter, E.; Rich, A. *EMBO J* **1992**, *11*, 3787–3796.

(24) Zhang, S.; Lockshin, C.; Cook, R.; Rich, A. *Biopolymers* **1994**, *34*, 663–672.

(25) Holmes, T. C.; de Lacalle, S.; Su, X.; Liu, G.; Rich, A.; Zhang, S. *Proc. Natl. Acad. Sci. U.S.A.* **2000**, *97*, 6728–6733.

(26) Xiong, H.; Buckwalter, B. L.; Shieh, H. M.; Hecht, M. H. *Proc. Natl. Acad. Sci. U.S.A.* **1995**, *92*, 6349–6353.

(27) Caplan, M. R.; Schwartzfarb, E. M.; Zhang, S.; Kamm, R. D.; Lauffenburger, D. A. *Biomaterials* **2002**, *23*, 219–227.

(28) Wang, K.; Keasling, J. D.; Muller, S. J. *Inter. J. Biol. Macromol.* **2005**, *36*, 232–240.

(29) Chou, P. Y.; Fasman, G. D. *Biochemistry* **1974**, *13*, 222–245.

(30) Chou, P. Y.; Fasman, G. D. *Annu. Rev. Biochem.* **1978**, *47*, 251–276.

(31) Chou, P. Y.; Fasman, G. D. *Adv. Enzymol. Relat. Areas. Mol. Biol.* **1978**, *47*, 45–148.

(32) Caplan, M. R.; Moore, P. N.; Zhang, S.; Kamm, R. D.; Lauffenburger, D. A. *Biomacromolecules* **2000**, *1*, 627–631.

(33) Vauthey, S.; Santoso, S.; Gong, H.; Watson, N.; Zhang, S. *Proc. Natl. Acad. Sci. U.S.A.* **2002**, *99*, 5355–5360.

(34) Yang, S. J.; Zhang, S. *Supramol. Chem.* **2006**, *18*, 389–396.

(35) Santoso, S.; Hwang, W.; Hartman, H.; Zhang, S. *Nano Lett* **2002**, *2*, 687–691.

(36) Maltzahn, von, G.; Vauthey, S.; Santoso, S.; Zhang, S. *Langmuir* **2003**, *19*, 4332–4337.

(37) Khoe, U.; Yang, Y.; Zhang, S. *Langmuir* **2009**, *25*, 4111–4114.

(38) Cui, H.; Webber, M. J.; Stupp, S. I. *Biopolymers* **2010**, *94*, 1–18.

(39) Hartgerink, J. D.; Beniash, E.; Stupp, S. I. *Proc. Natl. Acad. Sci. U.S.A.* **2002**, *99*, 5133–5138.

(40) Biesalski, M.; Tu, R.; Tirrell, M. V. *Langmuir* **2005**, *21*, 5663–5666.

(41) Hsu, L.; Cvetanovich, G. L.; Stupp, S. I. *J. Am. Chem. Soc.* **2008**, *130*, 3892–3899.

(42) Löwik, D. W. P. M.; Shklyarevskiy, I. O.; Ruizendaal, L.; Christianen, P. C. M.; Maan, J. C.; van Hest, J. C. M. *Adv. Mater.* **2007**, *19*, 1191–1195.

(43) Jiang, H.; Guler, M. O.; Stupp, S. I. *Soft Matter* **2007**, *3*, 454-462.

(44) Niece, K. L.; Czeisler, C.; Sahni, V.; Tysseling-Mattiace, V.; Pashuck, E. T.; Kessler, J. A.; Stupp, S. I. *Biomaterials* **2008**, *29*, 4501–4509.

(45) Hartgerink, J. D. *Science* **2001**, *294*, 1684–1688.

(46) Stendahl, J. C.; Rao, M. S.; Guler, M. O.; Stupp, S. I. *Adv. Funct. Mater.*

2006, *16*, 499–508.

(47) Jonge, L. T.; Leeuwenburgh, S. C. G.; Wolke, J. G. C.; Jansen, J. A. *Pharm. Res.* **2008**, *25*, 2357–2369.

(48) Guler, M. O.; Hsu, L.; Soukasene, S.; Harrington, D. A.; Hulvat, J. F.; Stupp, S. I. *Biomacromolecules* **2006**, *7*, 1855–1863.

(49) Niece, K. L.; Hartgerink, J. D.; Donners, J. J. J. M.; Stupp, S. I. *J. Am. Chem. Soc.* **2003**, *125*, 7146–7147.

(50) Behanna, H. A.; Donners, J. J. J. M.; Gordon, A. C.; Stupp, S. I. *J. Am. Chem. Soc.* **2005**, *127*, 1193–1200.

(51) Langer, R.; Vacanti, J. P. *Science* **1993**, *260*, 920–926.

(52) Semino, C. E.; Merok, J. R.; Crane, G. G.; Panagiotakos, G.; Zhang, S. *Differentiation* **2003**, *71*, 262–270.

(53) Narmoneva, D. A.; Oni, O.; Sieminski, A. L.; Zhang, S.; Gertler, J. P.; Kamm, R. D.; Lee, R. T. *Biomaterials* **2005**, *26*, 4837–4846.

(54) Prieto, A. L.; Edelman, G. M.; Crossin, K. L. *Proc. Natl. Acad. Sci. U.S.A.* **1993**, *90*, 10154–10158.

(55) Zhang, S.; Holmes, T. C.; DiPersio, C. M.; Hynes, R. O.; Su, X.; Rich, A. *Biomaterials* **1995**, *16*, 1385–1393.

(56) Kyle, S.; Aggeli, A.; Ingham, E.; McPherson, M. J. *Trends Biotechnol* **2009**, *27*, 423–433.

(57) Schachner, M. *Nature* **2000**, *405*, 747–748.

(58) Gelain, F.; Bottai, D.; Vescovi, A.; Zhang, S. *PLoS ONE* **2006**, *1*, e119.

(59) Semino, C. E.; Kasahara, J.; Hayashi, Y.; Zhang, S. *Tissue Eng* **2004**, *10*, 643–655.

(60) Ellis-Behnke, R. G.; Liang, Y.-X.; You, S.-W.; Tay, D. K. C.; Zhang, S.; So, K.-F.; Schneider, G. E. *Proc. Natl. Acad. Sci. U.S.A.* **2006**, *103*, 5054–5059.

(61) Ennett, A. B.; Mooney, D. J. *Expert. Opin. Biol. Ther.* **2002**, *2*, 805–818.

(62) Lutolf, M. P.; Hubbell, J. A. *Nat. Biotechnol.* **2005**, *23*, 47–55.

(63) Weinberg, C. B.; Bell, E. *Science* **1986**, *231*, 397–400.

(64) Shum-Tim, D.; Stock, U.; Hrkach, J.; Shinoka, T.; Lien, J.; Moses, M. A.;

Stamp, A.; Taylor, G.; Moran, A. M.; Landis, W.; Langer, R.; Vacanti, J. P.; Mayer, J. E., Jr. *Ann. Thorac. Surg.* **1999**, *68*, 2298–2304.

(65) Moldovan, N. I.; Ferrari, M. *Arch. Pathol. Lab. Med.* **2002**, *126*, 320–324.

(66) Vogel, V.; Baneyx, G. *Annu. Rev. Biomed. Eng.* **2003**, *5*, 441–463.

(67) Wang, X.; Horii, A.; Zhang, S. *Soft Matter* **2008**, *4*, 2388.

(68) Davis, M. E. *Circulation* **2005**, *111*, 442–450.

(69) Brandt, J.; Michler, G.; Vogel, J.; Henning, S. *Macromol. Symp.* **2010**, *294*, 109–119.

(70) Kisiday, J.; Jin, M.; Kurz, B.; Hung, H.; Semino, C.; Zhang, S.; Grodzinsky, A. J. *Proc. Natl. Acad. Sci. U.S.A.* **2002**, *99*, 9996–10001.

(71) Bokhari, M. A.; Akay, G.; Zhang, S.; Birch, M. A. *Biomaterials* **2005**, *26*, 5198–5208.

(72) Horii, A.; Wang, X.; Gelain, F.; Zhang, S. *PLoS ONE* **2007**, *2*, e190.

(73) Kumada, Y.; Zhang, S. *PLoS ONE* **2010**, *5*, e10305.

(74) Beniash, E.; Hartgerink, J. D.; Storrie, H.; Stendahl, J. C.; Stupp, S. I. *Acta. Biomater.* **2005**, *1*, 387–397.

(75) Silva, G. A.; Czeisler, C.; Niece, K. L.; Beniash, E.; Harrington, D. A.; Kessler, J. A.; Stupp, S. I. *Science* **2004**, *303*, 1352–1355.

(76) Harrington, D. A.; Cheng, E. Y.; Guler, M. O.; Lee, L. K.; Donovan, J. L.; Claussen, R. C.; Stupp, S. I. *J. Biomed. Mater. Res.* **2006**, *78A*, 157–167.

(77) Storrie, H.; Guler, M. O.; Abu-Amara, S. N.; Volberg, T.; Rao, M.; Geiger, B.; Stupp, S. I. *Biomaterials* **2007**, *28*, 4608–4618.

(78) Tashiro, K.; Sephel, G. C.; Weeks, B.; Sasaki, M.; Martin, G. R.; Kleinman, H. K.; Yamada, Y. *J. Biol. Chem.* **1989**, *264*, 16174–16182.

(79) Tysseling-Mattiace, V. M.; Sahni, V.; Niece, K. L.; Birch, D.; Czeisler, C.; Fehlings, M. G.; Stupp, S. I.; Kessler, J. A. *J. Neurosci.* **2008**, *28*, 3814–3823.

(80) Tysseling, V. M.; Sahni, V.; Pashuck, E. T.; Birch, D.; Hebert, A.; Czeisler, C.; Stupp, S. I.; Kessler, J. A. *J. Neurosci. Res.* **2010**, *88*, 3161–3170.

(81) Schlessinger, J.; Plotnikov, A. N.; Ibrahimi, O. A.; Eliseenkova, A. V.; Yeh, B. K.; Yayon, A.; Linhardt, R. J.; Mohammadi, M. *Mol. Cell.* **2000**, *6*, 743–

750.

(82) Ferrara, N.; Gerber, H.-P.; LeCouter, J. *Nat. Med.* **2003**, *9*, 669–676.

(83) Rajangam, K.; Behanna, H. A.; Hui, M. J.; Han, X.; Hulvat, J. F.; Lomasney, J. W.; Stupp, S. I. *Nano Lett* **2006**, *6*, 2086–2090.

(84) Rajangam, K.; Arnold, M. S.; Rocco, M. A.; Stupp, S. I. *Biomaterials* **2008**, *29*, 3298–3305.

(85) Stendahl, J. C.; Wang, L.-J.; Chow, L. W.; Kaufman, D. B.; Stupp, S. I. *Transplantation* **2008**, *86*, 478–481.

(86) D'Andrea, L. D.; Iaccarino, G.; Fattorusso, R.; Sorriento, D.; Carannante, C.; Capasso, D.; Trimarco, B.; Pedone, C. *Proc. Natl. Acad. Sci. U.S.A.* **2005**, *102*, 14215–14220.

(87) Webber, M. J.; Tongers, J.; Newcomb, C. J.; Marquardt, K.-T.; Bauersachs, J.; Losordo, D. W.; Stupp, S. I. *Proc. Natl. Acad. Sci. U.S.A.* **2011**, *108*, 13438–13443.

(88) Ruoslahti, E.; Pierschbacher, M. D. *Science* **1987**, *238*, 491–497.

(89) Xiao, S.-J.; Textor, M.; Spencer, N. D.; Sigrist, H. *Langmuir* **1998**, *14*, 5507–5516.

(90) Zhang, F.; Srinivasan, M. P. *Langmuir* **2004**, *20*, 2309–2314.

(91) Sargeant, T. D.; Rao, M. S.; Koh, C.-Y.; Stupp, S. I. *Biomaterials* **2008**, *29*, 1085–1098.

(92) Sargeant, T. D.; Guler, M. O.; Oppenheimer, S. M.; Mata, A.; Satcher, R. L.; Dunand, D. C.; Stupp, S. I. *Biomaterials* **2008**, *29*, 161–171.

(93) Addadi, L.; Weiner, S. *Proc. Natl. Acad. Sci. U.S.A.* **1985**, *82*, 4110–4114.

(94) Wang, L.; Guan, X.; Du, C.; Moradian-Oldak, J.; Nancollas, G. H. *J. Phys. Chem. C.* **2007**, *111*, 6398–6404.

(95) Huang, Z.; Sargeant, T. D.; Hulvat, J. F.; Mata, A.; Bringas, P.; Koh, C.-Y.; Stupp, S. I.; Snead, M. L. *J. Bone. Miner. Res.* **2008**, *23*, 1995–2006.

(96) Koga, T.; Kitamura, K.-I.; Higashi, N. *Chem. Commun.* **2006**, 4897-4899.

(97) Koga, T.; Higuchi, M.; Kinoshita, T.; Higashi, N. *Chem. Eur. J.* **2006**, *12*, 1360–1367.

(98) Koga, T.; Matsuoka, M.; Higashi, N. *J. Am. Chem. Soc.* **2005**, *127*, 17596–

17597.

(99) Schneider, J. P.; Pochan, D. J.; Ozbas, B.; Rajagopal, K.; Pakstis, L.; Kretsinger, J. *J. Am. Chem. Soc.* **2002**, *124*, 15030–15037.

(100) Salick, D. A.; Pochan, D. J.; Schneider, J. P. *Adv. Mater.* **2009**, *21*, 4120–4123.

(101) Lamm, M. S.; Sharma, N.; Rajagopal, K.; Beyer, F. L.; Schneider, J. P.; Pochan, D. J. *Adv. Mater.* **2008**, *20*, 447–451.

(102) Haines, L. A.; Rajagopal, K.; Ozbas, B.; Salick, D. A.; Pochan, D. J.; Schneider, J. P. *J. Am. Chem. Soc.* **2005**, *127*, 17025–17029.

(103) Song, H.; Zhang, L.; Zhao, X. *Macromol. Biosci.* **2010**, *10*, 33–39.

(104) Meng, H.; Chen, L.; Ye, Z.; Wang, S.; Zhao, X. *J. Biomed. Mater. Res.* **2009**, *89B*, 379–391.

(105) Tang, C.; Shao, X.; Sun, B.; Huang, W.; Zhao, X. *Int. J. Mol. Sci.* **2009**, *10*, 2136–2145.

(106) Mi, K.; Wang, G.; Liu, Z.; Feng, Z.; Huang, B.; Zhao, X. *Macromol. Biosci.* **2009**, *9*, 437–443.

(107) Genové, E.; Schmitmeier, S.; Sala, A.; Borrós, S.; Bader, A.; Griffith, L. G.; Semino, C. E. *J. Cell. Mol. Med.* **2009**, *13*, 3387–3397.

(108) Quintana, L.; Muiños, T. F.; Genové, E.; Del Mar Olmos, M.; Borrós, S.; Semino, C. E. *Tissue. Eng. A.* **2009**, *15*, 45–54.

(109) Dégano, I. R.; Quintana, L.; Vilalta, M.; Horna, D.; Rubio, N.; Borrós, S.; Semino, C.; Blanco, J. *Biomaterials* **2009**, *30*, 1156–1165.

(110) Cigognini, D.; Satta, A.; Colleoni, B.; Silva, D.; Donegà, M.; Antonini, S.; Gelain, F. *PLoS ONE* **2011**, *6*, e19782.

(111) Gelain, F.; Panseri, S.; Antonini, S.; Cunha, C.; Donegà, M.; Lowery, J.; Taraballi, F.; Cerri, G.; Montagna, M.; Baldissera, F.; Vescovi, A. *ACS Nano* **2011**, *5*, 227–236.

(112) Kushwaha, M.; Anderson, J. M.; Bosworth, C. A.; Andukuri, A.; Minor, W. P.; Lancaster, J. R.; Anderson, P. G.; Brott, B. C.; Jun, H.-W. *Biomaterials* **2010**, *31*, 1502–1508.

(113) Andukuri, A.; Kushwaha, M.; Tambralli, A.; Anderson, J. M.; Dean, D. R.;

Berry, J. L.; Sohn, Y. D.; Yoon, Y.-S.; Brott, B. C.; Jun, H.-W. *Acta. Biomater.* **2011**, *7*, 225–233.

(114) Lo, P. K.; Metera, K. L.; Sleiman, H. F. *Curr. Opin. Chem. Biol.* **2010**, *14*, 597–607.

(115) Davis, J. T.; Spada, G. P. *Chem. Soc. Rev.* **2007**, *36*, 296–313.

(116) Wang, X.; Zhou, L.; Wang, H.; Luo, Q.; Xu, J.; Liu, J. *J. Colloid. Interface. Sci.* **2011**, *353*, 412–419.

(117) Li, Z.; Buerkle, L. E.; Orseno, M. R.; Streletzky, K. A.; Seifert, S.; Jamieson, A. M.; Rowan, S. J. *Langmuir* **2010**, *26*, 10093–10101.

(118) Marsh, A.; Silvestri, M.; Lehn, J.-M. *Chem. Commun.* **1996**, 1527-1538.

(119) Mascal, M.; Hext, N. M.; Warmuth, R.; Moore, M. H.; Turkenburg, J. P. *Angew. Chem. Int. Ed. Engl.* **1996**, *35*, 2204–2206.

(120) Fenniri, H.; Deng, B.-L.; Ribbe, A. E.; Hallenga, K.; Jacob, J.; Thiyagarajan, P. *Proc. Natl. Acad. Sci. U.S.A.* **2002**, *99 Suppl 2*, 6487–6492.

(121) Fenniri, H.; Deng, B.-L.; Ribbe, A. E. *J. Am. Chem. Soc.* **2002**, *124*, 11064–11072.

(122) Borzsonyi, G.; Johnson, R. S.; Myles, A. J.; Cho, J.-Y.; Yamazaki, T.; Beingessner, R. L.; Kovalenko, A.; Fenniri, H. *Chem. Commun.* **2010**, *46*, 6527-6529.

(123) Borzsonyi, G.; Alsbaiee, A.; Beingessner, R. L.; Fenniri, H. *J. Org. Chem.* **2010**, *75*, 7233–7239.

(124) Borzsonyi, G.; Beingessner, R. L.; Yamazaki, T.; Cho, J.-Y.; Myles, A. J.; Malac, M.; Egerton, R.; Kawasaki, M.; Ishizuka, K.; Kovalenko, A.; Fenniri, H. *J. Am. Chem. Soc.* **2010**, *132*, 15136–15139.

(125) Nicod, L. P. *Eur. Respir. Rev.* **2005**, *14*, 45–50.

(126) Journeay, W. S.; Suri, S. S.; Moralez, J. G.; Fenniri, H.; Singh, B. *Small* **2008**, *4*, 817–823.

(127) Journeay, W. S.; Suri, S. S.; Moralez, J. G.; Fenniri, H.; Singh, B. *Int. J. Nanomed.* **2008**, *3*, 373–383.

(128) Chun, A. L.; Moralez, J. G.; Fenniri, H.; Webster, T. J. *Nanotechnology* **2004**, *15*, S234–S239.

(129) Chun, S.; Xu, J.; Cheng, J.; Ding, L.; Winograd, N.; Fenniri, H. *J. Comb. Chem.* **2006**, *8*, 18–25.

(130) Hoffman, G. S.; Weyand, C. M.; Langford, C. A.; Goronzy, J. J. *Inflammatory Diseases of Blood Vessels*; John Wiley & Sons, Inc, **2012**.

(131) Fine, E.; Zhang, L.; Fenniri, H.; Webster, T. J. *Int. J. Nanomed.* **2009**, *4*, 91–97.

(132) Lin Chun, A.; Moralez, J. G.; Webster, T. J.; Fenniri, H. *Biomaterials* **2005**, *26*, 7304–7309.

(133) Puleo, D. *Biomaterials* **1999**, *20*, 2311–2321.

(134) Zhang, L.; Hemraz, U. D.; Fenniri, H.; Webster, T. J. *J. Biomed. Mater. Res.* **2010**, *95A*, 550–563.

(135) Chang, C. K.; Wu, J. S.; Mao, D. L.; Ding, C. X. *J. Biomed. Mater. Res.* **2001**, *56*, 17–23.

(136) Zhang, L.; Chen, Y.; Rodriguez, J.; Fenniri, H.; Webster, T. J. *Int. J. Nanomed.* **2008**, *3*, 323–333.

(137) Zhang, L.; Rodriguez, J.; Raez, J.; Myles, A. J.; Fenniri, H.; Webster, T. J. *Nanotechnology* **2009**, *20*, 175101–175113.

(138) Zhang, L.; Rakotondradany, F.; Myles, A. J.; Fenniri, H.; Webster, T. J. *Biomaterials* **2009**, *30*, 1309–1320.

(139) Puelacher, W. C.; Mooney, D.; Langer, R.; Upton, J.; Vacanti, J. P.; Vacanti, C. A. *Biomaterials* **1994**, *15*, 774–778.

(140) Grande, D. A.; Halberstadt, C.; Naughton, G.; Schwartz, R.; Manji, R. *J. Biomed. Mater. Res.* **1997**, *34*, 211–220.

(141) Nehrer, S.; Breinan, H. A.; Ramappa, A.; Shortkroff, S.; Young, G.; Minas, T.; Sledge, C. B.; Yannas, I. V.; Spector, M. *J. Biomed. Mater. Res.* **1997**, *38*, 95–104.

(142) Brun, P.; Abatangelo, G.; Radice, M.; Zacchi, V.; Guidolin, D.; Daga Gordini, D.; Cortivo, R. *J. Biomed. Mater. Res.* **1999**, *46*, 337–346.

(143) Chen, Y.; Bilgen, B.; Pareta, R. A.; Myles, A. J.; Fenniri, H.; Ciombor, D. M.; Aaron, R. K.; Webster, T. J. *Tissue. Eng. C.* **2010**, *16*, 1233–1243.

(144) Suri, S. S.; Rakotondradany, F.; Myles, A. J.; Fenniri, H.; Singh, B.

Biomaterials **2009**, *30*, 3084–3090.

(145) Chen, Y.; Song, S.; Yan, Z.; Fenniri, H.; Webster, T. J. *Int. J. Nanomed.* **2011**, *6*, 1035–1044.

(146) Song, S.; Chen, Y.; Yan, Z.; Fenniri, H.; Webster, T. J. *Int. J. Nanomed*. **2011**, *6*, 101–107.

Chapter 2

Peptide-Functionalized Rosette Nanotubes for Bone Tissue Engineering[†]

2.1 Introduction

Tissue engineering is an interdisciplinary field of research that relies on the principles of chemistry, biology, engineering, material science, and medicine in order to design novel materials that can repair or replace portions of, or an entire damaged tissue. Advances in the design of smart synthetic biomaterials that can interact with cells and mimic the nanoscale features in tissues, have allowed for the exploration of this field in almost all types of soft and hard tissues including bone, cartilage, blood vessels, brain, skin and liver.[1,2] Bone and cartilage tissue engineering in particular, has seen tremendous attention over the past two decades because of the wide range of costly bone complications resulting from trauma or sport injuries, deterioration with age, and osteoporosis. The World Health Organization estimates that millions of people suffer from bone and joint diseases and injuries around the world. In 2000 for example, there were 9 million new osteoporotic fractures in the hip, forearm, and the vertebral region in Europe and the US. Furthermore, it is estimated that 1 in 3 women and 1 in 5 men over 50 will experience osteoporotic fractures in their lifetime.[3]

To repair or replace damaged parts of the natural bone tissues, load-bearing supports are used as substrates upon which cells attach, proliferate, and differentiate to restore the function of the natural bone. Traditionally, the treatment is clinically performed using metallic implant materials such as titanium

[†] Part of the self-assembly studies in this chapter are published in: Alsbaiee, A.; El Bakkari, M.; Fenniri, H. *Mater. Res. Soc. Proc.* **2011**, 1316, mrsf10-1316-qq12-18, USA.

(Ti) metal and its alloys. These implants have several advantages including high mechanical strength, durability, chemical stability, corrosion resistance and low toxicity.[4,5] There are still significant and unresolved problems associated with these implants however, such as their low biocompatibility, poor long-term stability, slow rate of osseointegration and low healing response, which result from poor structural and functional connections between bone and the implant surfaces.[6] This is because titanium is a non-physiological material, which results in insufficient osseointegration and connection between the juxtaposed bone tissue and the surface of the implant.[7] Unfortunately for many patients, these defects often result in the need for revision surgery, thereby causing tremendous pain and inconvenience as well as being financially taxing to the medical systems. Organic and inorganic coatings that mimic the natural components of the extracellular matrix in bone are thus required in order to establish a physiological transition between the non-physiological titanium and the physiological bone tissue.[8] These coatings will enhance the biocompatibility, decrease the inflammation, and increase the lifetime of the implant.

Several natural and synthetic materials, which mimic the structure and function of the extracellular matrix of bone, and thus increase the rate of osseointegration around the implant, have been used as 2-D coatings on Ti implants prior to the surgical installation. These include growth factors such as bone morphogenic proteins (BMPs) and RGD and KRSR peptides, DNA coatings, enzyme coatings, as well as inorganic coatings such as hydroxyapitite (HA). Unfortunately, these coatings lack strong adsorption and stability on the implant and are highly susceptible to enzymatic degredation.[7] Self-assembled nanomaterials in particular, have received tremendous interest over the past decade as coating materials on Ti implants due to their robust nature, biocompatibility, large surface area, capacity for chemical functionalization, and strong adsorption and stability on the surface. Furthermore, their nanostructural features can mimic the extracellular matrix of bone, in order to significantly promote selective protein adsorption and efficiently

stimulate new bone formation on the implant compared with conventional materials.[9]

Among the various self-assembled nanomaterials used for this purpose, nucleic-acid based nanomaterials such as rosette nanotubes (RNTs) have shown tremendous potential for these applications. These nanotubular architectures are self-assembled from a biomimetic synthetically-derived DNA hybrid molecule called the G∧C motif, which features the Watson-Crick donor-donor-acceptor hydrogen bonding array of guanine and acceptor-acceptor-donor hydrogen bonding array of cytosine.[10-12] Given their biologically inspired design, RNTs have high thermal (>90°C) and pH range (5-10) stability, and they possess dimensions that mimic the organic components of the natural extracellular matrix (ECM) in natural tissues. In addition, they can be functionalized with a variety of functional groups on their outer surface for applications in biology and materials chemistry. Several *in vitro* and *in vivo* studies have also demonstrated that RNTs are biocompatible and non-toxic, and are well-suited for biomedical applications such as bone tissue engineering.[13,14] For instance, lysine-functionalized RNTs (RNTs-K) increase osteoblast (bone-forming cells) adhesion when coated on titanium surface by at least 50%, whereas co-assembled mixture of the more bioactive RNTs-RGD with RNTs-K enhance cell adhesion on titanium by 124%.[15,16]

These promising results with cell adhesion have prompted us to explore the RNTs' ability to improve the Ti implants integration with the surrounding tissue, which is essential for the successful long-term treatment and rapid healing around the implant. To this end, Ti surface needs to promote facile bone generation and growth as well as calcium deposition. This can be achieved by coating the surface with osteogenic materials that promote bone cell proliferation and differentiation functions. Among the different osteogenic materials for this purpose are natural growth factors produced by bone cells and stored in the bone matrix such as the

transforming growth factor-β (TGF-β) and the BMPs.[17-19] In particular, BMP-2, BMP-7 and TGF-β1 are promising growth factors for enhanced bone formation around the implant.[20,21] These proteins serve as signaling agents for cells to promote replication, differentiation, protein synthesis and/or migration of proper cell types. Unfortunately, immobilizing these growth factors on the implant by physical adsorption is not without its challenges, since these proteins lack stability and sustainability on the surface and are highly susceptible to enzymatic degradation. Thus, for the success of these growth factors, they need to be delivered at an appropriate rate and under controlled release conditions. Self-assembled nanomaterials such as RNTs offer great potential to serve as scaffolds for growth factors delivery because of their nanostructured features that are favorable to bone cells and their stability on the implant surface. However, the covalent attachment of growth factors with RNTs can be challenging due to their large size, but short peptide sequences that mimic the growth factors' bioactivity can alternatively be used. Saito *et al*., for example, reported a 20-amino acid peptide sequence (KIPKASSVPTELSAISTLYL) derived from the "knuckle" region (bioactive region) of BMP-2 that promotes alkaline phosphatase activity in OB cells.[22] Kirkwood *et al*., also identified a 20-amino acid long (AISVLYFDDSSNVILKKYRN) peptide sequence in BMP-7 that promotes calcium deposition and mineralization processes in OB cells.[23] More recently, Chen and Webster identified three peptide sequences (10- or 11- amino acid long each), which are taken from the knuckle (bioactive) region of BMP-7, namely; **A** (SNVILKKYRN), **B** (KPSSAPTQLN) and **C** (KAISVLYFDDS).[24] Peptide B and a combination of A and B have been found to increase OB proliferation, while peptide C and its combinations AC, BC and ABC increase the calcium deposition of OB cells (Figure 2.1).

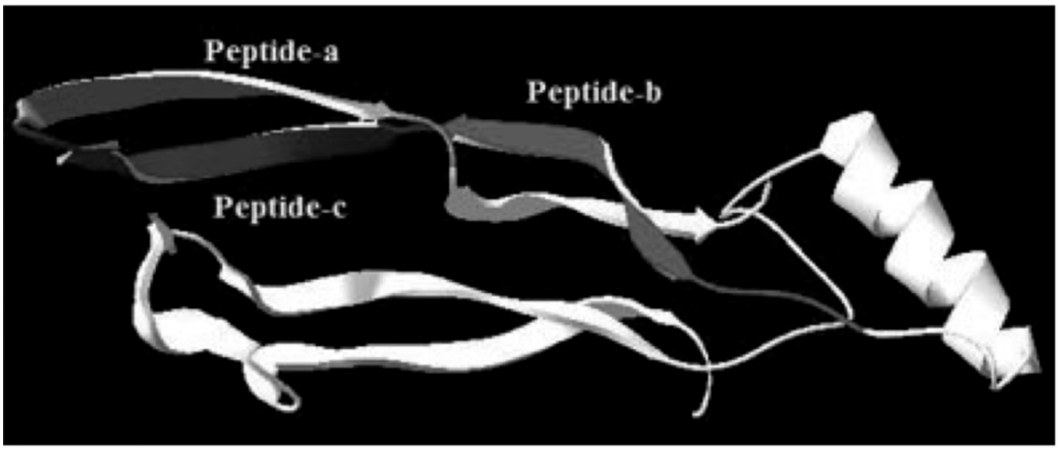

Figure 2.1. Schematic representation showing the 3-D structure of bone morphogenic protein-7 (BMP-7) and the peptides A, B, and C. (Used with permission. Copyright (2009) John Wiley & Sons, Inc).

To utilize these peptides in promoting bone cell functioning with the nanostructured features of the RNTs, the synthesis of three twin-G∧C motifs functionalized with the peptides A, B and C (called pA-TB, pB-TB, and pC-TB respectively) is described. Then I demonstrate the highly robust nature of the RNT scaffold by its ability to express these long peptides on the outer surface using self- and co-assembly approaches. Specifically, scanning, transmission and atomic force microscopy, UV-visible spectroscopy, circular dichroism and molecular modeling techniques are used to investigate the self-assembly of the three motifs in water and elucidate the peptide secondary structures on the outer surface of RNTs. Control peptides pA, pB, and pC are also considered and their intrinsic secondary structure in solution is elucidated using circular dichroism. In addition, the synthesis and self-assembly of a lysine functionalized twin-G∧C motif, K1-TB is described. I also examine the co-assembly of pA-TB, pB-TB and pC-TB with K1-TB in a 1:9 molar ratio to obtain multi-functionalized RNTs that can promote bone cell adhesion and functions at the same time. Circular dichroism in combination with microscopy studies are used to provide evidence for the formation of co-assembled RNTs.

2.2 Materials Design

Given their noncovalent mechanism of formation, the stability of the RNT assemblies depends mainly on the density (sterics) and net-charge (electrostatics)[25] of the surface functional groups. In order to accommodate large charged bioactive molecules (i.e. peptides) on the RNTs without compromising their self-assembly and stability, twin-G∧C motif was considered. This motif features two bicyclic G∧C bases linked via ethylene spacers. When self-assembled, the twin-RNT construct is substantially more stable than the single-RNTs (prepared from the single-G∧C motif) when identically functionalized and of equal length. This is because (a) the functional group density and net charge are reduced by a factor of 2; (b) the thermal stability of the nanotubes is enhanced as a result of preorganization, increased amphiphilic character and greater number of H-bonds per module (12 instead of 6); (c) the corresponding double rosettes are preorganized and maintained by 36-H bonds instead of 18 and (d) the resulting RNT is less congested and experiences reduced electrostatic repulsion on its surface.[25]

Next, the design included a lysine amino acid spacer followed by the bioactive peptides in pA-TB and pB-TB in order to make the peptides more accessible to bone cells. While the ω-amino side group of the lysine is linked to the twin-G∧C motif, the carboxyl group is attached to the N-termini of the peptides in the two conjugates (Figure 2.2). In the case of pC-TB however, no lysine spacer was incorporated since peptide C has -2 net charge, and adding a lysine spacer might reduce its solubility in water at neutral conditions.

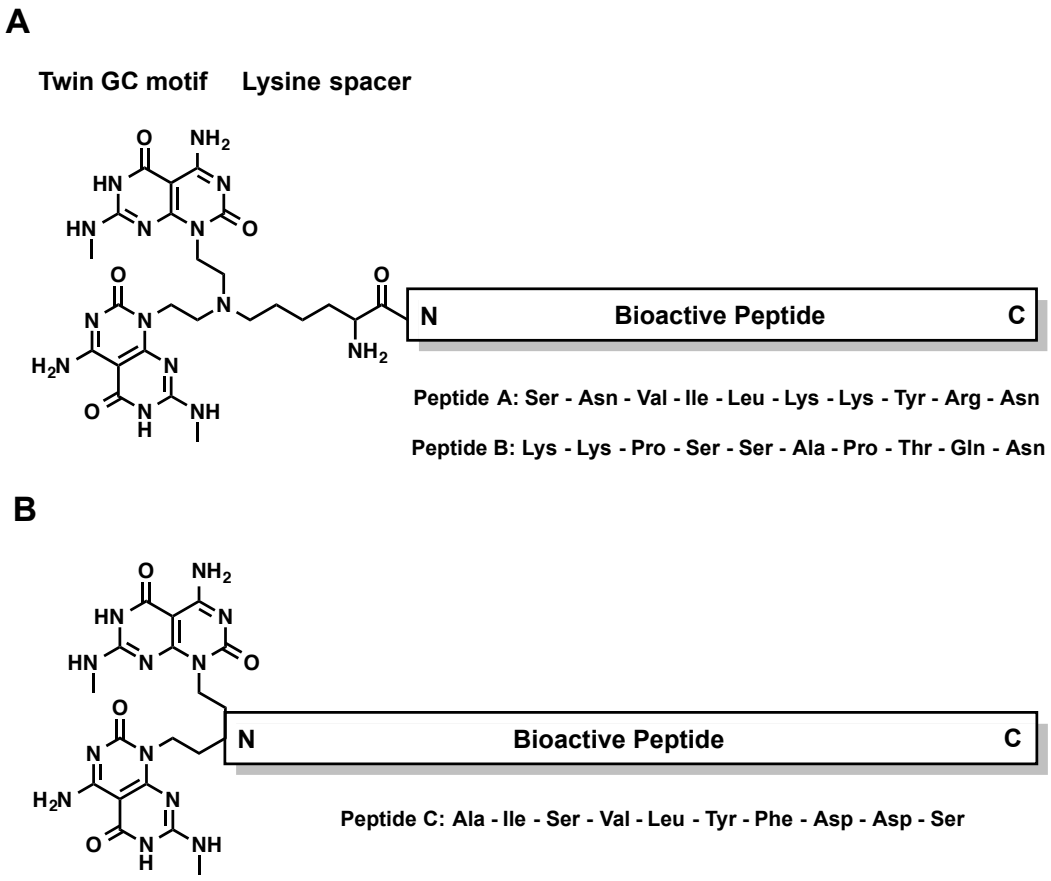

Figure 2.2. Schematic representation showing (A) twin G∧C motif, lysine spacer, and the bioactive peptides in the general design of pA-TB and pB-TB; (B) the general design of pC-TB.

According to the design in Figure 2.2, three twin G∧C-peptide conjugates were considered; pA-TB, pB-TB, and pC-TB (Figure 2.3, A). Lysine functionalized twin-G∧C (K1-TB) and the peptides with the lysine spacer pA, pB, and pC were also considered as controls (Figure 2.3, B and C respectively).

A

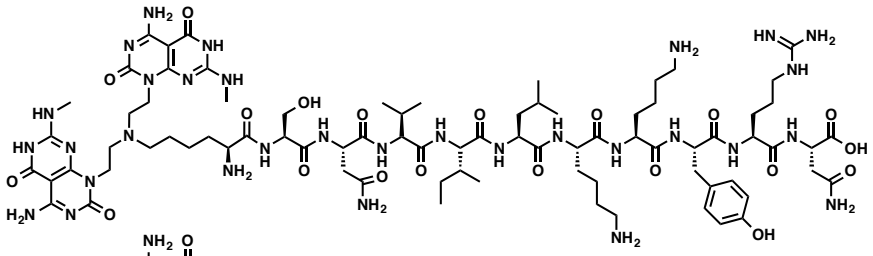

pA-TB

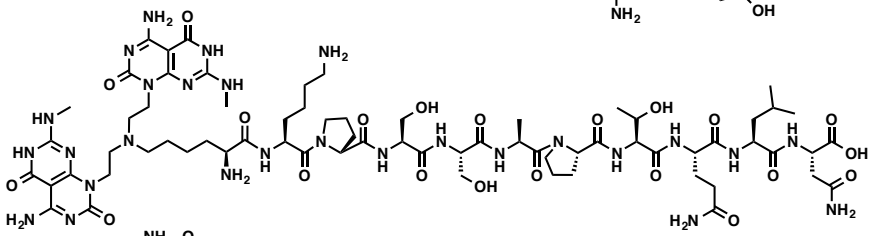

pB-TB

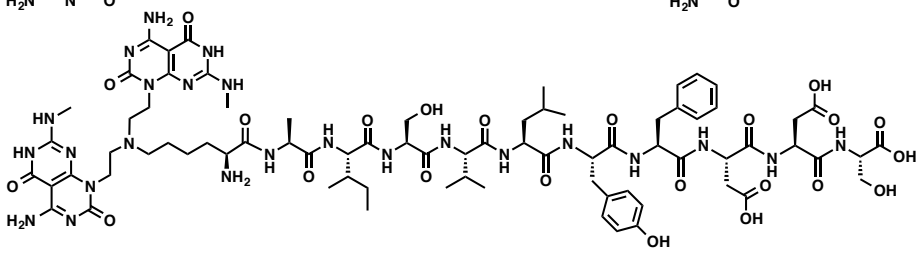

pC-TB

B

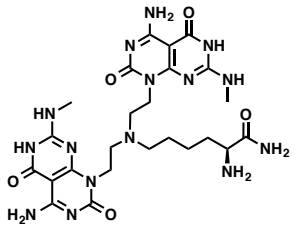

K1-TB

C

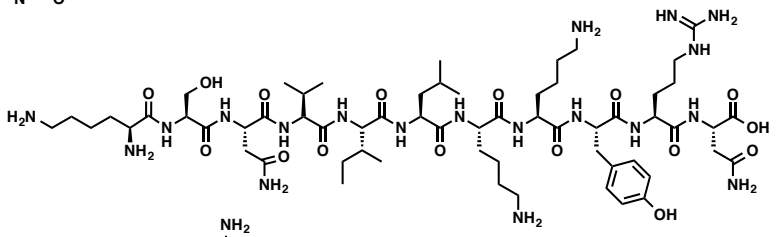

pA

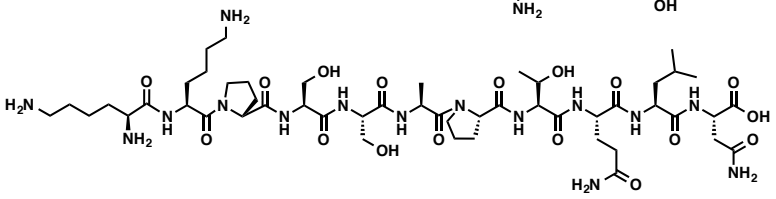

pB

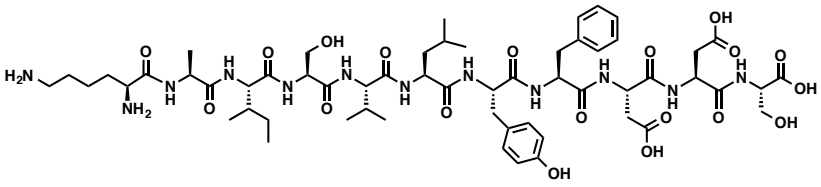

pC

Figure 2.3. Chemical structure of (A) peptide conjugates: pA-TB, pB-TB, and pC-TB respectively; (B) lysine functionalized twin-G∧C motif (K1-TB), and; (C) peptide controls: pA, pB, and pC respectively.

2.3 Synthesis

2.3.1 Synthesis of pA, pB, pC, pA-TB, pB-TB, and pC-TB

pA, pB, and pC were synthesized using a solid phase peptide synthesis strategy starting with 0.48 mmol/g 4-benzyloxybenzyl alcohol substituted Wang resin **2.1**. The first amino acid (in the C-terminus) of each of the three peptides (Fmoc-protected Asparagine in pA, and pB, and Asparatic acid in pC) **2.2** was anchored on the resin using N,N'-diisopropylcarbodiimide (DIC) catalyzed coupling reaction in the presence of 4-dimethylaminopyridine (DMAP) in anhydrous DMF. The resin was then washed and dried, and the degree of substitution was determined by spectroscopic quantification of the fulvene-piperidine adduct at 301 nm. After capping the residual unreacted hydroxyl groups on the resin by treating with 50% acetic anhydride in pyridine, the Fmoc protecting group was removed under basic conditions. The subsequent amino acids **2.5** were incorporated using cycles of amide coupling reactions in the presence of O-benzotriazole-N,N,N',N'-tetramethyl-uronium-hexafluoro-phosphate (HBTU) and DIPEA, followed by Fmoc deprotection under piperidine basic conditions. Finally, lysine amino acid spacers were incorporated to finish the synthesis (Figure 2.4).

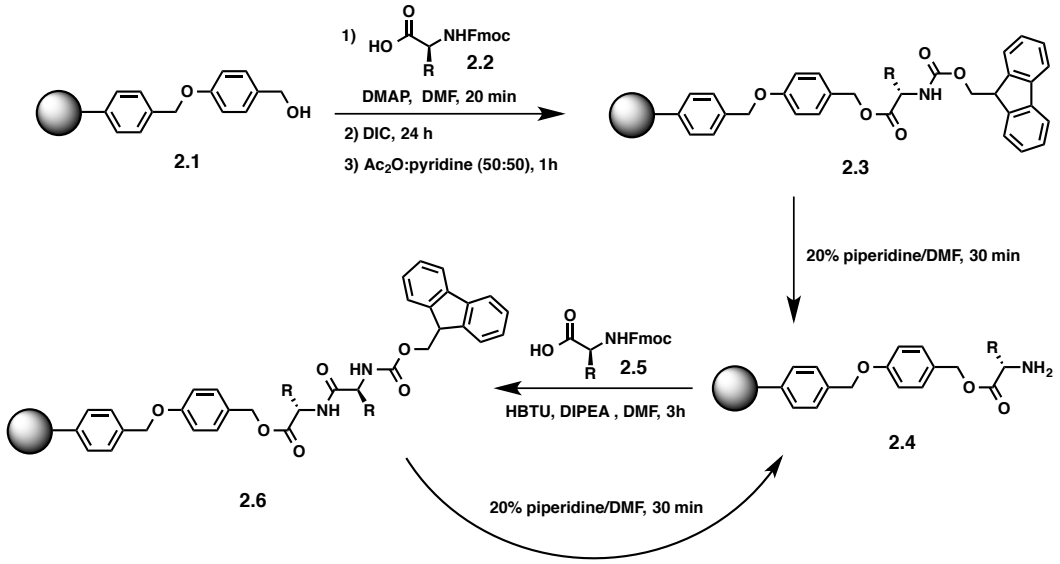

Figure 2.4. General synthesis of pA, pB and pC with the lysine spacer.

To isolate pA, pB, and pC, the peptide-loaded resins **2.7** were cleaved and deprotected under TFA acidic conditions to afford the three peptides as white solids (Figure 2.5).

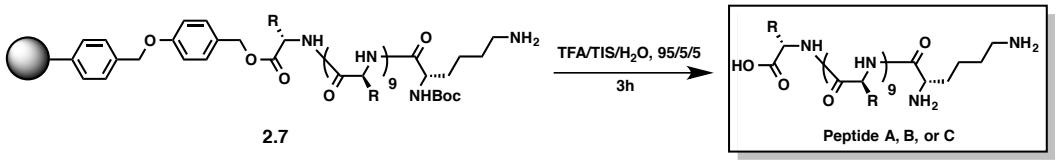

Figure 2.5. Cleavage of peptides A, B and C from the resin.

To synthesize peptide conjugates pA-TB, pB-TB, and pC-TB, the peptide-loaded resins **2.7** were coupled with G∧C base aldehyde **2.8** via a reductive amination strategy using $NaBH(OAc)_3$ and DIPEA to provide the twin-G∧C adducts. Notably, when the higher loading 0.65 mmol/g resin was used at the beginning of the synthesis instead, mono-G∧C adducts were mainly obtained, even after repeated couplings with aldehyde **2.8**. Deprotection using TFA acidic conditions then afforded conjugates pA-TB, pB-TB, pC-TB as white solids (Figure 2.6).

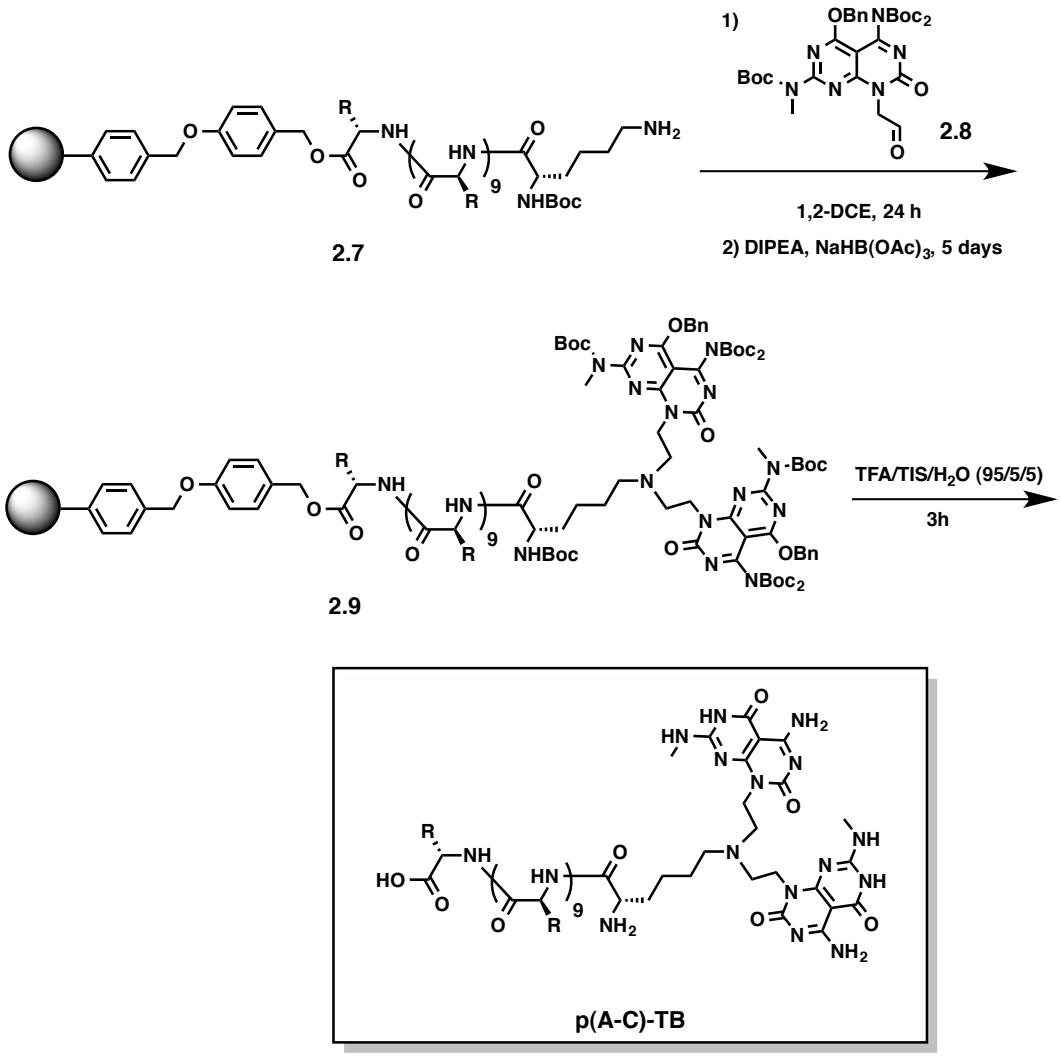

Figure 2.6. General synthesis of pA-TB, pB-TB and pC-TB.

2.3.2 Synthesis of K1-TB

Similar to the peptides and peptide conjugates, K1-TB was prepared using a solid phase peptide synthesis strategy. After anchoring the protected lysine on the 0.48 mmol/g substituted Wang resin **2.1** using DIC coupling procedure, Fmoc protecting group was removed under piperidine basic conditions. Reductive amination reaction with the protected G∧C base aldehyde **2.8** was then employed to obtain twin-G∧C conjugate **2.13**. Then TFA cleavage and deprotection afforded K1-TB as a white solid (Figure 2.7).

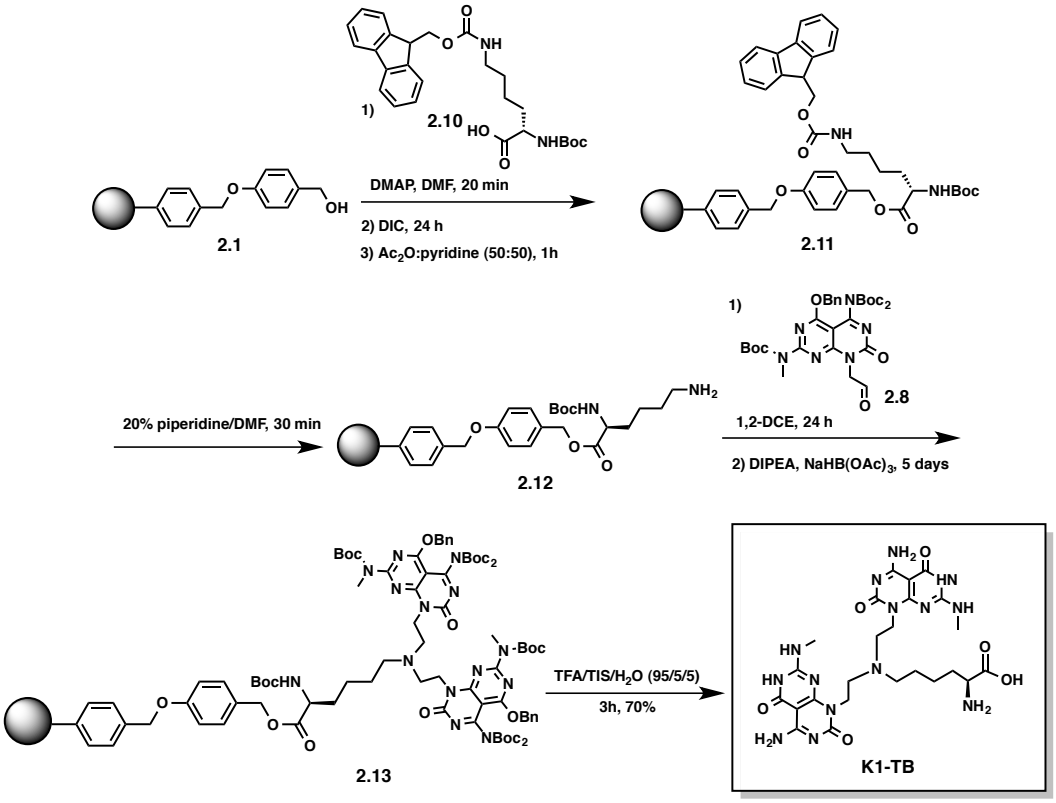

Figure 2.7. Synthetic procedure of K1-TB.

2.4 Purification and Characterization[‡]

The mass, NMR and elemental analyses of compound K1-TB revealed that it was pure and did not need further purification by HPLC. However, peptides p(A-C) and peptide conjugates p(A-C)-TB were obtained in 11 and 13 steps respectively, and further purification by HPLC was needed in order to obtain pure materials for the physical and biological studies. pA, pA-TB, pB, and pB-TB were very soluble in water and were purified on large scale by semi preparative HPLC (Figure 2.8, A-D). The pure compounds pA, pA-TB, pB, pB-TB were isolated in 16%, 20%, 18%, and 11% yields, respectively. The drop in the yield was attributed to the

[‡] Large-scale HPLC purification of the peptides and peptide conjugates were performed with the help of Mr. Rahul Agrawal.

time lag between the UV-Vis signal and the peptide takes to come out of the HPLC instrument. In order to avoid the contamination of the pure peptides with the adjoining signals of UV-Vis, isolation of peptide was done after the signal in UV-Vis started ascending and stopped before the signal approached the base line or a shoulder which may cause some loss of active product.

pC and pC-TB on the other hand were very low soluble in water and therefore their purification by HPLC was not achievable. However, analysis of the two compounds by trace-HPLC, ^{1}H NMR, and low- and high-resolution mass indicated that the crude materials were more than 87% pure, and they can be used without further purification.

All compounds pA, pA-TB, pB, pB-TB, pC, pC-TB, and K1-TB were fully characterized by elemental analysis, low- and high-resolution mass, and ^{1}H NMR. K1-TB was also characterized by ^{13}C NMR.

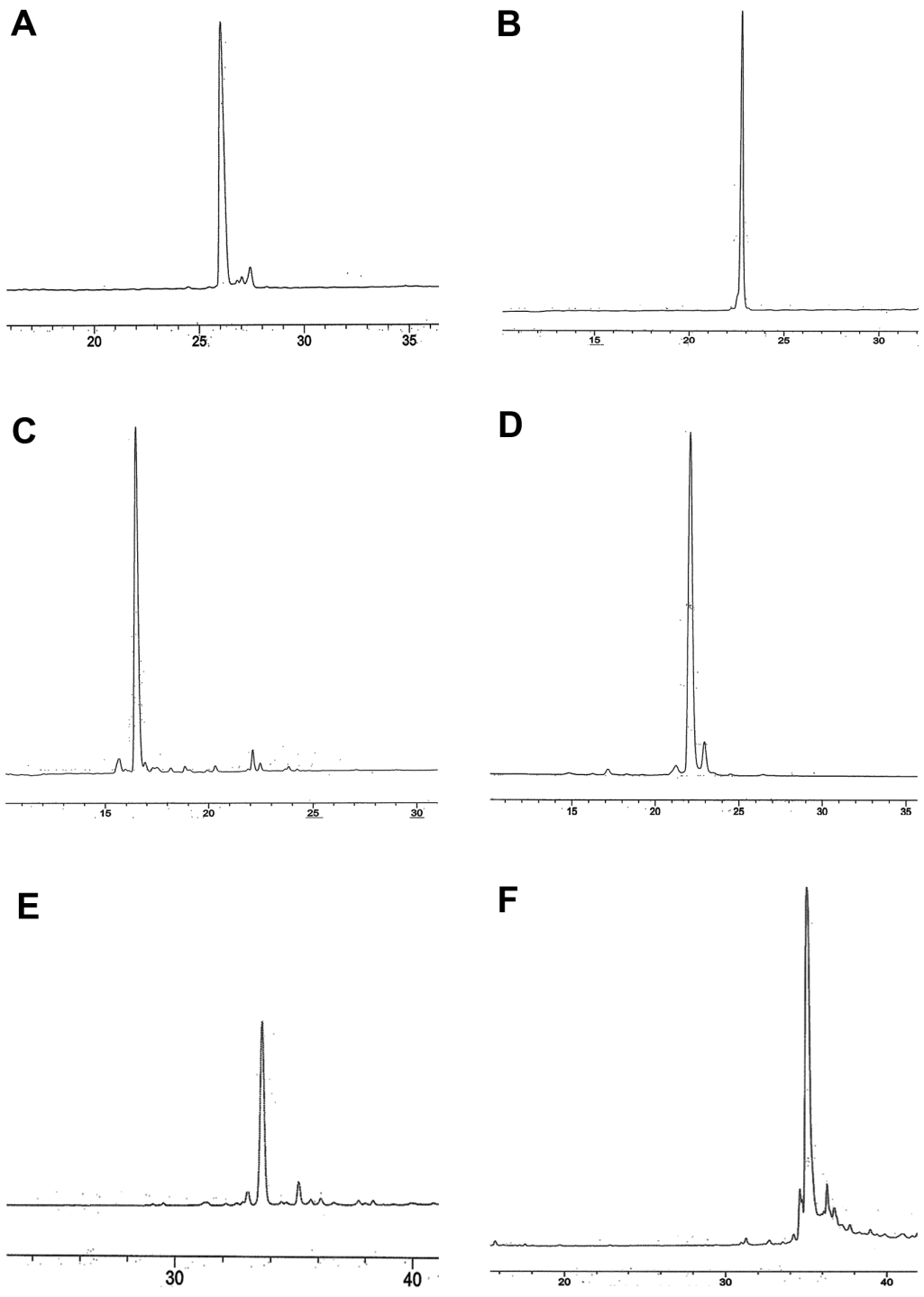

Figure 2.8. Trace-HPLC analyses of (A-F) pA, pA-TB, pB, pB-TB, pC, and pC-TB, respectively.

2.5 Self-Assembly Studies[§]

While the RGD-functionalized mono-G∧C construct failed to self-assemble into RNTs, the exceptional stability of the RNTs formed by the twin-G∧C motif successfully led to the display of oligopeptides such as RGD, KRSR and KSDGR.[16] However, the capability of the twin-G∧C RNTs to tolerate peptide sequences longer than 5 amino acids had not been explored. In principle, functionalizing RNTs with larger peptide sequences increases the density (steric) and electrostatic (charge) repulsion interactions on their outer surface, which may prevent or slower the self-assembly process. Given these challenges, in this section the twin-G∧C RNTs' ability to display the three 11-amino acid long peptides A, B, and C was explored. Furthermore, the RNTs' supramolecular chirality and the peptides' secondary structures on the periphery were elucidated.

The self-assembly processes of K1-TB, pA-TB, pB-TB and pC-TB were studied using CD and UV-Vis spectroscopy, and SEM, TEM, and AFM microscopy techniques. In all studies, stock solutions were prepared by dissolving the solids in water at 1 mg/ml concentrations. The solutions were then sonicated for 5 min and heated to 95°C, for a total of three cycles. For the spectroscopy studies, aliquots of the stock solutions were diluted to a final concentration of 5.0×10^{-5} M. For the electron microscopy studies however, the stock solutions were diluted to a final concentration of 0.01-0.1 mg/ml depending on the sample (Figure 2.9). Table 2.1 shows the measured pH values of the stock solutions (0.1 mg/ml) of pA, pB, pC, pA-TB, pB-TB, pC-TB, and K1-TB in water at neutral conditions.

[§] SEM, TEM and AFM studies of self-assembly were done by Dr. Jae-Young Cho.

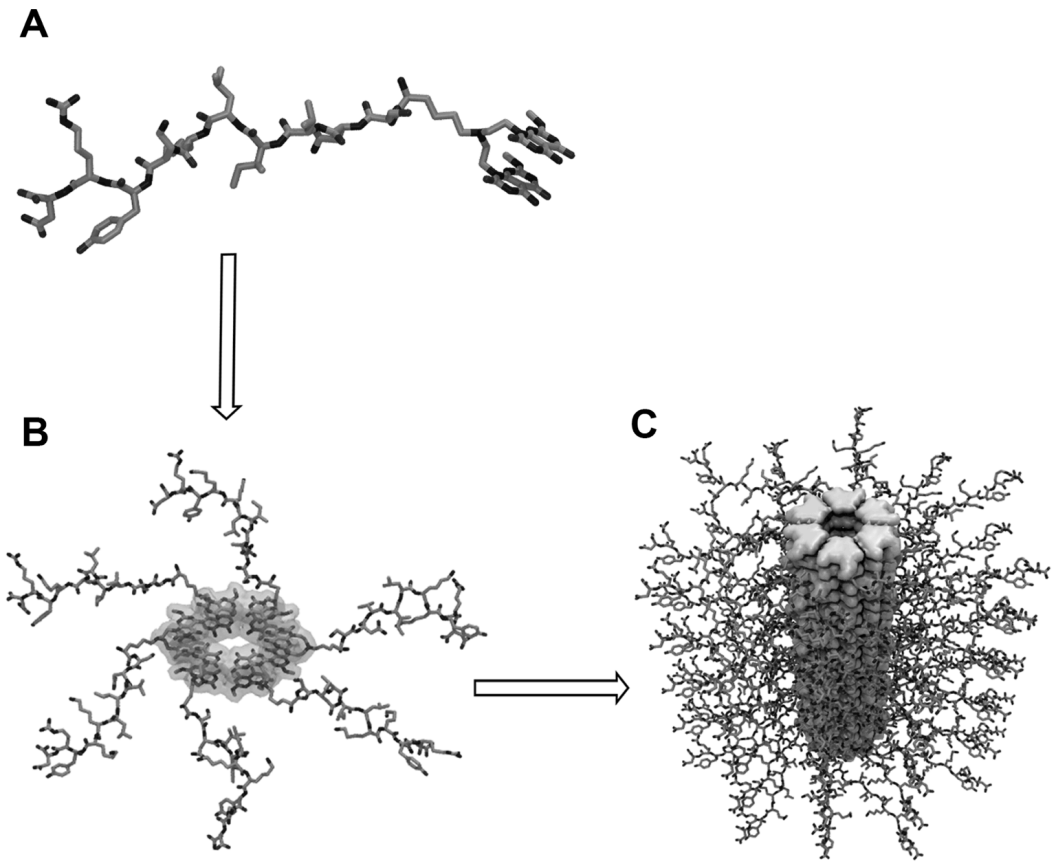

Figure 2.9. Unoptimized modeling showing (A) pA-TB motif; (B) a hexameric rosette formed by six pA-TB motifs; (C) the corresponding RNTs.

Table 2.1. Measured pH values of the stock solutions (0.1 mg/ml) after heating and sonication.

	pA	pB	pC	pA-TB	pB-TB	pC-TB	K1-TB
pH value	4.27	3.86	4.92	4.75	3.63	3.56	3.08

2.5.1 Self-Assembly of K1-TB

The UV-Vis profile of K1-TB revealed λ_{max} values at 234 nm and 286 nm, of which the absorbance values remained constant over time (Figure 2.10 A). These two absorption bands are pertained to the G∧C base chromophore.[10,12] Unlike the

mono-K1 motif (having single G∧C base), in which the UV-Vis absorption intensities decrease over time, the intensities of the two absorption bands in K1-TB did not change over the course of one week. This indicated that the self-assembly of K1-TB was very fast (within one hour). In the corresponding CD profile however, mirror image exciton spectrum was obtained having two negative bands at 301 nm and 252 nm and two positive bands at 235 nm and 202 nm (Figure 2.10 B), of which the intensities remained constant over time. The CD spectrum also featured a strong couplet centered at 244 nm, indicating a helical supramolecular chirality[26] of K1-TB as previously observed with mono-K1 and other chiral functionalized RNTs.[10]

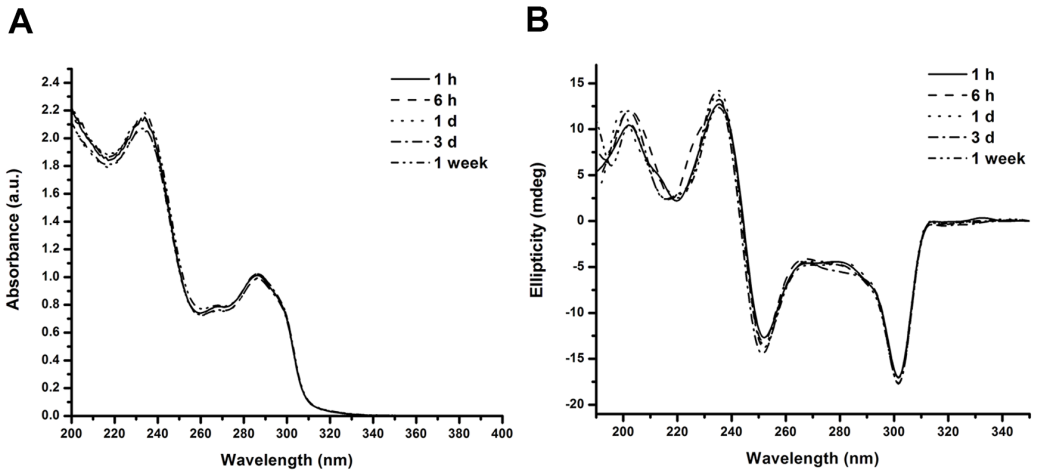

Figure 2.10. (A) Time-dependent UV-Vis study of K1-TB, (B) Time-dependent CD study of K1-TB. In both studies, a stock solution (7.9×10^{-4} M) was diluted to 5.0×10^{-5} M prior to each measurement and monitored over 7 days.

Variable temperature CD study was carried out on K1-TB motif in order to investigate the temperature at which the nanotubes are disassembled, i.e. the dynamicity of the RNTs. As shown in Figure 2.11 A, the CD profile of K1-TB was found to persist up to a temperature of *ca*. 60°C, after which the exciton spectrum started to vanish indicating disassembly. Consistent with the design criteria of the twin motif, K1-TB RNTs had a higher thermostability than the

mono-G∧C analogue K1, which begin to lose its structural integrity at *ca.* 45°C.[10] Since the CD profile of K1-TB was fully restored upon cooling the 90°C aqueous solution to room temperature (Figure 2.11 B), this established the complete reversibility of the self-assembly process.

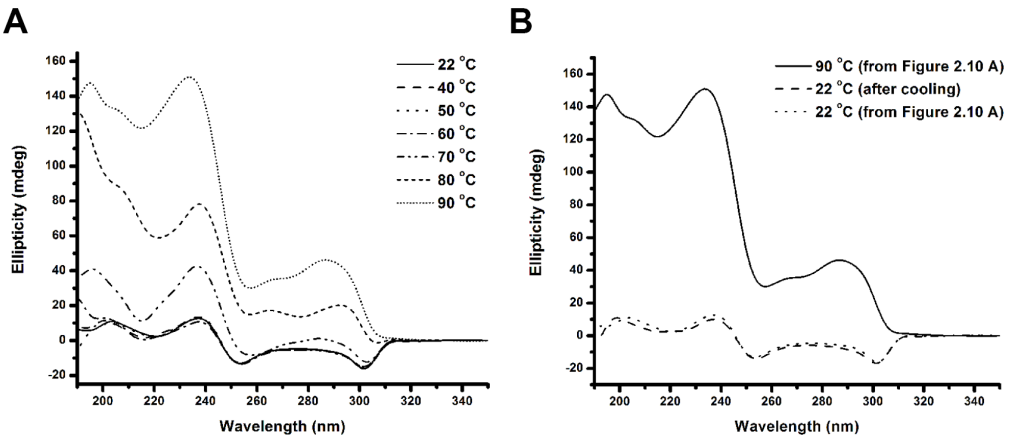

Figure 2.11. (A) Variable-temperature CD study of K1-TB. (B) Comparison of the 22°C spectrum from (A) with the CD spectrum at 22°C after cooling. In this study, a stock solution (7.9×10^{-4} M) was diluted to (5.0×10^{-5} M) prior to measurement and heated in increments of 18°C or 10°C between 22°C and 90°C.

The SEM studies shown in Figure 2.12 A-C indicated rapid self-assembly of K1-TB (within one day) to form long RNTs of which the morphology did not change over time, consistent with the UV-Vis and CD results. The average outer diameter of the RNTs was found to be 3.5 $\pm$ 0.1 nm and 3.1 $\pm$ 0.2 nm from the TEM and AFM studies, respectively (Figure 2.12 D and E).

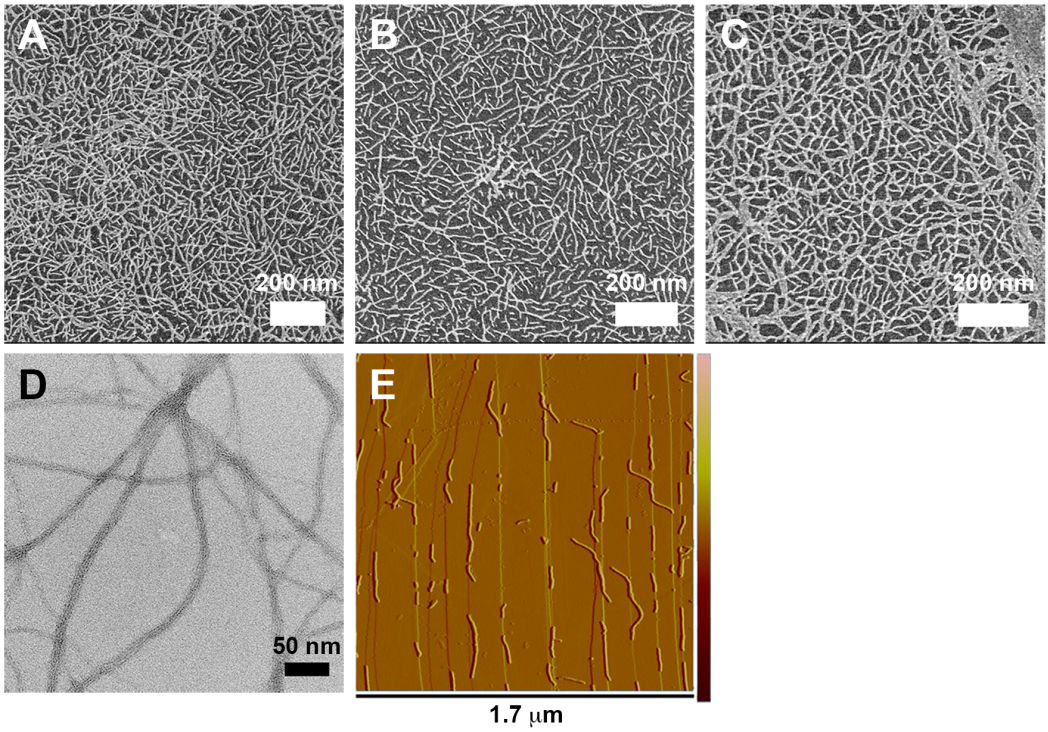

Figure 2.12. (A-C) SEM images of K1-TB (0.0125 mg/ml) after 1 day, 3 days, and 1 week, respectively. (D) TEM image of K1-TB (0.0125 mg/ml). (E) AFM image in amplitude mode of K1-TB (0.0125 mg/ml).

2.5.2 Self-Assembly of pA-TB, pB-TB, and pC-TB

The self-assembly of the peptide conjugates pA-TB, pB-TB and pC-TB were next examined and compared with the peptides pA, pB and pC. While pA-TB, pB-TB, pA, and pB were readily soluble in water, the hydrophobic nature of pC prevented it and pC-TB from solubilizing in water to any appreciable extent. Similar to the K1-TB motif, the UV-Vis profiles of both pA-TB and pB-TB revealed λ_{max} values at 232 nm and 283 nm (due to the G∧C base chromophore), of which the intensities did not change over time (Figure 2.13 A,B). The time-dependent CD spectrum of pA-TB however, provided an insight into the kinetics of its self-assembly into RNTs. At the higher wavelength regions in the CD spectrum, pA-TB presented a couplet centered around 245 nm and a negative band at 302 nm

similar to K1-TB, but only after 6 hours (Figure 2.13 C). Similarly, pB-TB presented a couplet at 248 nm and a negative band at 303 nm in an analogous fashion (Figure 2.13 D). The slow growth in intensities of the CD signals of pA-TB and pB-TB reflected their slower self-assembly compared with K1-TB. Evidently, the long peptide chains create steric and charge repulsion on the surface of RNTs during the self-assembly process. More importantly, the CD profiles of pA-TB and pB-TB RNTs indicated a helical supramolecular chirality, which is induced by the intrinsically chiral peptide chains on the periphery. However, due to the multiple chiral centers and dynamic nature of the peptides, the supramolecular chirality of pA-TB and pB-TB RNTs is not as well defined as in K1-TB. This is evident by the lower amplitudes of the CD signals of the two motifs, particularly for pA-TB. At 252 nm, the amplitudes of the CD signals of pA-TB (-3.29 mdeg) and pB-TB (-9.45 mdeg) were 76% and 31% lower than K1-TB (-13.8 mdeg) respectively, after 1 week of aging (Figure 2.13 C).

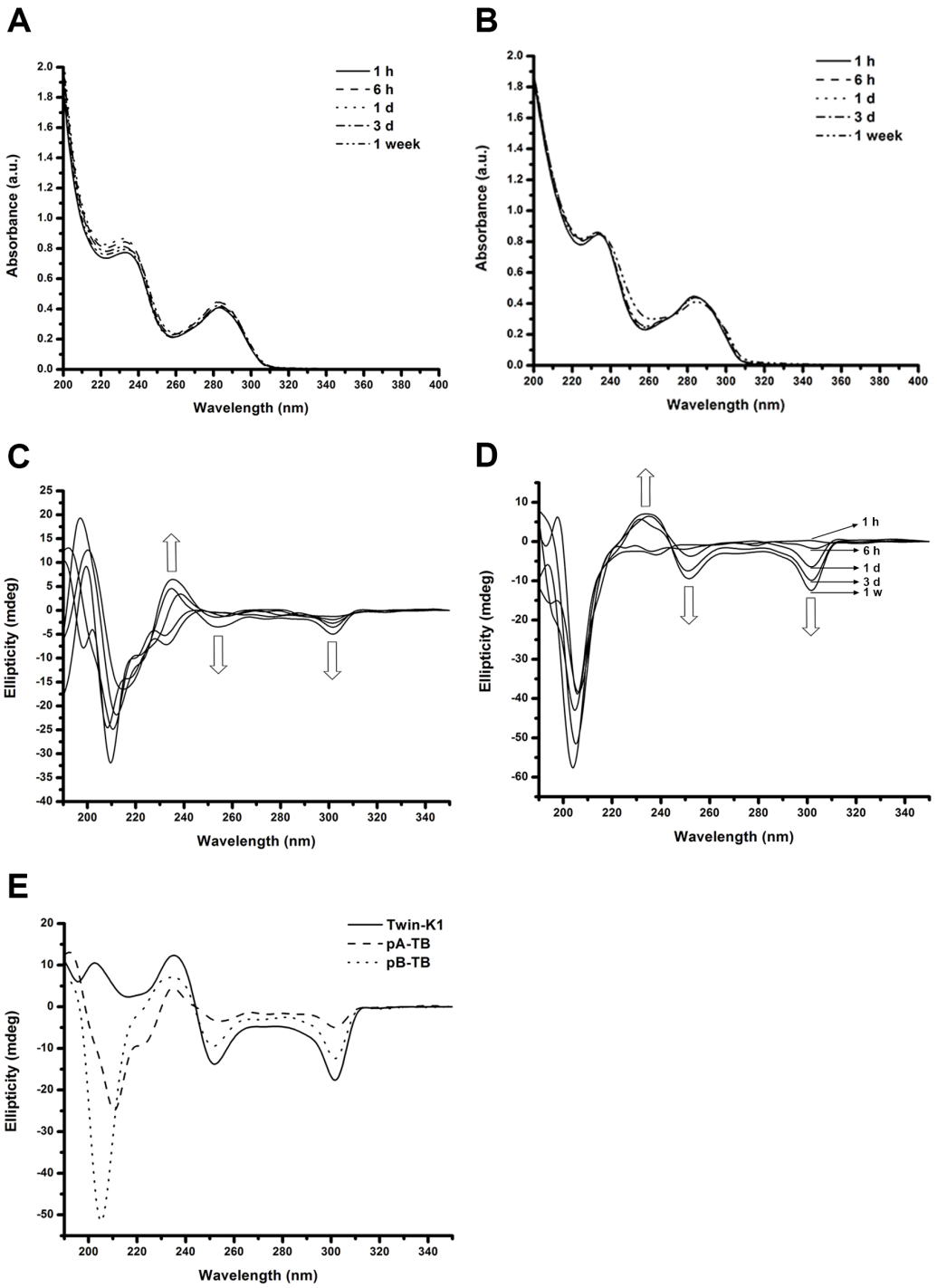

Figure 2.13. (A,B) Time-dependent UV-Vis studies of pA-TB and pB-TB, respectively; (C,D) Time-dependent CD studies of pA-TB and pB-TB, respectively; (E) Comparison of the CD spectra of pA-TB, pB-TB, and K1-TB

after 1 week of aging. In all studies, the stock solutions (7.9×10^{-4} M) were diluted to 5.0×10^{-5} M prior to each measurement.

The time-dependent CD spectra of pA-TB and pB-TB provided insight into the peptide secondary structures and the G∧C chromophore organization during the self-assembly process. Focusing on the far UV (below 220 nm) and therefore the peptide-absorbing region of the CD spectra, pA-TB revealed multiple bands between 190 nm and 220 nm after 1 hour of aging time (Figures 2.14). Evidently, the peptide assumed various secondary structures at the beginning of the self-assembly where rosettes and short stacks of rosettes predominate. The strong negative band at 199 nm for example, is characteristic of random coil behavior, whereas the positive band at 190 nm, strong negative band at 210 nm and weaker negative band at 220 nm may indicate β-sheet and also α-helical conformations.[27] After 7 days, the surface peptides of the pA-TB RNTs exhibited a CD signature that featured mainly a strong minima at 210 nm, which reflects an average structure between random coil (as predicted by the molecular modeling simulations (see section 2.7), and β-sheet conformations. Likewise, the CD signature of the free peptide A had strong minima at 208 nm with very similar shape (Figures 2.14). The lower amplitude of the CD signal at 208 nm in pA-TB compared to that of pA is due to the overlap with the second positive absorption band of the G∧C chromophore in this region.

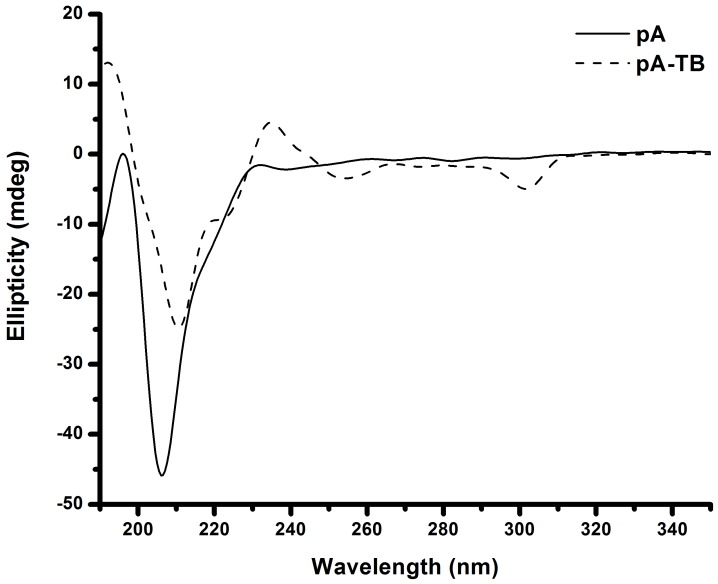

Figure 2.14. Comparison of the CD spectra of pA-TB and pA after 1 week of aging. The stock solutions (7.9×10^{-4} M) were diluted to 5.0×10^{-5} M prior to each measurement.

For pB-TB, MD simulations predicted a strong propensity for the peptide to have predominant random coil rather than α-helix, β-turn or β-sheet conformations on the surface of the RNT (see section 2.7). Indeed, the strong negative bands observed between 200-205 nm in the CD spectra obtained during the one week study, suggested mainly random coil structures for both pB (Figures 2.15 A) and pB-TB (Figures 2.15 B). Similar to pA-TB, the intensity of the peptide negative band in the CD spectrum of pB-TB was lower than that of pB.

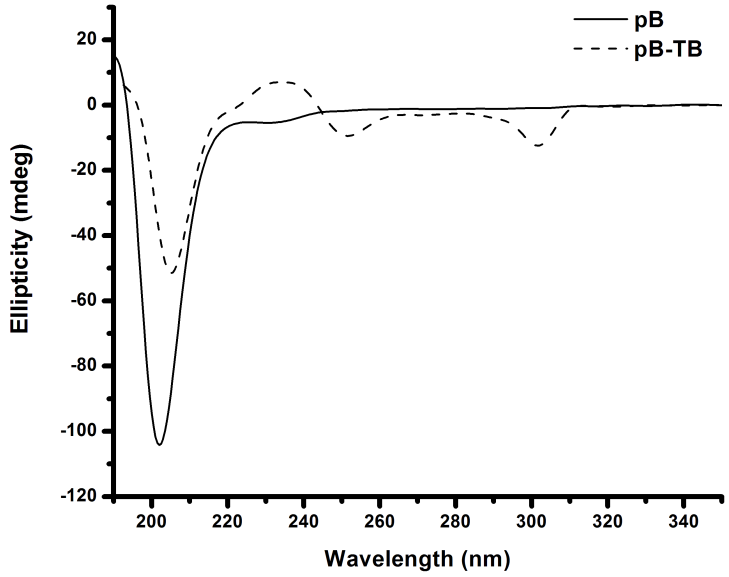

Figure 2.15. (A) Comparison of CD spectra of pB-TB and pB after 1 week of aging. The stock solutions (7.9×10^{-4} M) were diluted to 5.0×10^{-5} M prior to each measurement.

In conclusion, the CD results indicated that the self-assembly of the peptide-TB conjugates into RNTs do not alter the secondary structures of the free peptides, which is important to preserving their inherent bioactivity. This is evident by the similar peptide secondary structures in the self-assembled pA-TB and pB-TB RNTs and the free peptides pA and pB, respectively.[28]

The SEM imaging studies of pA-TB and pB-TB indicated that both motifs successfully self-assembled into RNTs. While pA-TB formed short well-dispersed RNTs after 1 day, which grew longer as time had progressed (Figure 2.16 A-C), pB-TB self-assembled into predominately bundled short RNTs after 1 day and to bundles of longer RNTs after 3 days and 1 week (Figure 2.16 D-F). The formation of bundles in pB-TB *vs* well-dispersed RNTs in pA-TB is owing to the lower charge density of the peptide B having +1 net charge *vs* +3 net charge for the peptide A. Consistent with the CD results, the SEM studies indicated that the self-

assembly process of pA-TB and pB-TB was slower than that of K1-TB (days *vs* 1 hour or less). However, the formation of RNTs by both peptide conjugates is an impressive demonstration of the stability of the twin-RNT construct and its ability to tolerate steric and charge repulsion forces between the multi-charged peptide chains on the periphery. From the TEM images, the outer diameters of the pA-TB and pB-TB RNTs were measured to be 7.9 $\pm$ 0.2 nm and 7.3 $\pm$ 0.5 nm, respectively.

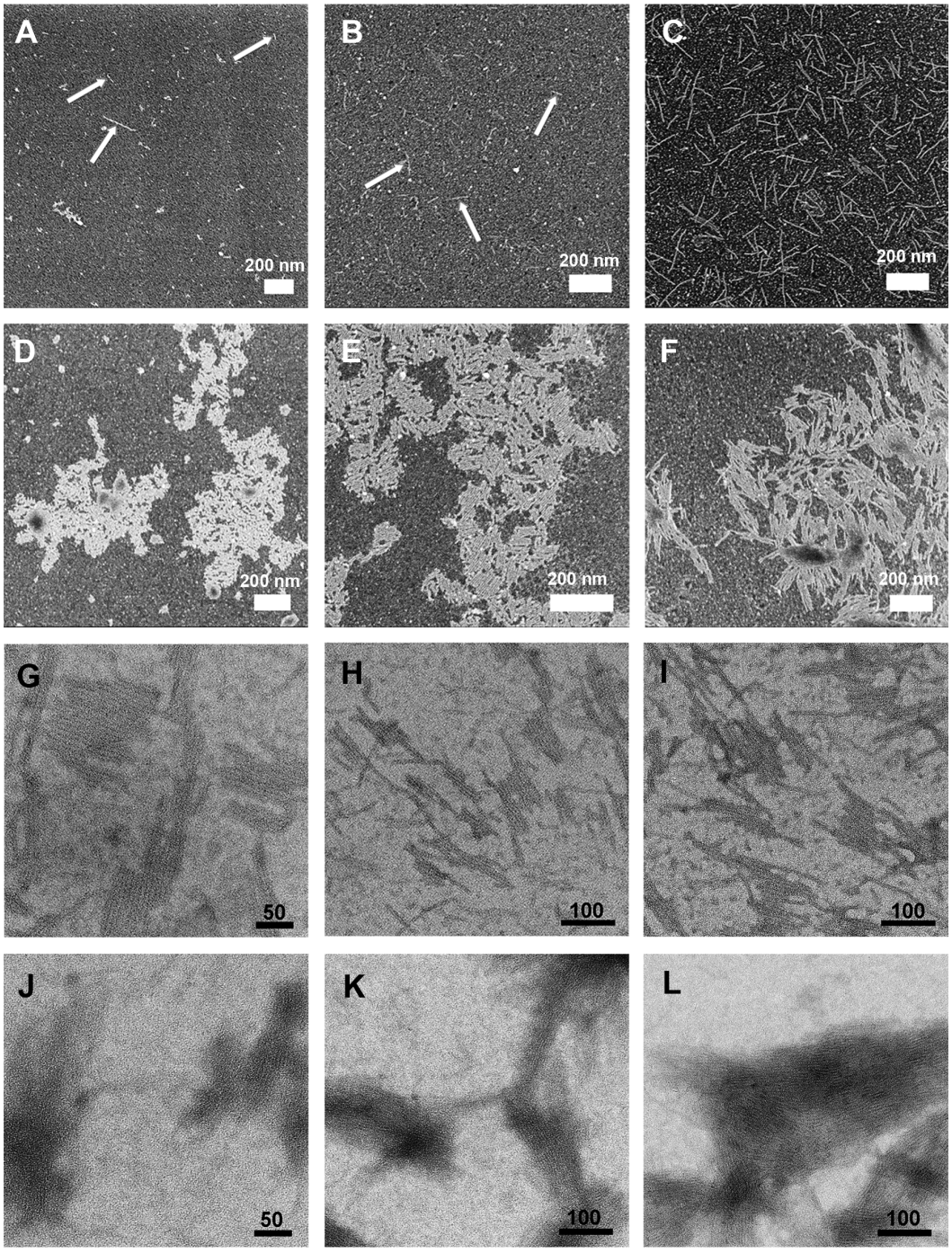

Figure 2.16. (A-C) SEM images of pA-TB (0.1 mg/ml) in water after 1 day, 3 days, and 1 week, respectively; (D-F) SEM images of pB-TB (0.1 mg/ml) in water after 1 day, 3 days, and 1 week, respectivel; (G-I) TEM images of pA-TB (0.1 mg/ml); and (J-L) TEM images of pB-TB (0.1 mg/ml) after 1 week of aging.

Unfortunately, pC and pC-TB motifs were not soluble in water even after repeated cycles of heating and sonication, which was reasoned to the hydrophobic nature of peptide C having five hydrophobic amino acids in its sequence and -1 net charge. As a result, both compounds crashed out of the solutions after couple of hours and no information could be obtained by physical characterization. While SEM imaging of pC-TB revealed no nanotubes formation (Figure 2.17 B), the time-dependent UV-Vis studies revealed two bands at 238 nm and 288 nm, which intensities gradually decreased until they vanish after 1 day due to the precipitation of the motif (Figure 2.17 A). Similarly, the CD absorption bands of pC-TB completely disappeared after 1 day. However, the CD spectra after 1 and 6 h revealed two negative bands at 226 and 242 nm and two positive bands at 200 and 212 nm owing to the peptide absorption. These absorption bands might indicate that the peptide adopted mainly α-helical secondary structures on the RNTs. On the other hand, pC gave silent CD spectra even after 1 h (Figure 2.17 C).

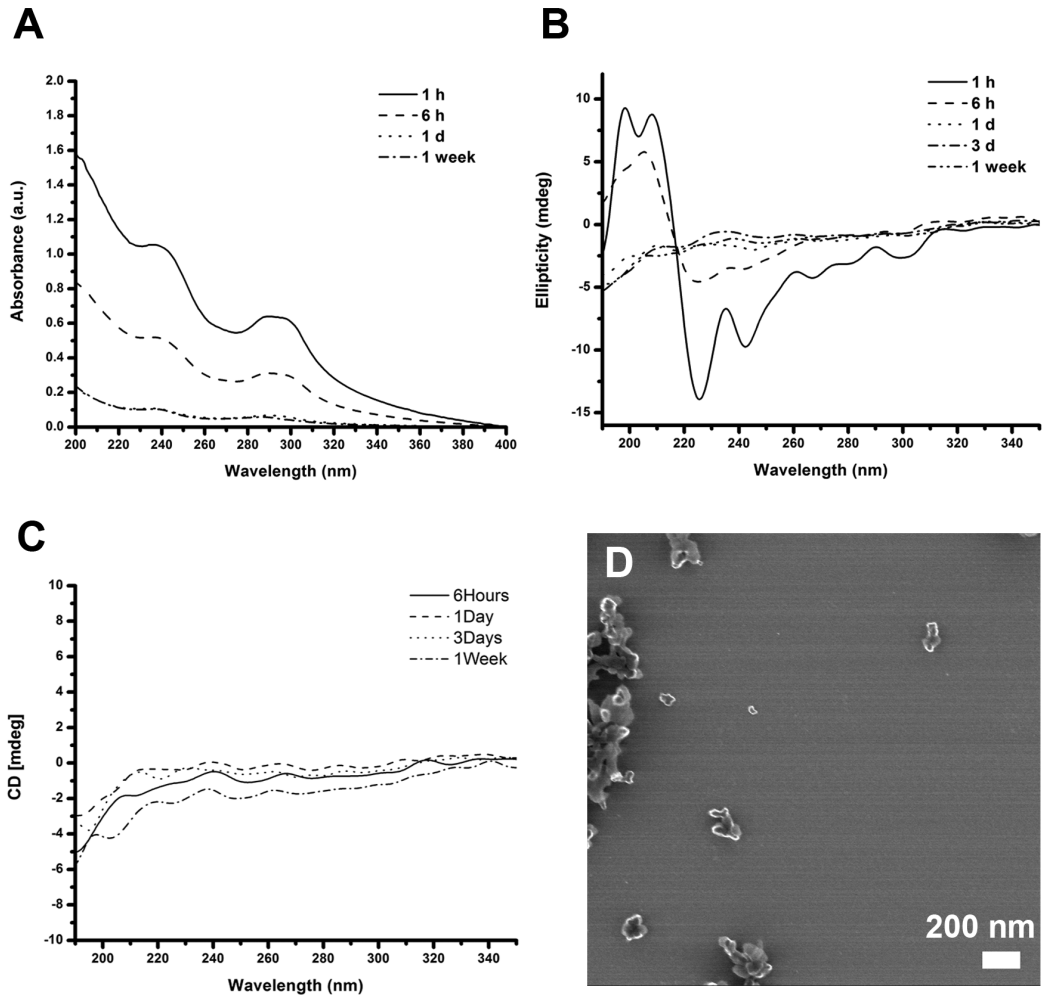

Figure 2.17. (A) Time-dependent UV-Vis study of pC-TB; (B) Time-dependent CD study of pC-TB; (C) Time-dependent CD study on pC; and (D) SEM image of pC-TB (0.1 mg/ml) in water after 2 weeks of aging.

2.6 Co-Assembly Studies**

In the previous section, the RNT's ability to tolerate long and multi-charged peptides on the periphery was demonstrated. However, the surface peptides are sterically congested in the self-assembled RNTs and thus the interaction with

** SEM and TEM studies of co-assembly were done by Dr. Jae-Young Cho.

bone cells will be limited to the terminal amino acids (in the C-termini) of the peptides. In other words, the whole peptide sequence may not be fully accessible to the cells (Figure 2.9). In this regard, co-assembly studies of each of the three peptide conjugates; pA-TB, pB-TB and pC-TB with K1-TB motif in 1:9 molar ratio were carried out in order to provide more space for the peptides on the RNTs for better osteogenic properties (Figure 2.18 C). It is also expected that the co-assembled RNTs (containing 90% of the K1-TB motif) will have cell adhesive properties similar to that of mono-K1 RNTs. In addition, since pC-TB motif did not form RNTs because of the low solubility of peptide C in water, the presence of the very soluble K1-TB motif might help to solubilize pC-TB and form the corresponding RNTs.

To this end, the outcome of co-assembly was to be investigated since no evidence of the formation of mixed-RNTs (having two different G∧C motifs) had been provided. Therefore, in the following sections I present the physical studies that were carried out in order to characterize the mixtures and to study the influence of co-assembly on the physical properties of the RNTs. In principle, upon mixing two different twin-G∧C motifs with different functionalities in solution, three possibilities could happen: 1) the formation of "self-assembled RNTs mixture" (Figure 2.18 A); 2) the formation of "block mixed RNTs" by the π-π stacking of the individual rosettes formed by each of the motifs (Figure 2.18 B); and 3) the formation of "random-mixed RNTs" (Figure 2.18 C). Although both the "block-mixed" and the "random-mixed" RNTs are co-assembled constructs, the latter model features randomly distributed peptides on the surface and is therefore more desired for the biological applications. Spectroscopy (UV-Vis and CD) and microscopy (SEM and TEM) techniques were used in the following experiments to demonstrate that the three co-assembled mixtures were indeed "random-mixed" RNTs.

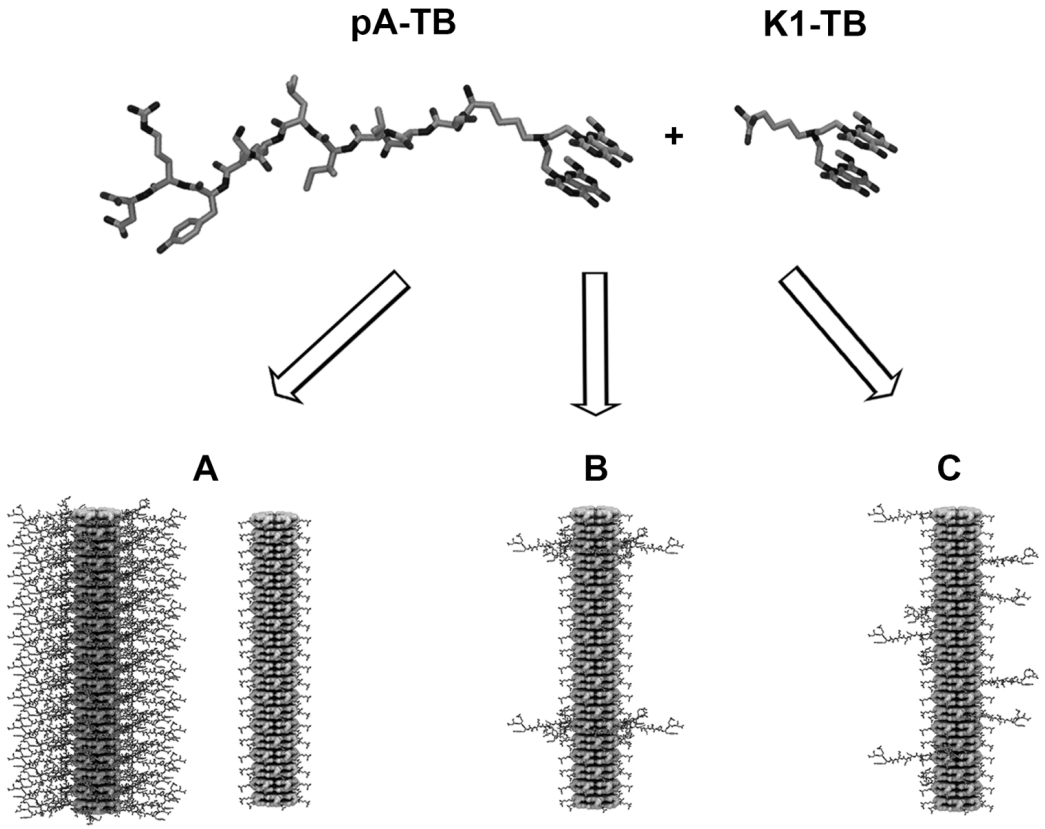

Figure 2.18. Unoptimized modeling showing (A) the "self-assembled RNTs mixture" formed by pA-TB and K1-TB motifs; (B) the "block-mixed RNTs" formed by the π-π stacking of rosettes formed by pA-TB and K1-TB motifs; and (C) the "random-mixed RNTs" formed by the co-assembly of pA-TB and K1-TB motifs.

2.6.1 Spectroscopic Studies of Co-Assembly

Circular Dichroism (CD) spectroscopy has evolved as an important technique to probe the inter- and intra-molecular interactions in supramolecular chemistry due to its high sensitivity to any perturbation in the chirality of the self-assembled systems. For instance, CD has been used in the literature to study the co-assembly of peptides and peptide amphiphiles since the CD profile of a peptide (in the region 190-240 nm) is very sensitive to any change in its secondary structure.[29-36] Other studies used this technique to characterize the co-assembly of chiral and

achiral entities into helical supramolecular structures.[37,38] Beginning with this knowledge from the literature, CD spectroscopy can be a very useful technique to provide information about the structure of the mixed-RNTs that are formed by the pA-TB:K1-TB, pB-TB:K1-TB, and pC-TB:K1-TB, 1:9 mixtures. As discussed in section 2.5, the helical supramolecular organization of the self-assembled RNTs formed by K1-TB, pA-TB, and pB-TB motifs led to unique exciton CD spectra featuring two negative bands at 301 and 252 nm and two positive bands at 235 and 202 nm, but with different amplitudes. As a result, the presence of 10% of pA-TB or pB-TB may have an influence on the supramolecular chirality of the K1-TB RNTs, which may lead to a significant change in the corresponding CD profile. The following experiments present the detailed time-dependent CD and UV-Vis studies that were carried out to characterize the three mixtures.

Experiment 1: In the first experiment, K1-TB and the three peptide-TB solids (9:1 molar ratio) were mixed in water to provide three 1 mg/mL stock solutions called "A". The solutions were then subjected to triplicate cycles of sonication for 5 min, followed by heating by heat gun to 95ºC. Under these conditions, any pre-existing self-assemblies can be disassembled (Figure 2.11). The stock solutions "A" were then left at room temperature for aging, and studied by UV-Vis, CD, and SEM over time.

For CD and UV-Vis studies, the stock solutions "A" were diluted to 5.0×10^{-5} M with respect to K1-TB prior to the measurements. For SEM studies, the stock solutions "A" were diluted to a 0.0125 mg/ml concentration prior to the grid preparation. Notably, during the preparation of the K1-TB:pC-TB solution, pC-TB motif fully dissolved and remained so upon cooling to room temperature. This was a good initial indication of its co-assembly with K1-TB.

Visualization of the solutions by SEM after 1 day of aging, verified the formation of RNTs in the three mixtures (Figure 2.19 B, D, and F). As might be expected for a 9:1 molar ratio, both the rapid rate of formation of the nanotubes and their

morphologies (i.e. well-dispersed long RNTs) were similar to the self-assembled K1-TB (the major component) RNTs. The inspection of the UV-Vis spectra of the mixtures revealed λ_{max} values at 232 nm and 286 nm for K1-TB:pA-TB and 231 nm and 287 nm for K1-TB:pB-TB and K1-TB:pC-TB, respectively (Figures 2.19 A, C, and E). The intensities of these bands did not change over time in agreement with the rapid (< 1h) assembly observed by microscopy.

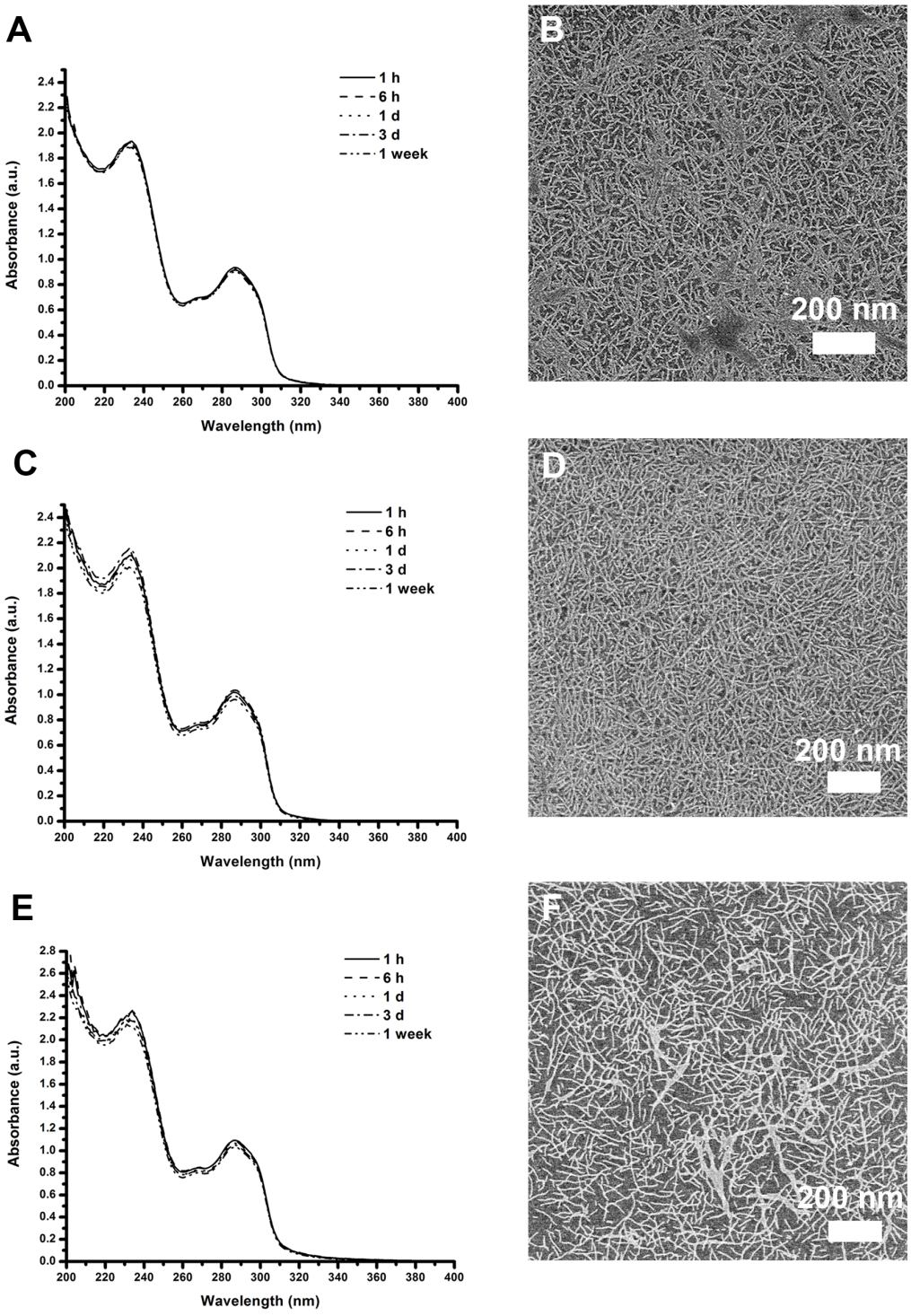

Figure 2.19. Time-dependent UV-Vis spectra (5.0×10^{-5} M) and SEM images (0.1 mg/ml) after 1 day, respectively of the 9:1 mixtures "A" of (A,B) K1-TB:pA-TB; (C,D) K1-TB:pB-TB; and (E,F) K1-TB:pC-TB.

In the corresponding time-dependent CD spectra, the profiles within the peptide absorbing regions (190-240 nm) of the three mixtures fluctuated over time, indicative of the dynamic nature of the peptides on the periphery of the RNTs (Figure 2.20 A-C). The K1-TB:pA-TB and K1-TB:pB-TB mixtures however, presented negative bands below 200 nm characteristic of random coil secondary structures. This was particularly evident with the K1-TB:pB-TB mixture after 1 week of aging (Figure 2.20 B) and was also predicted in the molecular modeling simulations (see section 2.7). On the other hand, the K1-TB:pC-TB mixture presented mainly two negative bands around 220 nm and 210 nm and a strong positive band around 200 nm, which is indicative of α-helix and β-sheet conformations.

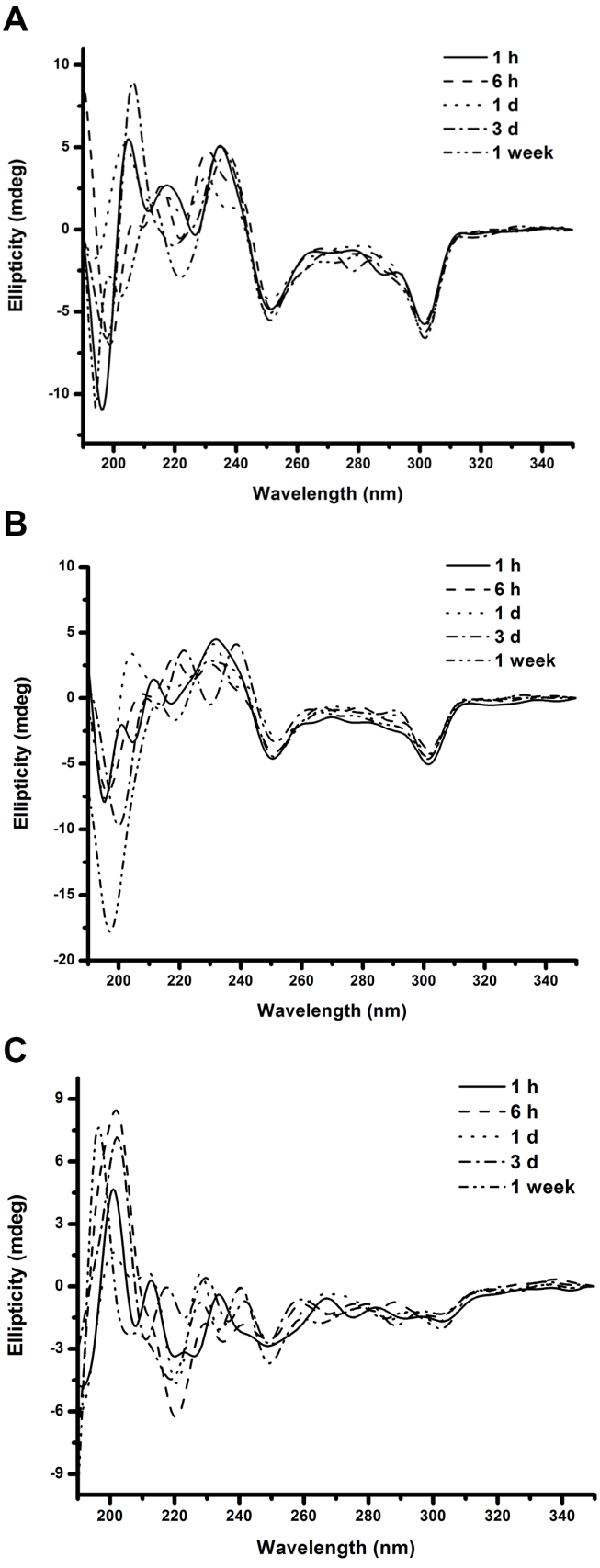
A
1 h
6 h
1 d
3 d
1 week
Ellipticity (mdeg)
Wavelength (nm)
B
1 h
6 h
1 d
3 d
1 week
Ellipticity (mdeg)
Wavelength (nm)
C
1 h
6 h
1 d
3 d
1 week
Ellipticity (mdeg)
Wavelength (nm)

Figure 2.20. Time-dependent CD spectra of the 9:1 mixtures "A" of (A) K1-TB:pA-TB; (B) K1-TB:pB-TB; and (C) K1-TB:pC-TB. The stock solutions (7.9×10^{-4} M) were diluted to 5.0×10^{-5} M prior to each measurement.

At the higher wavelength regions in the CD spectra, the profiles of the three mixtures "A" (Figure 2.20 A-C) featured the same couplet centered around 243 nm (or 244 nm) and a lower energy negative band at 301 nm (or 302 nm) as K1-TB, which intensities remained constant with time in agreement with the UV-Vis studies. However, the amplitudes of the absorptions in this region were significantly lower than that of K1-TB. Regarding the trough at 301 nm (or 302 nm) for example, the CD signal for K1-TB:pA-TB, K1-TB:pB-TB and K1-TB:pC-TB was ca. 65%, 75% and 89% lower than K1-TB respectively, after 7 days of aging (Figure 2.21). Evidently, the supramolecular chirality of the K1-TB RNTs was significantly disrupted by the presence of the peptide-TB motifs, even though they represent only 10% of the mixture.

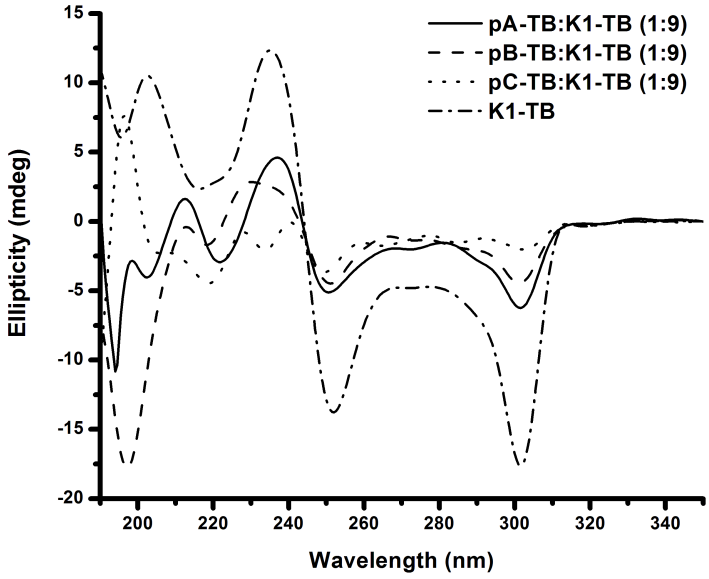

Figure 2.21. Comparison of the CD spectra after 1 week of aging of K1-TB (from Figure 2.10 B) and the three 9:1 mixtures "A" of K1-TB:pA-TB, K1-TB:pB-TB, and K1-TB:pC-TB at 9:1 molar ratios.

Two explanations can account for this observation. First is the co-assembly of the motifs to form "block-mixed" RNTs or "random-mixed" RNTs as shown in Figure 2.18 B and C, respectively. In this case, the dynamic nature of the peptides, their multi-chiral centers and conformational organization (i.e. random coil) are impediments to having an ordered organization of the surface groups for a well-defined chirality. In addition, inter-rosette electrostatic interactions between the lysine residue (of K1-TB) and the carboxylate group of the peptides may lead to a disruption of lysine organization on the outer surface. The formation of this type of salt bridge was observed during the molecular modeling of co-assembled RNTs formed from pB-TB and K1-TB (see section 2.7). Alternatively, the co-assembly may not have occurred, but rather, K1-TB self-assembled into RNTs. In this case, the chirality of the K1-TB nanotubes could be disrupted through electrostatic interactions with the peptide-TB motifs (or RNTs) on the outer surface. To decipher these two possibilities, the following control experiment was performed.

Experiment 2: In this experiment, aliquot of the pre-assembled stock solution of K1-TB was mixed with aliquots of the pre-assembled pA-TB, pB-TB, or pC-TB stock solutions after 1 week of aging in 9:1 molar ratio, and gently stirred together at room temperature. The resulting mixed stocked solutions called "B" herein were not subjected to sonication or heat in order to minimize their co-assembly. Prior to the CD measurements, the solutions were diluted to a final concentration of 5.0×10^{-5} M with respect to K1-TB.

In general, CD principles state that two separate chiral entities in solution present themselves as a linear combination in the spectra, taking into consideration their molar ratios.[39] As shown in Figure 2.22 D, the CD profiles in the RNT absorbing region of the mixtures "B" were well aligned in terms of the amplitude and

wavelength with the self-assembled K1-TB RNTs (the major component consisting 90% of the mixtures). This indicated that the K1-TB RNTs and the peptide-TB RNTs in solutions "B" were indeed separate entities. Since the CD profiles also did not change over time, this established their excellent kinetic stability, and that the RNTs are not dynamic at room temperature (Figure 2.22 A-C).

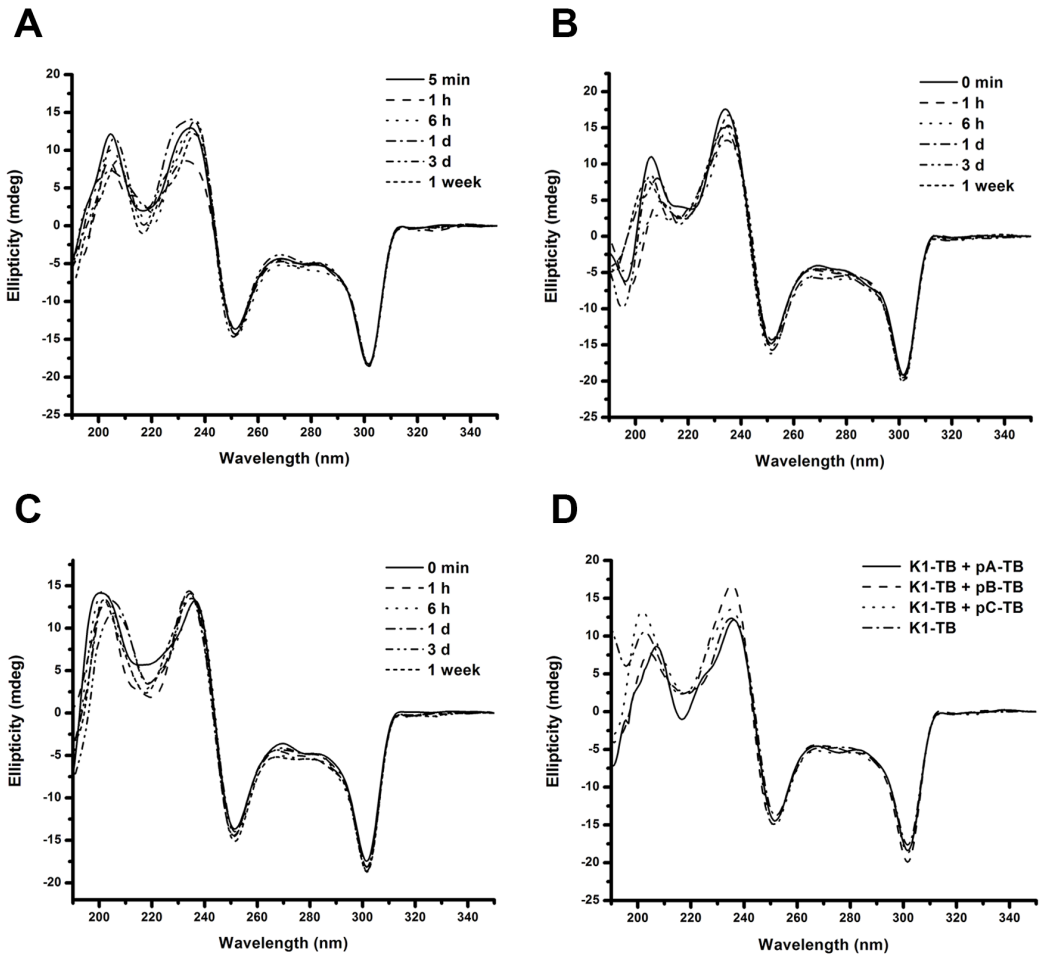

Figure 2.22. (A-C) Time-dependent CD spectra of the K1-TB:pA-TB, K1-TB:pB-TB, and K1-TB:pC-TB 9:1 mixtures "B", respectively; (D) Comparison of the CD spectra of the three mixtures "B" after 1 week and the CD spectrum of K1-TB after 1 week (from Figure 2.10 B).

Evidently, this study showed that electrostatic interactions between the peptide-TB RNTs and the K1-TB RNTs, do not disrupt the supramolecular chirality of the latter. In-turn, this strongly indicated that the CD profiles of mixtures "A" were that of the co-assembled RNTs. This was further supported by the molecular modeling predictions of co-assembled K1-TB:pB-TB RNTs, which showed that pB-TB motif is stable during a 10 ns simulation run, regardless of whether it is incorporated within the middle of the K1-TB RNT or within the terminal rosette (see section 2.7).

Experiment 3: In order to investigate whether we can promote the co-assembly in the pre-assembled mixtures "B" after 1 week, the three stock solutions "B" were subjected to heat (95°C) and sonication to ensure the disassembly of the peptide-TB RNTs and in particular the K1-TB RNTs, since they were found to disassemble after *ca*. 60°C (Figure 2.11 A). The resulting thermodynamic mixtures "C", obtained upon cooling to room temperature exhibited CD signal amplitudes at the higher wavelength regions (Figure 2.23), which were similar to the corresponding solutions "A" (Figure 2.20 A-C). Not only did this study show that the self-assembled mixtures "B" form co-assembled RNTs upon heating and sonication, but also the similar CD profile of the mixtures "A" and "C" indicated that the co-assembled RNTs formed in experiments 1 and 3 have same supramolecular organization.

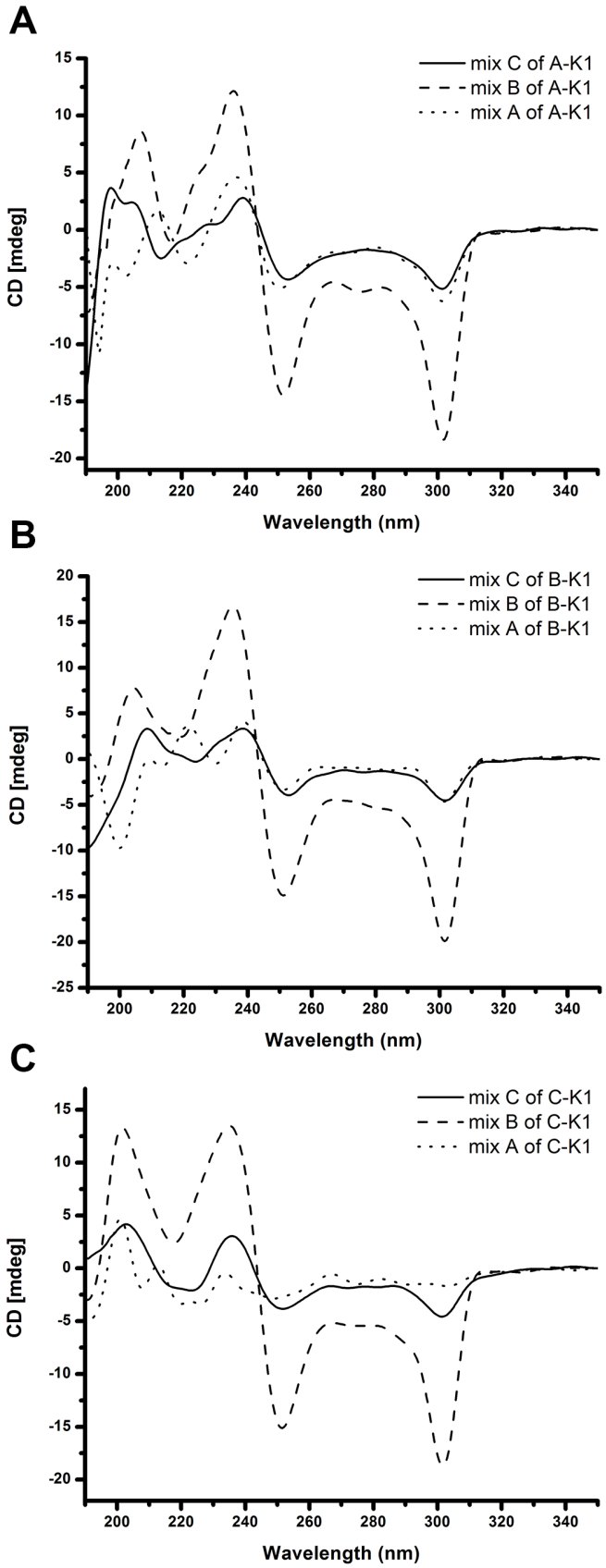
A
mix C of A-K1
mix B of A-K1
mix A of A-K1
CD [mdeg]
Wavelength (nm)
B
mix C of B-K1
mix B of B-K1
mix A of B-K1
CD [mdeg]
Wavelength (nm)
C
mix C of C-K1
mix B of C-K1
mix A of C-K1
CD [mdeg]
Wavelength (nm)

Figure 2.23. Comparison of CD spectra of mixtures "C" with mixtures "A" and "B" after 1 week of aging in (A) pA-TB:K1-TB; (B) pB-TB:K1-TB; and (C) pC-TB:K1-TB.

2.6.2 Microscopic Studies of Co-Assembly

Evidently, the CD results obtained from experiments 1-3 in the previous section indicated that co-assembled RNT constructs were obtained. However, these studies cannot provide information about the mode of spatial distribution of the motifs in the nanotubes, and thus cannot differentiate between "block-mixed" (Fig 2.18 B) and "random-mixed" co-assemblies (Fig 2.18 C) since the supramolecular chirality of K1-TB RNTs can be disturbed in both cases. Alternatively, measuring the outer diameter of the nanotubes by TEM can clearly distinguish between the two models. In general, "block-mixed" RNTs should consist of segments with >7 nm diameter (for peptide-TB rosettes) and major segments with 3.5 nm (for K1-TB rosettes) in the same scaffold, whereas "random-mixed" RNTs should have an average outer diameter that is in the range between the K1-TB and the peptide-TB nanotubes (i.e. 4-7 nm) depending on the molar ratio of the two motifs.

Since it would be difficult to determine the outer diameter change in the 1:9 mixtures, co-assembled solution "D" containing a mixture of pB-TB:K1-TB in 4:6 molar ratio was considered. Similar to the mixtures "A", the mixture "D" was prepared by dissolving pB-TB and K1-TB solids in water and then applying triplicate cycles of sonication for 5 min, followed by heating to 95ºC. SEM (Figure 2.24 A,B) and TEM images (Figure 2.25 B-D) were obtained after aging for 7 days. Noticeably, the morphology of the RNTs was different than both the self-assembled pB-TB (Figure 2.16 F) and K1-TB (Figure 2.12 C) RNTs, in that there was no bundling, short nanotubes, and a less dense network, which clearly indicated that both motifs were incorporated in the same RNT scaffold (Figure 2.24).

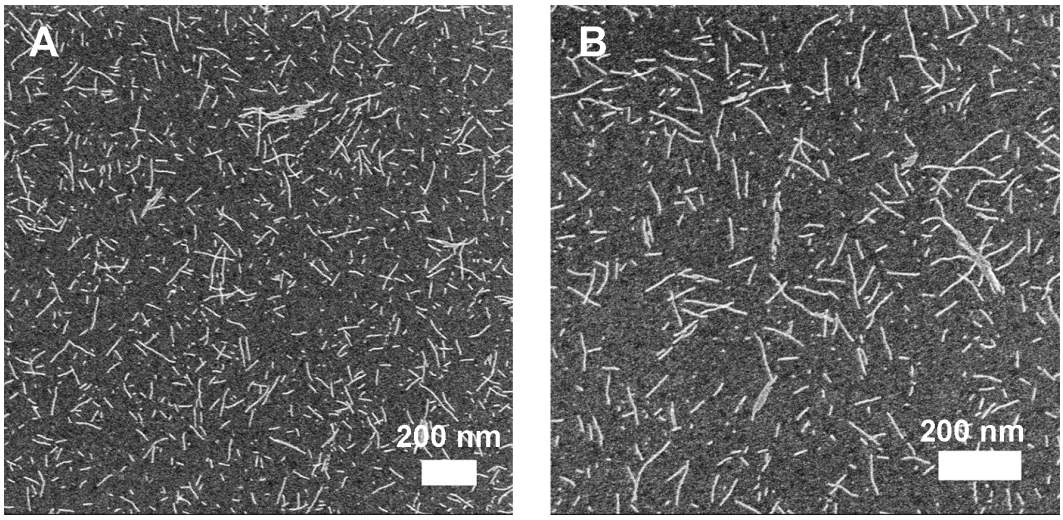

Figure 2.24. SEM images of the co-assembled pB-TB:K1-TB 4:6 mixture (0.0125 mg/ml) after 1 week of aging.

From the TEM measurements, Figure 2.25A was obtained which shows a plot of a random sampling of 30 diameter measurements taken of the co-assembled RNTs. Importantly, these measurements showed that the RNTs mainly had segments comprised of co-assembled rosettes (4.6 nm – 7 nm) that have larger diameter than K1-TB RNTs (3 nm – 3.5 nm) and smaller diameter than pB-TB RNTs (7.1 nm – 7.5 nm). Table 2.2 shows the average diameter and the standard deviation of the co-assembled 4:6 mixture compared with that of the self-assembled pB-TB and K1-TB RNTs. Evidently, the random distribution of the outer diameter of the co-assembled RNTs along with the relatively high standard deviation indicate that the two motifs are randomly distributed, and the co-assembled RNTs are indeed "random-mixed".

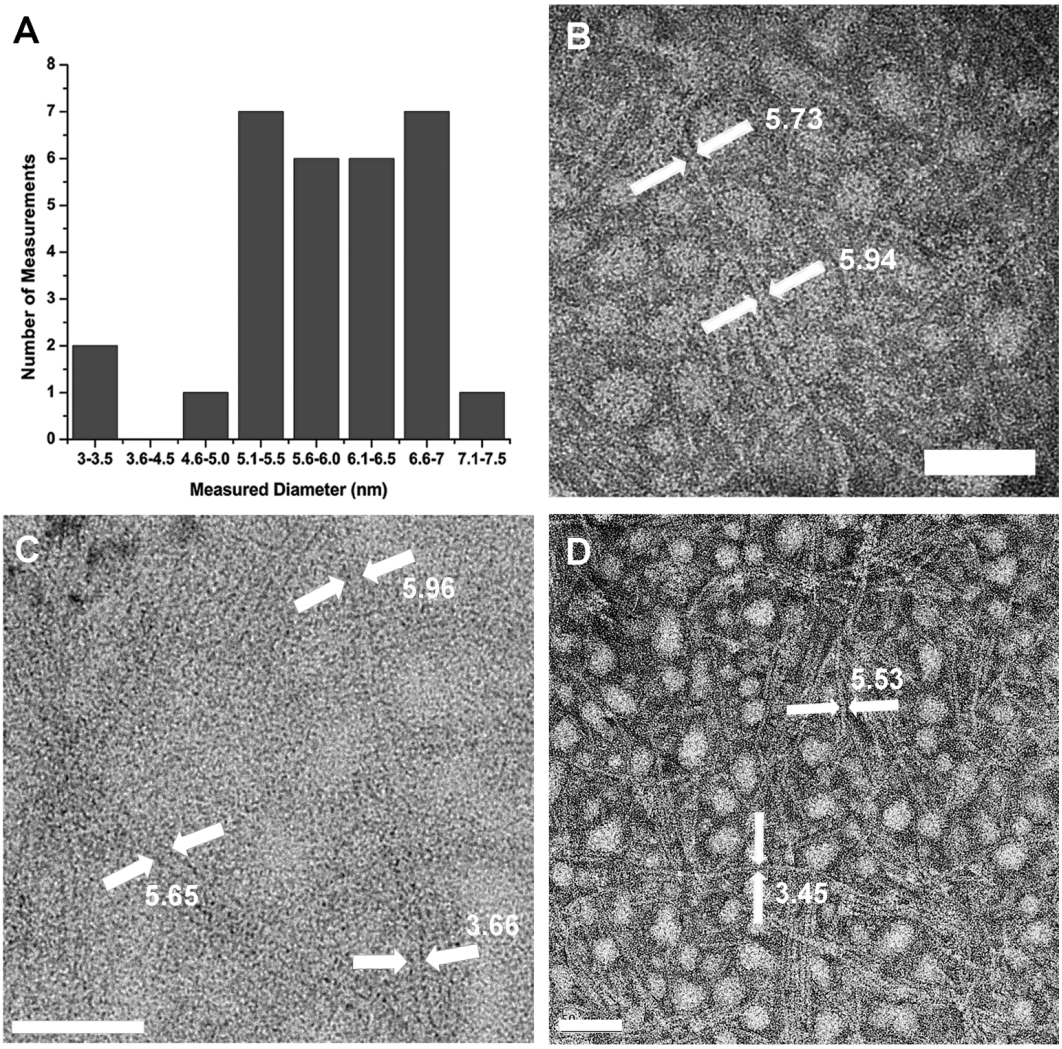

Figure 2.25. (A) Graph of the number of measurements from the TEM images of pB-TB:K1-TB (4:6 molar ratio) *vs*. measured diameter values (nm); (B-D) TEM images of pB-TB:K1-TB (4:6 molar ratio, 0.0125 mg/mL). Scale bars 50 nm.

Table 2.2. Comparison of the average outer diameter and standard deviation of the RNTs from K1-TB, pB-TB, and the co-assembled mixture "D".

	K1-TB	**pB-TB**	**4:6 co-assembled mixture**
Average (nm)	3.47	7.26	5.81
STD (nm)	0.12	0.45	0.91

2.7 Modeling of Self- and Co-Assembly[††]

2.7.1 K1-TB RNTs

The modeling of the twin-G∧C core was based on the previously reported G0 twin-motif.[25] A lysine tail was attached to the core in the all trans conformation. MD simulations were then run to provide the structure in Figure 2.26.

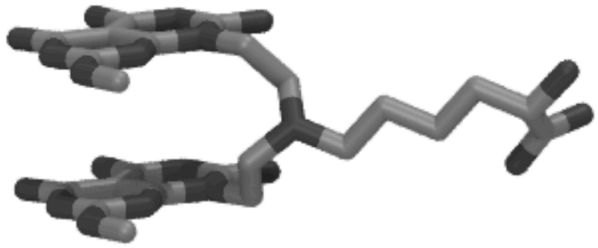

Figure 2.26. Molecular model of K1-TB.

The starting conformation of the K1-TB RNT was generated to consist of 10 rosette rings. The RNT was then solvated in approximately 30,000 water molecules and sixty chloride anions were added to neutralize the system. After equilibration of the solvent molecules by 100 ps NVT followed by 500 ps NPT simulation under 1 bar at 25°C, a 10 ns NPT simulation under 1 bar at 25°C was carried out as the production run. Snapshots from the trajectory were saved every 1 ps. All MD simulations were run in Amber10

[††] The modeling studies of self- and co-assembly were performed by Dr. Takeshi Yamazaki.

using ff99SB[40] and GAFF.[41] The partial charges for RNTs were assigned based on the OPLS2005 force field in MacroModel 9.9.

Figure 2.27 shows the snapshots taken every 2 ns from the MD trajectory. These snapshots suggest that the K1-TB RNT is stable in water during the 10 ns simulation period.

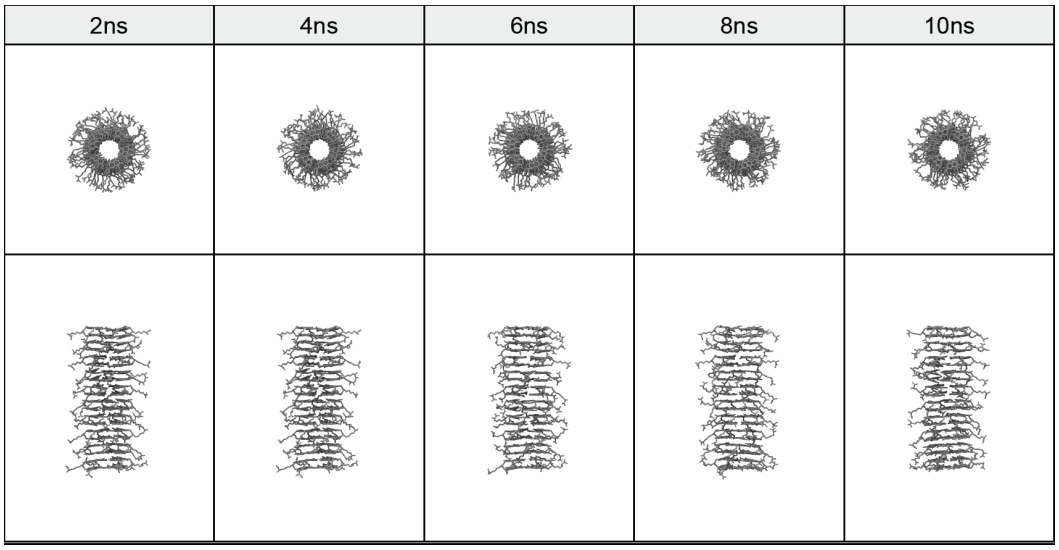

Figure 2.27. Snapshots taken every 2 ns from the MD trajectory for K1-TB RNT.

2.7.2 pA-TB and pB-TB RNTs

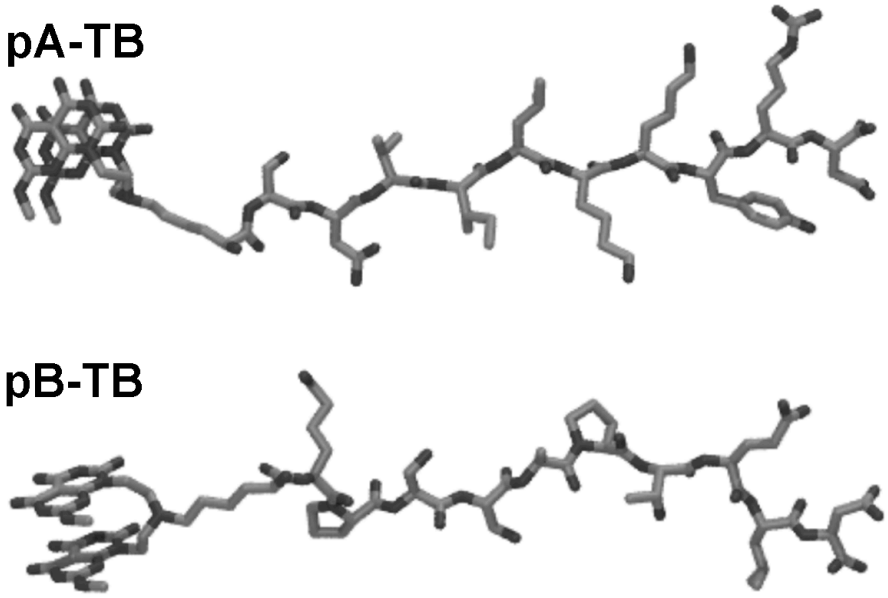

Figure 2.28. Optimized models showing the 3D structure of pA-TB and pB-TB motifs.

The structures of pA-TB and pB-TB in Figure 2.28 were generated in the same manner as K1-TB described above. The starting conformations of the respective RNTs were formed to consist of 10 rosette rings. The RNTs were then solvated in water molecules (75,000-140,000) and 240 and 120 chloride anions respectively, were added to neutralize the system. After the equilibration of the solvent molecules by 100 ps NVT followed by 1 ns NPT simulation under 1 bar at 25°C, a 10 ns NPT simulation under 1 bar at 25°C was carried out as the production run. Snapshots from the trajectory were saved every 1 ps. The MD simulation was set up and run in the same way as the above MD simulation.

The snapshots taken every 2 ns from the MD trajectory (Figure 2.29 and 2.30) suggest that the pA-TB and pB-TB supramolecular architecture is stable during the 10 ns simulation time. The appearance frequencies of the secondary structures (helix, sheet, turn, or coil) for the corresponding peptides on the surface of the RNTs were analyzed by PTRAJ, a utility program for processing trajectory in AmberTool. Table 2.3 shows the percentage of each secondary structure for the

MD trajectory from 3ns to 10 ns. The peptide side-chains almost always take a random coil conformation (Figures 2.29 and 2.30). While β-turn and β-sheet secondary structures were also observed, the α-helix structure was rarely observed.

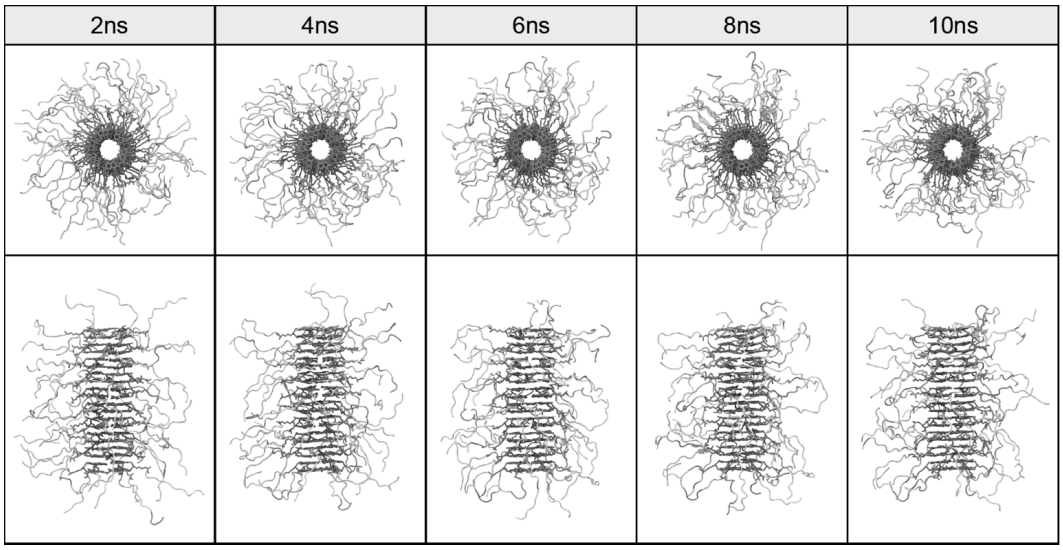

Figure 2.29. Snapshots taken every 2 ns from the MD trajectory for the pA-TB RNT.

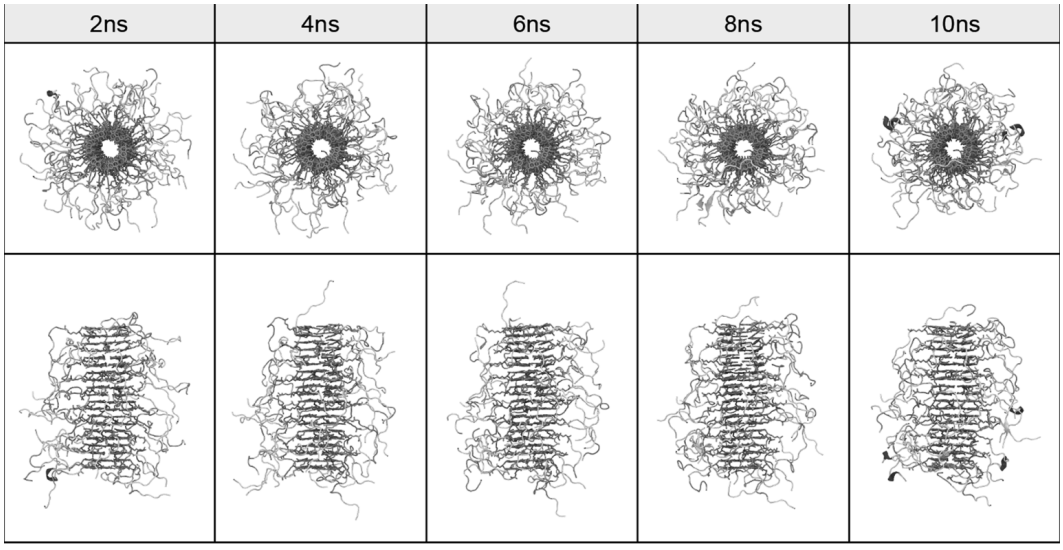

Figure 2.30. Snapshots taken every 2 ns from the MD trajectory for pB-TB RNT.

Table 2.3. Appearance frequency of the α-helix, β-sheet, β-turn and random coil secondary structures for pA-TB and pB-TB.

	α-helix	**β-sheet**	**β-turn**	**Random Coil**
pA-TB	0.04	1.8	1.2	96.96
pB-TB	0.5	3.0	4.4	92.1

2.7.3 Co-Assembly of K1-TB with pB-TB

MD simulations for the co-assembly of K1-TB with only one pB-TB motif were carried out. Co-assembled RNTs were prepared using a 9:1 molar ratio of K1-TB and pB-TB motif. Thus, the present modeling can be considered as an extreme situation in which the peptide side-chain does not have any interaction with neighboring peptide side-chains. In addition, the actual co-assembled RNTs' stability and secondary peptide chain structures may be interpolated between the modeling of the co-assembled RNT of K1-TB with only one pB-TB and the modeling of pB-TB RNT alone which was presented above.

Two co-assembled RNTs were constructed in which pB-TB motif was placed in the middle of the RNT or on the edge of the RNT (Figure 2.31). The latter one was investigated to determine if solvent molecules surrounding the peptide side-chain "pull out" the pB-TB motif from the RNT. Therefore, if the pB-TB motif is stable in this position, other K1-TB or pB-TB motifs in solution would be able to further stack to elongate the RNT. If it is not stable, then only K1-TB motifs in the solution can come and join this RNT (the stability of K1-TB RNT was confirmed in the modeling study above) and eventually, the transformation from the co-assembled RNT to the K1-TB RNT may occur.

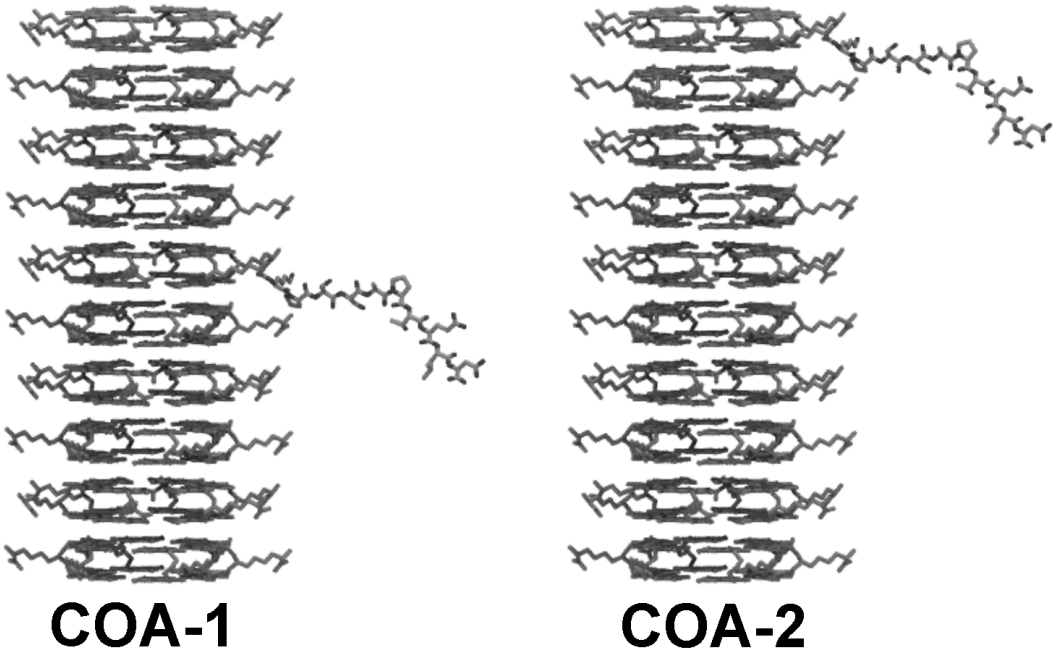

Figure 2.31. Co-assembled K1-TB:pB-TB RNT whereby the pB-TB is placed in the (A) middle of the RNT (called COA-1) or (B) on the edge of the RNT (called COA-2).

For each co-assembly RNTs, the starting conformation consisting of 10 rosette rings was generated. The co-assembled RNTs were then solvated in approximately 35,000 to 40,000 water molecules and 61 chloride anions were added to neutralize the system. After the equilibration of solvent molecules by 100 ps NVT followed by 1 ns NPT simulation under 1 bar at 25°C, 10 ns NPT simulation under 1 bar at 25°C was carried out as the production run. Snapshots from the trajectory were saved every 1 ps. The MD simulation was set up and ran in the same way as the above MD simulations. Figures 2.32 and 2.33 show the snapshots taken every 2 ns from the MD trajectory. These suggest that both co-assembled RNTs COA-1 and COA-2 are stable during the 10 ns simulation time. Importantly, in the case of COA-2, it was found that the pB-TB motif stays as a member of the rosette ring, indicating that further self-assembling processes to

elongate the co-assembled RNT can occur when either K1-TB or pB-TB motif approach the RNT.

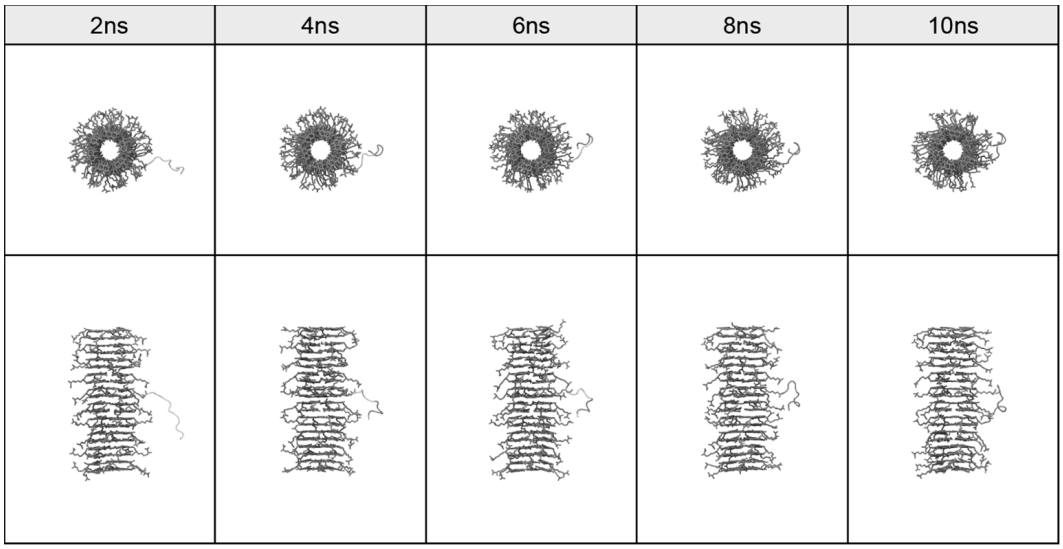

Figure 2.32. Snapshots taken every 2 ns from the MD trajectory for the K1-TB:pB-TB RNT in which pB-TB was placed in the middle of the RNT (i.e. COA-1).

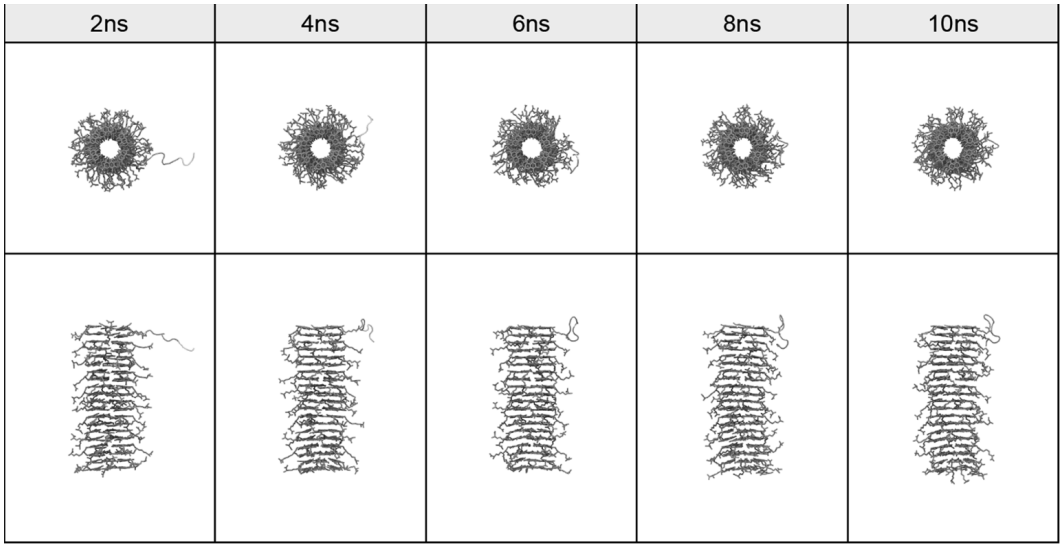

Figure 2.33. Snapshots taken every 2 ns from the MD trajectory for the K1-TB:pB-TB RNT in which pB-TB was placed on the edge of the RNT (i.e. COA-2).

The appearance frequencies of the peptide side-chain secondary structures for COA-1 and COA-2 were analyzed as described above. Table 2.4, which shows the percentage of each secondary structure for the MD trajectory from 3 ns to 10 ns, suggests that the peptide side-chains mainly adopt a random coil structure (Figures 2.32 and 2.33). Turn and sheet secondary structures were also observed, but the helix structure was rarely observed.

Table 2.4. Appearance frequency of the helix, sheet, turn and coil secondary structures for COA-1 and COA-2.

	α-helix	**β-sheet**	**β-turn**	**Random Coil**
COA-1	15.98	0.01	19.18	64.83
COA-2	0.1	1.9	15.5	82.5

It is interesting to see that the frequency of helix structure in the COA-1 model is relatively high compared to COA-2. During the present MD simulation for the COA-1, the anionic carboxylate of asparagine terminal residue of peptide B and the cationic ammonium of lysine residue of K1-TB motifs form a strong salt bridge, and it seems that this side-chain arrangement is enhancing the helix formation. Figure 2.34 shows the representative conformation of the salt bridge between the asparagine and the lysine residues. In the right panel of Figure 2.34, the asparagine residue of the peptide side-chain of pB-TB motif is explicitly shown as are the hydrogen atoms of the lysine residues of K1-TB.

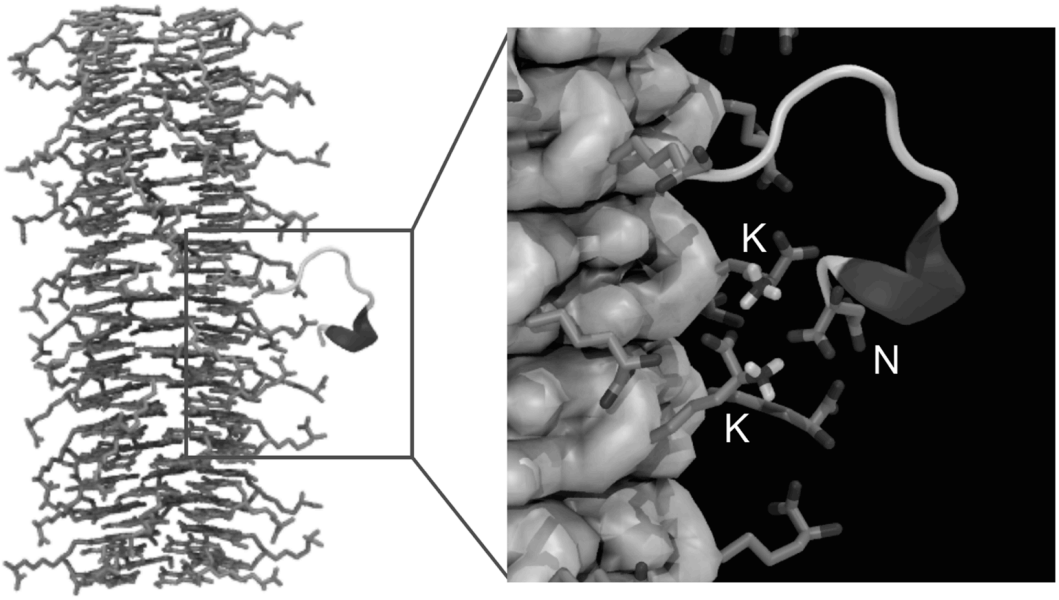

Figure 2.34. (A) Representative conformation of COA-1 and (B) illustration of the salt bridge formed between the asparagine and lysine residue.

2.8 Conclusions

In this chapter, we described the synthesis and self-assembly of rosette nanotubes (RNTs) from twin-G∧C motifs, which are functionalized with lysine and the peptide sequences A, B and C taken from the knucle region of the bone morphogenic protein-7. In addition to demonstrating the impressive ability of the twin-RNT construct to bear structurally unique long peptides on the outer surface through self-assembly, the supramolecular chirality of the RNTs and the peptides secondary structure were elucidated by CD spectroscopy. The self-assembly process was also monitored by UV-Vis, SEM, TEM and AFM techniques. The co-assembly of K1-TB with the peptide-functionalized motifs pA-TB, pB-TB and pC-TB in a 9:1 molar ratio was also examined. Time-dependent CD studies along with TEM imaging provided evidence of the co-assembly and the formation of "random-mixed" RNTs.

2.9 Experimental

2.9.1 Self- and Co-Assembly Procedure

Stock solutions of 1 mg/ml were prepared by dissolving the peptides and the twin-G∧C motifs in deionized water (dH_2O). The solutions were subjected to triplicate cycles of sonication for 5 min, and heating by heat gun to 95ºC. Then the solutions were left at room temperature for aging. Aliquots of the stock solutions were diluted with water to a final concentration of 5.0×10^{-5} M for CD and UV-Vis measurements, and to 0.1 or 0.0125 mg/ml for SEM, TEM, and AFM imaging studies.

2.9.2 SEM Imaging

Aliquots of the stock self- and co-assembled solutions (0.1 mg/ml) were diluted with deionized (dH_2O) to a final concentration of 0.1-0.01 mg/ml depending on the sample prior to imaging. The SEM grids were prepared by depositing a droplet of the diluted solutions on a carbon-coated 400-mesh copper grid (Electron Microscopy Sciences) for 10 seconds before blotting the grid using filter paper. The grid was then dried by air, and heated on hotplate (100ºC). SEM images were obtained without negative staining at 10-30 kV accelerating voltage, 20 μA and a working distance of 5-8 mm using a high resolution Hitachi S–4800 cold field emission SEM.

2.9.3 TEM Imaging

Similar to the SEM imaging, the grids for TEM were prepared by depositing a droplet of the diluted stock solutions on a carbon-coated 400-mesh copper grids (Electron Microscopy Sciences) for 10 s. After blotting the grids using filter paper, the grids were negatively stained by depositing one droplet of uranyl acetate (2% aqueous for the water) for 5 min. The grids were then blotted, dried in air and in the vacuum hotplate. TEM investigations were carried out on a JEOL 2200 FS TEM – 200kV Schottky field emission instrument equipped with an in-

column omega filter. Bright field TEM images were acquired using an energy filtered zero loss beam (slit width 10 ev).

2.9.4 AFM Imaging

One drop of the diluted solutions was deposited on mica substrate for 10 s, and then the excess solutions were blotted using a filter paper. AFM imaging was carried out using a Digital Instruments/Veeco Instruments MultiMode Nanoscope IV AFM equipped with an E scanner. For obtaining optimized height profiles, silicon cantilevers (MikroMasch USA, Inc.) with low spring constants of 4.5 N/m were used in tapping mode (TM-AFM). To obtain a clear image from the surface, a low scan rate (0.5-1 Hz) and amplitude set-point (1 V) were chosen during the measurements.

2.9.5 General Methods

All materials were synthesized using a solid phase peptide synthesis (SPPS) strategy in 12 ml disposable syringe. Commercial reagents were used as purchased. ^{1}H and ^{13}C NMR spectra were recorded in the specified deuterated solvents. The NMR data is presented as follows: chemical shift, peak assignment, multiplicity, coupling constant, integration. The following abbreviations were used to explain the multiplicities: s = singlet, d = doublet, t = triplet, m = multiplet.

2.9.6 General Purification by HPLC

Large scale purification of peptides was done using semi-prep HPLC after optimizing the purification conditions by analytical grade HPLC. Column specifications of analytical grade HPLC are Agilent, Zorbax S8-C18, size 4.6×250mm, 5µm. Mobile phase composed of a mixture of 2 components; A: Water + 1% Acetonitrile + 0.1% Trifluoroacetic acid and B: 100%Acetonitrile + 0.1% Trifluoroacetic acid. Flow rate of 1mL/min was used with an injection volume of 10µL having a sample concentration of 1mg/mL. Gradient elution

program was used consisting of 0-3 min, 100% A; 3-40 min, 0%-20% B; 41-48 min, 100% B and 49-56 min, 100% A. Peptide A elutes at 25.8 min and stops at 26.3 min while using UV Vis detector at 220nm. Peptide A-Twin K1 elution extends from 22.5 min and stops at 23.1 min while using UV Vis detector at 220 nm. Using the same gradient elution system, Peptide B elutes at 16.3 min and stops at 16.8 min while using UV Vis detector at 254 nm. Peptide B-Twin K1 elutes at 22.1 min and stops at 22.6 min detected by UV Vis at 254 nm. After the isolation of the peptide of interest, its LC-MS is done every time to confirm the presence of peptide.

After optimizing the purification conditions in analytical grade HPLC, Phenomenex semi-prep HPLC was used with column specifications of Gemini, C18 110A, size 250×10.00mm, 5 micron. Same mobile phase system was used however, the flow rate was raised to 2mL/min, injection volume of 100µL with sample concentration of 10mg/mL and gradient program was modified as 0-1 min, 0-10 % B; 1-25 min, 10-20% B; 26-32 min, 100% B and 33-40 min, 0% B. Using semi prep HPLC, Peptide A elutes from 10.4 min to 10.9 min, Peptide A-Twin K1 elutes from 18.0 min to 18.7 min while using UV Vis detector at 220 nm confirmed by LC-MS. Peptide B elution time extends from 9.6 min to 10.3 min and Peptide B-TB elution time is from 9.3 min to 9.8 min using UV Vis detector at 254 nm, confirmed by LC-MS. K1-TB, pC and pC-TB were not purified by HPLC.

2.9.7 Materials Synthesis and Characterization

General Synthesis

The first amino acid (in the C-terminus) of the three peptides (or lysine in K1-TB) was anchored on the resin by treating 4-Benzyloxybenzyl alcohol substituted Wang resin (500 mg, 0.24 mmol) with a mixture of the Fmoc-protected amino acid (4.2 eq), 4-dimethylaminopyridine (DMAP) (0.8 eq) and anhydrous DMF (3 mL) in a disposable syringe. After 20 min, N,N'-diisopropylcarbodiimide (DIC)

(4.2 eq) was added and the mixture was shaken at room temperature overnight. The solution was then filtered under vacuum and the resin was washed with CH_2Cl_2, MeOH, DMF (4x10 mL each). After drying overnight, the degree of substitution on the resin was determined by spectroscopic quantification of the fulvene-piperidine adduct **2.3** at 301 nm, which was performed by conducting UV-Vis measurements of three resin samples. The degree of substitution was mathematically calculated using the expression below.

$$\text{Substitution degree} = \frac{101 \times \text{Absorbance}}{7.8 \times \text{mass of resin (mg)}}$$

The residual unreacted hydroxyl groups on the resin were then capped by treating the resin with 50:50 acetic anhydride/pyridine (4x10 mL, 10 min each for synthesis of pA, pB and pC; 8 mL for 5 min then 8 mL for 20 min for K1-TB).

2.9.7.1 K1-TB

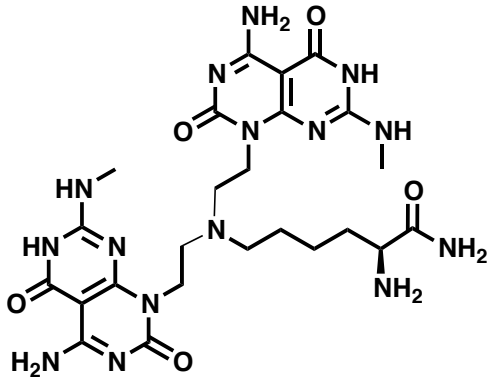

The Fmoc protecting group on the ω-amino position of **2.11** was removed by treating the resin with 20% piperidine in DMF (8 mL, 5 min then 8 mL, 20 min), followed by filtering and washing the resin with CH_2Cl_2, MeOH and DMF (4x10

mL each). The free ω-amino group of **2.12** was then coupled with the aldehyde **2.8** (410 mg 0.64 mmol) in 1,2-dichloroethane (6 mL) for 6 h. After adding $NaBH(OAc)_3$ (162 mg, 0.77 mmol) and DIPEA (*N,N*-diisopropylethylamine) (0.2 mL, 1.2 mmol), the mixture was shaken for 5 days. The motif was then cleaved from the resin by treating with TFA/triisopropyl silane (TIS)/H_2O (95/2.5/2.5, 10 mL) for 3 h. TFA was subsequently removed under vacuum to provide a white powder which was washed and sonicated with diethyl ether and then centrifuged for a total of 10 times. After drying under vacuum for 2 days, 213 mg of K1-TB (70%) was isolated as a white solid.

High-res ESI-MS (positive): Expected for $C_{24}H_{35}N_{14}O_6$, 615.2864, found 615.2867.

^{1}H NMR (600 MHz, DMSO-d6 + TFA-d) δ (ppm): 4.13-4.40 (m, 4H), 3.89 (t, J = 5.4 Hz, 1H), 3.10-3.50 (m, 6H), 2.68 (s, 3H), 2.66 (m, 3H), 1.60-1.80 (m, 2H), 1.40-1.50 (m, 2H), 1.10-1.35 (m, 2H).

^{13}C NMR (600 MHz, D_2O+few drops TFA-*d*) δ (ppm) 172.4, 163.0, 160.7, 156.7, 156.4, 149.9, 83.4, 53.4, 50.8, 37.5, 30.0, 28.5, 23.0, 22.2.

Elemental analysis: calculated for [K1-TB + 2MeCN + 4TFA + Et_2O + $3H_2O$], C: 37.77, H: 4.04, N:17.62. Found: C: 37.62, H: 4.12, N: 17.87.

2.9.7.2 pA, pB, and pC

The Fmoc protecting group was removed by shaking the resin with 20% piperidine in DMF (8 mL, 5 min then 8 mL, 20 min), followed by filtering and washing the resin with CH_2Cl_2, MeOH and DMF. To couple the subsequent amino acids, a solution of the Fmoc-protected amino acid **2.5** (4.0 eq), O-benzotriazole-N,N,N',N'-tetramethyl-uronium-hexafluoro-phosphate (HBTU) (4 eq) and DIPEA (8 eq) in DMF (8 mL) was activated by stirring for 3 min. The mixture was added to the resin **2.4** and shaken for 3 h. The Kaiser test[42] was then performed to confirm that the coupling was the complete. In the case of

incomplete coupling, the coupling reaction was repeated for 1.5 h. After synthesizing the 11-amino acid peptides and removing the Fmoc group from the N-termini (using the same procedure as described above), the peptides were cleaved from the resin (and the side-chain protecting groups were removed) by treating with a TFA/TIS/H_2O solution (95/2.5/2.5, 10 mL) for 3 h at room temperature (Figure 2.5). The beads were then filtered and the TFA solutions were concentrated *in vacuo*. The white solids were washed and sonicated with diethyl ether and then centrifuged for a total of 10 times. Drying under high vacuum, provided the peptides A, B and C.

Peptide A (pA)

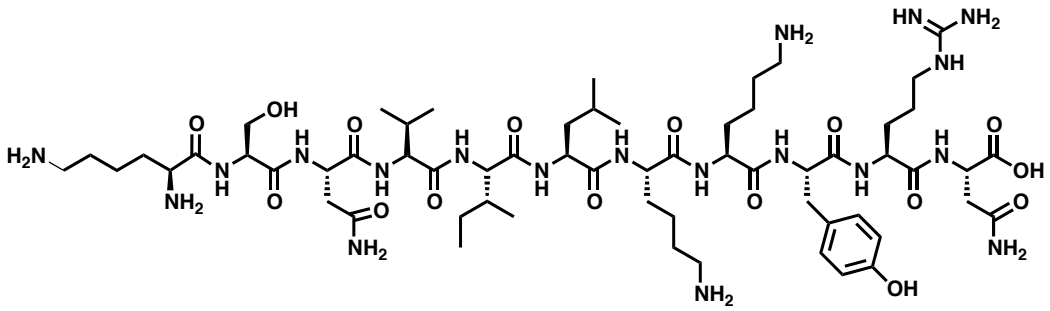

Purification by HPLC on a reverse-phase semipreparative column (0-10% of B in A for 1 min, followed by 10-20% of B in A for 24 min, where B is (99.9% acetonitrile + 0.1% trifluoroacetic acid) and A is (98.9% water + 1% acetonitrile + 0.1% trifluoroacetic acid), flow rate 2 mL/min, retention time 10.4 min) provided pA as a white solid in 16% yield.

High-res ESI-MS (positive): Expected for $C_{61}H_{107}N_{19}O_{16}$, 1362.8221, found 1362.8304.

^{1}H NMR (600 MHz, DMSO-d6 + TFA-d) δ (ppm): 7.00 (d, *J* = 8.4 Hz, 2H), 6.64 (d, *J* = 8.4 Hz, 2H), 4.63 (t, *J* = 7.8 Hz, 1H), 4.55 (t, *J* = 6.0 Hz, 1H), 4.45-4.48 (m, 2H), 4.28-4.30 (m, 3H), 4.21 (d, *J* = 6.6 Hz, 1H), 4.17-4.22 (m, 3H), 4.12 (d, *J*

= 9.0 Hz, 1H), 3.85 (t, *J* = 6.0 Hz, 1H), 3.56-3.64 (m, 2H), 3.34-3.38 (m, 2H), 3.10 (t, *J* = 6.6 Hz, 2H), 2.91-2.96 (m, 1H), 2.88 (s, 1H), 2.67-2.77 (m, 8H), 1.91 (sextet, *J* = 6.6 Hz, 1H), 1.00-1.80 (m, 28H), 0.85 (d, *J* = 6.6 Hz, 6H), 0.76-0.81 (m, 12H).

Elemental analysis: calcd for [peptide A + 1.5 MeCN + 8.5 TFA + $2H_2O$], C: 40.05, H: 5.14, N: 11.82. Found: C: 39.87, H: 5.35, N: 11.65.

Peptide B (pB)

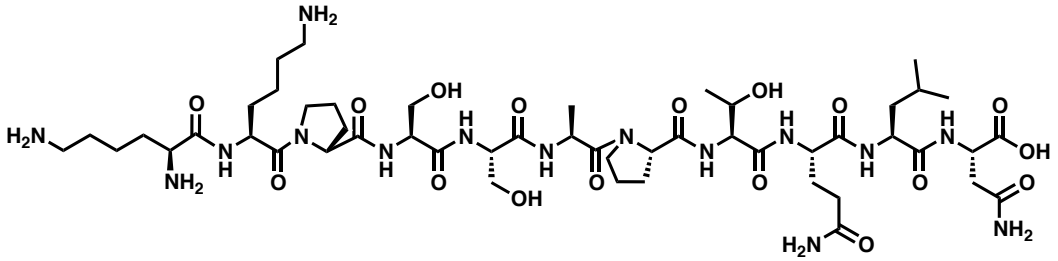

Purification by HPLC on a reverse-phase semipreparative column (0-10% of B in A for 1 min, followed by 10-20% of B in A for 24 min, where B is (99.9% acetonitrile + 0.1% trifluoroacetic acid) and A is (98.9% water + 1% acetonitrile + 0.1% trifluoroacetic acid), flow rate 2 mL/min, retention time 9.6 min) provided pA as a white solid in 18% yield.

High-res ESI-MS (positive): Expected for $C_{50}H_{88}N_{15}O_{17}$, 1170.6483, found 1170.6468.

^{1}H NMR (600 MHz, DMSO-d6 + TFA-d) δ (ppm): 4.35-4.50 (m, 8H), 4.23-4.38 (m, 5H), 4.16 (d, *J* = 4.2 Hz, 1H), 4.01 (m, 1H), 3.80 (t, *J* = 6.0 Hz, 1H), 3.50-3.72 (m, 6H), 2.76 (m, 2H), 2.10 (t, *J* = 7.8 Hz, 2H), 2.00-2.10 (m, 2H), 1.30-2.0 (m, 25H), 1.20 (d, *J* = 6.6 Hz, 3H), 1.04 (d, *J* =6.6 Hz, 3H), 0.86 (d, *J* = 6.6 Hz, 3H), 0.81 (d, *J* = 6.6 Hz, 3H).

Elemental analysis: calcd for [peptide B + Et_2O + 7.5 TFA], C: 39.47, H: 5.02, N: 10.01. Found: C: 39.43, H: 5.05, N: 10.37.

Peptide C (pC)

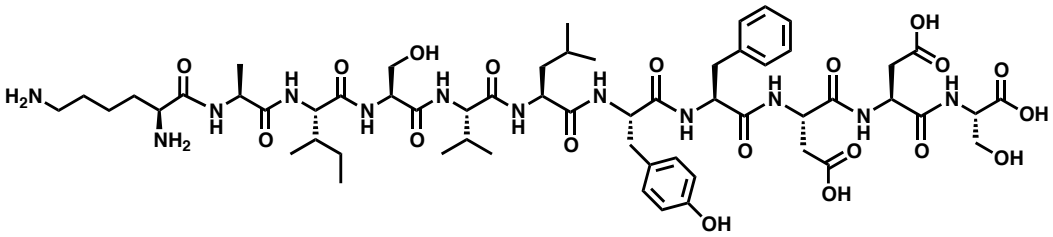

Yield 64% (crude). No HPLC purification.

High-res ESI-MS (positive): Expected for $C_{58}H_{88}N_{12}O_{19}$, 1257.6367, found 1257.6380.

^{1}H NMR (600 MHz, DMSO-d6 + TFA-d) δ (ppm): 7.22-7.23 (m, 4H), 7.11-7.19 (m, 1H), 6.92 (dd, *J* = 9.0 Hz, 4.2 Hz, 2H), 6.59 (dd, *J* = 9.0 Hz, 5.4 Hz, 2H), 4.64 (t, *J* = 6.6 Hz, 1H), 4.57 (t, *J* = 6.0 Hz, 1H), 4.50-4.55 (m, 2H), 4.35-4.46 (m, 4H), 4.20-4.25 (m, 3H), 4.15 (d, *J* = 6.6 Hz, 1H), 3.77 (t, *J* = 6.0 Hz, 1H), 3.71 (dd, *J* = 10.8 Hz, 4.8 Hz, 1H), 3.63 (dd, *J* = 10.8 Hz, 4.2 Hz, 1H), 3.58 (dd, *J* = 10.2 Hz, 6.0 Hz, 1H), 3.52 (dd, *J* = 10.8 Hz, 6.0 Hz, 1H), 2.90-3.05 (m, 1H), 2.65-2.88 (m, 5H), 1.96 (sextet, *J* = 6.6 Hz, 1H), 1.61-1.78 (m, 4H), 1.44-1.55 (m, 4H), 1.29-1.43 (m, 6H), 1.24 (d, *J* = 6.6 Hz, 3H), 1.02-1.12 (m, 1H), 0.70-0.84 (m, 18H).

Elemental analysis: calcd for [peptide C + 0.2Et_2O + 1.35TFA], C: 51.79, H: 6.46, N: 11.79. Found: C: 55.78, H: 6.86, N: 11.81.

2.9.7.3 pA-TB, pB-TB, and pC-TB

The peptidyl resin **2.7** was treated with the aldehyde **2.8** (4.0 eq) in 1,2-dichloroethane (1,2-DCE) for 6 h. $NaBH(OAc)_3$ (4.8 eq) and DIPEA (7.2 eq)

were then added and the mixture was shaken for 5 days. The solution was then drained, and the resin was washed with CH_2Cl_2, MeOH, DMF (4x10 mL each). Completion of the coupling was confirmed using the Kaiser test. The peptide conjugates were then cleaved from the resin by treating with the TFA/TIS/H_2O solution (95/2.5/2.5) for 3 h. After removing TFA under vacuum, the white solids were washed and sonicated with diethyl ether and centrifuged 10 times before drying under high vacuum.

pA-TB

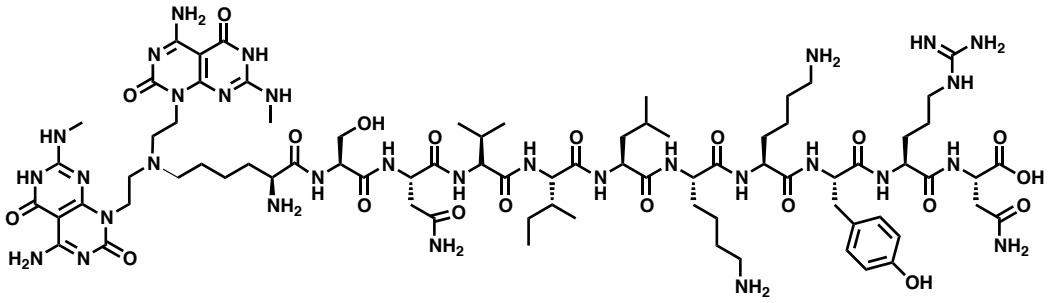

Purification by HPLC on a reverse-phase semipreparative column (0-10% of B in A for 1 min, followed by 10-20% of B in A for 24 min, where B is (99.9% acetonitrile + 0.1% trifluoroacetic acid) and A is (98.9% water + 1% acetonitrile + 0.1% trifluoroacetic acid), flow rate 2 mL/min, retention time 18.0 min) provided pA-TB as a white solid in 20% yield.

High-res MALDI-MS (positive): Expected for $C_{79}H_{128}N_{31}O_{20}$, 1830.9952, found 1830.9936.

^{1}H NMR (600 MHz, DMSO-d6 + TFA-d) δ (ppm): 7.00 (d, *J* = 8.4 Hz, 2H), 6.64 (d, *J* = 8.4 Hz, 2H), 4.63 (t, *J* = 7.8 Hz, 1H), 4.56 (t, *J* = 6.0 Hz, 1H), 4.45-4.48 (m, 2H), 4.28-4.30 (m, 3H), 4.22 (d, *J* = 6.0 Hz, 1H), 4.17-4.22 (m, 3H), 4.12 (d, *J* = 7.8 Hz, 1H), 3.88 (t, *J* = 6.0 Hz, 1H), 3.52-3.64 (m, 6H), 3.34-3.38 (m, 2H), 3.10 (t, *J* = 7.2 Hz, 2H), 3.00 (t, *J* = 5.4 Hz, 2H), 2.93 (s, 3H), 2.91 (s, 3H), 2.90-

2.95 (m, 2H), 2.67-2.74 (m, 8H), 1.91 (sextet, *J* = 6.6 Hz, 1H), 1.00-1.80 (m, 28H), 0.85 (d, *J* = 6.6 Hz, 6H), 0.76-0.81 (m, 12H).

Elemental analysis**:** calcd for [pA-TB + 17H_2O + 20TFA + 2.5MeCN], C: 32.95, H: 4.20, N: 10.38. Found: C: 32.67, H: 4.05, N: 10.52.

pB-TB

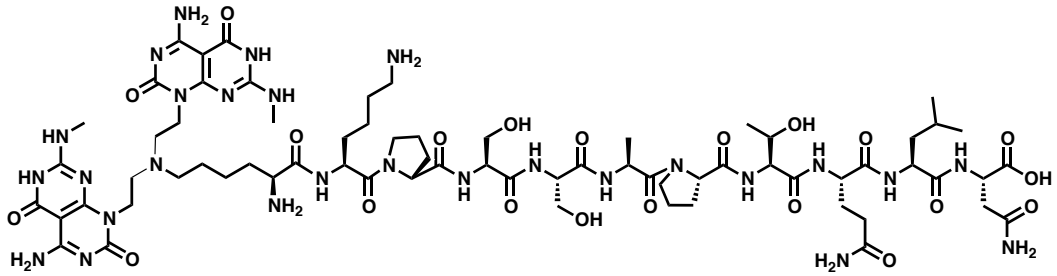

Purification by HPLC on a reverse-phase semipreparative column (0-10% of B in A for 1 min, followed by 10-20% of B in A for 24 min, where B is (99.9% acetonitrile + 0.1% trifluoroacetic acid) and A is (98.9% water + 1% acetonitrile + 0.1% trifluoroacetic acid), flow rate 2 mL/min, retention time 9.3 min) provided pB-TB as a white solid in 11% yield.

High-res MALDI-MS (positive): Expected for $C_{68}H_{108}N_{27}O_{21}$, 1638.8213, found 1638.8201.

^{1}H NMR (600 MHz, DMSO-d6 + TFA-d) δ (ppm): 4.35-4.50 (m, 8H), 4.23-4.33 (m, 5H), 4.15 (d, *J* = 4.2 Hz, 1H), 4.01 (t, *J* =5 .4 Hz, 1H), 3.83 (t, *J* = 6.0 Hz, 1H), 3.50-3.70 (m, 12H), 3.25-3.40 (m, 2H), 2.93 (s, 3H), 2.90 (s, 3H), 2.76 (m, 2H), 2.10 (t, *J* = 7.8 Hz, 2H), 2.00-2.10 (m, 2H), 1.30-1.90 (m, 25H), 1.20 (d, *J* = 6.6 Hz, 3H), 1.04 (d, *J* = 6.6 Hz, 3H), 0.86 (d, *J* = 6.6 Hz, 3H), 0.81 (d, *J* = 6.6 Hz, 3H).

Elemental analysis: calcd for [pB-TB + 8.5H_2O + 11.8TFA], C: 35.07, H: 4.36, N: 12.05. Found: C: 35.27, H: 4.64, N: 11.93.

pC-TB

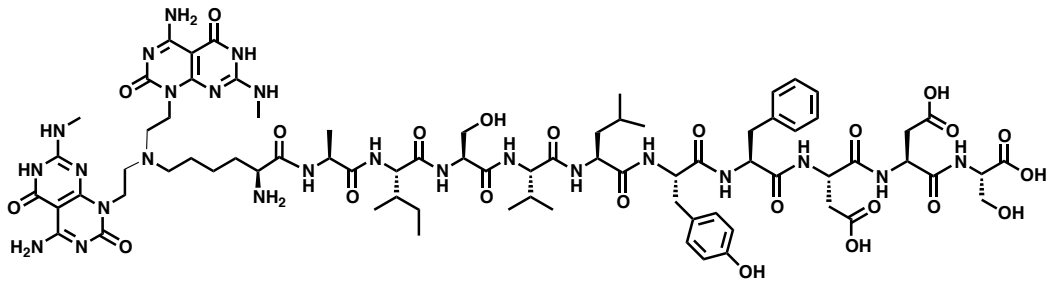

51% yield (crude). No HPLC purification.

High-res MALDI-MS (positive): for $C_{76}H_{109}N_{24}O_{23}$, 1725.8097, found 1725.8210. ^{1}H NMR (600 MHz, DMSO-d_6 + TFA-d) δ (ppm) 7.22-7.23 (m, 4H), 7.11-7.19 (m, 1H), 6.92 (dd, J = 8.4 Hz, 3.0 Hz, 2H), 6.58 (dd, J = 8.4 Hz, 3.6 Hz, 2H), 4.64 (t, J = 7.2 Hz, 1H), 4.57 (t, J = 6.0 Hz, 1H), 4.50-4.55 (m, 2H), 4.35-4.45 (m, 4H), 4.25 (t, J = 4.2 Hz, 1H), 4.20-4.22 (m, 2H), 4.15 (d, J = 6.0 Hz, 1H), 3.80 (t, J = 6.0 Hz, 1H), 3.71 (dd, J = 10.8 Hz, 4.8 Hz, 1H), 3.63 (dd, J = 10.8 Hz, 4.2 Hz, 1H), 3.48-3.60 (m, 7H), 3.03 (d, J = 12.0 Hz, 1H), 2.93 (s, 3H), 2.90 (s, 3H), 2.64-2.88 (m, 6H), 1.96 (sextet, J = 6.6 Hz, 1H), 1.62-1.79 (m, 6H), 1.44-1.52 (m, 1H), 1.29-1.43 (m, 7H), 1.24 (d, J = 6.6 Hz, 3H), 1.02-1.12 (m, 1H), 0.70-0.84 (m, 18H).

Elemental analysis: calcd for [pC-TB + Et_2O + 3.6TFA], C: 47.38, H: 5.54, N: 15.21. Found: C: 47.38, H: 5.64, N: 15.18.

2.10 References

(1) Cui, H.; Webber, M. J.; Stupp, S. I. *Biopolymers* **2010**, *94*, 1–18.

(2) Yanlian, Y.; Ulung, K.; Xiumei, W.; Horii, A.; Yokoi, H.; Shuguang, Z. *Nano Today* **2009**, *4*, 193–210.

(3) Johnell, O.; Kanis, J. A. *Osteoporos. Int.* **2006**, *17*, 1726–1733.

(4) Rautray, T. R.; Narayanan, R.; Kwon, T.-Y.; Kim, K.-H. *J. Biomed. Mater. Res.* **2010**, *93B*, 581–591.

(5) Breme, J.; Steinhäuser, E.; Paulus, G. *Biomaterials* **1988**, *9*, 310–313.

(6) Molenberg, A.; Schwarz, F.; Herten, M.; Berner, S.; de Wild, M.; Wieland, M. *Mat.-wiss. u. Werkstofftech.* **2009**, *40*, 31–35.

(7) Jonge, L. T.; Leeuwenburgh, S. C. G.; Wolke, J. G. C.; Jansen, J. A. *Pharm. Res.* **2008**, *25*, 2357–2369.

(8) Geetha, M.; Singh, A. K.; Asokamani, R.; Gogia, A. K. *Prog. Mater. Sci.* **2009**, *54*, 397–425.

(9) Zhang, L.; Webster, T. J. *Nano Today* **2009**, *4*, 66–80.

(10) Fenniri, H.; Deng, B.-L.; Ribbe, A. E.; Hallenga, K.; Jacob, J.; Thiyagarajan, P. *Proc. Natl. Acad. Sci. U.S.A.* **2002**, *99 Suppl 2*, 6487–6492.

(11) Fenniri, H.; Deng, B.-L.; Ribbe, A. E. *J. Am. Chem. Soc.* **2002**, *124*, 11064–11072.

(12) Fenniri, H.; Mathivanan, P.; Vidale, K. L.; Sherman, D. M.; Hallenga, K.; Wood, K. V.; Stowell, J. G. *J. Am. Chem. Soc.* **2001**, *123*, 3854–3855.

(13) Journeay, W. S.; Suri, S. S.; Moralez, J. G.; Fenniri, H.; Singh, B. *Int. J. Nanomed.* **2008**, *3*, 373–383.

(14) Journeay, W. S.; Suri, S. S.; Moralez, J. G.; Fenniri, H.; Singh, B. *Small* **2008**, *4*, 817–823.

(15) Chun, A. L.; Moralez, J. G.; Fenniri, H.; Webster, T. J. *Nanotechnology* **2004**, *15*, S234–S239.

(16) Zhang, L.; Hemraz, U. D.; Fenniri, H.; Webster, T. J. *J. Biomed. Mater. Res.* **2010**, *95A*, 550–563.

(17) Babensee, J. E.; McIntire, L. V.; Mikos, A. G. *Pharm. Res.* **2000**, *17*, 497–504.

(18) Solheim, E. *Int. Orthop.* **1998**, *22*, 410–416.

(19) Lind, M.; Deleuran, B.; Thestrup-Pedersen, K.; Søballe, K.; Eriksen, E. F.; Bünger, C. *APMIS* **1995**, *103*, 140–146.

(20) Reddi, A. H.; Cunningham, N. S. *J. Bone. Miner. Res.* **1993**, *8 Suppl 2*,

S499–502.

(21) Friedlaender, G. E.; Perry, C. R.; Cole, J. D.; Cook, S. D.; Cierny, G.; Muschler, G. F.; Zych, G. A.; Calhoun, J. H.; LaForte, A. J.; Yin, S. *J. Bone Joint Surg. Am.* **2001**, *83-A Suppl 1*, S151–8.

(22) Saito, A.; Suzuki, Y.; Ogata, S. I.; Ohtsuki, C.; Tanihara, M. *Biochim. Biophys. Acta.* **2003**, *1651*, 60–67.

(23) Kirkwood, K.; Rheude, B.; Kim, Y. J.; White, K.; Dee, K. C. *J. Oral. Implantol.* **2003**, *29*, 57–65.

(24) Chen, Y.; Webster, T. J. *J. Biomed. Mater. Res.* **2009**, *91A*, 296–304.

(25) Moralez, J. G.; Raez, J.; Yamazaki, T.; Motkuri, R. K.; Kovalenko, A.; Fenniri, H. *J. Am. Chem. Soc.* **2005**, *127*, 8307–8309.

(26) Gottarelli, G.; Lena, S.; Masiero, S.; Pieraccini, S.; Spada, G. P. *Chirality* **2008**, *20*, 471–485.

(27) Greenfield, N. J. *Nat. Protoc.* **2006**, *1*, 2876–2890.

(28) Bock, J. E.; Gavenonis, J.; Kritzer, J. A. *ACS Chem. Biol.* **2013**, *8*, 488–499.

(29) Behanna, H. A.; Donners, J. J. J. M.; Gordon, A. C.; Stupp, S. I. *J. Am. Chem. Soc.* **2005**, *127*, 1193–1200.

(30) Li, F.; Martens, A. A.; Åslund, A.; Konradsson, P.; de Wolf, F. A.; Cohen Stuart, M. A.; Sudhölter, E. J. R.; Marcelis, A. T. M.; Leermakers, F. A. M. *Soft Matter* **2009**, *5*, 1668–1673.

(31) Besenius, P.; Goedegebure, Y.; Driesse, M.; Koay, M.; Bomans, P. H. H.; Palmans, A. R. A.; Dankers, P. Y. W.; Meijer, E. W. *Soft Matter* **2011**, *7*, 7980–7983.

(32) Behanna, H. A.; Rajangam, K.; Stupp, S. I. *J. Am. Chem. Soc.* **2007**, *129*, 321–327.

(33) Jung, J. P.; Nagaraj, A. K.; Fox, E. K.; Rudra, J. S.; Devgun, J. M.; Collier, J. H. *Biomaterials* **2009**, *30*, 2400–2410.

(34) Choi, S.-J.; Jeong, W.-J.; Kim, T.-H.; Lim, Y.-B. *Soft Matter* **2011**, *7*, 1675-1677.

(35) Ramachandran, S.; Tseng, Y.; Yu, Y. B. *Biomacromolecules* **2005**, *6*, 1316–1321.

(36) Ryadnov, M. G.; Ceyhan, B.; Niemeyer, C. M.; Woolfson, D. N. *J. Am. Chem. Soc.* **2003**, *125*, 9388–9394.

(37) Cao, H.; Jiang, J.; Zhu, X.; Duan, P.; Liu, M. *Soft Matter* **2011**, *7*, 4654-4660.

(38) Molla, M. R.; Das, A.; Ghosh, S. *Chem. Commun.* **2011**, *47*, 8934–8936.

(39) Berova, N.; Nakanishi, K.; Woody, R. W. *Circular dichroism : principles and applications, 2nd ed.* Wiley-VCH: New York, **2000**.

(40) Hornak, V.; Abel, R.; Okur, A.; Strockbine, B.; Roitberg, A.; Simmerling, C. *Proteins* **2006**, *65*, 712–725.

(41) Wang, J.; Wolf, R. M.; Caldwell, J. W.; Kollman, P. A.; Case, D. A. *J Comput. Chem.* **2004**, *25*, 1157–1174.

(42) Kaiser, E.; Bossinger, C. D.; Colescott, R. L.; Olsen, D. B. *Anal. Chim. Acta.* **1980**, *118*, 149–151.

Chapter 3

Towards Radiolabeled Rosette Nanotubes for Scintigraphic Studies

3.1 Introduction

As demonstrated earlier and discussed in Chapter 2, RNTs have many desirable features that make them excellent candidates for biomedical applications, including their metal-free and bio-inspired design, water solubility and high tolerance for a variety of large bioactive groups including amino acids and peptides.[1-9] RNTs can also incorporate hydrophobic drug molecules[5,9-12] such as tamoxifen (TAM) and dexamethasone (DEX), and slowly release these cargoes at physiological conditions for drug delivery applications.[13,14] As a result, RNTs may serve as a multi-functional scaffold that can be modified with cell-targeting peptides on the surface, and loaded in the interior with drugs for site-specific drug delivery.

For successful drug delivery, however, the RNT scaffold should not cause inflammatory responses upon treatment, and should be excreted from the body without causing short- or long-term side effects. In this regard, previous *in vitro* and *in vivo* studies have demonstrated that RNTs are biocompatible and nontoxic, and do not cause inflammatory responses. Journeay *et al* for example, demonstrated that lysine functionalized RNTs were well tolerated by the Human Calu-3 pulmonary epithelial cells *in vitro*, and do not induce a robust inflammatory response in human macrophage white cells.[15,16] *In vivo* pulmonary studies, however, showed that RNTs cause no inflammatory response at low concentration, and only low acute toxicity at high concentrations.[17] However, these studies cannot provide information about the interaction of the RNTs with the biological systems and their bio-distribution. It is therefore necessary to

develop labeling strategies of the RNTs in order to facilitate their *in vitro* and *in vivo* studies and understand their cellular uptake, pharmacological kinetics, and their distribution in the biological systems.

Of the various molecular labeling technologies, non-invasive radiolabeling imaging techniques based on radionuclides such as positron emission tomography (PET) and single photon emission computed tomography (SPECT) have received tremendous attention and have had a significant impact on many aspects of healthcare.[18,19] Using radioactive imaging probes (called molecular tracers), these techniques allow for noninvasive visualization, monitoring and tracking of drugs, drug carriers, and biological processes at the *in vitro* and *in vivo* levels. Radiolabeling techniques have also been used in drug development and optimization such as understanding the drug interaction and distribution in the biological systems, and optimizing the sufficient and safe dosage for the treatment. In principle, radionuclides that are synthetically attached to the bioactive molecule provide an analytical signal (gamma rays), which is detected by nearby gamma cameras to produce two- or three-dimensional images that can provide information about the spatial distribution of the molecules that are attached to the tracer. The resolution of these images depends mainly on the tracer and the gamma cameras.[18]

PET and SPECT are among the most sensitive molecular imaging techniques that are currently used for imaging function *in vivo*. Several excellent comprehensive reviews are available, which describe the different tracers and radionuclides that have been developed in the two methods.[18,19] In the following sections, a general description of PET and SPECT as well as a comparison between the two techniques is presented.

3.1.1 Single Photon Emission Computed Tomography (SPECT)

Single Photon Emission Computed Tomography (SPECT) imaging is one of the most clinically used techniques for molecular imaging. The radionuclides used in SPECT decay by emitting γ-rays, which are detected by low-resolution gamma cameras. Several radionuclides are used in this technique, including iodine-123 (^{123}I), technetium-99m (^{99m}Tc), and rhenium-188/186 ($^{186/188}$Re), which have longer half-life than those used in PET imaging (Table 3.1). Therefore, although SPECT imaging provides images of lower resolution than PET imaging, the use of longer-lived radionuclides and lower cost gamma cameras make SPECT more practical and clinically used than PET.[18]

Table 3.1. Different radionuclides used in SPECT imaging and their half-lives.

Radionuclide	^{123}I	^{99m}Tc	$^{186/188}$Re	^{111}In	^{67}Ga	^{201}Tl
Half-life/h	13.2	6	17	67.9	78.3	73.1

Among the different radionuclides used for SPECT, ^{99m}Tc is the most heavily used radionuclide (over 90% of all the current clinical imaging studies) since it can be produced from the decay of its longer-lived parent nuclide, ^{99}Mo (half-life = 67 h) using commercially available generator systems.[18,20,21] Likewise, the radioactive $^{186/188}$Re is a very common renal imaging agent, which is used for the same purpose. Due to the similar chemistry between Re and Tc metals, the radiolabeling done with $^{186/188}$Re can be translated to ^{99m}Tc without further optimization, and $^{186/188}$Re is often used when it is difficult to work with ^{99m}Tc due to its shorter half-life and more expensive production.[20,21]

The incorporation of ^{99m}Tc or $^{186/188}$Re into a molecule requires a selective ligand to chelate the metal and form a stable complex *in vivo*. Several ligands have been developed, which typically contain at least one sulfhydryl group that forms a stable S-Metal bond upon complexation. Mercaptoacetyl triglycine (MAG_3) (shown in Figure 3.1 A) is one of the most commonly used ligands for both

isotopes.[22-26] From a structural standpoint, this ligand contains a sulfhydryl atom typically protected with a benzoyl group that requires deprotection prior to chelation with Re or Tc. It also features a free carboxyl group that is not involved in chelation and can be used as a handle to link other groups via amide bond. Various bioactive groups such as sugars,[27,28] immune globulins,[27] peptides,[22,25] and siRNA,[29] to only name a few, have been functionalized with MAG_3. Other ligands featuring sulfur-containing amino acids such as cysteine have also been developed (Figure 3.1 B).[23,30-32] After preparation of the ligand-functionalized biomolecule, the complexation with Tc or Re is done at the last step. Since the half-lives of radioactive ^{99m}Tc or $^{186/188}$Re are 6h and 17h, respectively, the complexation reaction needs to be rapid and efficient and the radioactive complex should be obtained with high radiochemical yield and purity.[18]

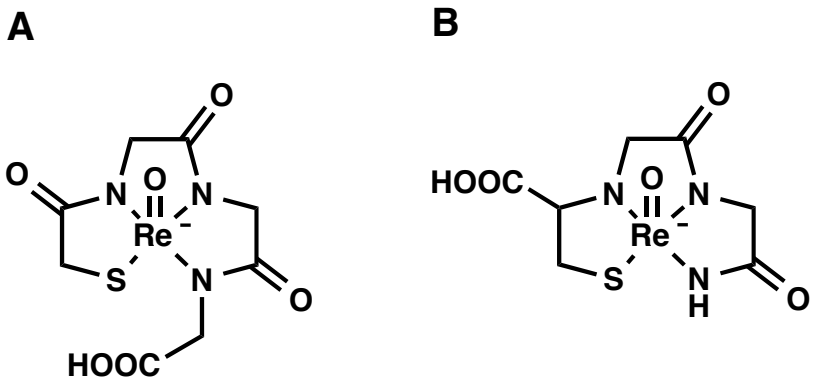

Figure 3.1. (A) MAG_3 complex with Re metal, and (B) complex of a cysteine-containing ligand (Gly-Gly-Cys) with Re metal.

3.1.2 Positron Emission Tomography (PET)

In PET imaging, the radionuclides emit a positively charged particle called the positron, which travels a short distance in the surrounding tissue before it annihilates by combining with an electron (Figure 3.2). Upon annihilation, the positron and the electron are converted into two γ-photons at approximately 180° to each other. The pair of γ-rays is detected by surrounding detectors, which

provide information about the spatial distribution of the radionuclide-attached molecule as a function of time.[18] Table 3.2 shows the most commonly used nuclides along with their decay half-life.

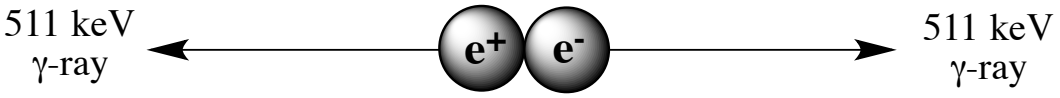

Figure 3.2. The annihilation of a positron with an electron producing two γ-rays at 180°.

Table 3.2. The different radionuclides used in PET imaging and their half-lives.

Radionuclide	^{11}C	^{13}N	^{15}O	^{18}F	^{64}Cu	^{68}Ga	^{76}Br	^{124}I
Half-life/min	20.3	10	2	110	762	68.1	972	60192

Although all nuclides shown in Table 3.2 can be used for PET imaging, ^{11}C or ^{18}F nuclides are the most currently used probes. The reason being is that both nuclides are indistinguishable from the nonradioactive counterparts, and therefore their introduction into the biomolecule causes minimal disturbance. This particular feature provides PET imaging with its main advantage over SPECT. While replacement of carbon-12 with carbon-11 produces only a negligible isotope effect, the substitution of a hydrogen atom by a fluorine atom induces only a slight steric perturbation since fluorine and hydrogen are similar in size.[18] However, radiolabeling with ^{18}F is more practical and favorable for *in vivo* studies since it has a longer half-life of 110 min.

As in SPECT, the introduction of the radionuclide in PET is employed at the latest possible stage in the synthesis to maximize the utility of the isotope. Thus, the synthesis and purification should not exceed two or three times the half-life of the radionuclide. Several fluorine-containing tags have been developed, which can be linked to the biomolecule at the end of the synthesis. Fluorobenzene derivatives such as *p*-fluorobenzoate are among the most commonly used tags for labeling

with ^{18}F.[33-36] To covalently connect this tag with the biomolecule, N-succinimidyl 4-[^{18}F]fluorobenzoate (SFB) reagent is reacted with an amine-functionalized biomolecule under basic conditions (Figure 3.3). The coupled product is then purified by HPLC prior to the *in vivo* study.

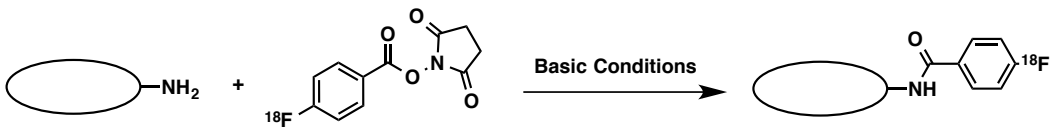

Figure 3.3. The coupling reaction of the radioactive SFB reagent with an amine-functionalized biomolecule for PET imaging studies.

In this chapter we present radiolabeling strategies of the RNTs for PET and SPECT imaging studies. The chelation (for SPECT) and the coupling (for PET) reactions, the purification, and the self-assembly studies were developed with the cold nuclides, and optimized within the half-life of the radioactive counterparts. Details of the developed strategies are presented in the following sections.

3.2 Development of RNTs for SPECT Imaging[‡‡]

3.2.1 Materials Design

As discussed in section 3.1.1, sulfhydryl-containing ligands such as MAG_3 and cysteine-containing peptides are the most widely used ligands for SPECT imaging. Therefore, in this section two twin-G∧C motifs, which are functionalized with lys-gly-gly-gly-cys pentapeptide (called TB-lGGGC) (**3.1**) and MAG_3 (called TB-MAG_3) (**3.2**), respectively, are presented. While an ethylene diamine spacer was inserted between the ligand and twin-G∧C in **3.2** in

[‡‡] This part of the chapter is published in: 1) Alsbaiee, A.; St. Jules, M.; Beingessner, R. L.; Fenniri, H. *Tet. Lett*. **2012**, *53*, 1645-1651. 2) Alsbaiee, A.; St. Jules, M.; Beingessner, R. L.; Fenniri, H. *Mater. Res. Soc. Proc.* **2011**, 1316, mrsf10-1316-qq03-12, USA.

order to facilitate the metal chelation reaction by reducing the steric hindrance, the lysine residue acts as a spacer in TB-lGGGC motif **3.1**. Upon chelation, both motifs form oxo rhenium complexes having -1 net charge on the metal (called TB-lGGGC-ReO **3.3** and TB-MAG_3-ReO **3.4**, respectively). Complexes **3.3** and **3.4** in turn were to self-assemble into RNTs within the half-life of the radioactive Re and Tc metals.

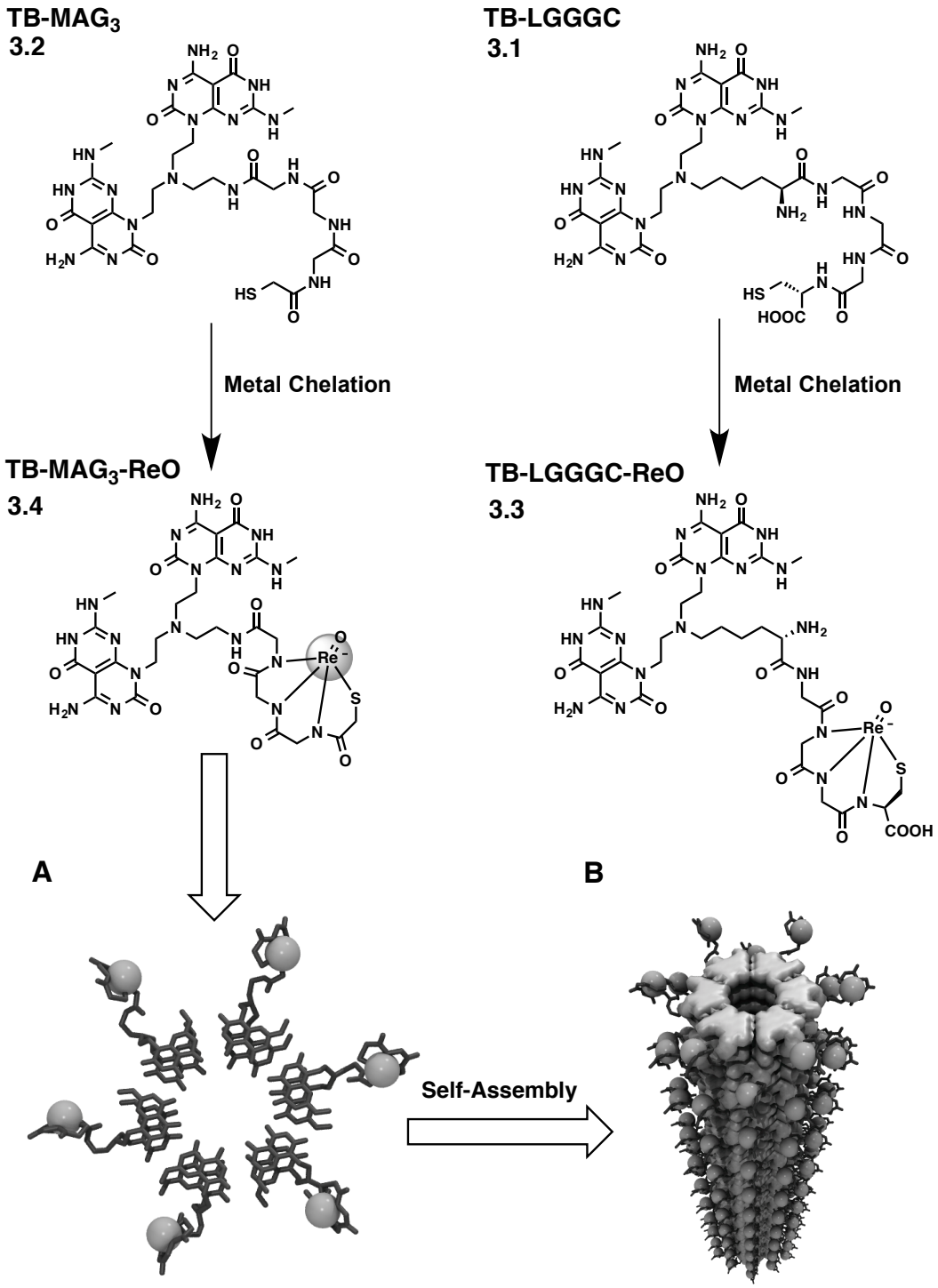

Figure 3.4. A schematic review showing TB-lGGGC (**3.1**) and TB-MAG_3 (**3.2**) motifs, and the corresponding TB-lGGGC-ReO (**3.3**) and TB-MAG_3-ReO (**3.4**)

complexes. (A) a modeling showing the rosettes formed by **3.4**; and (B) the corresponding RNTs.

3.2.2 Synthesis

3.2.2.1 TB-LGGGC-ReO Complex

To synthesize TB-LGGGC ligand **3.1**, a standard Fmoc solid phase peptide synthesis approach similar to that used for the synthesis of the peptides in the chapter 2 was employed. To anchor cysteine on 0.65 mmol/g 4-benzyloxybenzyl alcohol substituted Wang resin (**3.6**), MSNT coupling reagent (2,4,6-mesitylenesulfonyl-3-nitro-1,2,4-triazolide) in DCM was used, which was reported to give a high yield of substitution of cysteine amino acid on the hydroxymethyl resins with a low percentage of racemization.[37] After washing the resin and drying under vacuum, spectroscopic quantification of fulvene-piperidine adduct **3.7** at 301 nm revealed a substitution yield of 78%. The residual unreacted hydroxyl groups were then capped by treating the resin with 50% acetic anhydride in pyridine and washing, then the Fmoc protecting group was removed under 20% piperidine/DMF basic conditions.

The subsequent three glycine amino acids **3.9** were coupled to the peptide on the resin using three cycles of amide coupling reactions in the presence of O-benzotriazole-N,N,N',N'-tetramethyl-uronium-hexafluoro-phosphate (HBTU) and DIPEA, followed by Fmoc deprotection using 20% piperidine/DMF. Finally, the lysine amino acid spacer was coupled to the tetra-peptide to finish the synthesis (Figure 3.5).

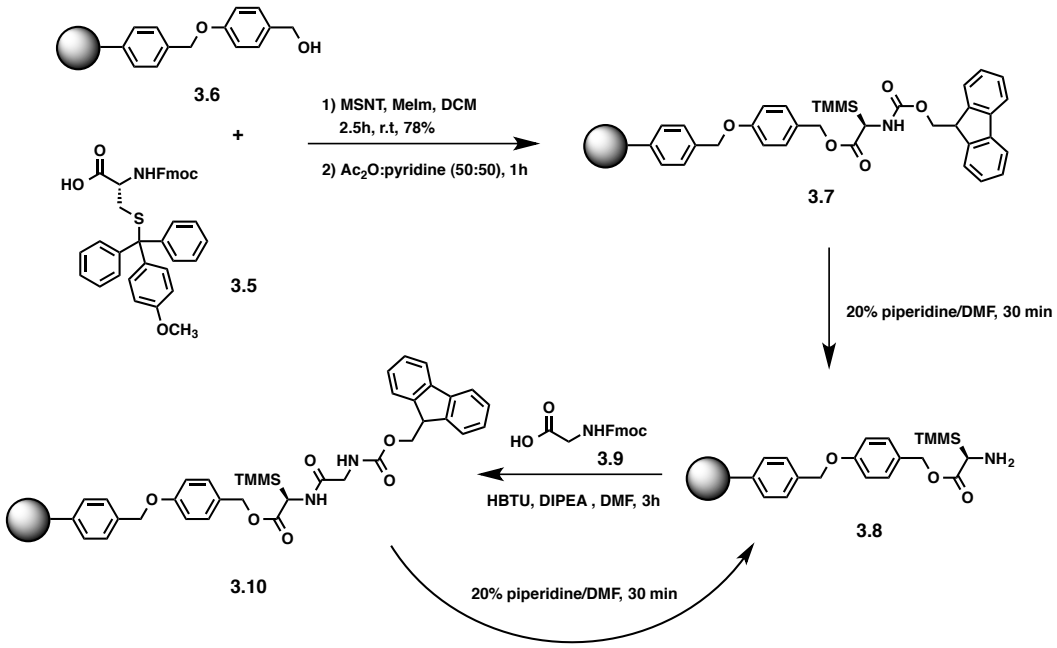

Figure 3.5. Synthesis of pentapeptide LGGGC on the resin.

To synthesize TB-peptide conjugate **3.1**, aldehyde **3.12** was reacted with the peptide-substituted resin **3.11** under reductive conditions using $NaBH(OAc)_3$ and DIPEA to provide TB-adduct **3.13**. Deprotection under TFA acidic conditions then afforded compound **3.1** as a white solid (Figure 3.6).

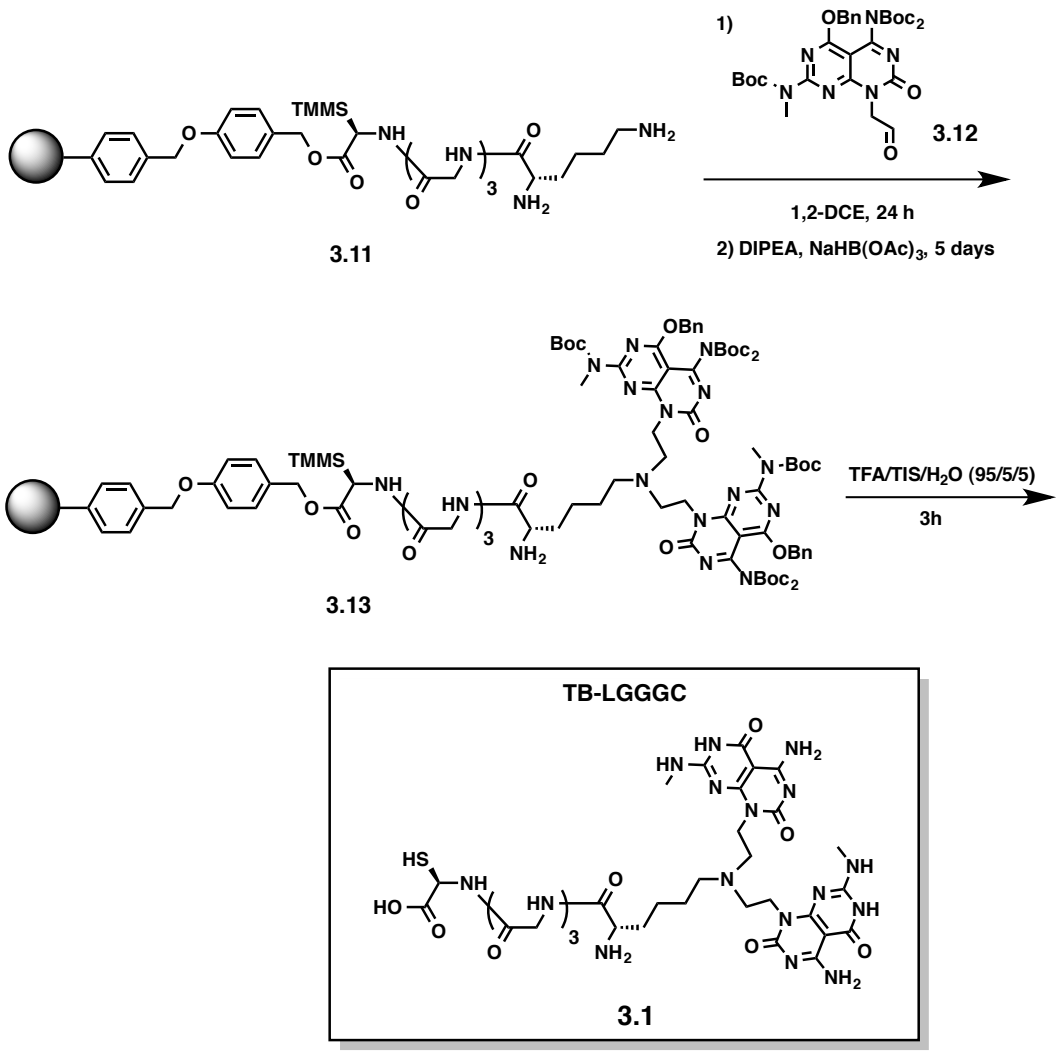

Figure 3.6. Synthesis of TB-LGGGC conjugate.

Compound **3.1** was characterized by low-resolution electrospray mass and high-resolution MALDI. Although the mass analyses indicated that compound **3.1** was major, many other unidentified impurities were found. All subsequent purification attempts by HPLC failed due to the very low solubility of the compound in water. Thus, the crude compound **3.1** was examined for the chelation reaction with rhenium in the form of $ReOCl_3(PPh_3)_2$ without further purification. Several chelation conditions from the literature were examined along with the developed conditions described in section 3.2.2.2 (Table 3.3), but unfortunately no complex **3.3** was obtained even after long reaction times (Figure 3.7). This was rationalized

by the presence of many impurities in the crude compound **3.1**, which were not separable due to the low solubility of **3.1** in water. Thus, TB-LGGGC (**3.1**) ligand was abandoned.

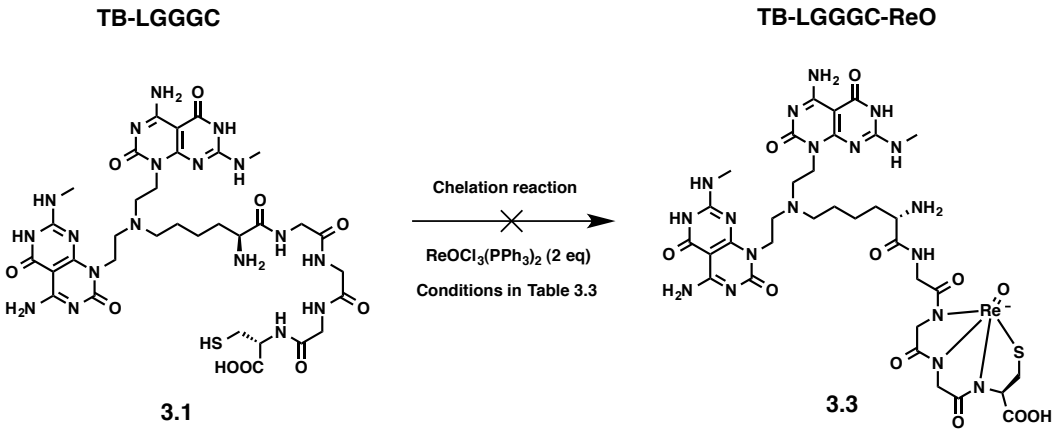

Figure 3.7. Unsuccessful chelation of TB-LGGGC (**3.1**) with $ReOCl_3(PPh_3)_2$.

Table 3.3. Unsuccessful chelation trials of TB-LGGGC (**3.1**).

Solvent system	Base	T°C	Time (h)	Result
DMF/MeOH 50:50	MeONa (20 eq)	RT	24	No Rxn
DMF/MeOH 80:20	MeONa (20 eq)	RT	24	No Rxn
DMF	No base	RT	24	No Rxn
DMF/Water 50:50	NaOH 0.05 N pH 9	RT	24	No Rxn

3.2.2.2 TB-MAG$_3$-ReO Complex

The synthesis of the benzoyl protected TB-MAG_3 motif was developed previously by a former group member. The benzoyl protected MAG_3 ligand (**3.17**) was synthesized starting with the commercially available thioglycolic acid, and using a modified literature method as shown in Figure 3.8.[38]

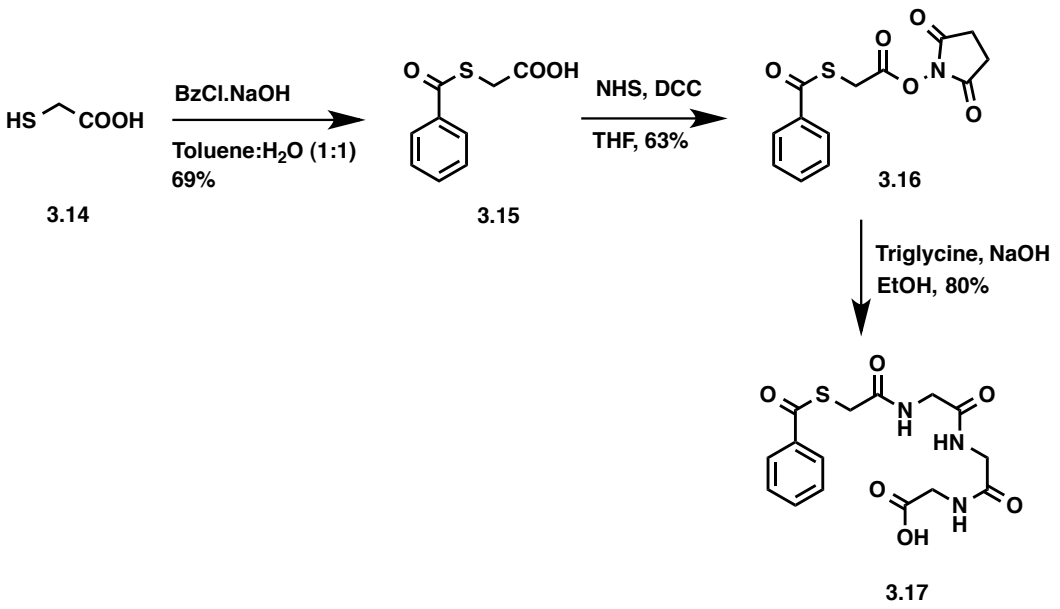

Figure 3.8. Synthetic procedure of the benzoyl protected MAG_3 ligand.[38]

Having obtained MAG_3-Bz (**3.17**) ligand, Boc protected ethylene diamine spacer was coupled to carboxyl group of **3.17** to obtain compound **3.18**. TFA deprotection of the Boc group, followed by double reductive amination reaction with the protected G∧C base aldehyde **3.12** afforded compound **3.19**. TB-MAG_3-Bz motif **3.20** was then obtained after TFA deprotection of compound **3.19** (Figure 3.9).

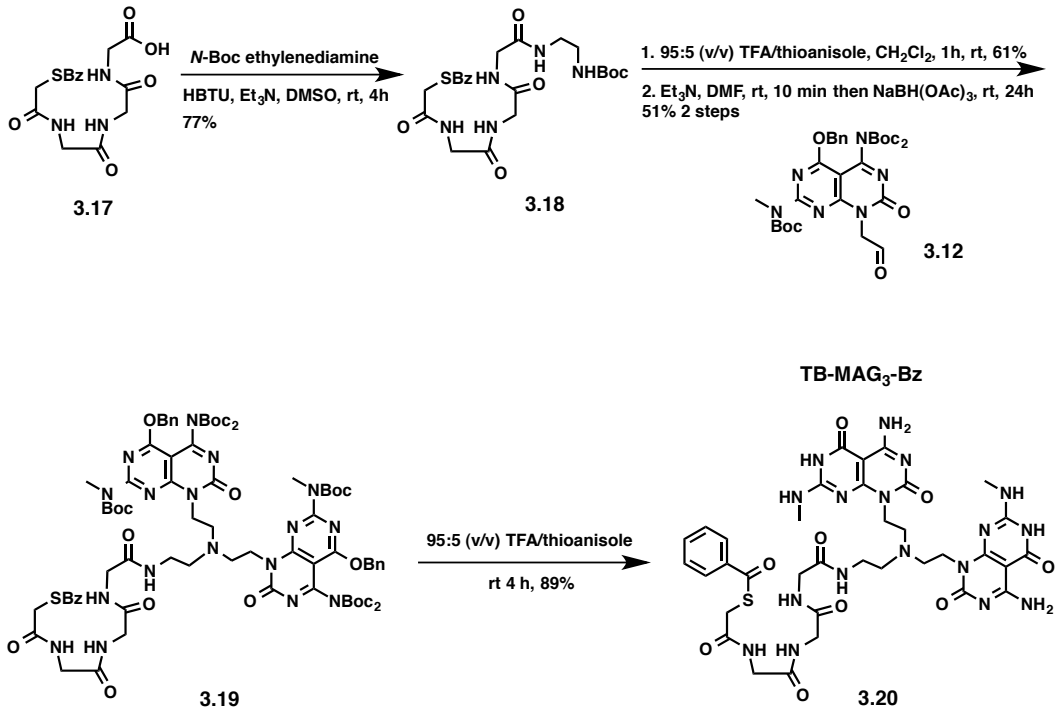

Figure 3.9. Synthetic procedure of the benzoyl protected TB-MAG_3 motif.[39]

With compound **3.20** in hand, my subsequent task was the removal of the benzoyl protecting group followed by the chelation with cold Re. While the removal of the Bz group is performed *in situ* during the chelation with the metal, two methods were used in the literature for the chelation reaction since the oxidation state of Re in the complex is +5. In the first method, ReO_4^- (perrhenate) reagent complex, in which Re features +7 oxidation state is used, and a reducing agent such as $SnCl_2$ is added *in situ* in order to reduce the metal to +5 oxidation state prior to chelation.[25] In another approach, ligand exchange reaction with reagent complexes having Re in +5 oxidation state (such as oxotrichlorobis-(triphenylphosphine)-rhenium(V) or $ReOCl_3(PPh_3)_2$) is used.[22] It was reasoned that $SnCl_2$ reducing agent may react with the G∧C base, and I thus decided to pursue the second approach for the SPECT imaging of RNTs (Figure 3.10).

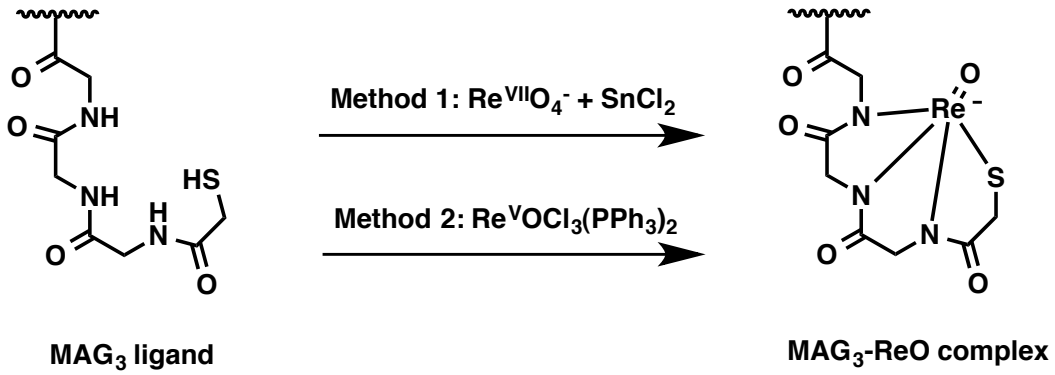

Figure 3.10. General scheme showing the two typical methods used in the literature for the chelation of MAG_3 with Re.

Several typical conditions described in the literature for the deprotection-chelation reactions were examined. These involved either a one-step Bz deprotection-chelation protocol or an *in situ* Bz deprotection under basic conditions, followed by the addition of Re in the form of $ReOCl_3(PPh_3)_2$. While various bases (NaOH[22], pyridine[40,41] or Et_3N), solvents (MeOH, DMF), temperatures (rt to 80°C), and reaction times were examined to for the chelation, only starting material was isolated under these conditions (Figure 3.11) (Table 3.4).

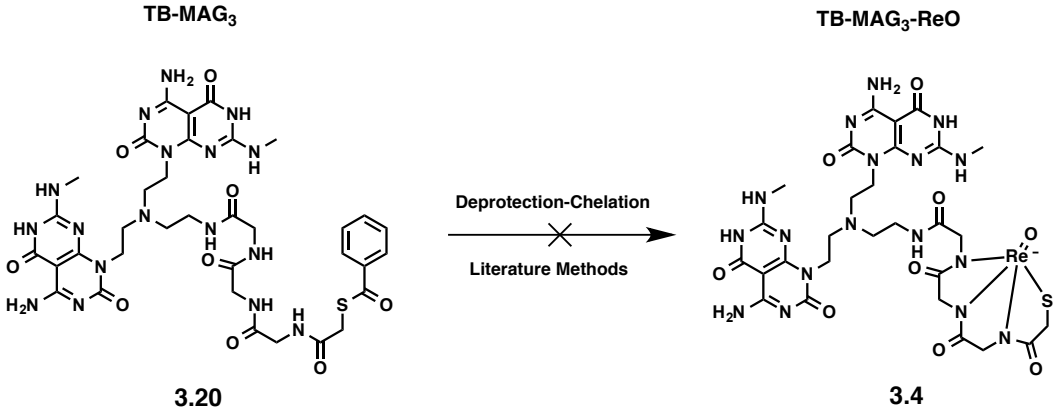

Figure 3.11. Unsuccessful literature methods for the deprotection-chelation reaction.

Table 3.4. The unsuccessful deprotection-chelation attempts from the literature.

Rhenium complex reagent	Solvent system	Base	T°C	Time (h)
$ReOCl_3(PPh_3)_2$	62% MeOH/ Water	0.05 N NaOH, pH 8	70	6
$ReOCl_3(PPh_3)_2$	DMF/ 5%MeOH	1 % Pyridine	80	24
$ReOCl_3(PPh_3)_2$	DMF	Et_3N (4eq)	80	4
$ReOCl_3(PPh_3)_2$	DMF/ MeOH	Et_3N (10 eq)	80	4
$ReOCl_3(PPh_3)_2$	DMF	No base	50	24

This unfavorable outcome was reasoned to the low solubility of compound **3.19** in MeOH, which is a common solvent for this reaction. Therefore, a mixture of DMF and MeOH was a better solvent choice in this case. I also considered removing the benzoyl group prior to the chelation (in two steps) to improve the solubility of the starting material in the medium. A review of the literature found that NaOMe in MeOH was used to deprotect the sulfhydryl-Bz protecting group in cysteine amino acid during solid phase peptide synthesis.[42] As well, careful examination of the electrospray mass traces of the reactions in Table 3.4 revealed that the reagent complex $ReOCl_3(PPh_3)_2$ had been oxidized to the very stable perrhenate (ReO_4^-)[43] anion, and therefore degassing the solvents and the medium to remove oxygen was evidently important for this reaction. Taking these parameters into consideration, a deprotection-chelation test reaction was carried out on the benzoyl protected MAG_3 ligand (**3.17**). Compound **3.17** was dissolved in degassed MeOH, and treated with NaOMe (15 eq) under argon for 1 h, then a solution of the complex $ReOCl_3(PPh_3)_2$ (1.5 eq) in degassed DMF was added, and the mixture was stirred at room temperature under argon for additional 4 h (Figure 3.12). Not only did the color of the solution turn into brownish during the first

hour, but also the electrospray mass analysis over time revealed that **3.17** had completely converted into complex **3.22** after 4 h.

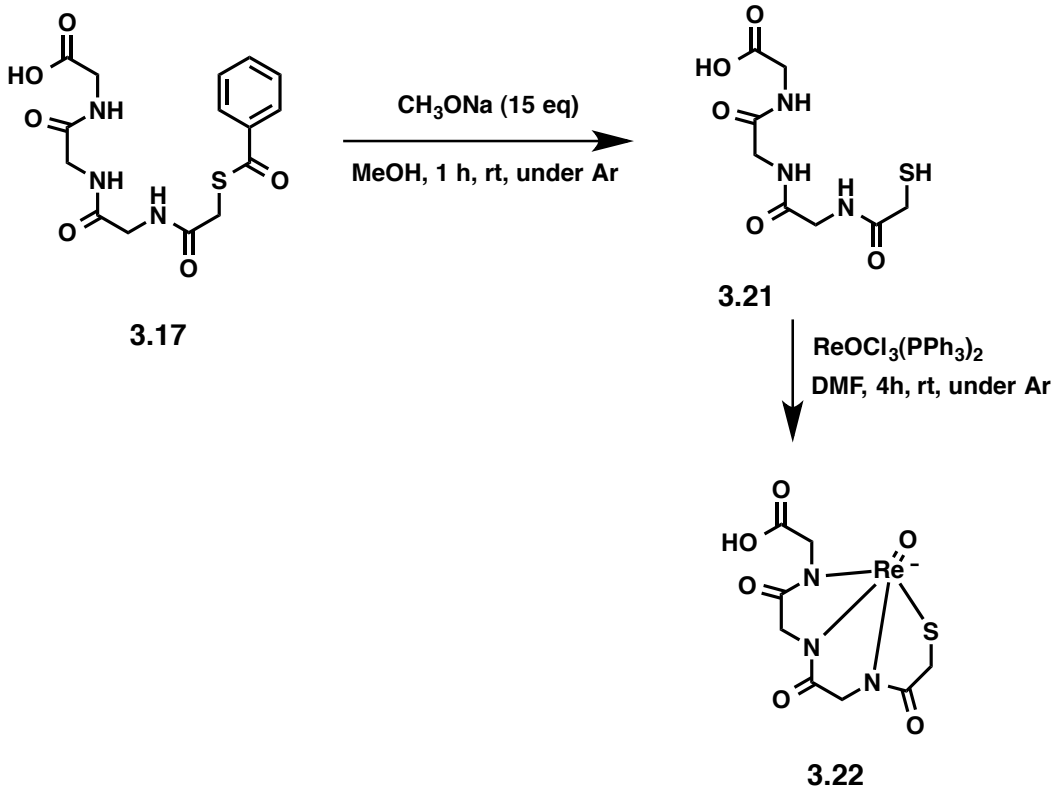

Figure 3.12. Two-steps one-pot deprotection-chelation test reaction on MAG_3 ligand.

The successful deprotection-chelation conditions with MAG_3 ligand (**3.17**) was then applied on the protected TB-MAG_3-Bz compound **3.20**, which was treated with NaOMe (15 eq) in degassed MeOH for 1 h, and then with a solution of $ReOCl_3(PPh_3)_2$ (1.5 eq) in DMF that was also degassed (Figure 3.13). After stirring for 4 h at room temperature, diethyl ether was added to precipitate a brown solid, which was purified by washing with DCM (x3) and hexane (x3). I was pleased to observe that with these conditions, complex **3.4** was obtained, but unfortunately with many other unidentified impurities even after washing with various organic solvents.

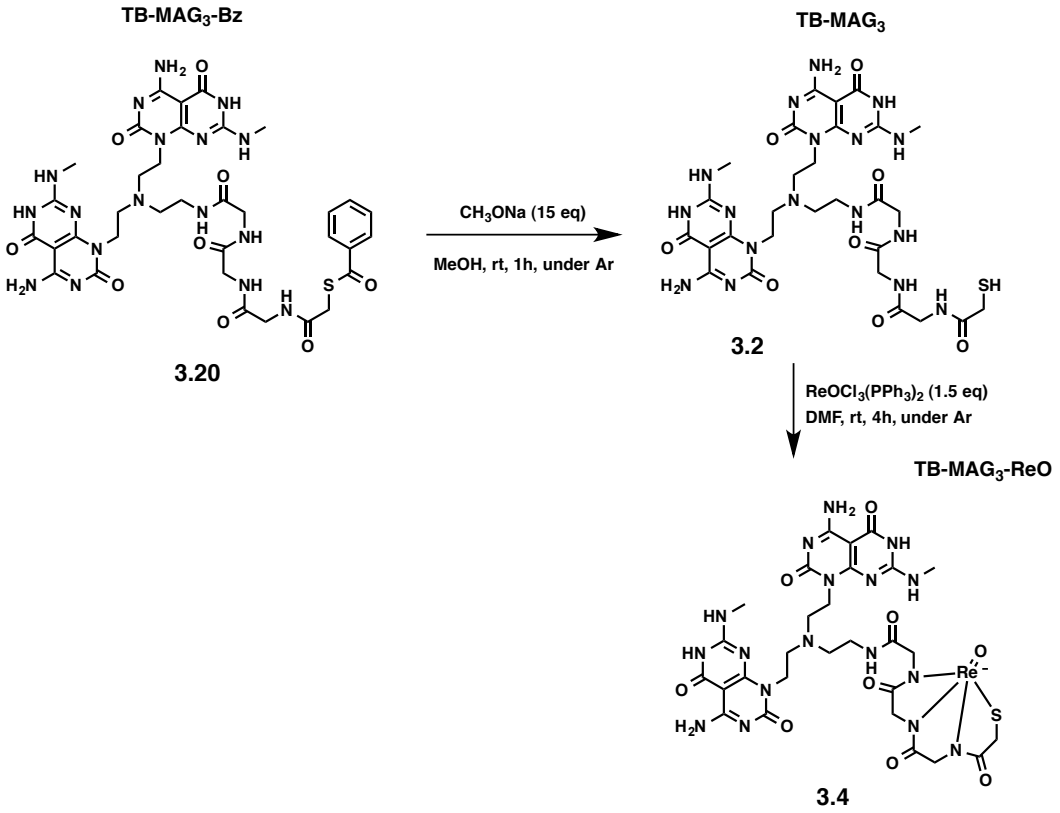

Figure 3.13. Two-steps one-pot deprotection-chelation reaction to obtain complex TB-MAG_3-ReO.

Although these reaction conditions successfully led to the formation of TB-MAG_3-ReO complex **3.4**, 5 h were required for the reaction, and the complex needed further purification by HPLC. Unfortunately, purification attempts by HPLC failed due to the low solubility of the complex in water. Therefore, further optimization of the reaction was needed in order to shorten the reaction time and to improve the yield of the complex to avoid the need for HPLC purification. After extensive efforts, it was found that simply a one-step protocol worked very well in which **3.20** was treated with $ReOCl_3(PPh_3)_2$ (2 eq) and NaOMe (20 eq) concurrently, in a 1:1 mixture of degassed DMF:MeOH for 30 min at room temperature (Figure 3.14). These conditions led to complex **3.4** with very few impurities. However, precipitation of the brown solid by diethyl ether and washing with few organic solvents provided the pure complex **3.4** in 94% yield,

which did not need HPLC purification as was found by the ^{1}H NMR and low- and high-resolution mass analyses. Complex **3.4** was also characterized by IR, and the Re=O absorption was identified at 973.0 cm^{-1}.

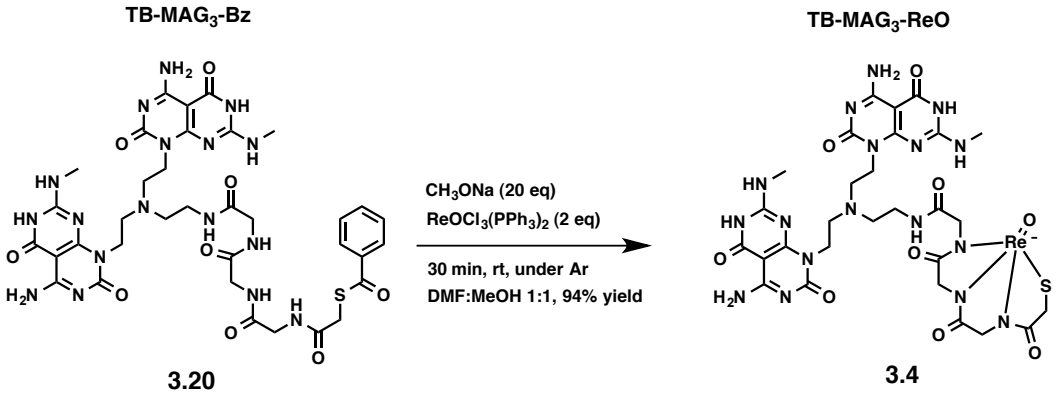

Figure 3.14. The optimized one-pot deprotection-chelation reaction to obtain complex TB-MAG$_3$-ReO (**3.4**) in high purity.

3.2.3 Self-Assembly Studies[§§]

3.2.3.1 Experimental Studies

The self-assembly of complex **3.4** was investigated in water and DMSO at neutral conditions. UV–Vis spectroscopy first established the absorbance profiles pertaining to the growth of the RNTs over time. As shown in Figure 3.15A, the compound (4.8 x 10^{-5} M) presents a hypochromic effect occurring over time at two λ_{max} values that range between 287–288 nm and 234–236 nm, which corresponds to the absorption of the π-π stacked twin G∧C bases. The alternative hyperchromic effect noted during the variable temperature UV–Vis experiments of **3.4**, highlights the reversible nature of this self-assembly process as the system is heated Figure 3.15B.

[§§] SEM imaging was done with the help of Dr. Jae-Young Cho. TEM and AFM imaging were done by Dr. Jae-Young Cho.

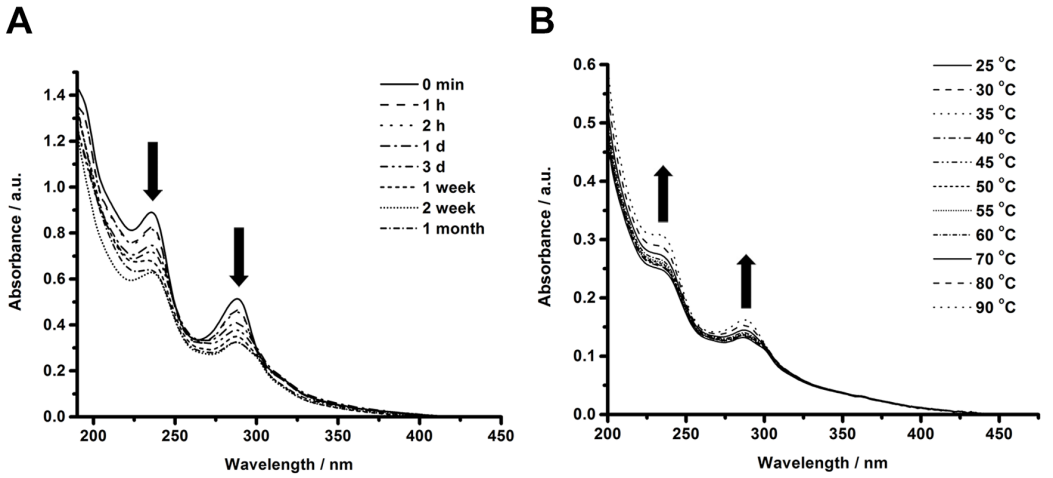

Figure 3.15. UV-Vis studies of **3.3** (A) Growth study of RNTs over time (4.8×10^{-5} M). (B) Variable-temperatures spectra at increments of 5 °C or 10 °C between 25 °C and 90 °C (4.8×10^{-5} M).

Scanning electron microscopy (SEM), transmission electron microscopy (TEM), and atomic force microscopy (AFM) were used to further characterize the RNT assemblies. Figure 3.16A-D shows representative SEM images of **3.4** (0.05 mg/mL) in water (A,B) and DMSO (C,D). From the corresponding TEM studies in DMSO (Figure 3.16E), the average RNT diameters were measured to be 4.7 ± 0.4 nm. Molecular modeling of the **3.4** RNTs (discussed in section 3.2.3.2), which was approximated by replacing the Re atom with carbon to simplify the calculations, resulted in an RNT diameter of 4.7 nm. Even though this value is only an approximation due to the replacement of the Re atom with carbon, it compares well with our experimental values. Overall, it is evident from these studies that there is no barrier to the self-assembly process by the presence of the Re-chelated MAG_3 ligand on the surface of the RNTs.

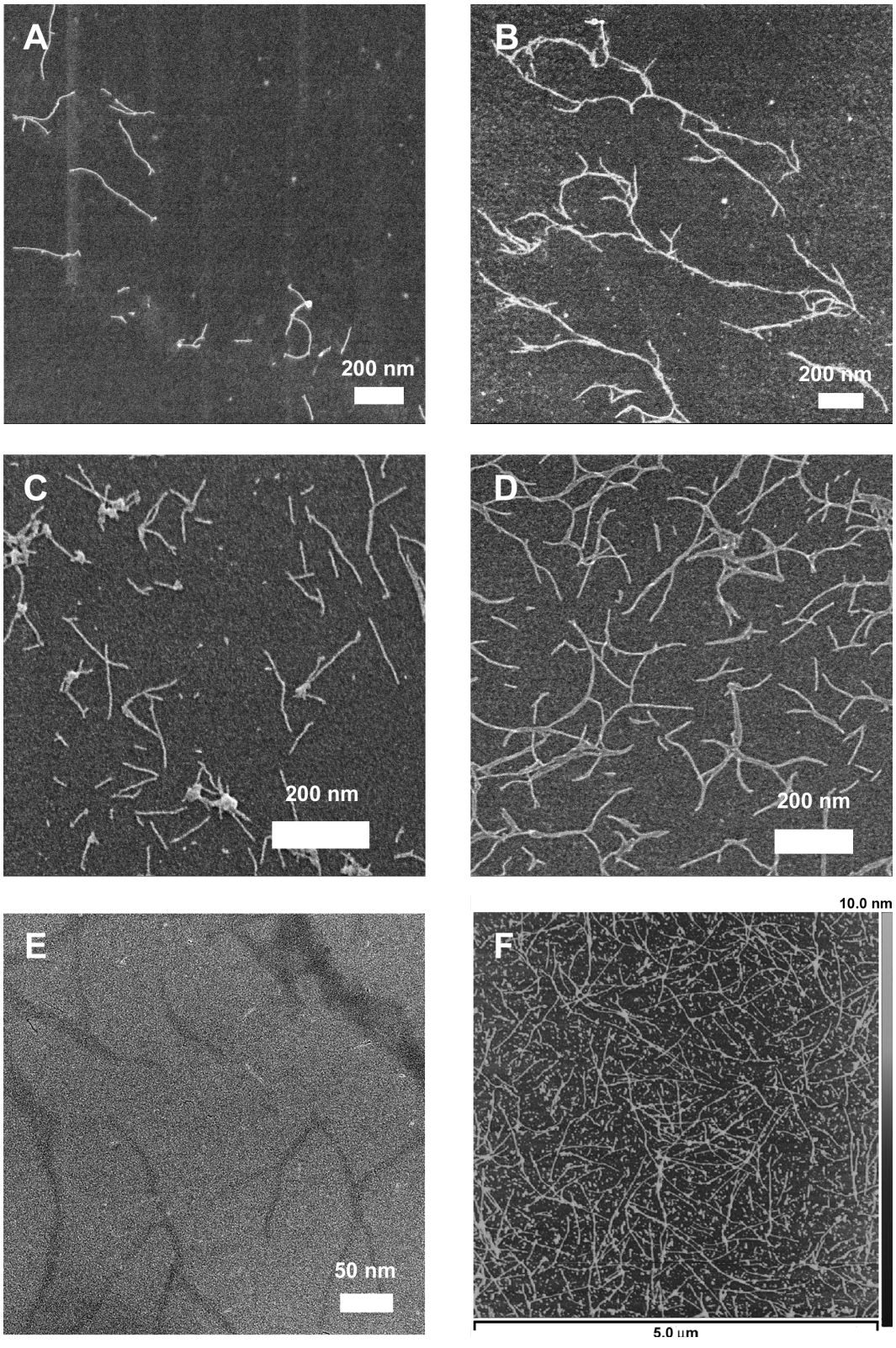
A
200 nm
B
200 nm
C
200 nm
D
200 nm
E
50 nm
F
10.0 nm
5.0 µm

Figure 3.16. (A,B) SEM images of **3.3** (0.05 mg/ml) in water after 1 week of aging. (C,D) SEM images of **3.3** (0.05 mg/ml) in DMSO after 1 week and 2 weeks respectively. (E) TEM image of **3.3** (0.05 mg/ml) in DMSO after 2 weeks, and (C) AFM of **3.3** (0.05 mg/ml) in DMSO after 2 weeks.

3.2.3.2 Molecular Modeling[***]

The total free energy of the rhenium chelated MAG_3 RNT **3.4** was obtained as a sum of the internal energy calculated by molecular mechanics (Macromodel 8.5) and the solvation free energy calculated by 3D-RISM theory[44] with the OPLS force field.[45]

In order to simplify the modeling, the structure in Figure 3.17a was used for whereby the rhenium (or technetium) atom was replaced with carbon. The charge of the MAG_3 complex therefore changed from -1 to 0. It was assumed that the orientation of the MAG_3 group is determined mainly by the steric interaction in the RNT. By changing the two dihedral angles indicated by the arrows, the orientation of MAG_3 was sampled and optimized according to the X-ray conformation.[46] The G∧C group was also fixed according to the previous twin-RNT modeling.[11] Each of the resulting 9 (3x3) conformers was multiplied and arranged to form the RNTs consisting of 7 double-rosette stacks. The energies of 9 RNTs in the GB/SA water model were calculated and compared and the RNT consisting of the conformer in Figure 3.17b was found to be the most stable. The resulting hexameric rosette and RNT self-assembled from this stable conformer is shown in Figure 3.17c and 3.17d respectively. The diameter of the RNTs was determined to be 4.7 nm.

[***] Modeling studies were done by Dr. Takeshi Yamazaki.

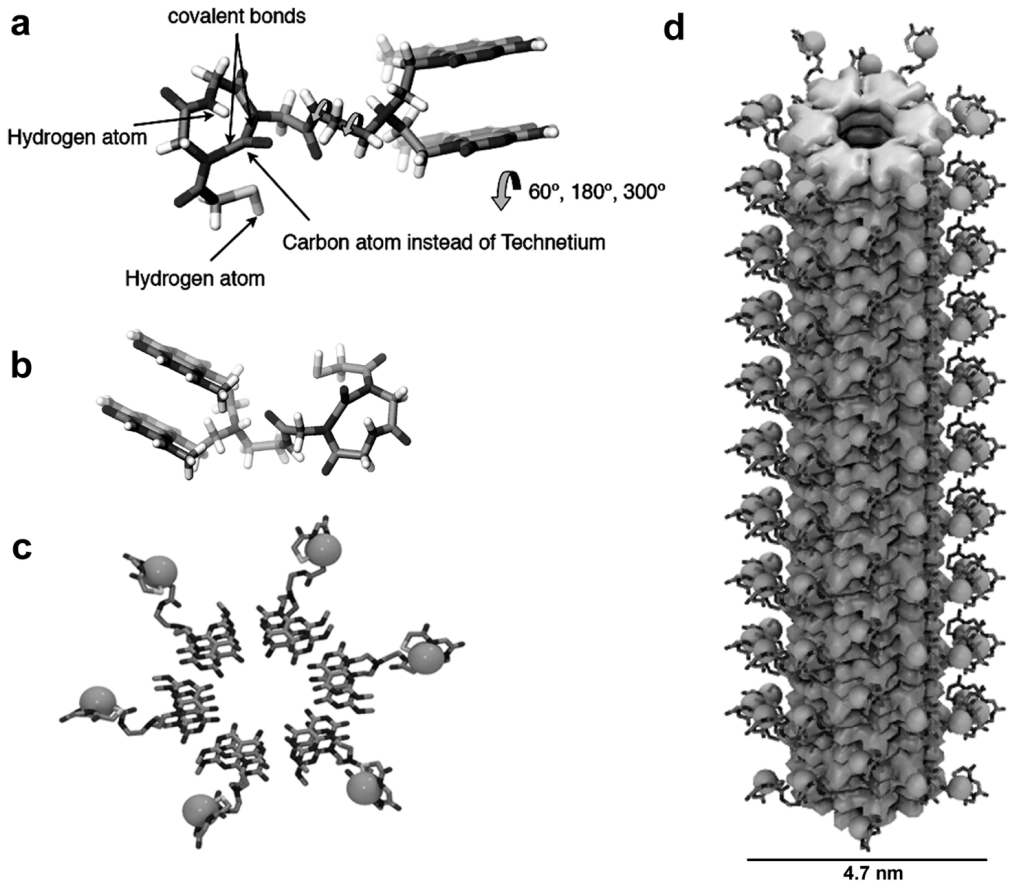

Figure 3.17. (a) Compound TB-MAG$_3$-ReO (**3.4**), with carbon replacing the technetium or rhenium atom; (b) Most stable conformation of (a); (c) Hexameric rosette; and (d) RNT self-assembled from (b). Hydrogen atoms have been omitted for clarity. The spheres represent the Tc/Re atoms that would be chelated in place of the carbon atom used.

3.2.4 Experimental

3.2.4.1 Self-Assembly Procedure

Stock solutions of compound **3.4** in water or DMSO were prepared by dissolving the solid to a final concentration of 1 mg/ml. The solutions were then sonicated for 5 min, and heated by heat gun to 95ºC. This cycle was repeated for two more times, then the solutions were left at room temperature for aging. Aliquots of the

stock solutions were diluted with water to a final concentration of 4.8×10^{-5} M for UV-Vis measurements, and to 0.05 mg/ml for SEM, TEM, and AFM imaging studies.

3.2.4.2 SEM Imaging

Aliquots of the stock self-assembled solutions (0.1 mg/ml) in water or DMSO were diluted a final concentration of 0.05 mg/ml in the corresponding solvent. The SEM grids were prepared by depositing a droplet of the diluted solutions on a carbon-coated 400-mesh copper grid (Electron Microscopy Sciences) for 10 seconds before blotting the grid using filter paper. The grid was then dried by air, and heated on hotplate (100ºC). SEM images were obtained without negative staining at 10-30 kV accelerating voltage, 20 μA and a working distance of 5-8 mm using a high resolution Hitachi S–4800 cold field emission SEM.

3.2.4.3 TEM Imaging

A drop of the RNT sample at the specified concentration was deposited onto a carbon-coated 400-mesh copper grid, then blotted after 10 s. The samples were stained by depositing one droplet of uranyl acetate (2% aqueous for the water) for 120 s each. The grid was then blotted, dried in air and then by vacuum hotplate. TEM investigation was carried out on a JEOL 2200 FS TEM – 200kV Schottky field emission instrument equipped with an in-column omega filter. Bright field and high-angle annular dark-field (HAADF) TEM images were acquired using energy filtered zero loss beam (slit width 10ev). SEM images (without staining) were recorded using a high resolution Hitachi S-4800 cold field emission SEM operating at an accelerating voltage of 5 kV and a working distance of ~ 3.0 mm.

3.2.4.4 AFM Imaging

For the AFM measurements, clean mica substrates (1×1 cm^2) were prepared and the samples were deposited by spin-coating at 3500 rpm for 30 s to remove the

excess precipitation. The sample was observed using a Digital Instruments/Veeco Instruments MultiMode Nanoscope IV AFM equipped with an E scanner. For obtaining the optimized height profiles, silicon cantilevers (MikroMasch USA, Inc.) with low spring constants of 4.5 N/m were used in tapping mode (TM-AFM). A low scan rate (0.5-1 Hz) and amplitude setpoint (1 V) provided a clear image during the measurements.

3.2.4.5 General Methods

All reagent grade solvents were purified using a solvent purification system. Reactions were performed under N_2 or Argon unless otherwise stated. All NMR characterizations were performed on a 600 MHz NMR with the solvents indicated used as internal references. The NMR data is presented as follows: chemical shift, multiplicity, coupling constant and integration.

3.2.4.6 Compounds Synthesis and Characterization

Compound TB-LGGGC (3.1)

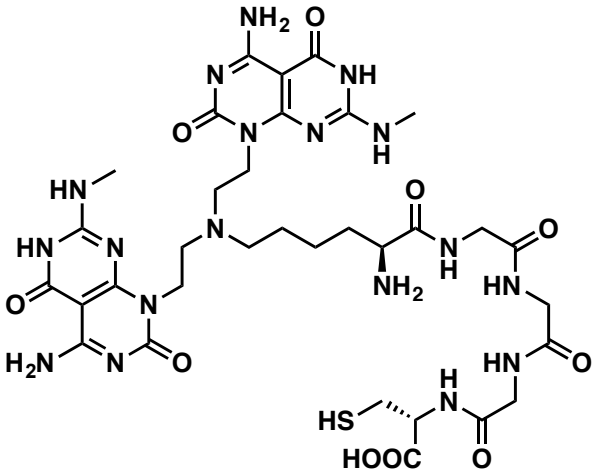

The protected cysteine amino acid was anchored on the resin by treating 4-Benzyloxybenzyl alcohol substituted Wang resin (500 mg, 0.32 mmol) with a mixture of Fmoc-Cys(Tr)-OH (571 mg, 0.98 mmol), methylimidazole (MeIm) (58

µl, 0.73 mmol), 2,4,6-mesitylenesulfonyl-3-nitro-1,2,4-triazolide (MSNT) (289 mg, 0.98 mmol) and DCM (3 mL) in a disposable syringe. The mixture was shaken at room temperature for 1.5 h, and then the solution was filtered under vacuum and the resin was washed with CH_2Cl_2, MeOH, DMF (4x10 mL each). After drying overnight, the degree of substitution on the resin was determined by spectroscopic quantification of fulvene-piperidine adduct **3.7** at 301 nm, which was performed by conducting UV-Vis measurements on three resin samples. The degree of substitution was mathematically calculated using the expression below.

$$\text{Substitution degree} = \frac{101 \times \text{Absorbance}}{7.8 \times \text{mass of resin (mg)}}$$

The residual unreacted hydroxyl groups on the resin were then capped by treating the resin with 50:50 acetic anhydride/pyridine (8 mL for 5 min then 8 mL for 20 min). The Fmoc protecting group was removed by shaking the resin with 20% piperidine in DMF (8 mL, 5 min then 8 mL, 20 min), followed by filtering and washing the resin with CH_2Cl_2, MeOH and DMF.

To couple the subsequent amino acids, a solution of the Fmoc-protected amino acid **3.9** (4.0 eq), O-benzotriazole-N,N,N',N'-tetramethyl-uronium-hexafluoro-phosphate (HBTU) (4 eq) and DIPEA (8 eq) in DMF (8 mL) was activated by stirring for 3 min. The mixture was added to resin **3.8** and shaken for 3 h. Kaiser test[47] was then performed to confirm that the coupling was complete. In the case of incomplete coupling, the reaction was again repeated for 1.5 h.

After synthesizing the penta-peptide and removing the Fmoc group from the N-terminus (using the same procedure as described above), the peptidyl resin **3.11** was treated with aldehyde **3.12** (4.0 eq) in 1,2-dichloroethane (1,2-DCE) for 6 h. $NaBH(OAc)_3$ (4.8 eq) and DIPEA (7.2 eq) were then added and the mixture was shaken for 5 days. The solution was then drained, and the resin was washed with

CH_2Cl_2, MeOH, DMF (4x10 mL each). Completion of the coupling was confirmed using Kaiser test. Peptide conjugate **3.13** were then cleaved from the resin by treating with the TFA/TIS/H_2O solution (95/2.5/2.5) for 3 h. After removing TFA under vacuum, the crude compound **3.1** was washed and sonicated with diethyl ether and centrifuged 10 times before drying under high vacuum.

High-res MALDI-MS (positive): Expected for $C_{79}H_{128}N_{31}O_{20}$, 1830.9952, found 1830.9936.

Compound TB-MAG$_3$-ReO (3.4)

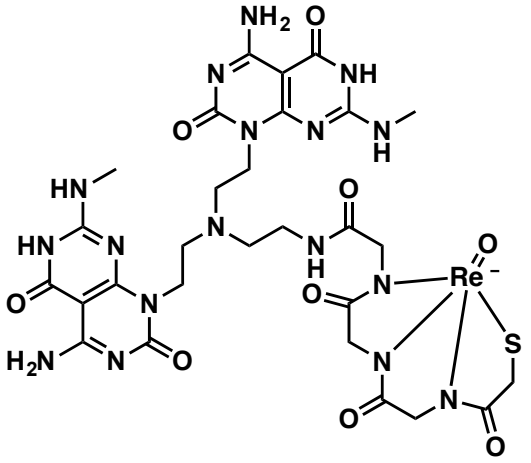

A 50:50 mixture of MeOH/DMF (2.5 mL) in a round bottom flask was degassed by bubbling argon for 30 min and then transferred to an argon filled round bottom flask containing a mixture of **3.19** (10.0 mg, 0.0082 mmol), $ReOCl_3(PPh_3)_2$ (14.5 mg, 0.016 mmol, 2 eq) and CH_3ONa (9.0 mg, 0.167 mmol, 20 eq). The suspension was stirred at room temperature while flashing with argon. After 30 min, the cloudy green solution turned into a cloudy brown color. Diethyl ether was then added to precipitate the brown complex **3.4** immediately. The complex **3.4** was then isolated by centrifugation and washed with diethyl ether (3x), hexane (3x), benzene (3x), chloroform (3x), CH_2Cl_2 (3x) and ddH_2O (2x). The solid was

then dried under vacuum to provide **3.3** as a brown solid ($C_{28}H_{35}N_{17}O_9SRe$, 8 mg, 94%).

High-res MALDI-MS (positive): Expected for $(M+2H^+)/z$ = 974.2238. Found 974.2234.
IR: 1634 (C=O amide), 1531 (C=N), 973.0 (Re=O).
^{1}H-NMR (600 MHz, DMSO-d_6 + 1 drop of TFA-d) δ (ppm): 4.45–4.43 (4H, m), 4.18–4.10 (2H, m), 3.81 (2H, s), 3.78–3.75 (2H, m), 3.72–3.70 (2H, m), 3.59 (4H, brs), 3.53–3.47 (4H, m), 2.96 (6H, br s).
Elemental analysis: Calcd for [M + 2MeOH]: C: 34.78, H: 4.18, N: 22.98. Found: C: 35.00, H: 4.47, N: 22.86.

3.3 Development of RNTs for PET Imaging

In section 3.2, a radiolabeling strategy of RNTs for SPECT imaging was presented, which is a very common and clinically used technique for studying the pharmacological properties of biomaterials since it relies on long-lived radionuclides and low-cost gamma cameras. However, SPECT has several disadvantages as a radiolabeling method such as low-resolution images and the presence of Tc or Re complexes, which may interact with the biological systems and interfere in the *in vivo* studies leading to undesirable side effects. PET imaging technique in contrast uses radionuclides that cause minimal disturbance and interference with the biological systems, as well produces high-resolution images.[18] To take advantage of these features and to provide another radiolabeling method of RNTs for *in vivo* studies, this section presents a radiolabeling strategy of RNTs with *p*-fluorobenzoate for PET imaging technique.

3.3.1 Materials Design

In order to construct G∧C motifs that can be coupled with *p*-fluorobenzoate in one step prior to self-assembly, two twin-G∧C motifs functionalized with terminal primary amino groups were considered. The first motif is functionalized with aminobutyl group, and is called TB-AB (**3.23**) (Figure 3.18A). This motif has good solubility in water due to the presence of the amino group. However, upon coupling with *p*-fluorobenzoate, the amino group will be capped, which may decrease the solubility of this motif in water. Therefore, another twin-G∧C motif, which is functionalized with PEG_3-propylamine chain (called TB-PEG_3-NH_2 (**3.24**)) was considered (Figure 3.18B). Due to the presence of the triethylene glycol spacer, this motif has better solubility in water even after coupling with *p*-fluorobenzoate.

A

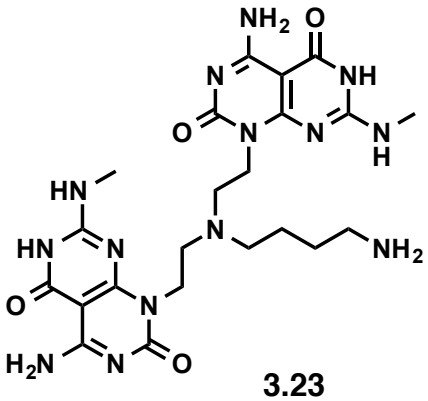

3.23

B

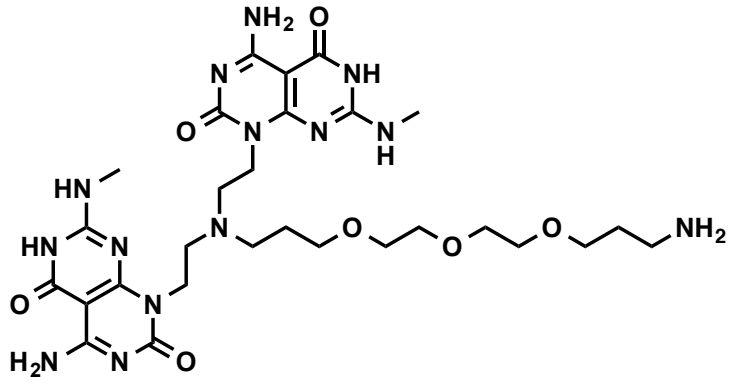

3.24

Figure 3.18. The chemical structures of the (A) twin G∧C-butylamine (TB-BA) motif (**3.23**); and (B) twin G∧C-PEG_3-propylamine (TB-PEG_3-NH_2) motif (**3.24**).

3.3.2 Synthesis

3.3.2.1 The TB-BA motif

TB-BA motif **3.23** was synthesized by a former group member in two steps using the procedure that is shown in Figure 3.19.

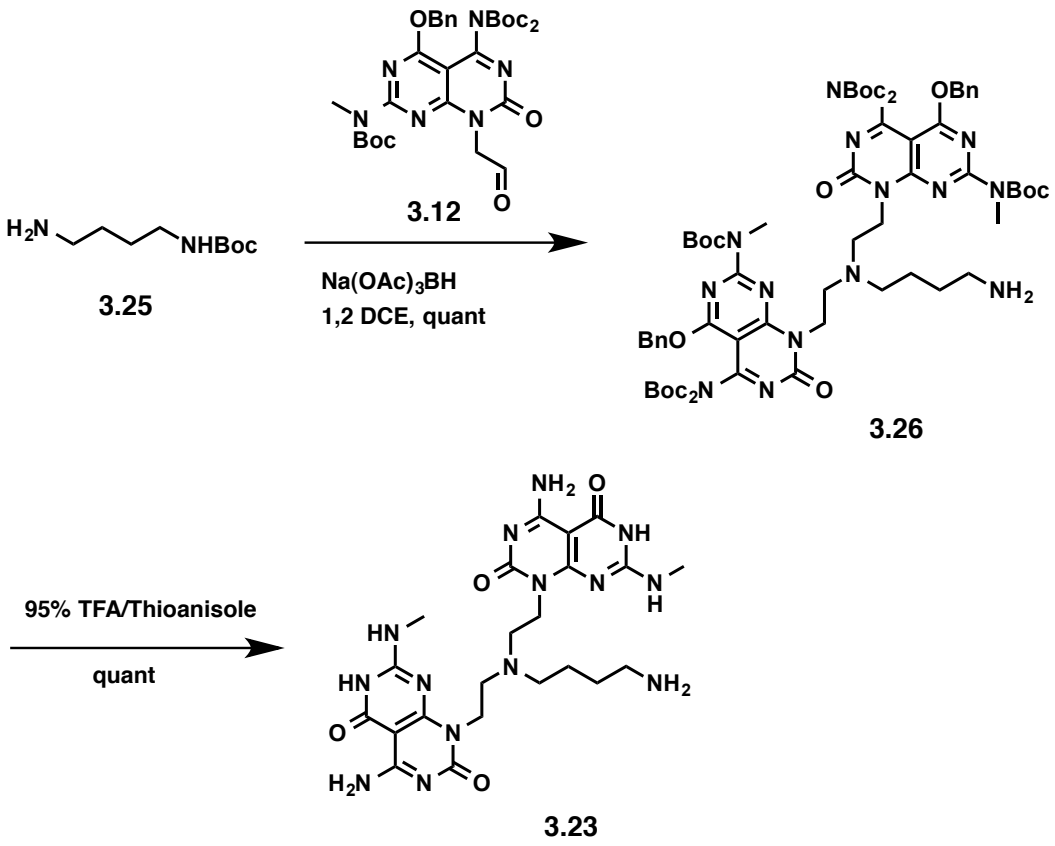

Figure 3.19. Synthetic procedure of the TB-BA motif (**3.23**).

To couple **3.23** with *p*-fluorobenzoate, succinimide *p*-fluorobenzoate (SFB) reagent was used. Ideally, the coupling reaction should be rapid (favorably within 30 min) and quantitative in order to avoid the need for HPLC purification since the half-life of the radioactive ^{18}F isotope is only 110 min (Table 3.2). Several coupling conditions were examined using borate buffer (pH 8.5) at 45°C in ACN[35], DMF, or DMSO solvents. However, in all attempts only starting material was recovered and no product was obtained even after adding up to 2 eq of SFB and long reaction times (Figure 3.20).

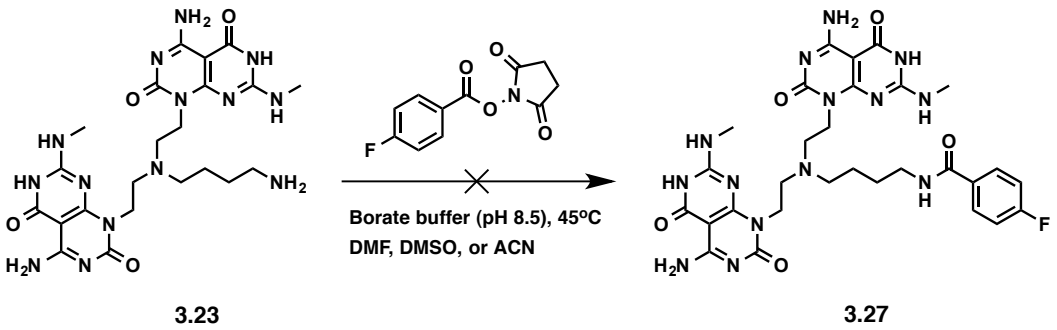

Figure 3.20. Unsuccessful coupling reactions of **3.23** with SFB.

In further attempts, the coupling reaction of compound **3.23** with SFB was repeated in DMSO and DMF using DIPEA as a base. In these trials, **3.23** and DIPEA were dissolved in DMSO or DMF while stirring in oil bath at 50°C, then a solution of SFB (1.5 eq) in DMSO or DMF respectively, was added dropwise over one minute. Monitoring the reaction in DMSO over time revealed the formation of 50% of the coupled product **3.27**, which did not increase over time. On the other hand, very little product (<10%) was found in DMF (Figure 3.21) (Table 3.5).

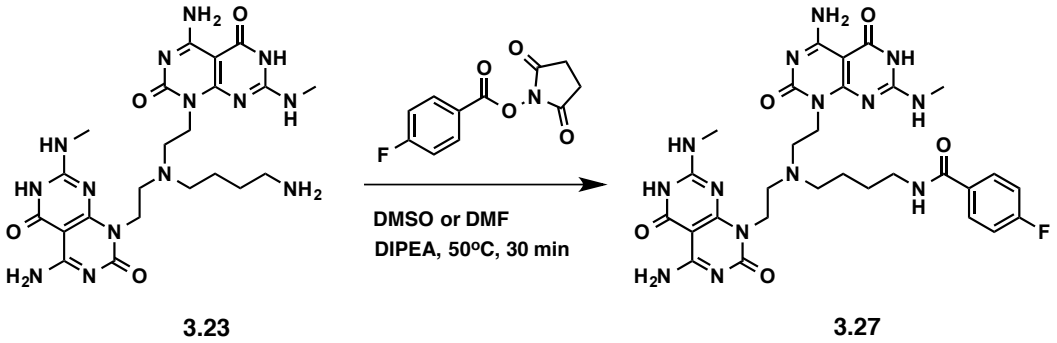

Figure 3.21. Successful coupling conditions of compound **3.23** with SFB.

Table 3.5. Coupling conditions of compound **3.23** with SFB.

Solvent	Base	T°C	Result 3.27/3.23
DMSO	DIPEA (6 eq)	50	50/50
DMF	DIPEA (6 eq)	50	10/90

Although 1.5 eq of SFB was added in the previous reactions, no complete coupling was obtained. Therefore, the reaction was further attempted in DMSO using conditions that are summarized in Table 3.6. Unfortunately, no more than 60% conversion was obtained even after long reactions time (more than two hours).

Table 3.6. Trials of the coupling reaction of **3.23** with SFB in DMSO.

Eq of SFB	Eq of DIPEA	T°C	Concentration of 3.23 (mg/ml)	Result: 3.27/3.23
1.5	10	50	10	60/40
1.5	10	50	5	50/50
1.5	10	50	5	50/50
2	5	50	2	50/50
2	15	50	2	50/50
5	10	50	1	60/40
10	10	60	0.5	60/40

It was then reasoned that it would be difficult to achieve complete conversion of **3.23** into the coupled product **3.27** within one hour. The reason I believe is because the free amino group in **3.23** is adjacent to the twin-G∧C motif, and thus the coupling reaction is sterically hindered.

3.3.2.1 The TB-PEG$_3$-NH$_2$ Motif

In order to overcome the steric problem in TB-BA motif **3.23**, TB-PEG$_3$-NH$_2$ motif **3.24** was prepared, which featured a long spacer consisting of triethylene

glycol chain between the twin-G∧C motif and the primary amino group. In addition to the less steric hindrance, the presence of the triethylene glycol spacer increases the solubility of motif **3.24** in water compared to **3.23**.

To synthesize **3.24**, mono Boc protected di-propylamine triethylene oxide **3.28** spacer was first prepared by reacting the commercially available di-propylamine triethylene oxide with Boc_2O in 1,4-dioxane in 66% yield. Compound **3.28** was then reacted with the protected G∧C base aldehyde **3.12** in the presence of $NaBH(OAc)_3$ to provide compound **3.29** in 70% yield. Deprotection of **3.29** under TFA/Thioanisole acidic conditions then led to motif **3.24** in 67% yield (Figure 3.22).

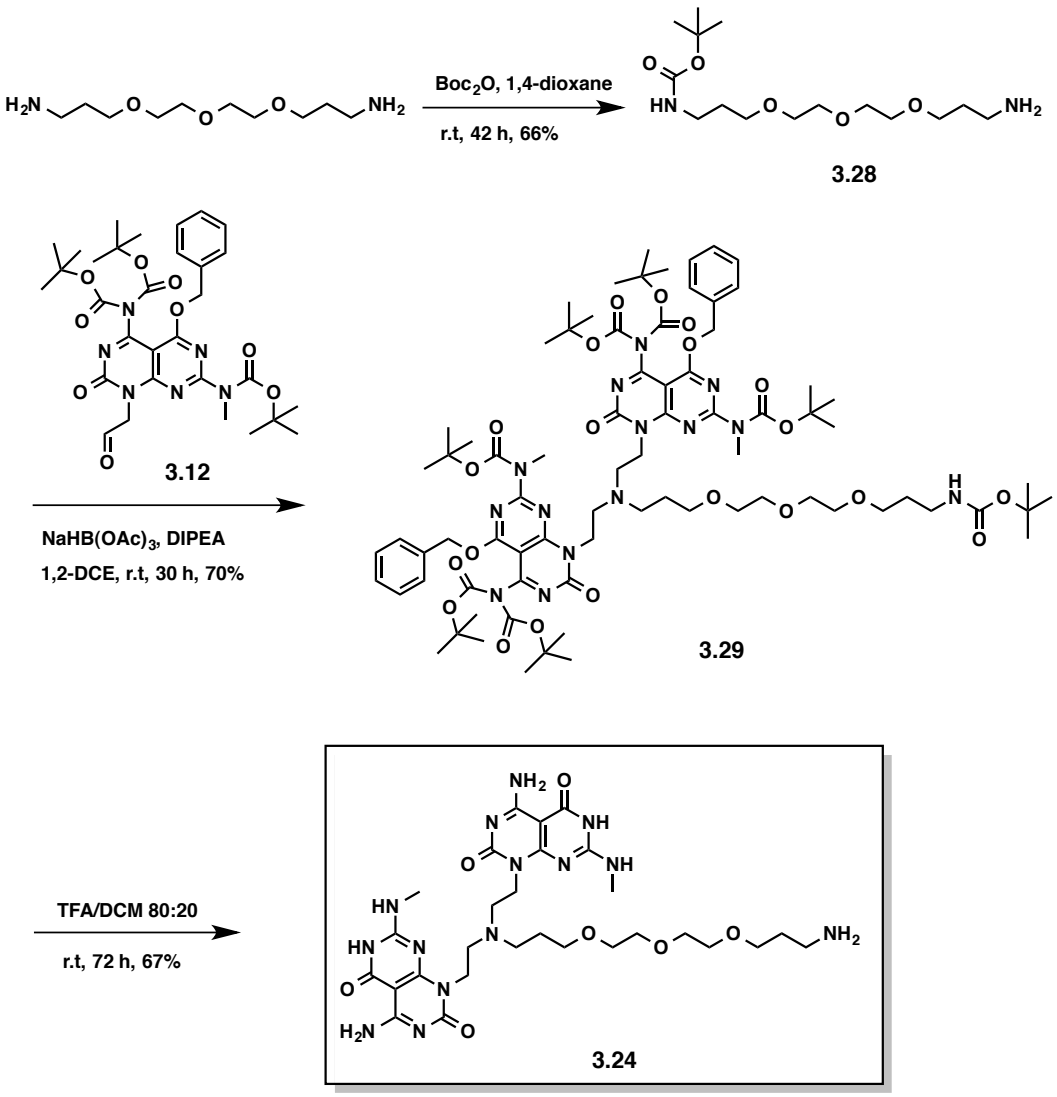

Figure 3.22. Synthetic procedure of motif **3.24**.

With compound **3.24** in hand, coupling reaction with SFB was then investigated using the procedure that was developed for **3.23** motif (Table 3.6). Motif **3.24** was initially mixed with DIPEA (10 eq) in DMSO and stirred in an oil bath at 40°C, SFB (1.5 eq) solution in DMSO was then added dropwise over one minute, and then the mixture was stirred at 40°C for 5-10 min. Under these conditions, compound **3.24** had completely converted to the coupled product **3.30** as revealed by the mass and ^{1}H NMR analyses (Figure 3.23). Diethyl ether was then added and a white precipitate formed, which was centrifuged and washed two times with

diethyl ether. Careful analysis of compound **3.30** by low- and high-resolution mass, and ^{1}H and ^{13}C NMR, revealed that the compound was very pure and did not need HPLC purification as well the yield of the reaction was found to be 75%. It turned out that the presence of DIPEA in the medium was essential as no reaction occurred in the absence of the base. Heating in an oil bath at 40°C was also important since it was found that the reaction took more than 24 h when it was carried out at room temperature.

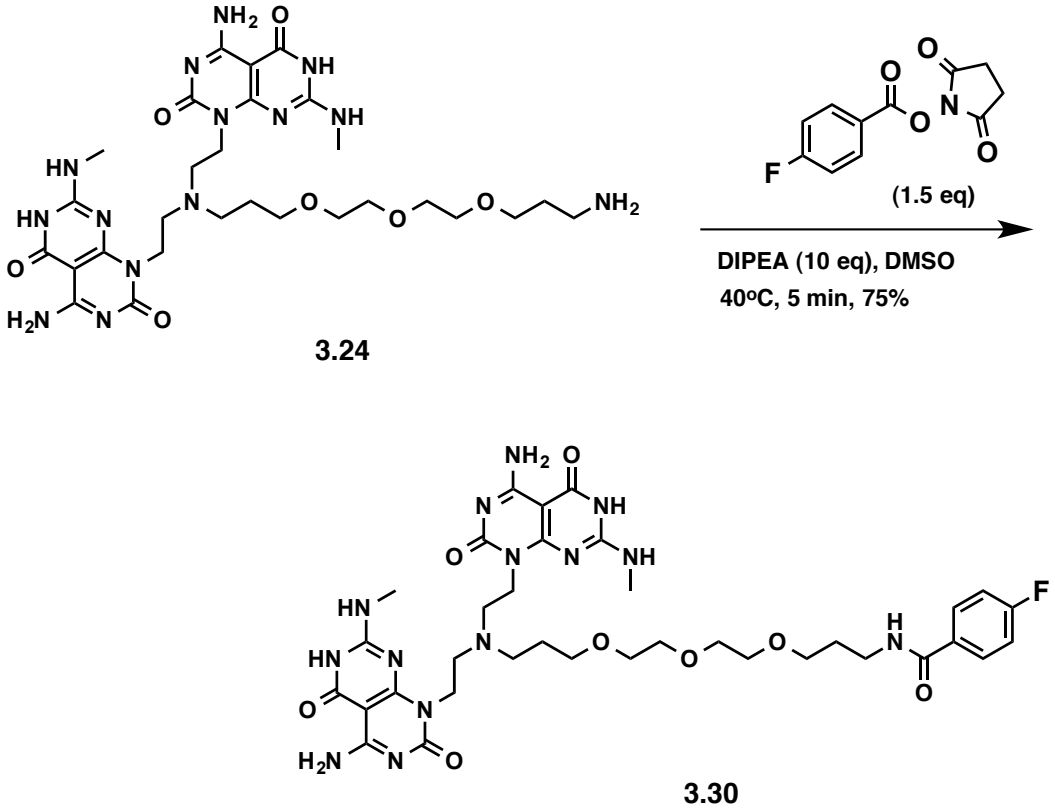

Figure 3.23. Coupling reaction of compound **3.24** with SFB.

Having successfully obtained complete coupling of **3.24** with SFB, premade mixtures of compounds **3.24** and **3.30** were also considered for the co-assembly studies. Using the same reaction conditions described in Figure 3.23 but adding 0.5 and 0.25 eq of SFB, solid mixtures containing 1:1 and 1:3 of **3.30** and **3.24**,

respectively were obtained. The amounts of the two compounds in the mixtures were verified by ^{1}H NMR and mass analyses.

3.3.3 Self- and Co-Assembly Studies[†††]

After the coupling reaction of **3.24** with SFB, the next step in the radiolabeling strategy was the self-assembly of **3.30** into RNTs within the half-life of the ^{18}F radionuclide. To investigate the self-assembly of compounds **3.24** and **3.30**, stock solutions of 1 mg/ml in water were prepared and subjected to three cycles of heating in an oil bath at 40°C for 5 min then sonication for 3 min. SEM grids were prepared after 1.5h of aging at room temperature. Motif **3.24** was readily soluble in water, and its analysis by SEM revealed well-dispersed RNTs (Figure 3.24 A,B). **3.30** on the other hand formed a cloudy solution at room temperature, which contained large bundles of RNTs as found by the SEM analysis of the cotton-filtered solution (Figure 3.24 C,D). To obtain a clear solution, the cotton-filtered solution of **3.30** was filtered using a 0.45 μm frit, but the bundles of RNTs were completely removed during the filtration (Figure 3.24 E,F). In order to increase the solubility of **3.30** in water, it was dissolved in a mixture of water and 5% DMSO and then subjected to triple cycles of sonication and heating at 40°C. Although **3.30** was more soluble in the presence of DMSO (no precipitation), the solution was still cloudy even after cotton filtration, and no RNTs were found (Figure 3.24 G,H).

[†††] SEM imaging was done with the help of Dr. Jae-Young Cho.

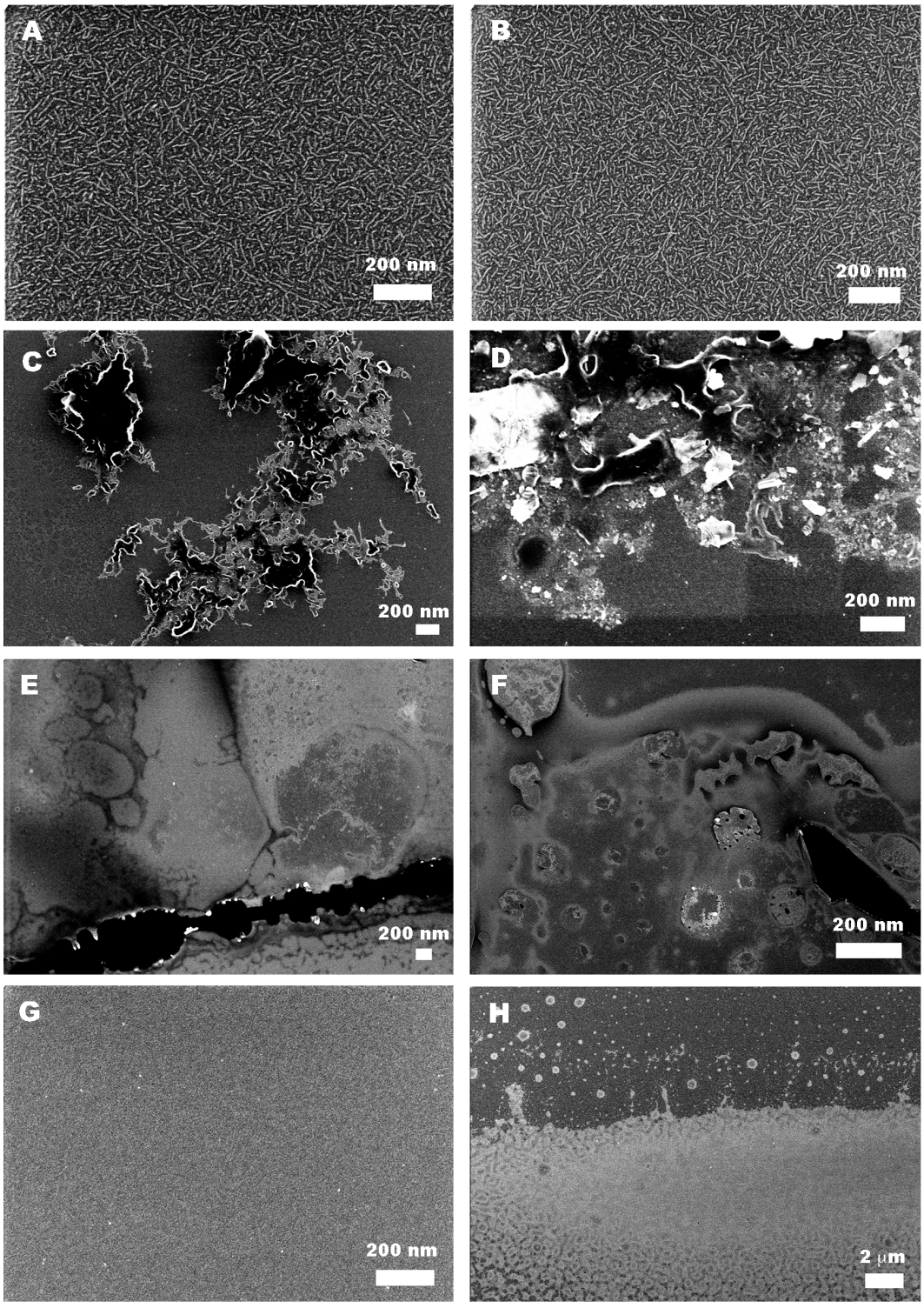

Figure 3.24. (A,B) SEM images of **3.24** (0.1 mg/ml) in water after 1.5h of aging; (C,D) SEM images of the cotton-filtered solution of **3.30** (0.1 mg/ml) in water after 1.5h of aging; (E,F) SEM images of the 0.45 μm frit-filtered **3.30** solution

(0.1 mg/ml) in water after 1.5h of aging; and (G,H) SEM images of the cotton-filtered solution of **3.30** (0.1 mg/ml) in water + 5% DMSO after 1.5h of aging.

As a means to solubilize compound **3.30** in water, a co-assembly strategy with **3.24** was next examined. The pre-synthesized 1:1 and 1:3 mixtures of **3.30**:**3.24** (described in section 3.3.2) were dissolved in water and subjected to triple cycles of heating in an oil bath at 40°C for 5 min then sonication for 3 min. SEM grids were prepared after 1.5h of aging at room temperature. The SEM analysis of the 1:1 mixture revealed bundles of RNTs and other unidentified random aggregates, and the solution was cloudy even after cotton filtration. This indicated that compound **3.30** was not fully co-assembled and the 1:1 mixture cannot be used for the radiolabeling studies (Figure 3.25 A,B). The 1:3 mixture on the other hand, formed a clear solution after heating and sonication and contained well-dispersed RNTs (Figure 3.25 C,D) having very similar morphology to the RNTs formed by **3.24** motif alone (Figure 3.24 A,B). This indicated that at least 75% of **3.24** was needed to solubilize **3.30** in water and to obtain co-assembled RNTs, which can be used for the radiolabeling studies.

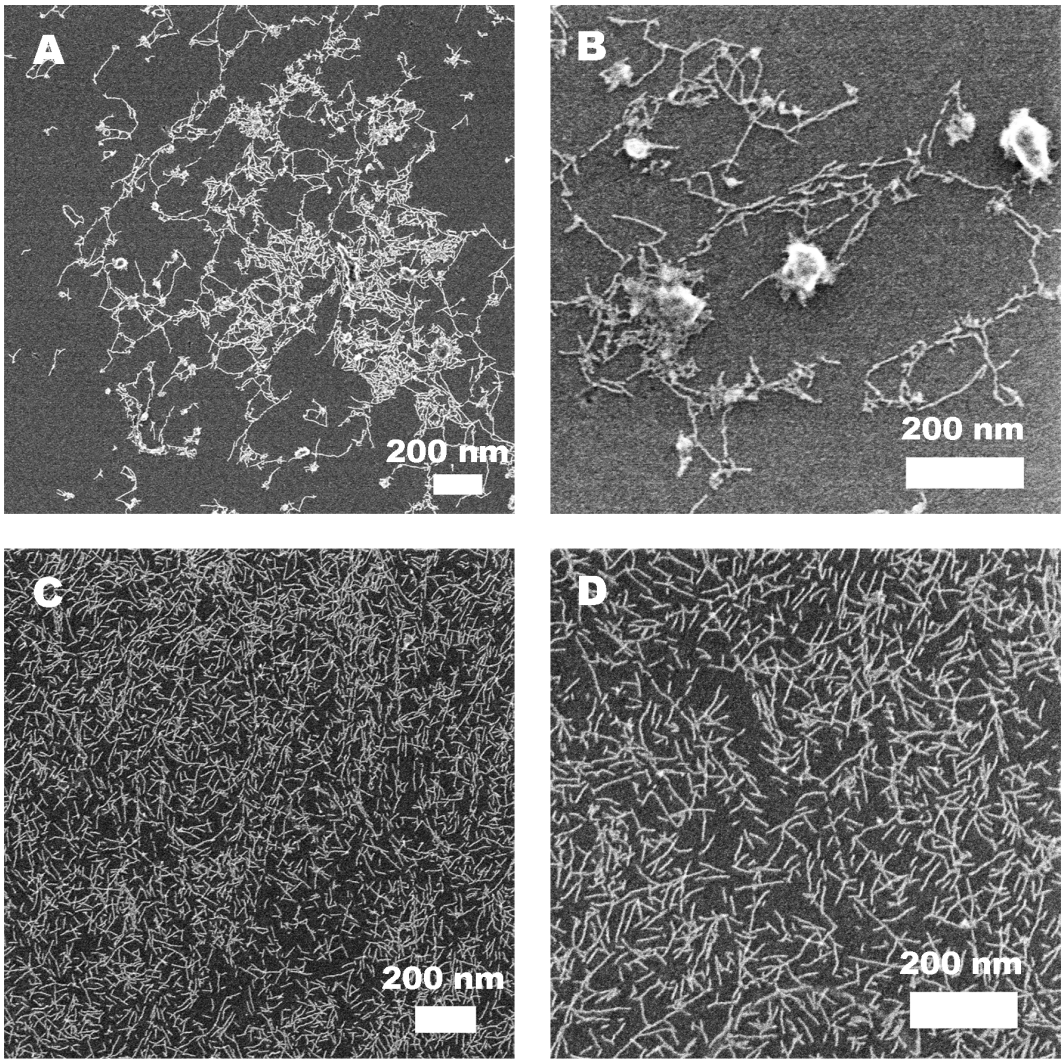

Figure 3.25. (A,B) SEM images of 1:1 mixture of **3.30:3.24** (0.1 mg/ml) in water after 1.5h of aging; (C,D) SEM images of 1:3 mixture of **3.30:3.24** (0.1 mg/ml) in water after 1.5h of aging.

3.3.4 Experimental

3.3.4.1 Self- and Co-assembly Procedures

Stock solutions of 1 mg/ml were prepared by dissolving the solids in water. Triple cycles of heating in oil bath at 40°C for 5 min then sonication for 3 min were then applied. The solutions were then left at room temperature for aging.

3.3.4.2 SEM Imaging

Aliquots of the stock solutions (0.1 mg/ml) in water were diluted a final concentration of 0.1 mg/ml. The SEM grids were prepared by depositing a droplet of the diluted solutions on a carbon-coated 400-mesh copper grid (Electron Microscopy Sciences) for 10 seconds before blotting the grid using filter paper. SEM images were obtained without negative staining at 10-30 kV accelerating voltage, 20 μA and a working distance of 5-8 mm using a high resolution Hitachi S–4800 cold field emission SEM.

3.3.4.3 General Methods

All reagent grade solvents were purified using a solvent purification system. All NMR characterizations were performed on a 600 MHz NMR with the solvents indicated used as internal references. The NMR data is presented as follows: chemical shift, multiplicity, coupling constant and integration.

3.3.4.4 Compounds Synthesis and Characterization

Compound 3.28

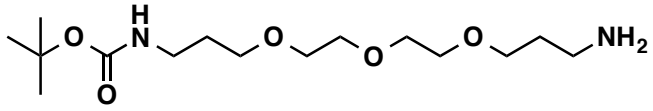

A solution of 4,7,10-trioxa-1,13-tridecanediamine (20 g, 90.78 mmol) in 1,4-dioxane (130 mL) was treated with Boc-anhydride (2.47 g, 11.34 mmol). The mixture was stirred at room temperature for 42 h. The solvent was removed, and the resulting yellow oil was purified by silica gel flash chromatography (2-10% MeOH in CH_2Cl_2) to produce the oil **3.28** in 66% ($C_{15}H_{33}N_2O_5$, 2.38 g) yield.

High-resolution Positive ESI-MS: Expected for $[M+H]^+/z$, 321.2384. Observed 321.2372.

^{1}H-NMR (600 MHz, CD_2Cl_2) δ (ppm): 5.1 (s, 1H), 3.64-3.51 (m, 12H), 3.21 (d, *J* = 6.9 Hz, 2H), 2.79 (t, *J* = 8 Hz, 2H), 1.76-1.69 (m, 4H), 1.52 (s, 2H), 1.42 (s, 9H).

^{13}C-NMR (150 MHz, CD_2Cl_2) δ (ppm): 155.0, 69.2, 68.9, 66.7, 48.0, 37.6, 30.4, 28.6, 27.3. Each of the signals 69.2, 66.7, and 68.9 had two overlapping signals.

Compound 3.29

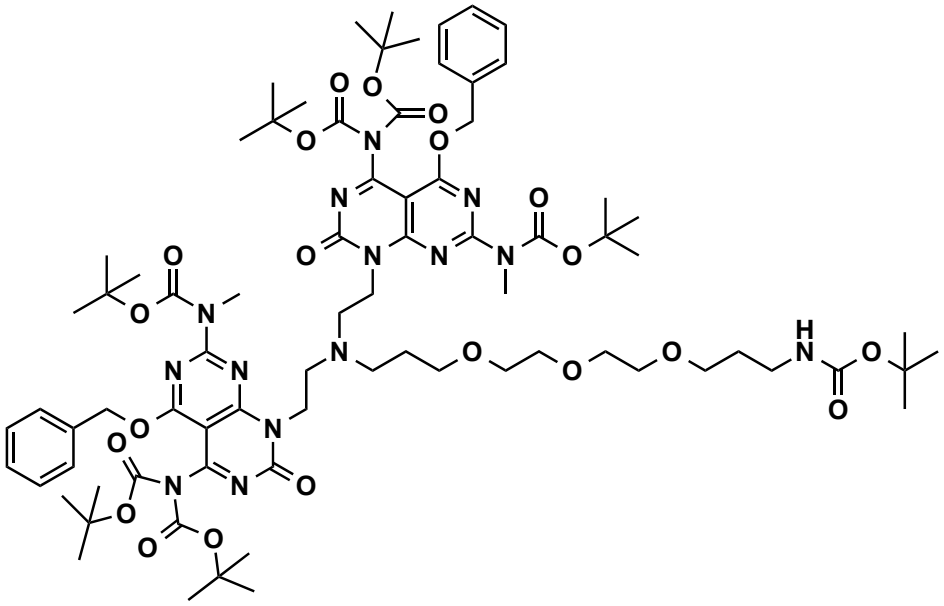

To a stirred solution of compound **3.28** (0.054 g, 0.168 mmol) and DIEA (0.088 mL, 0.5 mmol) in 1,2 DCE (6 mL), the aldehyde **3.12** (0.214 g, 0.34 mmol) was added at room temperature under N_2. The solution was stirred for 30 min before sodium triacetoxy borohydride (0.170 g, 0.8 mmol) was added and the resulting mixture was stirred for an additional 20h. Aldehyde **3.12** (0.107 g, 0.168 mmol) and sodium triacetoxy borohydride (0.085 g, 0.4 mmol) were then added to the

mixture and stirred for another 6 h. The reaction mixture was diluted with DCM (50 mL) and then washed with water (20 mL), citric acid 10% (30 mL), $NaHCO_3$ 5% (30 mL), brine (20 mL), dried over Na_2SO_4 and concentrated. Flash chromatography of the residue over alumina gel (60-90% EtOAc in hexanes) gave **3.29** ($C_{77}H_{112}N_{14}Na_2O_{21}$, 185 mg, 70%) as a pale yellow oil.

High-res ESI-MS (positive): Expected for $[M+2Na^{+2}]/z$, 807.3955. Observed, 807.3956.

^{1}H-NMR (600 MHz, CD_2Cl_2) δ (ppm): 7.47-7.33 (m, 10H), 5.58 (s, 4H), 5.07 (br, 1H, NH), 4.38 (t, *J* = 7.2 Hz, 4H), 3.61-3.57 (m, 4H), 3.55-3.53 (m, 4H), 3.52-3.46 (s, 10H), 3.18-3.15 (m, 2H), 2.89 (t, *J* = 7.8 Hz, 4H), 2.77 (t, *J* = 7.2 Hz, 2H), 1.75-1.69 (m, 4H), 1.55 (s, 18H), 1.40 (m, 9H), 1.33 (s, 36H).

^{13}C-NMR (150 MHz, CD_2Cl_2) δ (ppm): 166.1, 161.8, 161.6, 160.8, 156.3, 155.9, 153.1, 149.8, 135.8, 129.0, 128.9, 93.2, 84.0, 83.2, 71.05, 71.01, 70.75, 70.7, 70.4, 69.9, 69.6, 51.7, 51.5, 41.9, 39.1, 35.4, 30.6, 30.3, 28.7, 28.6, 28.4, 28.3, 28.2, 28.1.

Compound 3.24

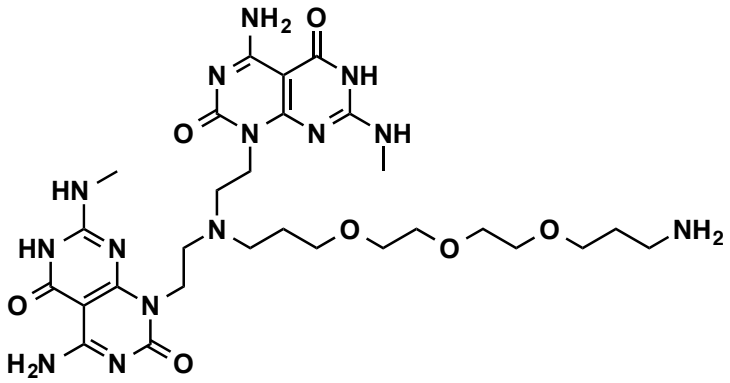

Compound **3.29** (0.194 g, 0.126 mmol) was stirred in a solution of TFA (8 mL) and DCM (2 mL) for 72 h. Et_2O (60 mL) was then added to the reaction mixture

and the white precipitate formed, was centrifuged down. The residual solid was resuspended in Et_2O, sonicated and centrifuged down. This process was repeated until the spotting of the Et_2O produced no UV active spot. The white solid was dried under vacuum for 72 h to yield the desired compound **3.24** ($C_{28}H_{45}N_{14}O_7$, 0.095 g, 67%).

High-res MALDI-MS (positive): Expected for $[M+H]^+/z$, 689.359. Observed 689.3592.

^{1}H-NMR (600 MHz, TFA-d) δ (ppm): 6.79 (br, 2H, NH_2), 4.79-4.58 (m, 4H), 3.92-3.68 (m, 18H), 3.38-3.34 (m, 2H), 3.15-3.12 (m, 6H), 2.18-2.17 (m, 2H), 2.06-2.03 (m, 2H).

^{13}C-NMR (150 MHz, D_2O / TFA-d) δ (ppm): 163.6, 162.6, 157.9, 157.6, 151.3, 84.2, 71.4, 71.2, 71.2, 71.1, 71.0, 69.4, 54.6, 53.6, 41.4, 38.8, 29.1 , 27.7, 24.8.

Elemental analysis: Calculated for [M + 3.5TFA + 1.7H_2O], C: 37.68, H: 4.61, N: 17.62, found C: 37.47, H: 4.39, N: 17.89.

Compound 3.30

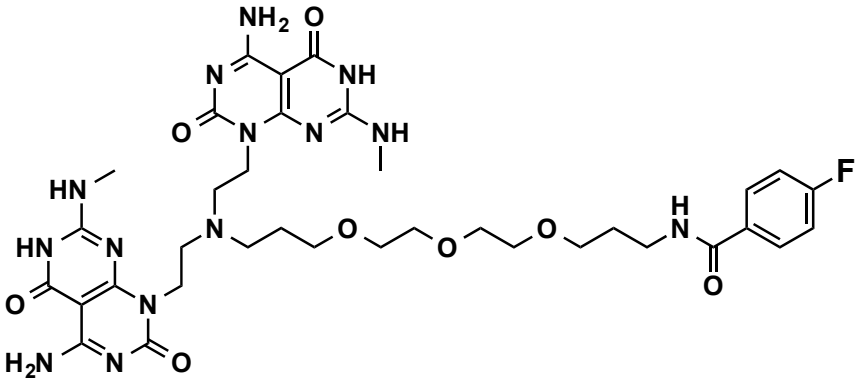

To a solution of compound **3.24** (30 mg, 0.027 mmol) in DMSO (15 mL), succinimidyl fluorobenzoate (SFB) (13 mg, 0.054 mmol) and DIPEA (47 µl, 0.27 mmol) were added, and the mixture was stirred at 40°C for 5 min. Diethyl ether

(20 mL) was then added, and the white precipitate (compound **3.30**) was isolated and washed with diethyl ether for 2 times in a centrifuge tube. After drying under vacuum at 40°C for 2 days, compound **3.30** ($C_{35}H_{47}FN_{14}O_8$, 19 mg) was obtained in 75% yield.

High-res MALDI-MS (positive): Expected for $[M+H]^+/z$, 811.8574. Observed 811.3755.

^{1}H-NMR (600 MHz, TFA-d) δ (ppm): 7.84 (br, 2H), 7.21 (m, 2H), 4.85-4.70 (m, 4H), 3.90-3.75 (m, 18H), 3.20-3.15 (m, 8H), 2.24-2.14 (m, 4H).

^{13}C-NMR (600 MHz, 90% DMSO-d_6 + 10% TFA-d) δ (ppm): 171.6, 166.8, 165.2, 163.3, 162.8, 162.3, 155.6, 155.3, 154.6, 149.5, 149.1, 129.7, 129.6, 82.0, 81.4, 69.0, 68.9, 68.8, 68.5, 68.3, 67.5, 67.4, 65.4, 52.3, 38.8, 37.0, 27.0, 26.9, 26.5, 22.6.

Elemental analysis: calcd for [M + 0.9TFA + 1.5H_2O], C: 47.00, H: 5.46, N: 21.85. Found C: 46.71, H: 5.31, N: 21.46.

3.4 Conclusions

For the goal of facilitating the *in vitro* and *in vivo* studies and understanding the pharmacological properties of rosette nanotubes (RNTs), in this chapter I developed two radiolabeling strategies of RNTs for single photon emission computed tomography (SPECT) and positron emission tomography (PET) imaging techniques. For SPECT imaging, two twin-G∧C motifs were developed which are functionalized with LGGGC pentapeptide and mercaptoacetyl triglycine (MAG_3) ligands respectively. While the latter was successfully chelated with cold rhenium (Re) metal in 30 min to form TB-MAG_3-ReO complex **3.4**, the former failed to form Re complex due to its low solubility in water and unsuccessful HPLC purification. The self-assembly process of complex **3.4** was investigated in water at physiological conditions using UV-Vis, SEM, TEM and AFM techniques. The resulting RNTs' diameter was measured to be 4.7 ± 0.4 nm

in agreement with the molecular modeling calculations of 4.7 nm. Overall, the chelation, purification, and self-assembly of complex **3.4** were optimized to occur within the half-life of the radioactive $^{186/188}$Re radionuclide.

For PET imaging however, two twin-G∧C motifs functionalized with free primary amino groups were developed. A TB-AB (**3.23**) motif featuring twin-G∧C functionalized with aminobutyl group, and a more water-soluble TB-PEG_3-NH_2 (**3.24**) motif featuring twin-G∧C functionalized with PEG_3-propylamine chain, were developed. Given that the latter motif features less steric hindrance around the amino group, it was successfully coupled with succinimide *p*-fluorobenzoate (SFB) in 5 min. Although the coupled product **3.30** did not form RNTs due to its low solubility in water, co-assembly approach with 75% of motif **3.24** gave well-dispersed co-assembled RNTs. Finally, the coupling with SFB, the purification, and the self- or co-assembly of **3.30** were optimized within the half-life of the radioactive ^{18}F radionuclide.

3.5 References

(1) Fenniri, H.; Deng, B.-L.; Ribbe, A. E.; Hallenga, K.; Jacob, J.; Thiyagarajan, P. *Proc. Natl. Acad. Sci. U.S.A.* **2002**, *99 Suppl 2*, 6487–6492.

(2) Zhang, L.; Rodriguez, J.; Raez, J.; Myles, A. J.; Fenniri, H.; Webster, T. J. *Nanotechnology* **2009**, *20*, 175101–175113.

(3) Lin Chun, A.; Moralez, J. G.; Webster, T. J.; Fenniri, H. *Biomaterials* **2005**, *26*, 7304–7309.

(4) Suri, S. S.; Rakotondradany, F.; Myles, A. J.; Fenniri, H.; Singh, B. *Biomaterials* **2009**, *30*, 3084–3090.

(5) Fenniri, H.; Mathivanan, P.; Vidale, K. L.; Sherman, D. M.; Hallenga, K.; Wood, K. V.; Stowell, J. G. *J. Am. Chem. Soc.* **2001**, *123*, 3854–3855.

(6) Zhang, L.; Rakotondradany, F.; Myles, A. J.; Fenniri, H.; Webster, T. J. *Biomaterials* **2009**, *30*, 1309–1320.

(7) Fine, E.; Zhang, L.; Fenniri, H.; Webster, T. J. *Int. J. Nanomed.* **2009**, *4*, 91–97.

(8) Alsbaiee, A.; Beingessner, R. L.; Fenniri, H. "Self-assembled nanomaterials for tissue engineering"; In "Nanomedicine: Technologies and Applications", Webster T J (ed). Woodhead Publishing Ltd, Cambridge, UK, **2012**, *Ch. 17*, pp. 490-533

(9) Borzsonyi, G.; Johnson, R. S.; Myles, A. J.; Cho, J.-Y.; Yamazaki, T.; Beingessner, R. L.; Kovalenko, A.; Fenniri, H. *Chem. Commun.* **2010**, *46*, 6527–6529.

(10) Borzsonyi, G.; Alsbaiee, A.; Beingessner, R. L.; Fenniri, H. *J. Org. Chem.* **2010**, *75*, 7233–7239.

(11) Moralez, J. G.; Raez, J.; Yamazaki, T.; Motkuri, R. K.; Kovalenko, A.; Fenniri, H. *J. Am. Chem. Soc.* **2005**, *127*, 8307–8309.

(12) Borzsonyi, G.; Beingessner, R. L.; Yamazaki, T.; Cho, J.-Y.; Myles, A. J.; Malac, M.; Egerton, R.; Kawasaki, M.; Ishizuka, K.; Kovalenko, A.; Fenniri, H. *J. Am. Chem. Soc.* **2010**, *132*, 15136–15139.

(13) Chen, Y.; Song, S.; Yan, Z.; Fenniri, H.; Webster, T. J. *Int. J. Nanomed.* **2011**, 1035–1044.

(14) Song, S.; Chen, Y.; Yan, Z.; Fenniri, H.; Webster, T. J. *Int. J. Nanomed.* **2011**, 101–107.

(15) Journeay, W. S.; Suri, S. S.; Moralez, J. G.; Fenniri, H.; Singh, B. *Small* **2008**, *4*, 817–823.

(16) Journeay, W. S.; Suri, S. S.; Moralez, J. G.; Fenniri, H.; Singh, B. *Small* **2009**, *5*, 1446–1452.

(17) Journeay, W. S.; Suri, S. S.; Moralez, J. G.; Fenniri, H.; Singh, B. *Int. J. Nanomed.* **2008**, *3*, 373–383.

(18) Pimlott, S. L.; Sutherland, A. *Chem. Soc. Rev.* **2010**, *40*, 149.

(19) Ametamey, S. M.; Honer, M.; Schubiger, P. A. *Chem. Rev.* **2008**, *108*, 1501–1516.

(20) R Dilworth, J.; J Parrott, S. *Chem. Soc. Rev.* **1998**, *27*, 43-55.

(21) Colton, R.; Peacock, R. D. *Q. Rev., Chem. Soc.* **1962**, *16*, 299-315.

(22) Guhlke, S.; Schaffland, A.; Zamora, P. O.; Sartor, J.; Diekmann, D.; Bender, H.; Knapp, F. F.; Biersack, H. J. *Nucl. Med. Biol.* **1998**, *25*, 621–631.

(23) Jankowsky, R.; Kirsch, S.; Reich, T.; Spies, H.; Johannsen, B. *J. Inorg. Biochem.* **1998**, *70*, 99–106.

(24) Hansen, L.; Cini, R.; Taylor, A.; Marzilli, L. G. *Inorg. Chem.* **1992**, *31*, 2801–2808.

(25) Ferro-Flores, G.; Ramírez, F. D. M.; Martínez-mendoza, M. G.; Murphy, C. A. de; Pedraza-lópez, M.; García-salinas, L. *J. Radioanal. Nucl. Chem.* **2002**, *251*, 7–13.

(26) Reyes, L.; Navarrete, M. *J. Radioanal. Nucl. Chem.* **2002**, *251*, 245–248.

(27) de Barros, A. L. B.; Cardoso, V. N.; Graças Mota, das, L.; Leite, E. A.; de Oliveira, M. C.; Alves, R. J. *Bioorg. Med. Chem. Lett.* **2010**, *20*, 2478–2480.

(28) de Barros, A. L. B.; Cardoso, V. N.; Graças Mota, das, L.; Leite, E. A.; de Oliveira, M. C.; Alves, R. J. *Bioorg. Med. Chem. Lett.* **2009**, *19*, 2497–2499.

(29) Kang, L.; Wang, R. F.; Yan, P.; Liu, M.; Zhang, C. L.; Yu, M. M.; Cui, Y. G.; Xu, X. J. *J. Nucl. Med.* **2010**, *51*, 978–986.

(30) Polyakov, V.; Sharma, V.; Dahlheimer, J. L.; Pica, C. M.; Luker, G. D.; Piwnica-Worms, D. *Bioconjugate Chem* **2000**, *11*, 762–771.

(31) Cheng, Z.; Chen, J.; Quinn, T. P.; Jurisson, S. S. *Cancer Res* **2004**, *64*, 1411–1418.

(32) Chen, J.; Cheng, Z.; Owen, N. K.; Hoffman, T. J.; Miao, Y.; Jurisson, S. S.; Quinn, T. P. *J. Nucl. Med.* **2001**, *42*, 1847–1855.

(33) Guggenberg, von, E.; Sader, J. A.; Wilson, J. S.; Shahhosseini, S.; Koslowsky, I.; Wuest, F.; Mercer, J. R. *Appl. Radiat. Isot.* **2009**, *67*, 1670–1675.

(34) Mäding, P.; Füchtner, F.; Wüst, F. *Appl. Radiat. Isot.* **2005**, *63*, 329–332.

(35) Hultsch, C.; Berndt, M.; Bergmann, R.; Wuest, F. *Appl. Radiat. Isot.* **2007**, *65*, 818–826.

(36) Richter, S.; Bergmann, R.; Pietzsch, J.; Ramenda, T.; Steinbach, J. R.; Wuest, F. *Biopolymers* **2009**, *92*, 479–488.

(37) HARTH FRITSCHY, E.; Cantacuzene, D. *J. Pept. Res.* **1997**, *50*, 415–420.

(38) Fritzberg, A. R.; Kasina, S.; Eshima, D.; Johnson, D. L. *J. Nucl. Med.* **1986**, *27*, 111–116.

(39) Alsbaiee, A.; Jules, M. S.; Beingessner, R. L.; Cho, J.-Y.; Yamazaki, T.; Fenniri, H. *Tet. Lett.* **2012**, *53*, 1645–1651.

(40) Riddoch, R. W.; Schaffer, P.; Valliant, J. F. *Bioconjugate Chem* **2006**, *17*, 226–235.

(41) Aufort, M.; Gonera, M.; Chaignon, N.; Le Clainche, L.; Dugave, C. *Eur. J. Med. Chem.* **2009**, *44*, 3394–3401.

(42) Zervas, L.; Photaki, I.; Ghelis, N. *J. Am. Chem. Soc.* **1963**, *85*, 1337–1341.

(43) Zamora, P. O.; Marek, M. J.; Knapp, F. F. *Appl. Radiat. Isot.* **1997**, *48*, 305–309.

(44) Yamazaki, T.; Fenniri, H.; Kovalenko, A. *Chemphyschem* **2010**, *11*, 361–367.

(45) Jorgensen, W. L.; Maxwell, D. S.; Tirado-Rives, J. *J. Am. Chem. Soc.* **1996**, *118*, 11225–11236.

(46) Grummon, G.; Rajagopalan, R.; Palenik, G. J. Inorg. *Chem.* **1995**, *34*, 1764-1772.

(47) Kaiser, E.; Bossinger, C. D.; Colescott, R. L.; Olsen, D. B. *Anal. Chim. Acta.* **1980**, *118*, 149–151.

Chapter 4

Towards Tetracyclic yG∧C Motif for Drug Delivery[‡‡‡]

4.1 Introduction

In the previous chapters, I developed peptide-functionalized rosette nanotubes (RNTs) for bone tissue engineering, and I presented two radiolabeling strategies of RNTs for *in vivo* biological studies.[1,2] I have thus demonstrated that RNTs have extensive functional group tolerance (stability) and exceptional control over the self-organization process, which is essential for biomedical applications. Not only can they be chemically modified on their outer surface, RNTs can also be structurally tuned to have dimensions (lengths, diameters) and properties that are suitable for incorporating hydrophobic drug molecules via non-covalent interactions for site-specific drug delivery applications. In this regards, it was demonstrated that RNTs that are formed by the bicyclic G∧C motif, which feature 1.1 nm inner diameter, have the potential to be loaded with a variety of hydrophobic anti-cancer drugs including dexamethasone and tamoxifen, and slowly release them in physiological media (Figure 4.1 A).[3,4] In order to extend the inner diameter of RNTs to 1.4 nm to encapsulate larger therapeutic agents, recently an extended tricyclic version of the G∧C base (called xG∧C), which had the same G and C H-bonding arrays but separated by a pyridine ring, was developed. The successful self-assembly of the xG∧C motif in organic and aqueous media to form stable RNTs was an impressive demonstration of the RNT's inner and outer diameter tunability through the synthetic modification of the G∧C unit (Figure 4.1 B).[5,6]

[‡‡‡] Part of this chapter is published in: Borzsonyi, G.; Alsbaiee, A.; Beingessner, R. L.; Fenniri, H. *J. Org. Chem.* **2010**, *75*, 7233-7239.

To test RNT's ability to tolerate further analogous expansion in the G∧C core and to further extend their inner diameter to 1.7 nm to encapsulate larger therapeutic agents, this chapter aims to develop a tetracyclic G∧C module (called yG∧C), which features the same peripheral G and C phases but separated by a naphthyridine core (Figure 4.1 C). Initially, the synthesis of an organic-soluble di-allyl yG∧C motif is described, and then its self-assembly in organic media to form RNTs is presented. Finally, progress towards the synthesis of a water-soluble di-lysine yG∧C motif is presented.

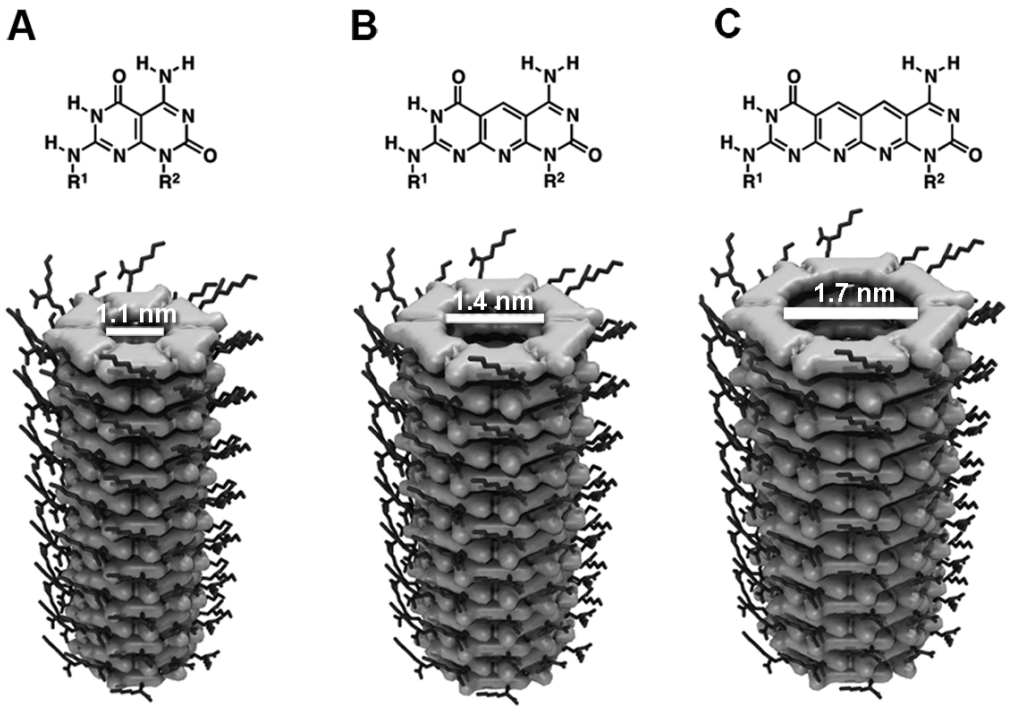

Figure 4.1. Self-complementary G∧C motifs from left to right: bicycle G∧C, tricycle xG∧C and tetracycle yG∧C and their self-assembly into RNTs with an inner diameter of 1.1 nm, 1.4 nm, and 1.7 nm, respectively.

4.2 Design of yG∧C

In earlier efforts to expand the bicyclic G∧C motif and therefore to extend the inner diameter of the RNTs, tricyclic xG∧C motif was developed in which a pyridine ring core was inserted between the G and C phase, while maintaining the 60° angle hydrogen bonding array of the G∧C motif.[5,6] In our design of a tetracyclic yG∧C motif, an expanded analog of the tricyclic xG∧C, a second pyridine ring was inserted between the G and C phases to maintain the molecule rigidity and planarity. Having the same 60° angle hydrogen bonding array of both G∧C and xG∧C motifs, yG∧C is expected to form hexameric supermacrocycles (rosettes) that define an extended inner space of 1.7 nm according to the modeling, which then π-π stack to form RNTs with 1.7 nm inner diameter.[7]

Organic soluble tetracyclic yG∧C motif, called di-allyl yG∧C, was designed having two peripheral allyl functional groups in order to increase its solubility in organic solvents. The appended allyl groups will also be used to functionalize this motif with hydrophilic molecules such as amino acids and peptides for biomedical applications (Figure 4.2).

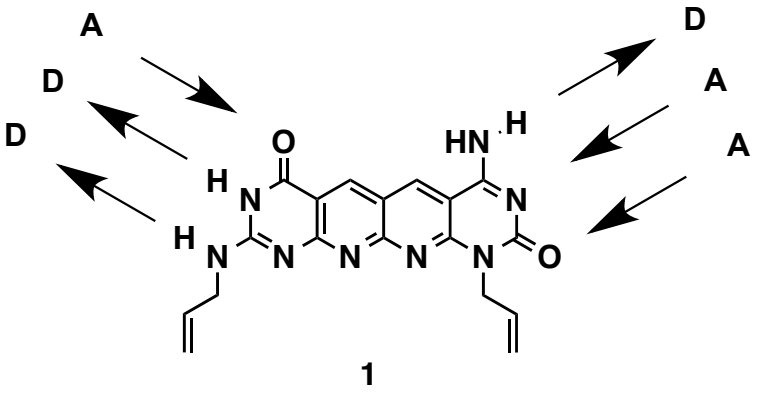

1

Figure 4.2. Di-allyl yG∧C motif. Arrows indicate the self-complementary H-bonding array of guanine and cytosine (A = H-bond acceptor, D = H-bond donor).

4.3 Proposed Synthetic Strategy

To synthesize di-allyl yG∧C motif **1**, I utilized the chemistry that was developed for the synthesis of the tricyclic di-allyl xG∧C and the mono-allyl yG∧C motifs.[6,7] Starting with the commercially available barbituric acid, my strategy aimed initially to prepare the tri-chloro substituted bicycle **2**, which would then be subjected to two consecutive aromatic substitution reactions (S_NAr) to provide the desired substitution pattern on the guanine ring. Next, the appended nitrile group would be converted to an aldehyde in order to install the second pyridine ring in the molecule (Figure 4.3).

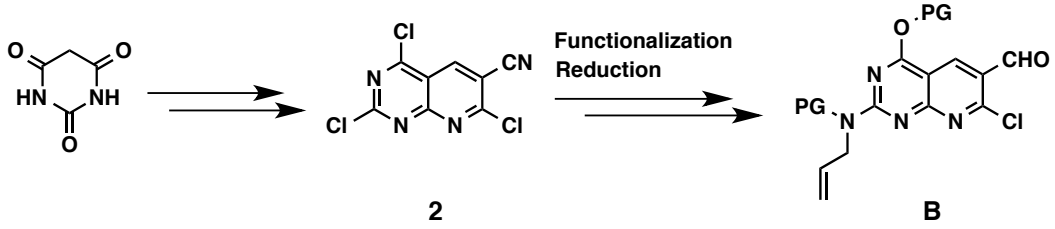

Figure 4.3. Proposed synthetic strategy of compound (**B**).

Two strategies were proposed to prepare the di-allyl tricyclic compound (**E**). The first strategy involved Knoevenagel condensation of compound (**B**) with malononitrile, followed with thermal cyclization (S_NAr mechanism) similar to that used earlier in the synthesis of bicycle **2**. Then S_NAr substitution reaction with allylamine would be employed to obtain compound (**E**) (Figure 4.4).

Strategy 1

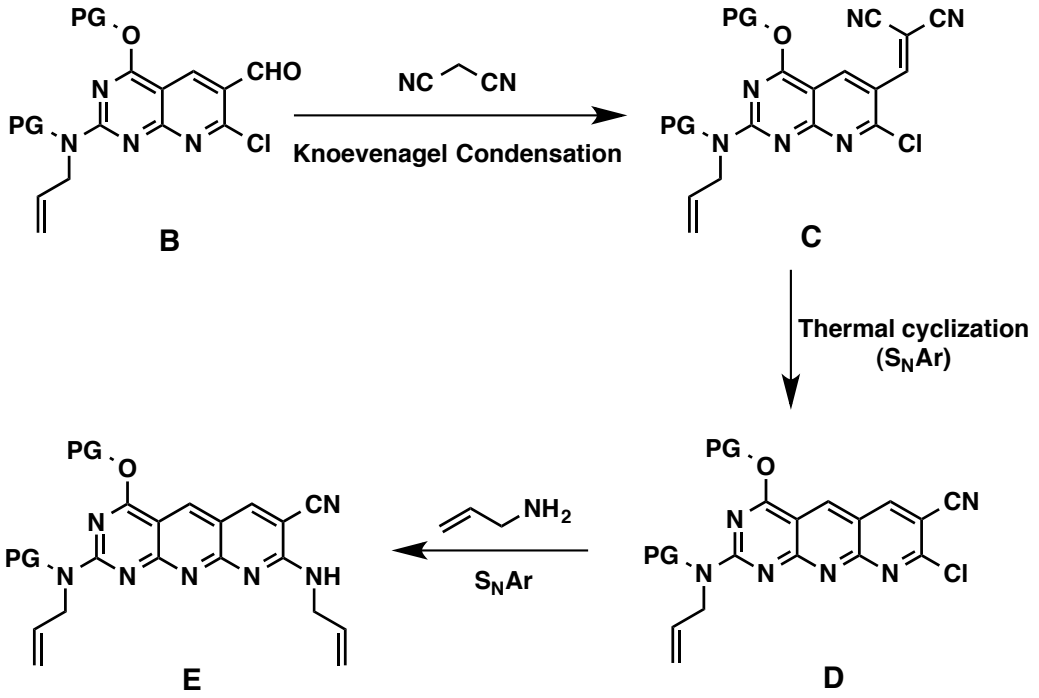

Figure 4.4. Proposed **Strategy 1** to install the second pyridine ring.

The second strategy however, begun with the displacement of chlorine in **B** with ammonia via S_NAr mechanism. Then the second pyridine ring would be constructed by condensation with malononitrile followed by base-induced cyclization (Friedländer reaction) according to the literature.[7] It would then be possible to functionalize the appended amino group in **G** with an allyl group using several approaches including S_N2, bi-phasic, reductive amination or S_NAr mechanisms (Figure 4.5).

Strategy 2

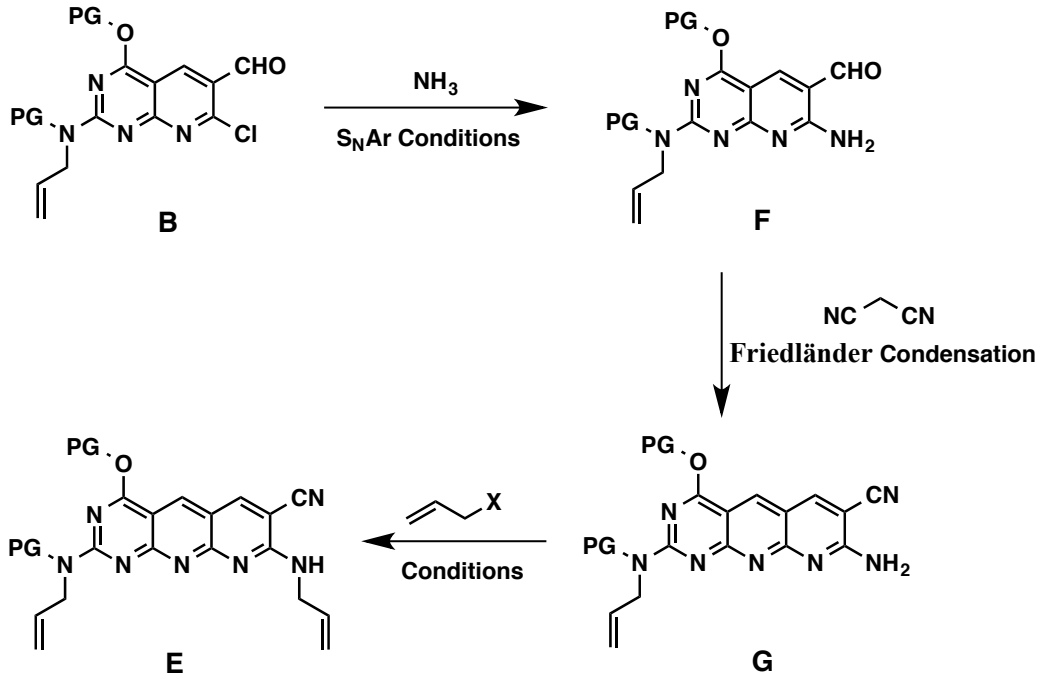

Figure 4.5. Proposed **Strategy 2** to install the second pyridine ring.

Finally, the guanine ring would be constructed using isocyanate reagents similar to that used in the synthesis of G∧C and xG∧C motifs[6,8,9], and di-allyl yG∧C motif **1** would be obtained after deprotection with TFA or HCl (Figure 4.6).

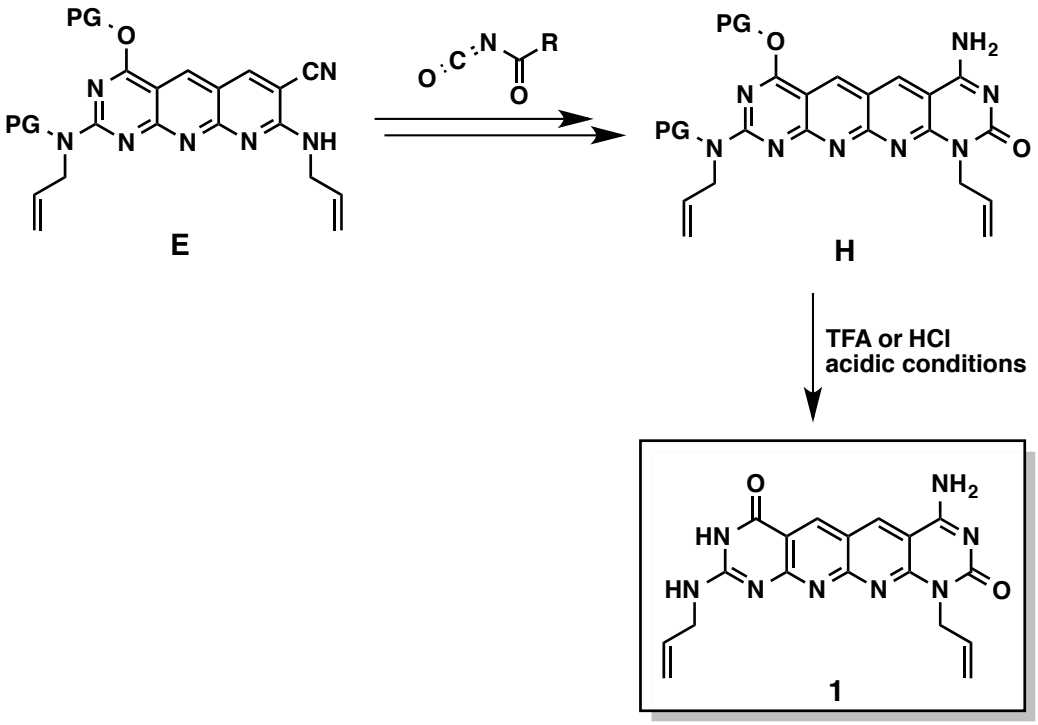

Figure 4.6. The formation of the guanine ring and the global deprotection under acidic conditions to provide di-allyl yG∧C motif **1**.

4.4 Synthesis

Similar to G∧C and xG∧C modules, my efforts towards the synthesis of di-allyl yG∧C motif **1** begun with the commercially available barbituric acid. I initially prepared compound **2** featuring tri-chloro substituents that can be selectively displaced via careful S_NAr reactions. According to an earlier report[6], the synthesis of compound **2** was achieved by Vilsmeier-Haack reaction on barbituric acid to obtain compound **3** in 91% yield. Knoevenagal condensation with malononitrile then led to compound **4** in 50% yield. Although it was reported[7] that heating compound **4** to 180°C in a round bottom flask capped with $CaSO_4$ tube leads to compound **2** in 75% yield, it was found that it is possible to perform this reaction at 160°C for 6 h to achieve 95% yield (Figure 4.7).

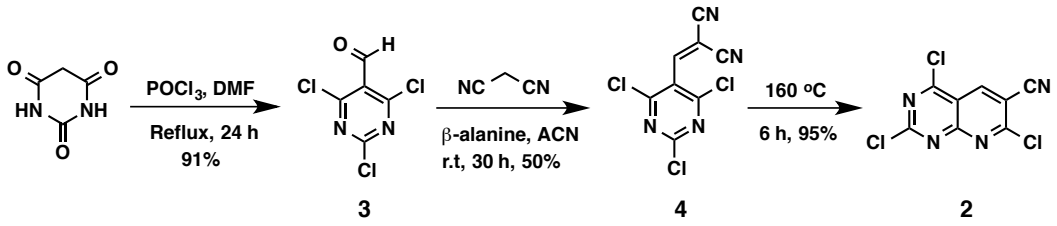

Figure 4.7. Synthetic route towards compound **2**.

Two consecutive S_NAr reactions were next examined in order to achieve the desired substitution pattern on the guanine side of the molecule. It was demonstrated in an earlier study that it is possible to selectively displace the three chloro substituents in compound **2** via consecutive S_NAr reactions with one equivalent of the appropriate nucleophile at low temperature. As shown in Figure 4.8, the three substituents can be displaced in the order 1-2-3 (decreased reactivity order).

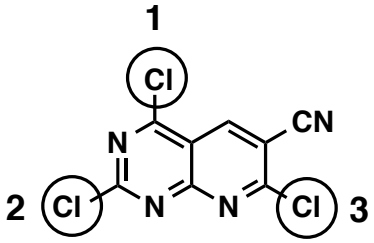

Figure 4.8. The order of reactivity of the three chloro substituents in compound **4**.

Thus, the first chloro substituent (in position 1) was displaced with a benzyloxy group, which would eventually generate the carbonyl in the guanine ring of the final molecule **1** after deprotection. Using 1.1 equivalents of benzyl alcohol and DIPEA as a base, it was found that it is possible to perform the reaction at -10°C instead of -40°C to afford compound **5** in 70% yield. Next, allylamine substituent was introduced in position 2 upon reaction of compound **5** with 1.1 equivalents of allylamine at -10°C in DCM to provide compound **6** in 70% yield (Figure 4.9).

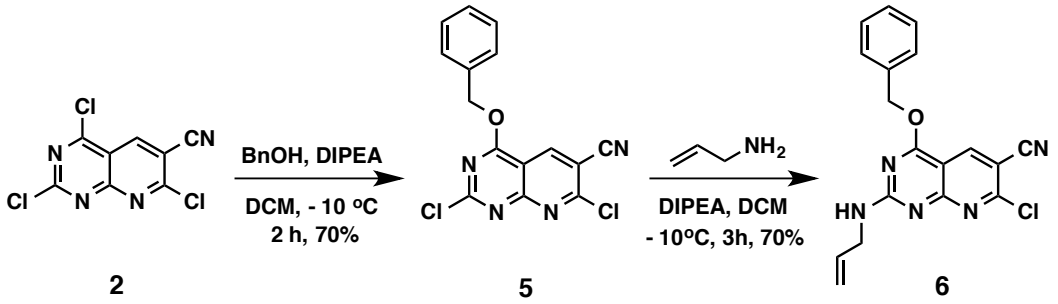

Figure 4.9. Consecutive S_NAr substitution reactions to provide the desired substitution pattern on the guanine ring.

In order to install the second pyridine ring according to the proposed strategy, it was necessary to convert the appended nitrile group in compound **6** to an aldehyde. It was reported earlier that treating compound **6** with 2 equivalents of DIBAL in DCM results in a 1:1 mixture of the aldehyde **7** and unreacted starting material. Further attempts to separate the two compounds failed due to their similar polarity. Thus, reducing the mixture with $NaBH_4$ was needed in order to separate the alcohol from the dihydropyridine product. Then PCC oxidation of the alcohol provided compound **7** at the end.[7]

However, it was found that it is possible to quantitatively obtain compound **7** in a single step by adding 2 equivalents of 1M DIBAL/DCM solution very slowly (over one hour) to the solution of compound **6** in DCM. The reaction was performed in careful anhydrous conditions and under argon. After 2 hours of stirring at room temperature, complete conversion was obtained and compound **7** was isolated in 80% yield (Figure 4.10).

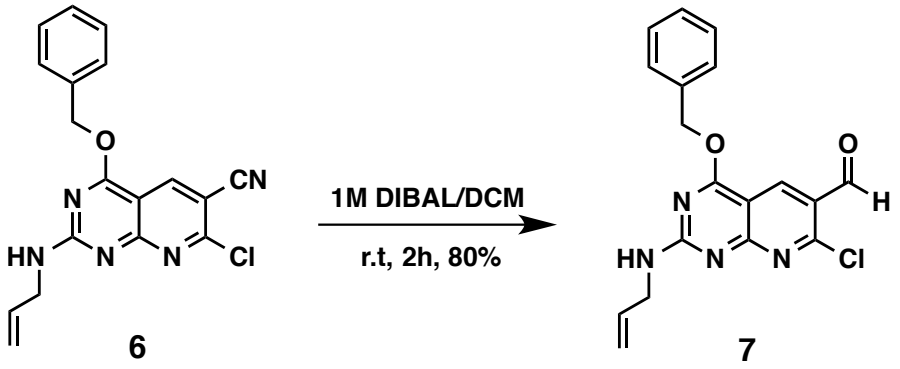

Figure 4.10. Nitrile reduction to the aldehyde.

In order to advance in the proposed strategy, protection of the appended allylamine group in compound **7** was needed to avoid its influence on the next steps. The Boc protection reaction of compound **7** was reported earlier[7] using Boc_2O in the presence of DMAP and DIPEA in THF. These conditions led to compound **8** after 2-3 days at room temperature in 73% yield. Adding more Boc_2O (up to 10 equivalents), varying the amounts of DIPEA and DMAP, or increasing the temperature (up to 40°C) did not help to improve the yield of the product or to shorten the reaction time. It was then decided to explore DCM instead of THF for this reaction, but this approach failed at room temperature even after long reaction time (several days) or when adding up to 10 equivalents of Boc_2O. This was reasoned to the low solubility of compound **7** in DCM at room temperature. Upon heating the suspension to 35°C however, clear solution of compound **7** in DCM was obtained, and the reaction went to completion after only 1 hour to provide compound **8** in 75% yield (Figure 4.11).

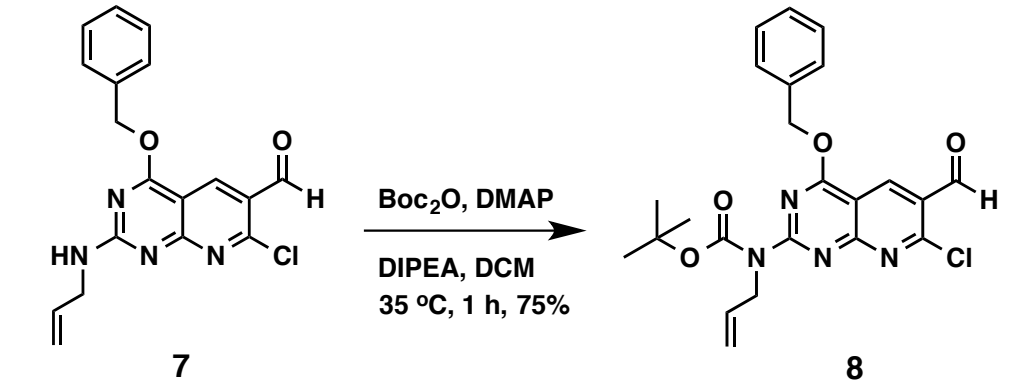

Figure 4.11. Boc protection reaction of compound **7**.

Having obtained the protected aldehyde **8**, Strategy 1 (Figure 4.4) was next examined to construct the second pyridine ring in the naphthyridine core. The first step in this strategy involved Knoevenagel condensation of **8** with malononitrile in acetonitrile using β-alanine as a catalyst, which led to compound **9** in 75% yield after column chromatography (Figure 4.12).

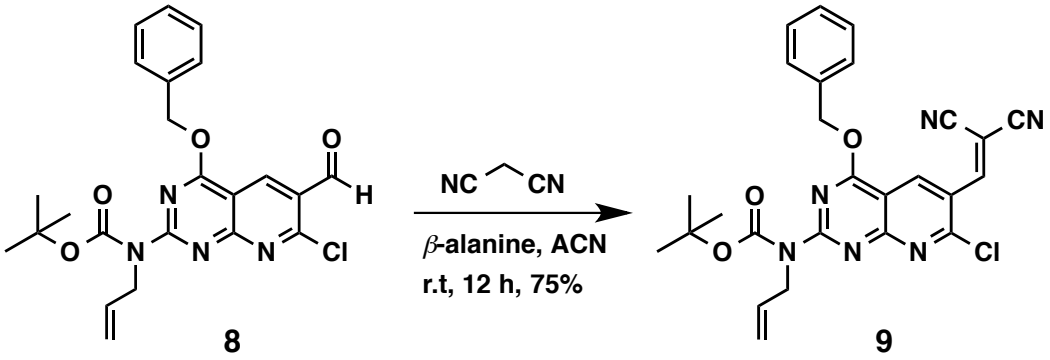

Figure 4.12. Knoevenagel condensation of **8** with malononitrile.

The next step in Strategy 1 involved thermal cyclization of compound **9** (S_NAr mechanism), in which it was heated to 180°C in a flask capped with a $CaSO_4$ tube for up to 24 h (dry conditions). Under these conditions and after 6 hours, a 2:8 mixture of Boc deprotected starting material **10** and Boc deprotected product **11**, respectively was found as revealed by mass and NMR analyses. This result suggested that Boc deprotection was faster than cyclization, and when the Boc

group is removed, the cyclization reaction is deactivated due to the electron donating effect of the appended allylamino group in compound **11** (Figure 4.13). In order to prevent Boc deprotection, the reaction was attempted at 160°C for 6 h, but same result was obtained (Figure 4.13). In further attempts, compound **9** was subjected to 120-140°C heating conditions, but no cyclization or Boc deprotection occurred even after 24 h and only the starting material was recovered.

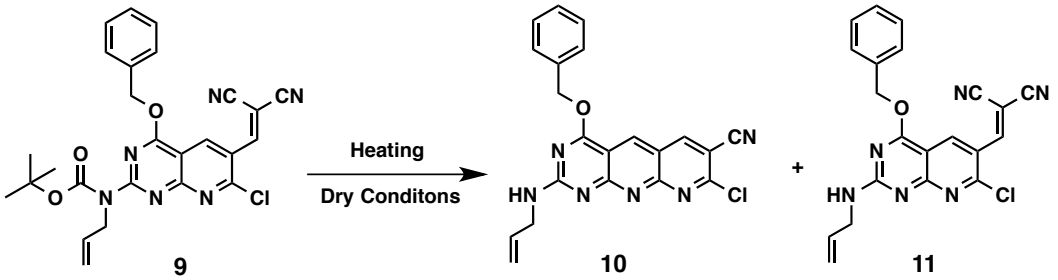

Figure 4.13. Thermal cyclization reaction under dry conditions.

As a means of preventing Boc deprotection upon heating, the cyclization reaction was next examined using wet conditions (in solution) in the presence or absence of a base. Compound **9** was subjected to 120°C heating conditions in several solvents in the absence or presence of triethylamine (TEA). When the reaction was performed in chlorobenzene in the absence of TEA, a mixture of 2:8 of the compounds **10** and **11**, respectively, was obtained. When TEA was added to this reaction however, complete decomposition of the starting material was observed. No reaction happened in toluene in the absence of TEA. Similarly, complete decomposition was found when the reaction was performed in DMF (Figure 4.14). The attempted wet heating conditions are summarized in Table 4.1.

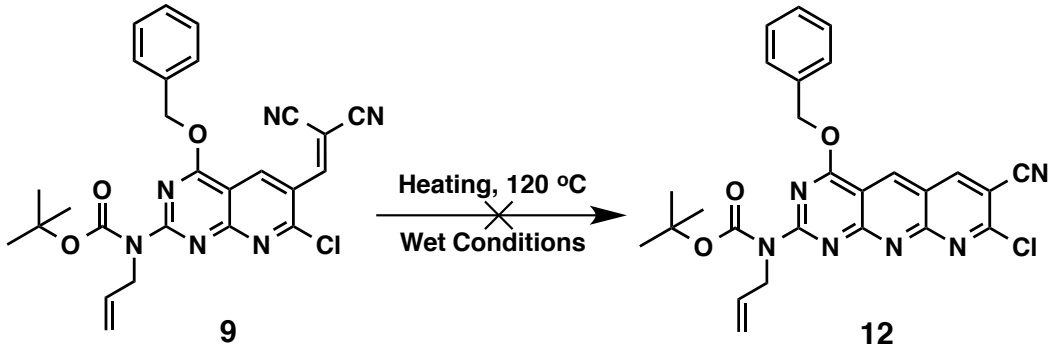

Figure 4.14. Thermal cyclization reaction using wet conditions.

Table 4.1. Summary of conditions attempted for the thermal cyclization reaction using the wet method.

T ^{o}C	Solvent	Base	Time	Result
120	Chlorobenzene	_	6 h	Boc Deprotection and cyclization
120	Chlorobenzene	TEA	6 h	Decomposition
120	DMF	_	6 h	Decomposition
120	Toluene	_	6 h	No Reaction
120	Toluene	TEA	6 h	Decomposition

After exploring the dry and wet conditions for the cyclization reaction, it was reasoned that it would be difficult to induce the cyclization without sacrificing the Boc protecting group on the allylamine. Thus I tried to generate compound **12** by subjecting the 2:8 mixture of **10**:**11** to Boc protection conditions. However, all Boc protection attempts failed, and the mixture was completely inert under these conditions (Figure 4.15). The lack of reactivity was attributed to the low nucleophilicity of the allylamino group due to the strong electron withdrawing effect of the nitrile groups in the two compounds.

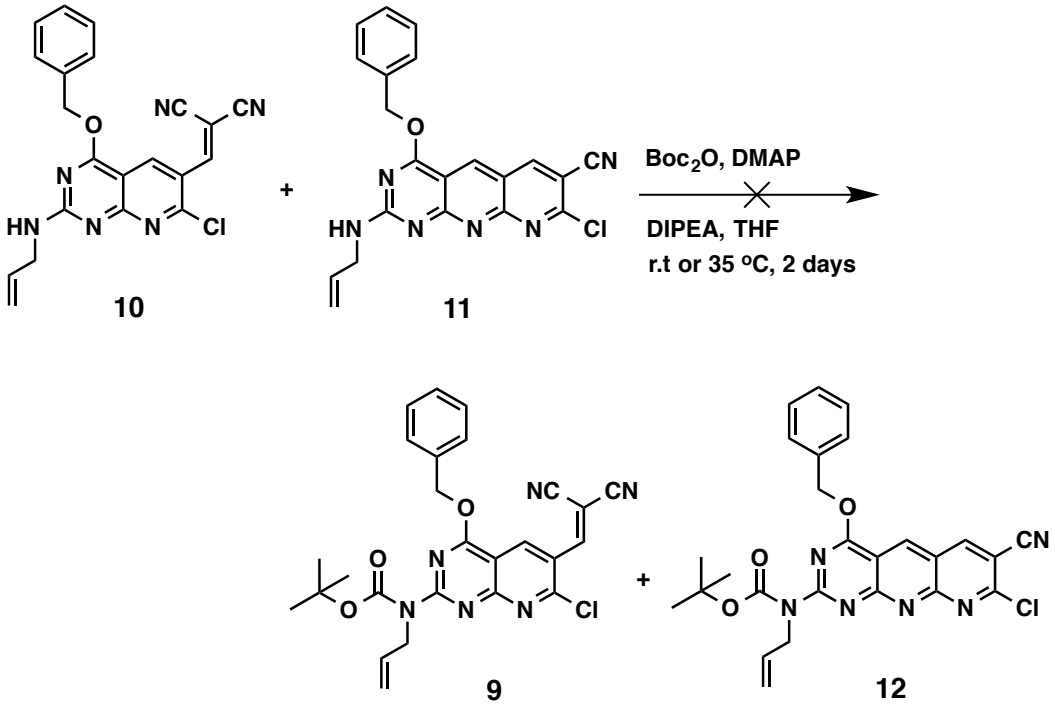

Figure 4.15. Boc protection attempt of the mixture obtained from the dry conditions (Figure 4.13) for the cyclization reaction.

Upon having difficulties in the thermal cyclization of compound **10**, I then decided to abandon Strategy 1 and explore Strategy 2 shown in Figure 4.5. The first task in this strategy was the displacement of the chloro substituent in **8** with ammonia. This reaction was reported earlier using 10 equivalents ammonia (2M NH_3 in *i*-PrOH) in THF at room temperature in the presence of 1.1 equivalents of DABCO (as a catalyst) and 1 equivalents of DIPEA as a base.[7] These conditions led to compound **13** in 35% yield along with 50% of the hydrolysis product **14**. The formation of **14** was reasoned to the trace water in the medium. In order to increase the yield of the reaction and minimize the hydrolysis, the reaction was repeated in careful anhydrous conditions. In a round bottom flask, analytically pure THF (from the solvent purification system) was dried with activated 4 Å molecular sieves, and anhydrous argon was bubbled for at least 10 min to remove atmospheric moisture. To this THF, compound **8**, 2M NH_3 in *i*-PrOH, DIPEA and

DABCO were added under argon and the solution was stirred while flashing with argon at room temperature. Under these conditions, compound **13** was isolated in 45% yield, and 30% of the hydrolysis product was found. Other impurities included 10% of compound **15** (Figure 4.16).

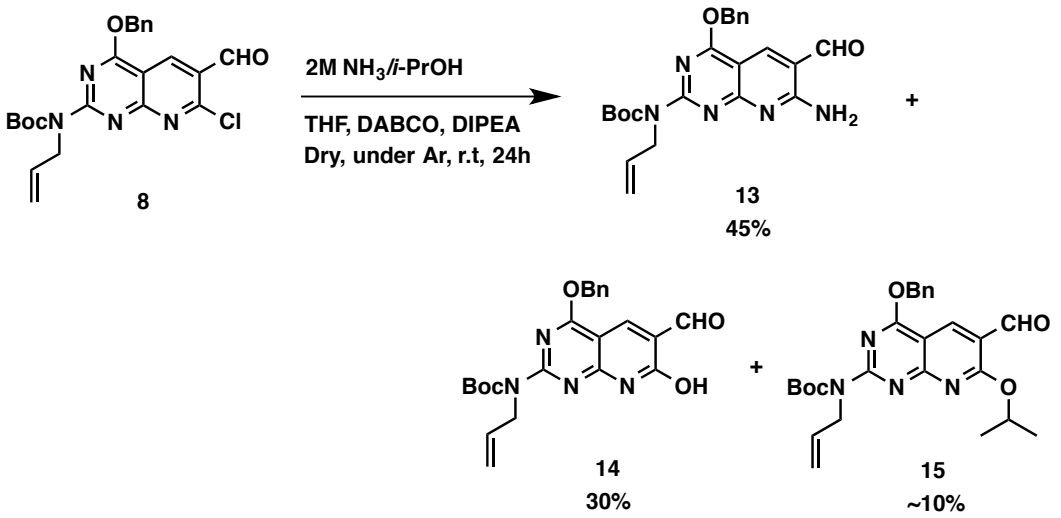

Figure 4.16. Displacement reaction with ammonia using 2M NH_3/*i*-PrOH reagent.

In another attempt, the commercially available 7M NH_3/MeOH solution was used instead of 2M NH_3/*i*-PrOH. However, the chloro substituent in **8** was mainly displaced with MeOH, and only trace amount of **13** was obtained (Figure 4.17). This was attributed to the smaller size (i.e. more nuleophilicity) of MeOH compared to *i*-PrOH.

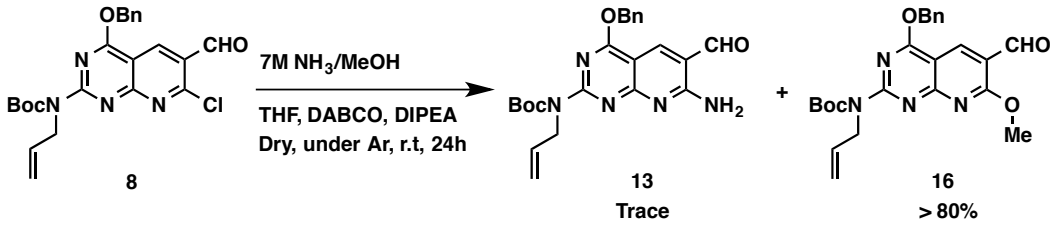

Figure 4.17. Displacement reaction with ammonia using 7M NH_3/MeOH reagent.

Finally, freshly prepared NH_3(sat)/THF solution was examined for this reaction. This solution was prepared by bubbling anhydrous NH_3 in dry THF for 10 min, then compound **8**, DIPEA and DABCO were added, and the mixture was stirred at room temperature for 24h. Under these conditions, compound **13** was isolated in 50% yield (Figure 4.18). Other impurities included 30% of the hydrolysis product **14** and trace amount of compound **17** having the benzyl group displaced with ammonia.

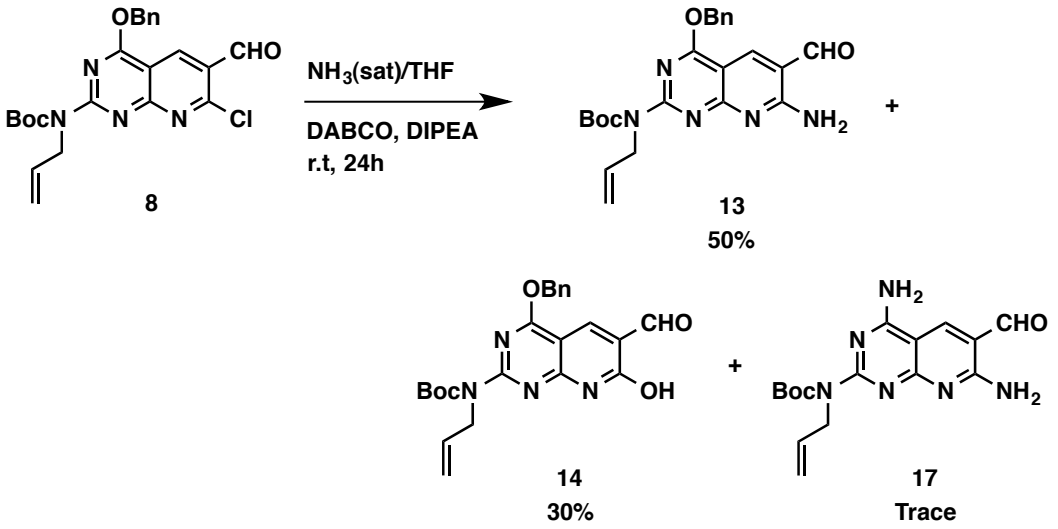

Figure 4.18. Displacement reaction with ammonia using freshly prepared NH_3(sat)/THF solution.

The second pyridine ring to be synthesized, Friedländer reaction between compound **13** and malononitrile was next examined. This reaction was previously reported using anhydrous pyridine as a solvent and 1.5 equivalents of malononitrile at room temperature.[7] Using these conditions, compound **18** was isolated in 85% yield after column chromatography (Figure 4.19).

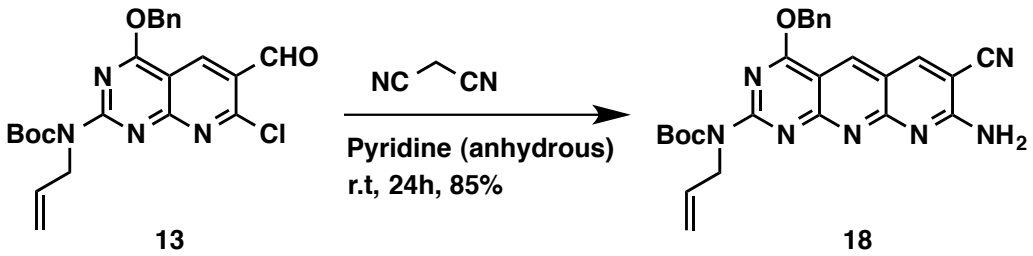

Figure 4.19. Friedländer reaction between **13** and malononitrile.

Our subsequent task was the introduction of the second allyl group on the appended amino group in **18**. To this end, several approaches were examined including reductive amination, nucleophilic aromatic substitution (S_NAr), and nucleophilic substitution (S_N2) reactions.

It was previously demonstrated that the reductive amination method using acrolein and $NaBH(OAc)_3$ in DCM at room temperature resulted in the reduction of the ring system and no product had formed (Gabor Borzsonyi, PhD thesis, University of Alberta). This reaction was explored further in 1,2-DCE using modified reductive amination conditions. Compound **18** was dissolved in anhydrous 1,2-DCE under argon, and 2 equivalents of acrolein was then added. After stirring for 6 h at room temperature, 1.0 equivalent of $NaBH(OAc)_3$ was added and the mixture was stirred under argon at room temperature overnight. Mass, TLC and NMR analyses of the mixture revealed that no reaction occurred and the starting material was recovered (Figure 4.20). This was attributed to the relatively low nucleophilicity of the allylamino group due to the strong electron withdrawing effect of the neighboring nitrile, and thus this approach was abandoned.

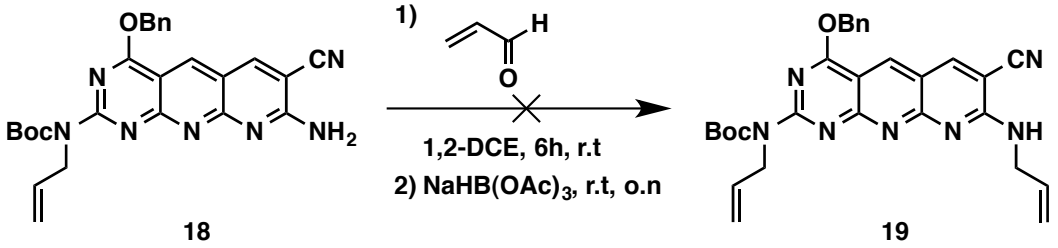

Figure 4.20. Allylation reaction using reductive amination conditions.

Our next approach involved nucleophilic aromatic substitution (S_NAr) reaction to displace the amino group with allylamine, and thus to take advantage of the strong electron withdrawing effect of the neighboring nitrile group. In this approach, compound **18** was dissolved in anhydrous THF, and 2 equivalents of allylamine was then added and the mixture was stirred at room temperature for several days. The analysis of the mixture over time indicated that no reaction occurred and the starting material was recovered. Adding more allylamine (up to 10 equivalents) and raising the reaction temperature to 50°C did not cause any change. Finally, the reaction was attempted in neat allylamine at 50°C, but no product was found, and this approach was also abandoned (Figure 4.21).

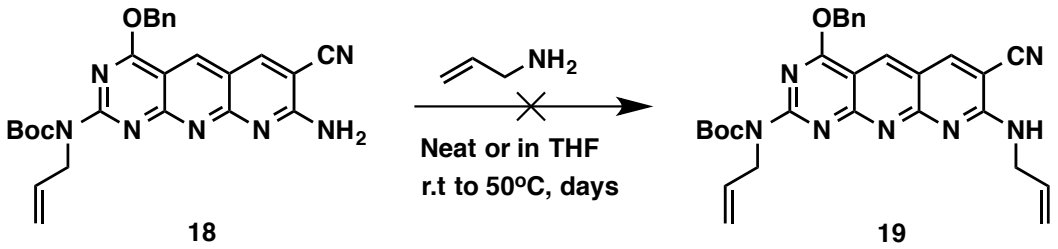

Figure 4.21. Allylation reaction using S_NAr conditions with allylamine.

Having the reductive amination and S_NAr approaches failed, my efforts next focused on the S_N2 strategy for the allylation reaction. I first examined the use of relatively strong bases such as NaH, and allylation reagents including allyl iodide and allyl bromide. When compound **18** in THF under argon was treated with 1 equivalent of both NaH and allyl iodide at 0°C, it completely decomposed within a few hours and no product **19** was obtained. This was reasoned to the reduction of the ring system by the hydride along with the formation of many other impurities, which were difficult to analyze. I then decided to abandon NaH and to explore other strong but less nucleophilic bases such as NaOMe and *t*-BuONa.

Initially, compound **18** in THF was treated with NaOMe (1 equivalents) and allyl iodide (1 equivalents) at -20°C, but no reaction occurred and only starting material was recovered. However, this reaction was repeated at 0°C, and this time the mass analysis after 12h revealed a 3:7 mixture of **19** and the starting material **18**, respectively. The mass analysis also revealed the formation of 20% (with respect to **18**) of an impurity having OH- added to the ring system, and the TLC and ^{1}H NMR analyses were complicated and difficult to interpret. Leaving the reaction for an additional day did not cause any change. In order to push the reaction to completion, additional 1.5 equivalents of allyl iodide was added but di- and tri-alkylated products started to form and the reaction was therefore stopped. Compound **19** was eventually isolated after column chromatography in 25% yield. The same result was obtained when the reaction was repeated using allyl bromide at 0°C in THF. However, when the reaction was performed at room temperature using allyl iodide or allyl bromide, complex mixture of impurities and by-products was found and no product could be isolated. DCM, chloroform and dioxane were also examined as solvents but no reaction took place, and only starting material was recovered. Other bases such as *t*-BuONa were also explored for this reaction, but the same results were obtained as with NaOMe (Figure 4.22).

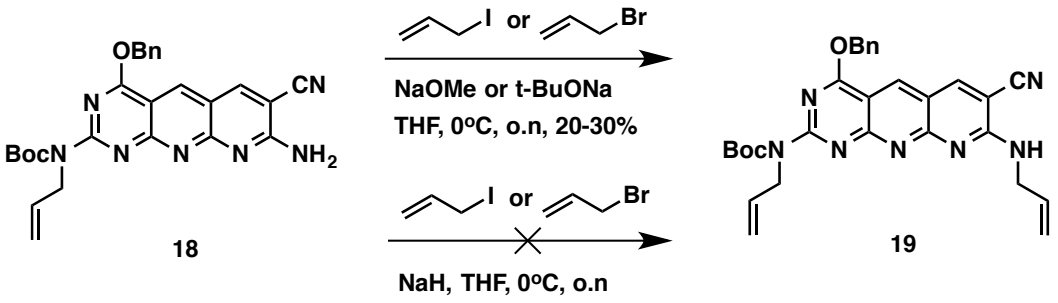

Figure 4.22. S_N2 allylation reaction attempts using strong bases.

With these rather low yields, I next explored the allylation reaction using phase transfer catalysis conditions. Initially, compound **18** was dissolved in DCM, and then allyl iodide (1 equivalent) was added. An aqueous phase of 50% NaOH containing tetrabutylammonium iodide (TBAI) as a phase transfer catalyst was

then added, and the mixture was stirred at room temperature overnight. The TLC and mass analyses over time revealed a complex mixture of by-products including a major by-product having OH- added to the ring system, and no product was found. In order to prevent the reaction of **18** with OH-, the reaction was repeated using a less basic aqueous phase of 25% NaOH while maintaining the other conditions. In a few hours, a 5:3:2 mixture of the mono- (**19**), di-, and tri-allyllated products respectively, was found. However, compound **19** was isolated after column chromatography in only 30% yield. This reaction was also conducted using chloroform instead of DCM as an organic phase, but only to yield the same result (Figure 4.23).

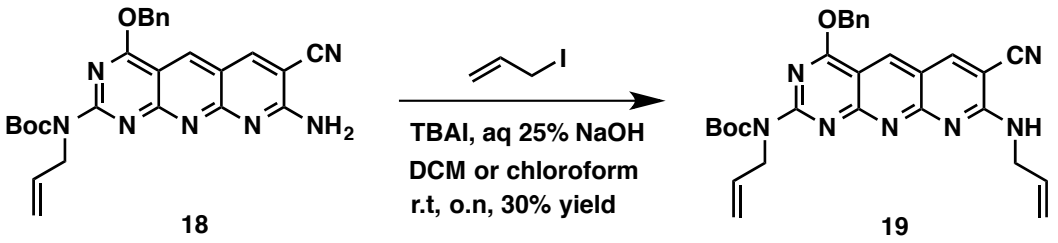

Figure 4.23. S_N2 allylation reaction attempts using phase transfer catalysis conditions.

While the previous S_N2 strategies using strong bases led to compound **19** in 20-30% yield, my final strategy included the use of weak bases (pKa ~10) such as triethylamine (TEA) and diisopropylethylamine (DIPEA). In the first attempt, compound **18** in THF was treated with allyl iodide (1.5 equivalents) and TEA (2 equivalents), and the mixture was then stirred at room temperature. Immediately a white precipitate formed, which was found to be the result of the reaction between allyl iodide and TEA. It was therefore reasoned that TEA is not a good base for this reaction, and a more hindered base such as DIPEA was needed.

Therefore, the reaction was varied out in THF using 1.5 equivalents of both allyl iodide and DIPEA at room temperature. This approach proved to be useful as the TLC and mass analyses revealed the formation of compound **19** over time.

However, the reaction was very slow, and less than 10% conversion was obtained after 7 days. Thus, 20 equivalents more of allyl iodide and 10 equivalents more of DIPEA were added to push the reaction to completion. After stirring for 12 h, complete conversion of compound **18** to the product **19** was obtained, which was isolated in 65% yield after column chromatography. After several trials, it was found that adding 7 equivalents of allyl iodide and 4 equivalents of DIPEA in THF at room temperature would lead to the same result in 12h (Figure 4.24). When the reaction was conducted at 45°C however, it was complete in 1h and gave similar yield.

Allyl bromide was also examined for this reaction. It was found that in order to achieve 65% yield, conditions including 20 equivalents of allyl bromide, 10 equivalents of DIPEA, and stirring for 4-5 days at room temperature were required. When the reaction was performed using allyl bromide at 45°C however, a reaction time of 12h was required to achieve 65% yield (Figure 4.24). The optimized conditions for the allylation reaction are summarized in Table 4.2.

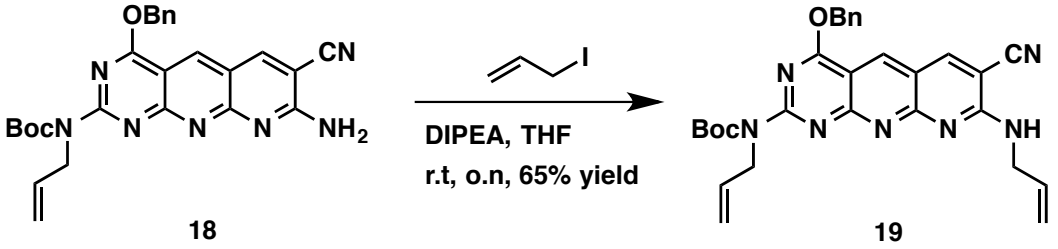

Figure 4.24. S_N2 allylation reaction using DIPEA as a base.

Table 4.2. Summary of successful conditions for the allylation reaction using DIPEA as a base.

T ^{o}C	Allyl reagent (equiv)	DIPEA equiv	Time	% Yield[a]
RT	Allyl iodide (7)	4	12 h	60-65
45	Allyl iodide (7)	4	1 h	60-65
RT	Allyl bromide (20)	10	4-5 days	60-65
45	Allyl bromide (20)	10	12 h	60-65

[a] Isolated yields.

The purity of **19** was confirmed by TLC and low- and high-resolution mass analyses. Figure 4.25 A and B show the low- and high-resolution mass spectra of **19** having only the compound peaks (no impurities). However, unlike compound **18** which gave a well-resolved ^{1}H NMR spectrum with sharp peaks, the ^{1}H NMR spectrum of compound **19** in $CDCl_3$ was broad and complex, and same was found in the corresponding ^{13}C NMR spectrum. Furthermore, no signals corresponding to the aromatic protons (on the naphthyridine core) in the region between δ (ppm) = 8-9 were found. The reason I believe is because, the presence of an additional allyl group in compound **19** makes the compound more hydrophobic and thus more susceptible to aggregation through hydrogen bonding and π-π stacking interactions, leading to complex NMR spectra. Additional NMR experiments were conducted in order to provide a well-resolved NMR spectrum. First, ^{1}H NMR of **19** in DMSO-d_6, MeOH-d_4, CD_2Cl_2, and Toluene-d_8 were studied, but similar broad and complex spectra were obtained as in $CDCl_3$. In order to break the aggregation, variable temperature ^{1}H NMR study of compound **19** in DMSO-d_6 at 25, 40, 60, and 80°C was conducted, but no change in the NMR spectrum was observed (Figure 4.25). Same study was also conducted in Toluene-d_8, but only to yield the same result.

A

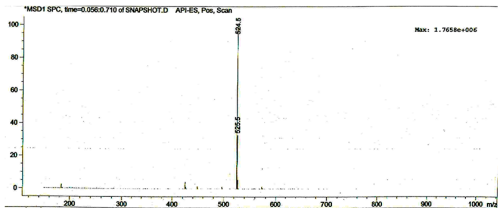
*MSD1 SPC, time=0.056:0.710 of SNAPSHOT.D API-ES, Pos, Scan
Max: 1.7658e+006
524.5
525.5
m/z

B

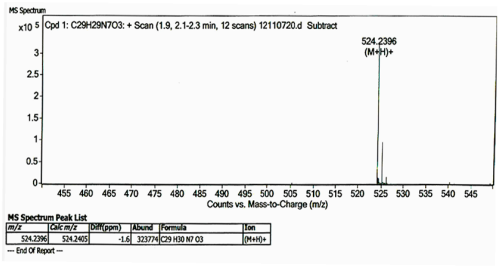
MS Spectrum
Cpd 1: C29H29N7O3: + Scan (1.9, 2.1-2.3 min, 12 scans) 12110720.d Subtract
524.2396
(M+H)+
Counts vs. Mass-to-Charge (m/z)
MS Spectrum Peak List
m/z | Calc m/z | Diff(ppm) | Abund | Formula | Ion
524.2396 | 524.2405 | -1.6 | 323774 | C29 H30 N7 O3 | (M+H)+
— End Of Report —

C

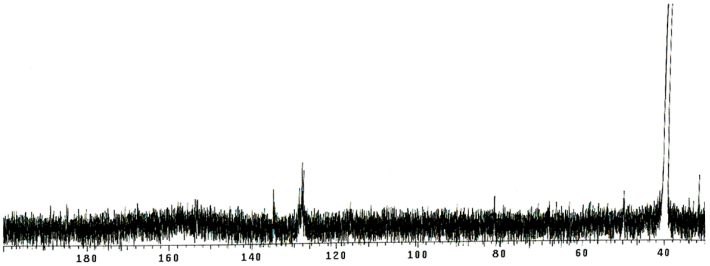
180
160
140
120
100
80
60
40

D

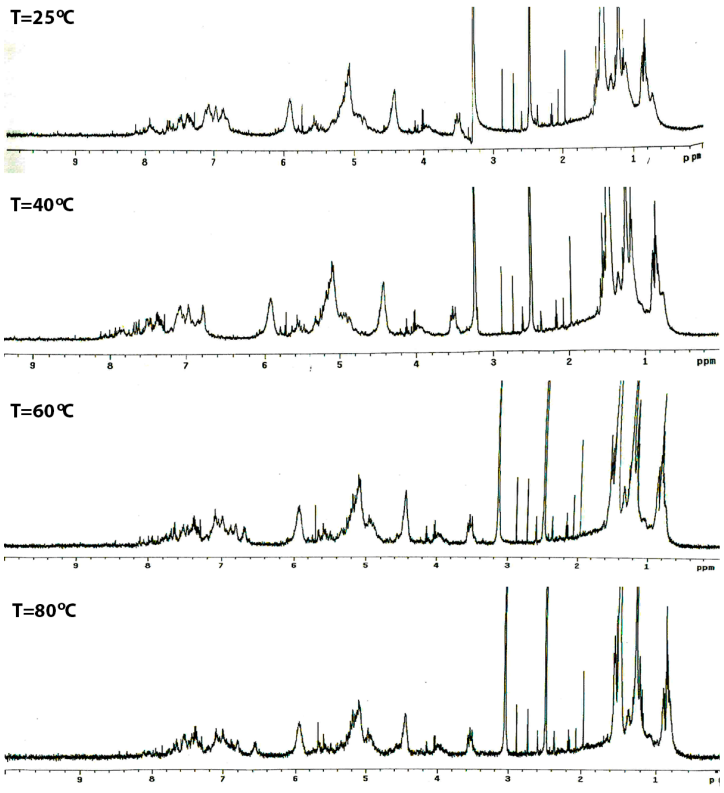
T=25℃
T=40℃
T=60℃
T=80℃
ppm

Figure 4.25. Characterization data for compound **19** (A) Low resolution mass; (B) High resolution mass; (C) ^{13}C NMR spectrum in DMSO-d_6 after 30000 scans; and (D) variable temperature ^{1}H NMR spectra in DMSO-d_6.

To provide additional and indirect evidence of **19**, it was then decided to fully deprotect it under TFA acidic conditions, and then to characterize the deprotected compound **20** by NMR in the presence of TFA-d in order to break the aggregation. Therefore, compound **19** was dissolved in a deprotection cocktail of 95:2.5:2.5 mixture of TFA, triisopropylethylamine (TIS), and H_2O, respectively. The solution was then stirred at 40°C for 1 h before removing TFA under vacuum (Figure 4.26). The orange solid (compound **20**) was then washed five times with diethyl ether and then dried under vacuum. It was then observed that compound **20** in DMSO-d_6 in the presence of 10% TFA-d gave resolved ^{1}H and ^{13}C NMR spectra with sharp peaks. In addition, compound **20** was also characterized by low- and high-resolution mass and elemental analyses (Figure 4.27).

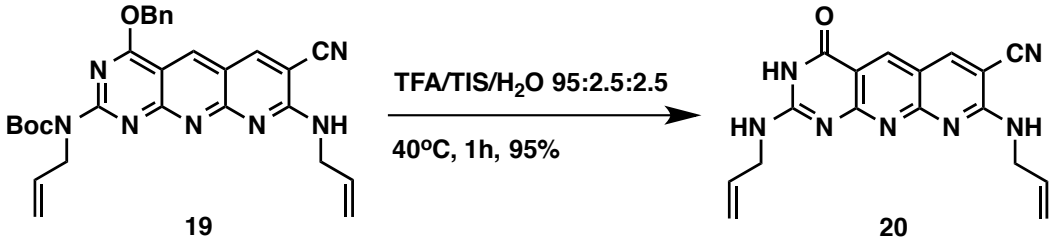

Figure 4.26. Deprotection of compound **19** under TFA acidic conditions.

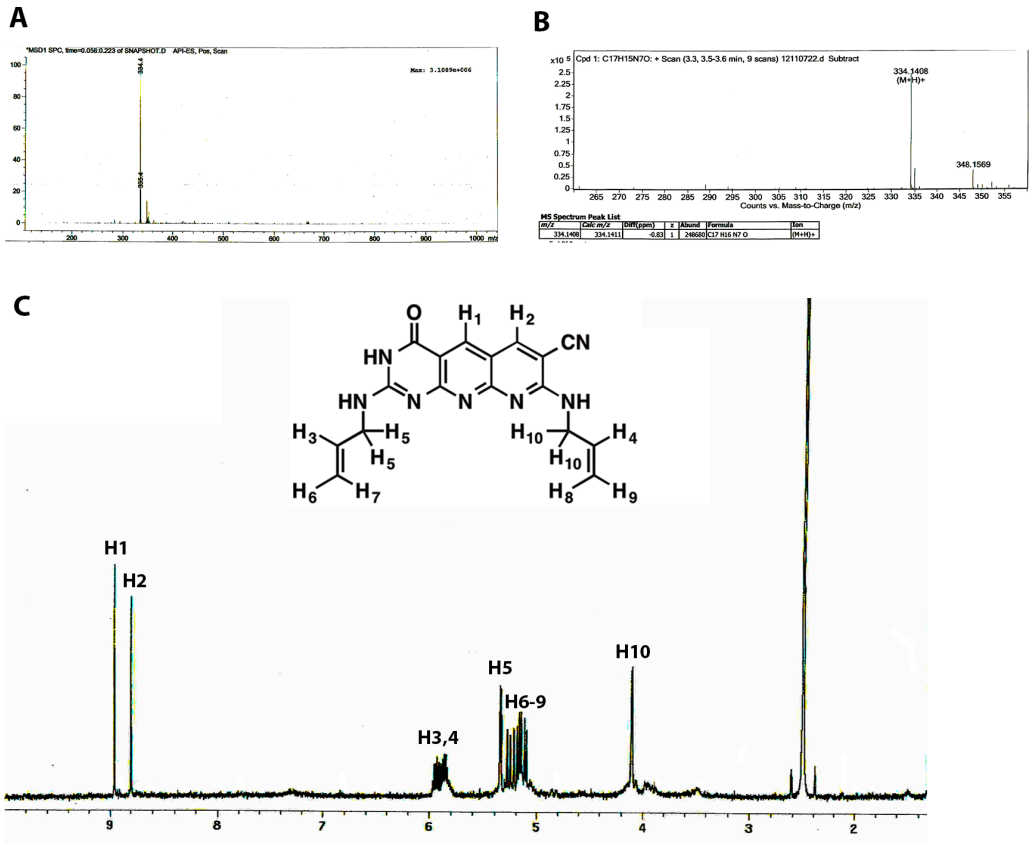

Figure 4.27. Characterization data of **20**. (A) Low resolution mass; (B) High resolution mass; and (C) ^{1}H NMR in DMSO-d_6 + 10% TFA-d with the proton assignments.

With compound **19** in hand, the subsequent task was to synthesize the fourth ring (cytosine ring). The synthesis was initially attempted using trichloroacetyl isocyanate (1-10 equivalents) in DCM at 0°C under argon. Although these conditions typically result in the formation of mixed urea adducts, the mass and TLC analyses indicated that no reaction happened even after several days and only starting material was recovered. The reaction was then conducted at room temperature using 2 equivalents of trichloroacetyl isocyanate in DCM and under argon. These conditions led to the formation of the mixture shown in Figure 4.28 after 3-4 h as revealed by the mass analysis. While compound **21** was a result of the reaction with the isocyanate group (the desired reaction), compound **22** was formed by the reaction of **19** with the carbonyl group in trichloroacetyl

isocyanate. The formation of 50% of **22** was attributed to the strong electron withdrawing influence of the trichloromethane moiety in trichloroacetyl isocyanate. Adding up to 10 equivalents more of trichloroacetyl isocyanate did not help to consume the starting material or to increase the amount of **21** in the mixture (Figure 4.28).

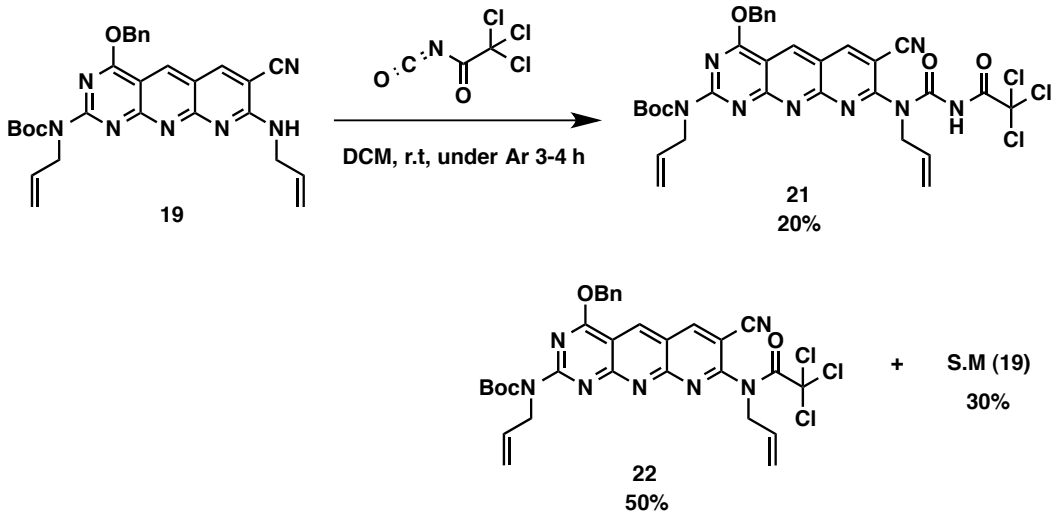

Scheme 4.28. Reaction of **19** with trichloroacetyl isocyanate.

In order to generate the urea adduct **23** and to close the ring, 2M NH_3/*i*-PrOH solution was added *in situ* to the above mixture (in Figure 4.28), and the solution was stirred at room temperature overnight. The analysis of the solution after 24h revealed a 2:8 mixture of the urea adduct **23** and starting material **19**, respectively (Figure 4.29). It was reasoned that compound **22** had generated back the starting material upon reaction with ammonia. Compound **23** was isolated after column chromatography in only ~20% yield. Although these conditions typically result in ring closure of the urea adduct,[6,7] the IR analysis of compound **23** revealed a strong absorption peak at 2220 cm^{-1} indicating the presence of the nitrile group, and that the cyclization did not occur.

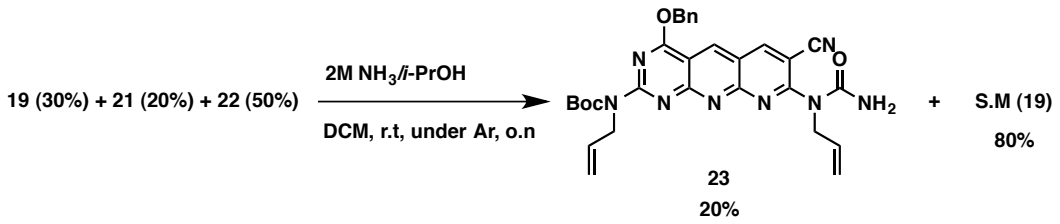

Figure 4.29. Reaction of the mixture in Figure 4.28 with ammonia.

Although compound **23** was successfully obtained using trichloroacetyl isocyanate, the poor yield was attributed to the more favored addition to the carbonyl group over the isocyanate. To overcome this challenge, N-9-Fluorenylmethoxycarbonyl isocyanate (Fmoc-isocyanate) reagent was next examined, which features less electron withdrawing Fluorenylmethoxy substituent. This reagent was used in the literature to obtain carbamate functionalities in Aziridinomitosene derivatives. [10-12] Although the use of this reagent resulted in the formation of 30% of the isocyanate adduct **24**, 50% of compound **25** was found along with 20% of starting material **19**. The subsequent addition of piperidine (2 equivalents) *in situ* after 4h generated the urea adduct **23** in 30% yield (Figure 4.30).

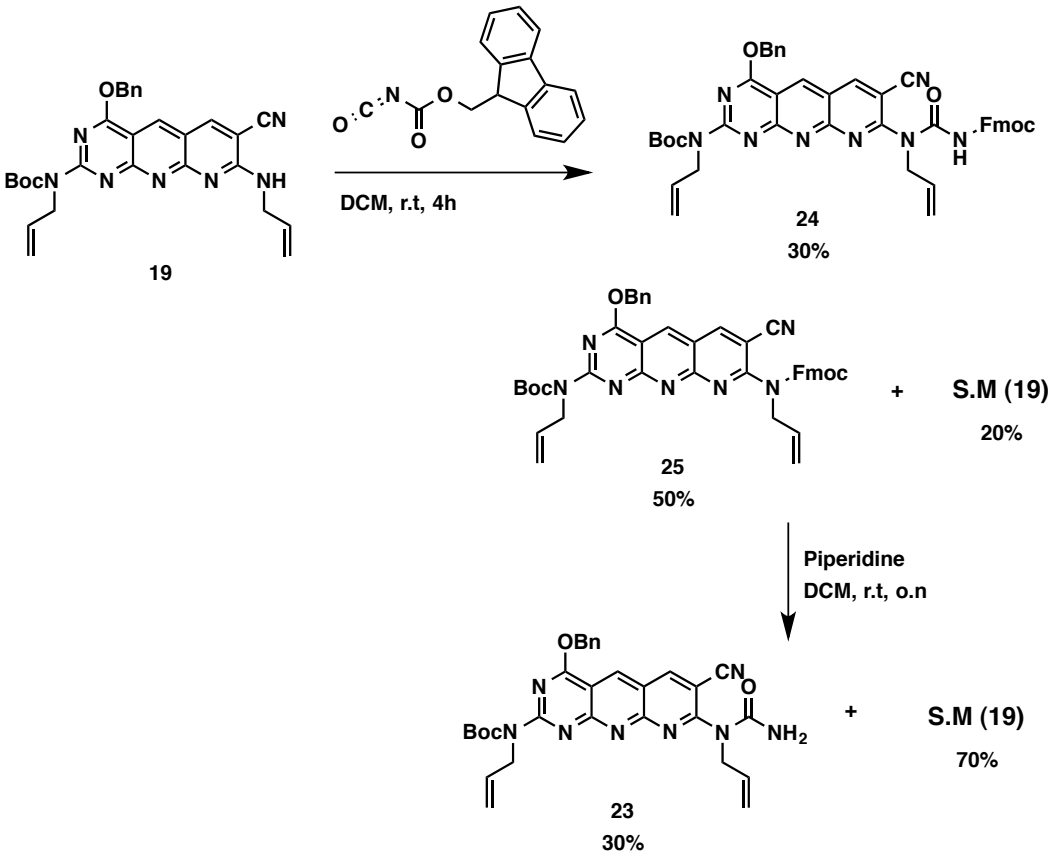

Figure 4.30. Reaction of **19** with Fmoc-isocyanate and the subsequent Fmoc deprotection.

Although the yield of **23** was improved to 30% when Fmoc-isocyanate was used, the carbonyl addition product **25** was still predominant. Thus I next examined the use of benzoyl isocyanate, which is a very mild reagent used during the synthesis of mono allyl yG∧C.[7] When compound **19** in DCM was treated with benzoyl isocyanate (10 equivalents) at room temperature, complete conversion into the mixed urea adduct **26** was found after only 1h, which was isolated after column chromatography in 80% yield (Figure 4.31). However, all attempts to cyclize **26** using strong bases (such as NaOMe and *t*-BuONa) failed (Figure 4.31). This was reasoned to the presence of the benzoyl group, which prevents the aromatization of the cytosine ring. To remove the benzoyl group in **26**, TFA acidic conditions are required, which also lead to the deprotection of the Bn and Boc groups in the

compound. Therefore, the approach using benzoyl isocyanate was also abandoned.

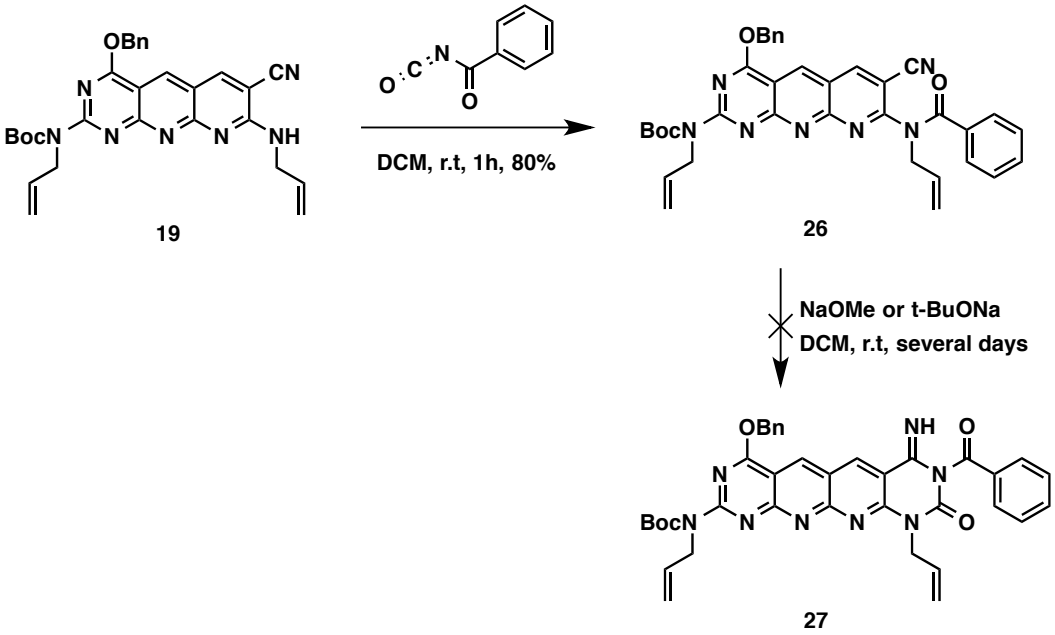

Figure 4.31. Reaction of **19** with Benzoyl isocyanate and the subsequent cyclization attempts using strong bases.

Although the urea adduct **23** was successfully obtained using trichloroacetyl isocyanate and Fmoc-isocyanate reagents, no more than 30% yield was achieved. Thus, a new reagent, namely N,N′-Disuccinimidyl carbonate (DSC), was examined for the cytosine ring synthesis. Although this reagent had not yet been used for cytosine ring synthesis, it was used in the literature to prepare carbamate, mixed urea, and amide functionalities.[13,14] It was therefore reasoned that with the two N-hydroxylsuccinimide leaving groups, this reagent could be used to generate the urea adduct **23** upon reaction with **19** and subsequent treatment with ammonia.

To test this approach, literature conditions using 2 equivalents of DSC and DIEPA at room temperature in acetonitrile were initially examined. However, no reaction took place even after heating to 40°C, and starting material **19** was recovered. Repeating this reaction without DIPEA also did not lead to any product formation.

Other literature conditions were also investigated including the use of 4 equivalents of DSC in DMF at 40°C, but no reaction occurred. Finally, new conditions using 7-10 equivalents of DSC in DCM or chloroform at 40°C were developed, which led to complete conversion of **19** to **28** after only 4h as revealed by mass analysis. Since the intermediate **28** was not stable, freshly prepared NH_3(sat)/DCM solution was added *in situ* to generate the urea adduct **23**, which was isolated after column chromatography in 77% yield (two-steps) (Figure 4.32). Similar to compound **19**, compound **23** gave complex ^{1}H NMR spectrum with broad peaks, thus it was only characterized by low- and high-resolution mass.

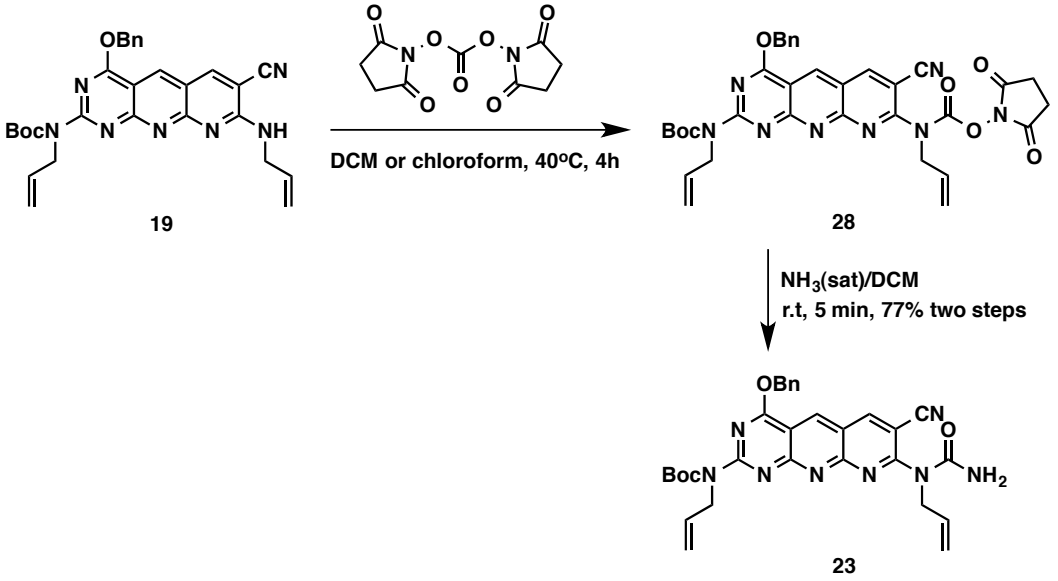

Figure 4.32. Successful reaction conditions of **19** with DSC and the subsequent reaction with ammonia to generate the urea adduct **23**.

The subsequent task was the ring closure of **23** to generate the protected tetracycle **29**. Compound **23** in DCM was initially treated with weak bases such as DIPEA and NH_3 at 40°C. After stirring for 1 week, no cyclization occurred as indicated by the presence of the nitrile absorption peak at 2220 cm^{-1} in IR spectroscopy. However, treatment of **23** with several strong bases at room temperature including t-BuONa, MeONa, and $NaNH_2$ in THF resulted in ring closure after 12h. Acidic workup using saturated aqueous NH_4Cl solution to neutralize the base was needed

to achieve 62% yield (Figure 4.33). If no acidic workup is applied however, the yield of **29** drops to less than 40% due to the reaction with the base during the removal of THF under vacuum.

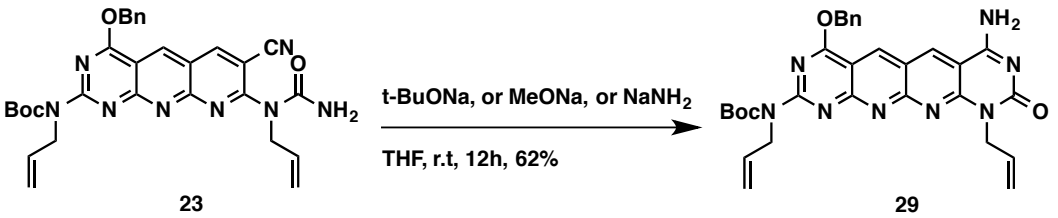

Figure 4.33. Ring closure reaction of **23** to generate the protected tetracycle **29**.

Finally, compound **29** was deprotected using TFA or HCl acidic conditions to obtain the TFA or HCl salts, respectively, of the final tetracycle **1**. Di-allyl yG∧C.TFA salt **30** was prepared by treating compound **29** with TFA/Thioanisole 95:5 mixture at 40°C for 1h. After removing TFA under vacuum, washing 5 times with diethyl ether and then drying under vacuum, compound **30** was obtained in 93% yield as an orange powder. Di-allyl yG∧C.HCl salt **31** on the other hand was prepared by treating compound **29** with 4N HCl/dioxane at 70°C for 3h (Figure 4.34).

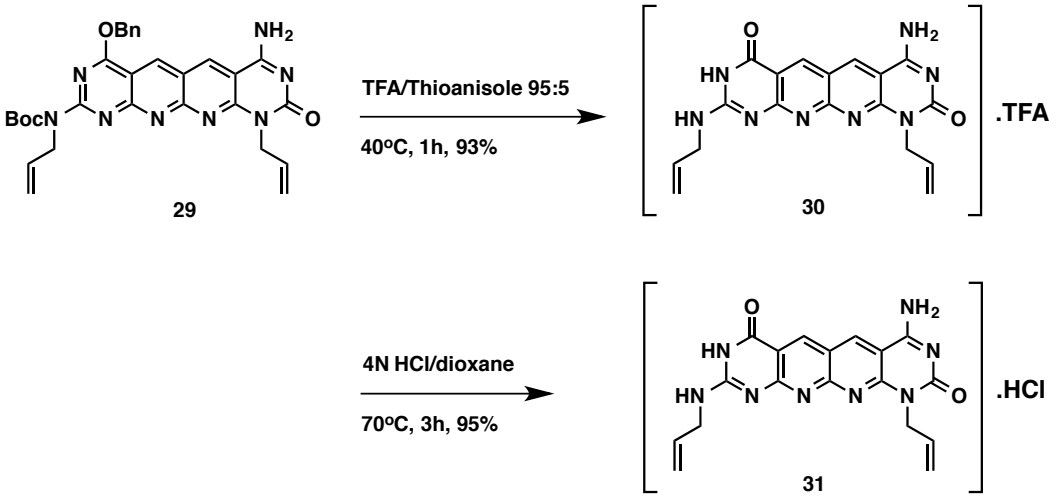

Figure 4.34. Preparation of the di-allyl yG∧C TFA and HCl salts.

Overall, the successful strategy toward di-allyl yG∧C module **30** (or **31**) included 13 steps with an overall yield of 1.6% and an average stepwise yield of 74% (Figure 4.35). Both compounds **30** and **31** were characterized by ^{1}H and ^{13}C NMR, low and high resolution mass, IR and elemental analysis.

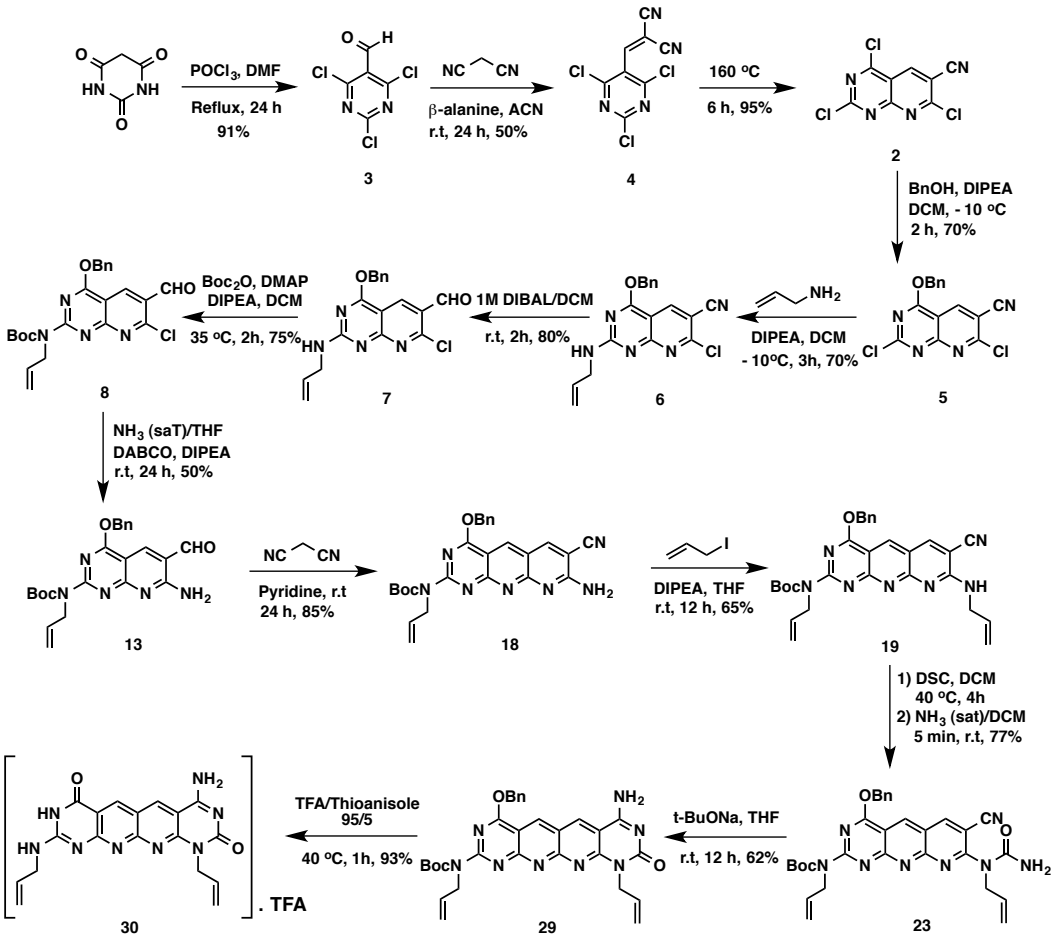

Figure 4.35. Overall successful strategy toward di-allyl yG∧C module **30**.

4.5 Self-Assembly Studies[§§§]

The self-assembly of di-allyl yG∧C.TFA salt **30** was studied in DMSO, MeOH and DMF using scanning electron microscopy (SEM) and transmission electron microscopy (TEM) techniques. Initially, 1 mg/ml solution of **30** in DMF was prepared and then subjected to different heating conditions (40-90°C) and left at room temperature for aging. Time-dependent SEM imaging studies revealed no nanotubes formation even after 2 weeks of aging. Self-assembly studies in DMSO and MeOH on the other hand, resulted in short nanotubes or bundles of nanotubes depending on the heating conditions that were initially applied. When 1 mg/ml solutions of **30** in MeOH and DMSO were heated to 70°C, well-dispersed short nanotubes were found by SEM in both solutions within one hour of aging (Figure 4.36 A,B), which remained short over time. While no nanotubes were found upon heating the MeOH and DMSO solutions above 80°C, heating conditions below 60°C resulted in bundles of nanotubes within one hour of aging (Figure 4.36 C,D).

[§§§] SEM and TEM microscopy studies of self-assembly were performed by Dr. Jae-Young Cho.

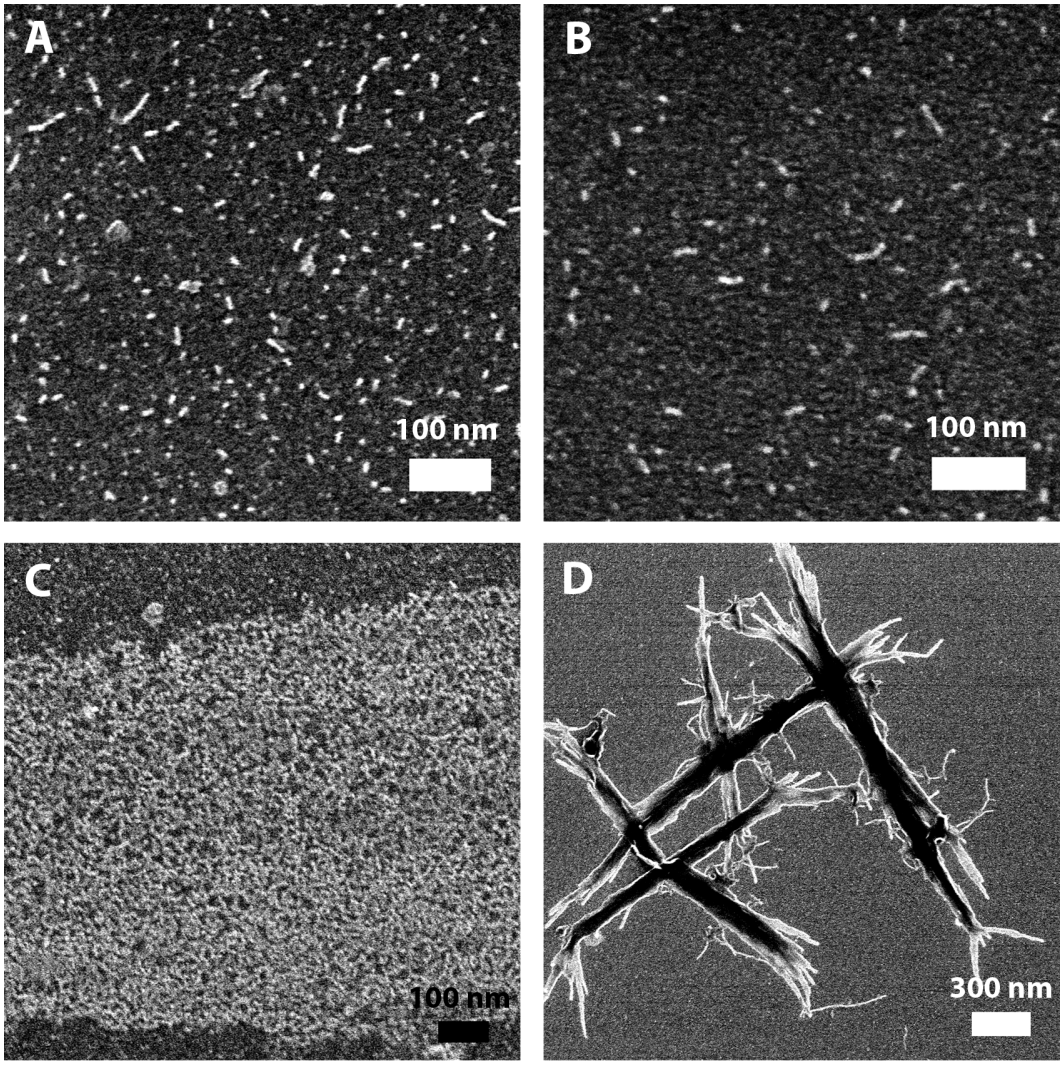

Figure 4.36. SEM images of **30** at 0.1 mg/ml concentration (A) in DMSO (70°C initial heating) after 1 week; (B) in MeOH (70°C initial heating) after 1h; (C) in DMSO (40°C initial heating) after 4 days; and (D) in DMSO (no initial heating) after 4 days.

The self-assembly of the HCl salt **31** was examined in DMSO using the heating conditions that resulted in nanotubes formation in the TFA salt **30** (heating to 70°C). However, SEM imaging revealed bundles of long and short nanotubes within 1 h of aging (Figure 4.37). The self-assembly of **31** in DMSO was also studied under other heating conditions (below and above 70°C), but similar bundles of nanotubes were found.

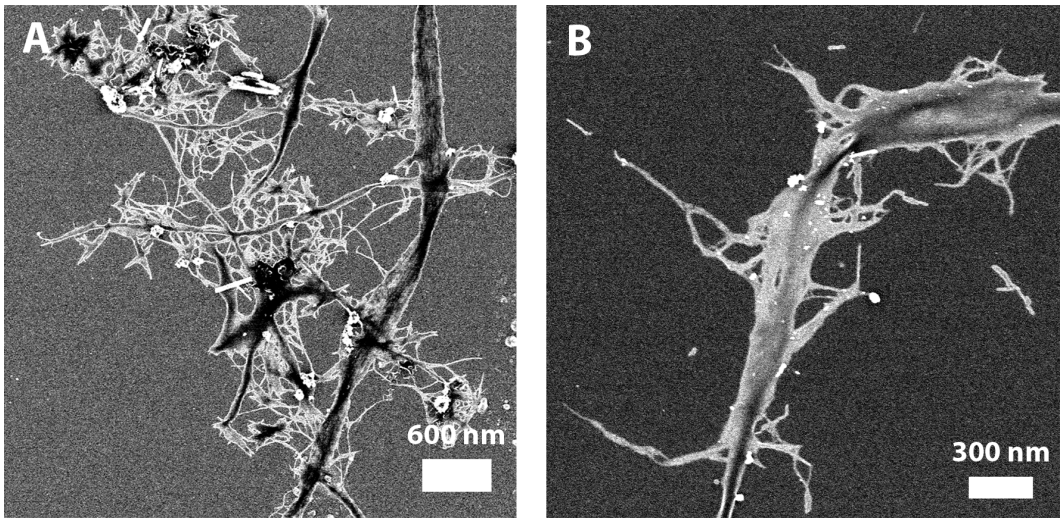

Figure 4.37. SEM images of **31** in DMSO (0.1 mg/ml) after 1 day at (A) 70^{o}C initial heating conditions; (B) no initial heating.

Since the DMSO solution of **30** under 70°C heating conditions resulted in well-dispersed short nanotubes, this solution was chosen for the TEM study in order to measure the outer diameter of the nanotubes and compare with the calculated value from the theoretical modeling. Thirty TEM measurements were made, and the nanotubes were found to have an average outer diameter of 4.00 ± 0.12 nm (Figure 4.38 A,B). This value was well aligned with the calculated diameter from the molecular modeling (see section 4.6) which was found to be 3.9 nm. This study established that the tetracyclic yG∧C motif self-assembled into nanotubes with diameter increase of 0.9 nm and 0.4 nm over the bicyclic G∧C (3.07 ± 0.15 nm) and tricyclic xG∧C (3.58 ± 0.13 nm) motifs, respectively (Figure 4.38 C).[5,6,8,15] The calculated and measured outer diameters of the RNTs by G∧C, xG∧C and yG∧C motifs are summarized in Table 4.3.

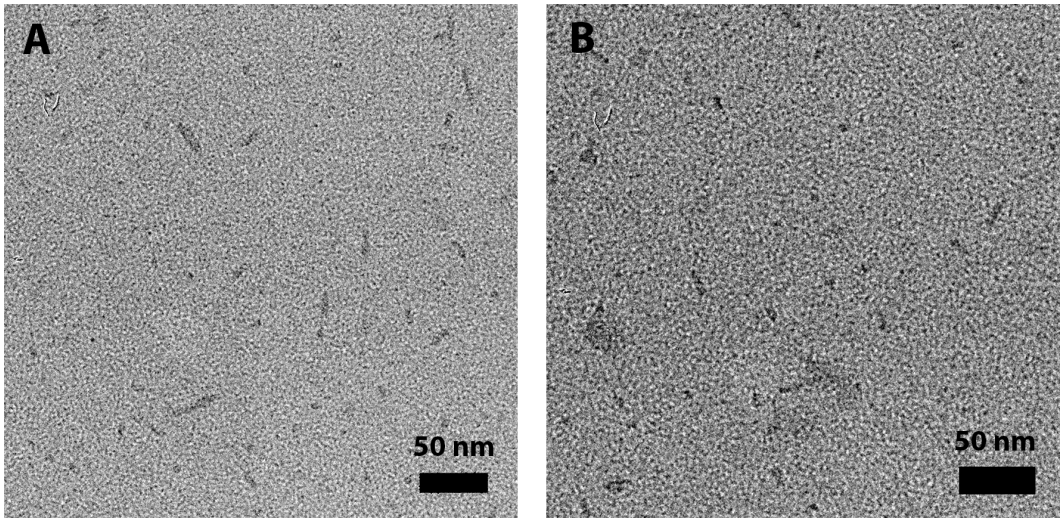

Figure 4.38. (A,B) Representative TEM images of **30** in DMSO at 0.1 mg/ml concentration after 1 week.

Table 4.3. Comparison of the calculated (molecular modeling) and measured (TEM) outer diameters of the RNTs by the G∧C, xG∧C and yG∧C.

	G∧C (bicycle)[15]	**xG∧C (tricycle)**[6]	**yG∧C (tetracycle)**
Measured (TEM)	3.07 ± 0.15 nm	3.58 ± 0.13 nm	4.00 ± 0.12 nm
Calculated (modeling)	3.1 nm	3.5 nm	3.9 nm

4.6 Molecular Modeling[****]

Based on the previous modeling procedures for diallyl G∧C and diallyl xG∧C, the conformational search for the diallyl side chain was conducted as follows.[6]

Step 1. The motif was minimized, then 64 conformers generated by varying dihedral angles by every 45° around two bonds as shown by the arrows in Figure 4.39.

[****] Modeling studies were conducted by Dr. Takeshi Yamazaki.

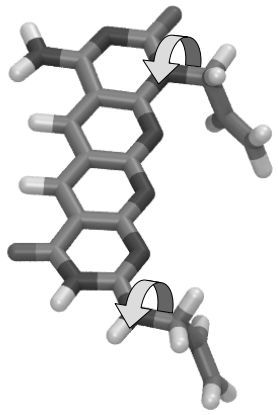

Figure 4.39. Varying the dihedral angles in the modeling of di-allyl yG∧C.

Step 2. Each of the 64 non–optimized conformers were multiplied and arranged to form a six–fold symmetry rosette maintained by 18 H–bonds. The rosette were then stacked in a tubular fashion with an inter–planar separation of 4.5 Å and a rotation angle of 30° per rosette along the main axis. This arrangement was based on previous work done on similar systems.

Step 3. Molecular models for the RNTs were generated using Macromodel 9.9. The RNT interaction models employed the OPLS2005 force field. The PRCG energy minimization was then applied to the 64 RNTs consisting each of 9 rosettes, with the top and bottom 2 rosettes as well as all the yG∧C bases fixed to reduce end effects. The central rosette in each of the optimized 64 RNTs was taken to finally construct RNTs composed of N=1–15 rosettes.

Step 4. In order to find the most stable RNT conformation in methanol, the free energy of RNT in methanol was defined as the sum of internal energy obtained by the molecular mechanics with Macromodel 9.9 and the solvation free energy obtained by the statistical mechanical theory of molecular liquid (3D-RISM theory). By comparing the free energies of each RNT conformations at N=15, it

was found that the following RNT conformation is the most stable among 64 conformations considered.

Finally, the outer diameter of the RNTs was found to be 38.76 Å, which is in agreement with the measured diameter by TEM (Figure 4.40).

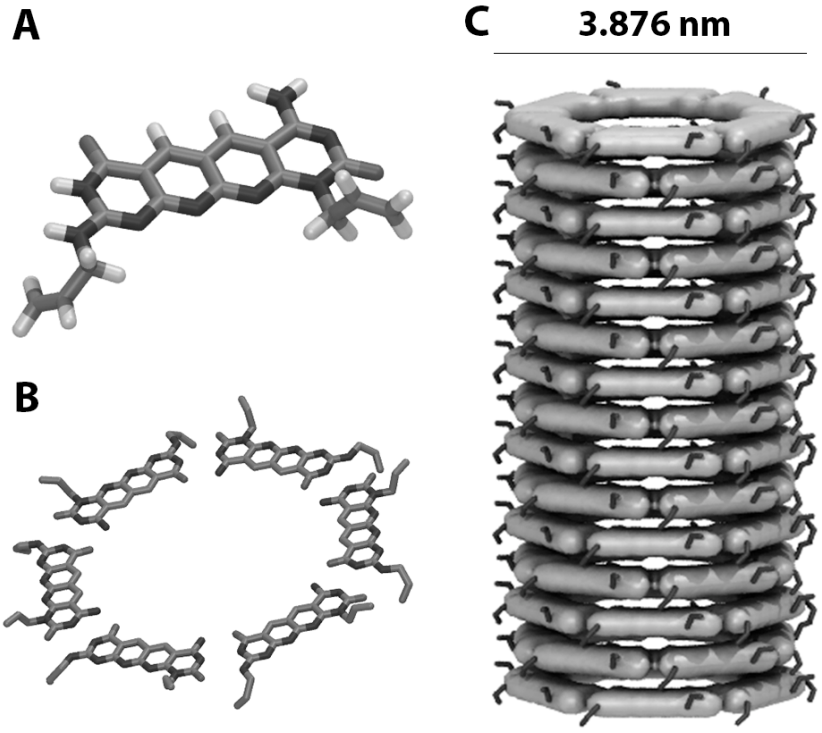

Figure 4.40. A modeling showing (A) the di-allyl yG∧C motif; (B) A hexameric rosette; and (C) the corresponding rosette nanotubes with the calculated outer diameter.

The association free energy as a function of number of rosette stacks shows that the yG∧C motif forms RNT in methanol (Figure 4.41).

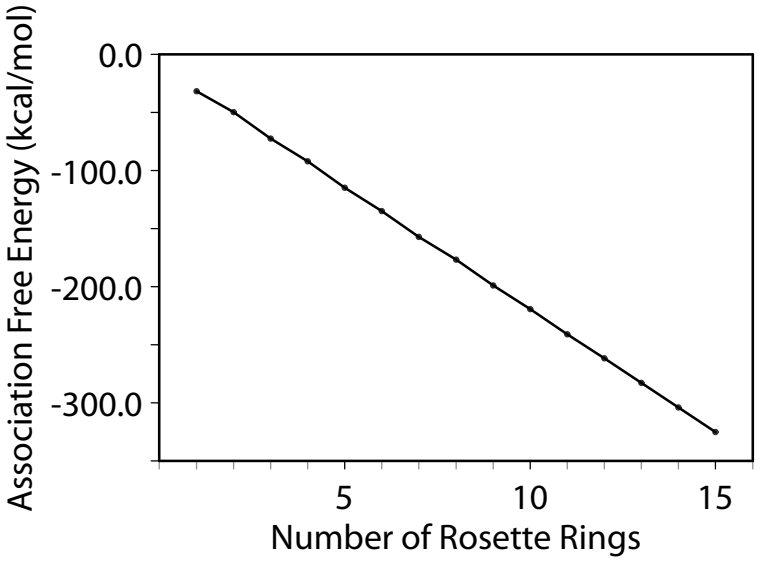

Figure 4.41. Association free energy as a function of number of rosette stacks.

4.7 Progress Toward Water Soluble Di-lysine yG∧C

In addition to the synthesis and self-assembly of the organic-soluble di-allyl yG∧C module **1**, I also explored the synthesis of water-soluble di-lysine yG∧C using a procedure that was used for the synthesis of the lysine-G∧C and lysine-xG∧C modules.[5,15] Starting with the protected tetracycle **29**, Boc protection reaction was initially employed to protect the appended amino group on the cytosine ring. In a straightforward reaction, compound **29** in THF was treated with Boc_2O (1.2 equivalents), DMAP (1 equivalent) and DIPEA (3 equivalents) at room temperature. After stirring for 3h, mass and TLC analyses revealed complete conversion of the starting material into compound **32**, which was then isolated after column chromatography in 73% yield (Figure 4.42).

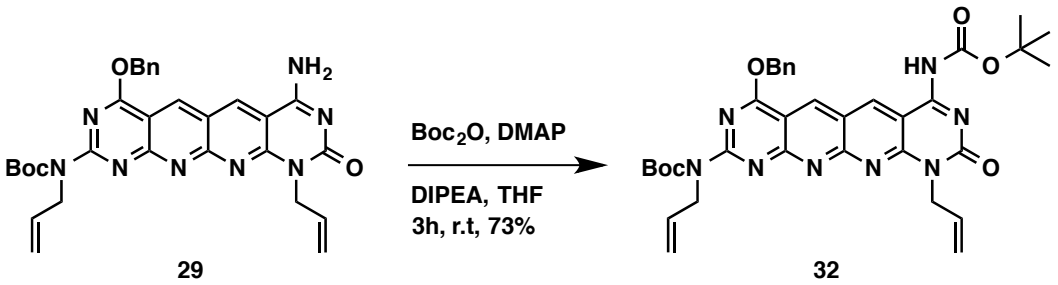

Figure 4.42. Boc protection reaction to obtain compound **32**.

I next explored the dihydroxylation reaction followed by oxidative cleavage to prepare di-aldehyde **34**. In two consecutive steps, compound **32** in THF was treated with 0.1M OsO_4/t-BuOH (0.64 equivalents) and 50% NMO/H_2O (6 equivalents) at room temperature for 6 h. After workup, the crude mixture was dissolved in DCM and then treated with $NaIO_4$ (4.5 equivalents) in water at room temperature for overnight. Compound **34** was eventually isolated in 57% (two-steps) after column chromatography (Figure 4.43).

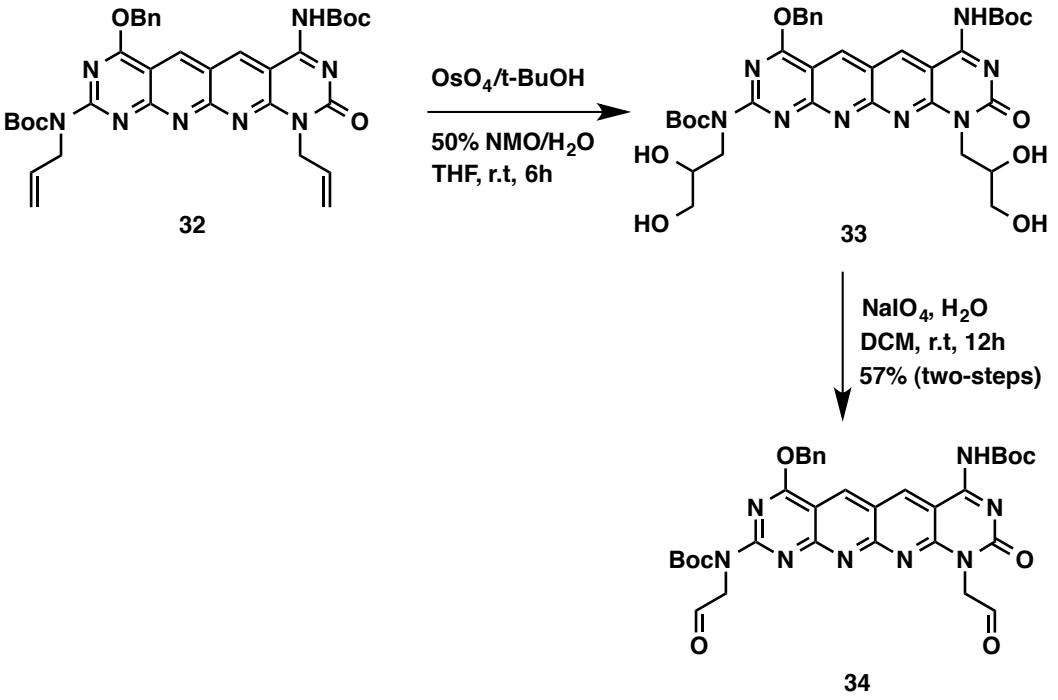

Figure 4.43. Dihydroxylation followed by oxidative cleavage to prepare compound **34**.

Having obtained di-aldehyde **34**, my subsequent task was the reductive amination with the protected lysine **35** in order to prepare the protected di-lysine module **36**. Compound **34** was initially treated with the protected lysine **35** (2.5 equivalents) and DIPEA (3 equivalents) in 1,2-DCE at room temperature for 10 min. $NaBH(OAc)_3$ (2.5 equivalents) was then added, and the mixture was stirred at room temperature for 24h. Mass and TLC analyses over time indicated that the starting material was completely decomposed and complex mixture of by-products had formed. In another attempt, the first step was extended to 4 h to allow the formation of the di-imine intermediate, and then $NaBH(OAc)_3$ was added and the mixture was stirred at room temperature overnight. Here again, compound **34** decomposed as soon as $NaBH(OAc)_3$ was added (Figure 4.44).

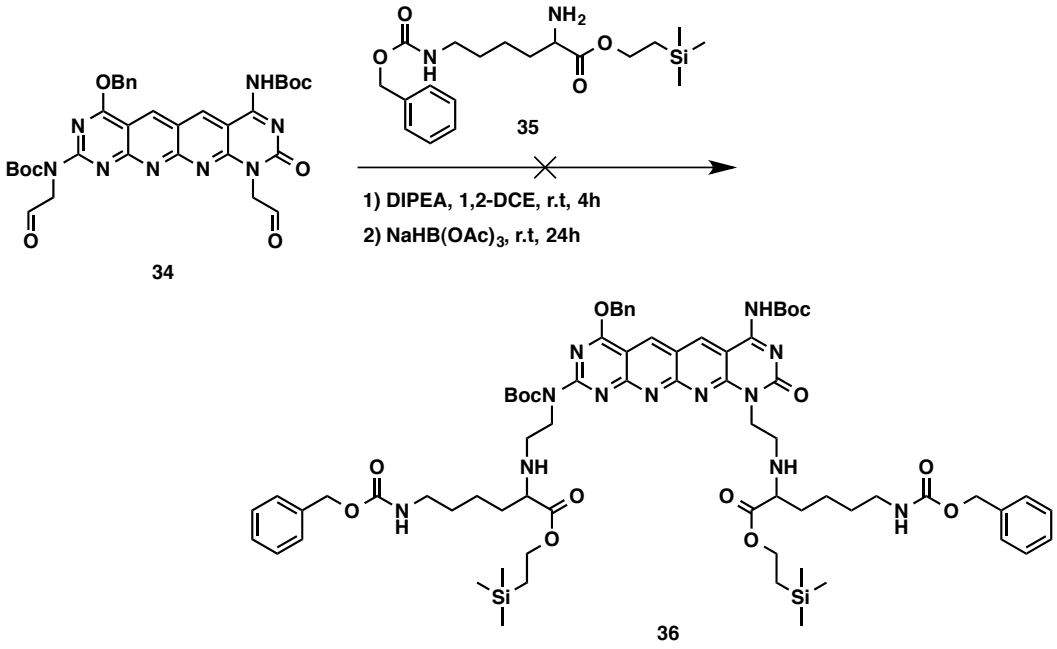

Figure 4.44. Unsuccessful reductive amination attempt to anchor two lysine amino acid moieties on the yG∧C module.

It was then reasoned that sodium triacetoxy borohydride had reacted with the ring system (probably reducing the naphthyridine core), leading to the decomposition

of compound **34**. Another possibility is that, sodium borohydride had deprotonated the appended Boc protected amino group on the cytosine ring, which might have caused the decomposition. Therefore, a possible solution to this problem is to protect the amino group in **29** with two Boc protecting groups. Not only can this remove the proton which may be responsible for the decomposition, it can also create more steric hindrance around the naphthyridine core, which may reduce the possibility of the reaction of $NaBH(OAc)_3$ with the ring system. I have not attempted the di-Boc protection strategy, but this would a logical future approach toward the di-lysine yG∧C module.

4.7 Conclusions and Outlook

The synthesis of di-allyl yG∧C module **1**, a tetracyclic variant of the bicyclic G∧C and tricyclic xG∧C motifs, was successfully developed. Starting with the commercially available barbituric acid, the overall successful strategy included 13 steps with 1.6% overall yield and 74% average stepwise yield. Self-assembly of yG∧C.TFA salt **30** in DMSO and MeOH successfully led to RNTs with a 4.0 nm outer diameter, which was in agreement with the molecular modeling calculations. Although short nanotubes were formed, the successful self-assembly of yG∧C was an impressive demonstration of the versatility of the RNT system and its tolerance for further expansion in the G∧C base.

Finally, progress towards the synthesis of water-soluble di-lysine yG∧C motif utilizing mono-Boc protection strategy was presented. Although the reductive amination step was unsuccessful due to the decomposition of di-aldehyde **34** under reductive conditions, other approaches could be pursued to anchor the two lysine amino acids on the molecule. For instance, di-Boc protection strategy could be utilized to provide more steric hindrance around the naphthyridine core. Alternatively, olefin metathesis approach with allyl functionalized lysine could be

employed, which would be a good strategy to avoid the use of reducing agents in the synthesis.

4.8 Experimental

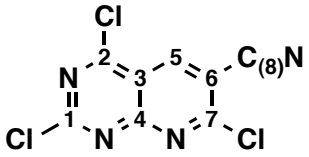

Synthesis of compound **2**. Compound **4** (40 g, 0.16 mol) was heated to 160°C in a round bottom flask capped with $CaSO_4$ drying tube for 6h in an oven. The solid was then dissolved in DCM and stirred for overnight, and then the suspension was filtered under vacuum. The filtrate was concentrated under reduced pressure to provide the analytically pure compound **2** ($C_8HCl_3N_4$, 38 g) in 95% yield as a brown solid. R_f = 0.5 (10 % EtOAc / Hexane).

Low-res ESI-MS (positive): Expected mass for $(M+H^+)/z$, 258.9. Observed, 258.7 $[(M+H^+)/z]$.

^{1}H-NMR (600 MHz, $CDCl_3$) δ (ppm): 8.95 (C_5H, sharp s, 1H).

^{13}C-NMR (600 MHz, $CDCl_3$) δ (ppm): 164.9 (C_4), 163.1 (C_1), 159.6 (C_7), 159.1 (C_2), 143.4 (C_5), 115.8 (C_3), 113.1 (C_8), 112.1 (C_6).

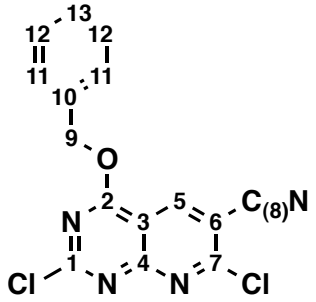

Synthesis of compound **5**. Compound **2** (10 g, 38.8 mmol) was dissolved in anhydrous DCM (500 mL) and cooled to -10°C. A mixture of benzyl alcohol (4.5 ml, 42.7 mmol) and DIPEA (7.5 ml, 43.1 mmol) was added dropwise over 1 h. The mixture was stirred at -10°C for a total of 2h, then the solvent was removed under vacuum. Recrystallization of the solid from $CHCl_3$ / Hexane afforded the pure compound **5** ($C_{15}H_8Cl_2N_4O$, 8.9 g) in 70% yield. R_f = 0.7 (30 % EtOAc / Hexane).[6]

Low-res ESI-MS (positive): Expected mass for $(M+H^+)/z$, 331.0. Observed, 331.4 $[(M+H^+)/z]$.

^{1}H-NMR (600 MHz, $CDCl_3$) δ (ppm): 8.80 (C_5H, sharp s, 1H), 7.53-7.44 ($C_{11-13}H$, m, 5H), 5.70 (C_9H, s, 2H).

^{13}C-NMR (600 MHz, $CDCl_3$) δ (ppm): 167.8 (C_2), 164.1 (C_4), 160.3 (C_1), 158.0 (C_7), 141.7 (C_5), 133.5 (C_{10}), 129.5 (C_{12}), 129.2 (C_{13}), 128.9 (C_{11}), 113.6 (C_8), 109.7 (C_3), 108.1 (C_6), 71.9 (C_9).

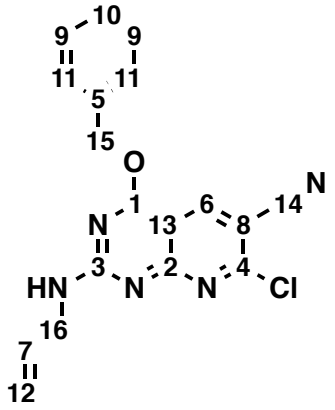

Synthesis of compound **6**. A suspension of compound **5** (10 g, 30 mmol) in DCM (700 mL) was treated with allyl amine (2.5 ml, 33 mmol) and DIPEA (10.5 mL, 60 mmol). The mixture was stirred at -10°C for 3h, then placed in -20°C fridge for overnight. The light yellowish precipitate was separated by filteration under vacuum, and then dried for 2 days under high vacuum to yield compound **6** ($C_{18}H_{14}ClN_5O$, 7.4 g, 70%). R_f = 0.2 (30 % EtOAc / Hexane).[7]

Low-res ESI-MS (positive): Expected for $(M+H^+)/z$, 352.1. Observed, 352.5 $[(M+H^+)/z]$.

^{1}H-NMR (600 MHz, DMSO-d_6, 90 °C) δ (ppm): 8.70 (C_6H, sharp s, 1H), 8.35 (NH, broad s, 1H), 7.54-7.35 ($C_{9\text{-}11}$H, m, 5H), 5.98-5.83 (C_7H, m, 1H), 5.59 (C_{15}H, s, 2H), 5.24-5.09 (C_{12}H, m, 2H), 4.08-4.07 (C_{16}H, m, 2H).

^{13}C-NMR (150 MHz, DMSO-d6, 90 °C) δ (ppm): 166.2 162.1 161.9 154.9 (C_1) (C_2) (C_3) (C_4), 141.3 135.2 134.4 (C_5) (C_6) (C_7), 128.2 128.1 128.0 (C_9) (C_{10}) (C_{11}), 115.6 115.2 104.9 100.7 (C_8) (C_{12}) (C_{13}) (C_{14}), 68.5 (C_{15}), 43.1 (C_{16}).

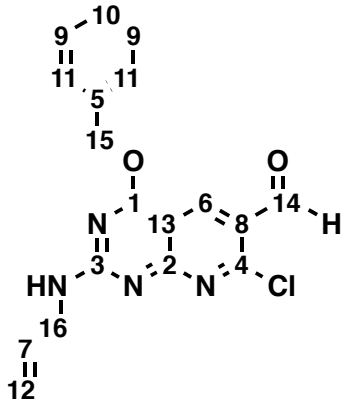

Synthesis of compound **7**. To a suspension of compound **6** (5 g, 14.2 mmol) in DCM (500 mL) added DIBAL-H solution in DCM (29 mL, 1M in DCM, 28.4 mmol) dropwise over 30 min. The suspension became clear orange solution after the full addition of the DIBAL-H solution. After stirring 2h at room temperature under argon, 1N HCl (100 mL) and MeOH (100 mL) were added and the mixture was stirred 30 min at room temperature. The DCM layer was separated, and the aqueous layer was further extracted with DCM several times. DCM layers were combined, dried over Na_2SO_4 and concentrated under reduced pressure. The crude solid was purified by column chromatography (SiO_2 0 – 1 % MeOH / DCM) to yield compound **7** as a yellow solid ($C_{18}H_{15}ClN_4O_2$, 4 g, 80%). R_f = 0.8 (3 % MeOH / DCM).

Low-res ESI-MS (positive): Expected mass for $(M+H^+)/z$, 355.5. Observed, 355.4 $[(M+H^+)/z]$.

^{1}H-NMR (600 MHz, $CDCl_3$, 50°C) δ (ppm): 10.37 ($C_{14}H$, s, 1H), 8.75 (C_6H, sharp s, 1H), 7.47-7.37 ($C_{9\text{-}11}H$, m, 5H), 6.25 (NH, brs, 1H), 6.00-5.97 (C_7H, m, 1H), 5.53 ($C_{15}H$, s, 2H), 5.32- 5.21 ($C_{12}H$, m, 2H), 4.31 ($C_{16}H$, m, 2H).

^{13}C-NMR (150 MHz, $CDCl_3$, 50°C) δ (ppm): 188.2 (C_{14}), 168.4 163.9 162.8 158.7 (C_1) (C_2) (C_3) (C_4), 136.8 135.3 134.0 (C_5) (C_6) (C_7), 129.04 129.01 128.6 123.7 (C_8) (C_9) (C_{10}) (C_{11}), 117.3 106.7 (C_{12}) (C_{13}), 69.8 (C_{15}), 44.5 (C_{16}).

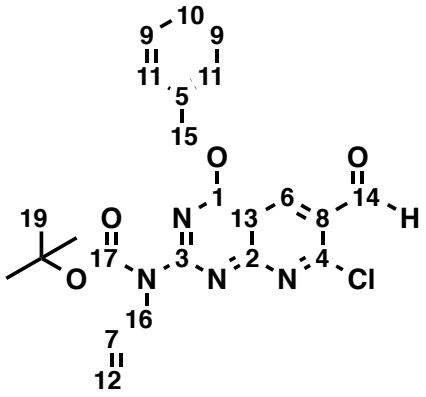

Synthesis of compound **8**. To a suspension of compound **7** (5.0 g, 14.1 mmol) in DCM (500 mL) added Boc_2O (7.7 g, 35.3 mmol), DMAP (344 mg, 2.8 mmol) and DIPEA (5.0 ml, 28.2 mmol). The mixture was stirred at 35°C for 2 h. dH_2O (200 mL) was then added, and the mixture was stirred vigorously at room temperature for 10 min before separating the DCM layer. The aqueous layer was then extracted with DCM (2x), and the combined organic layers were dried over Na_2SO_4. DCM was evaporated (rotavap) and the crude was purified by column chromatography (SiO_2 0 – 1 % MeOH / DCM) to yield compound **8** as a light yellowish solid ($C_{23}H_{22}ClN_5O_3$, 4.8 g, 75%). R_f = 0.9 (3 % MeOH / DCM).

Low-res ESI-MS (positive): Expected mass for $(M+H^+)/z$, 455.5. Observed, 455.4 $[(M+H^+)/z]$.

^{1}H-NMR (600 MHz, $CDCl_3$) δ (ppm): 10.43 ($C_{14}H$, s, 1H), 8.88 (C_6H, sharp s, 1H), 7.50-7.38 ($C_{9\text{-}11}H$, m, 5H), 6.02-5.98 (C_7H, m, 1H), 5.62 ($C_{15}H$, s, 2H), 5.25 ($C_{12}H$, dd, J = 17.4 Hz, 1.8 Hz, 1H), 5.12 ($C_{12}H$, dd, J = 10.8 Hz, 1.8 Hz, 1H), 4.74-4.72 ($C_{16}H$, m, 2H), 1.57 ($C_{19}H$, s, 9H).

^{13}C-NMR (150 MHz, $CDCl_3$) δ (ppm): 187.9 (C_{14}) 168.3 162.2 161.8 158.3 (C_1) (C_2) (C_3) (C_4) 152.6 (C_{17}), 136.9 134.8 133.5 (C_5) (C_6) (C_7), 128.9 128.8 128.7 125.6 (C_8) (C_9) (C_{10}) (C_{11}), 116.7 107.2 (C_{12}) (C_{13}), 82.7 (C_{18}), 70.3 (C_{15}), 49.9 (C_{16}) 28.1 (C_{19}).

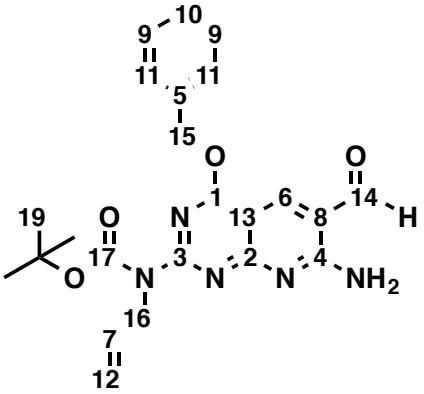

Synthesis of compound **13**. Compound **8** (100 mg, 0.22 mmol) was dissolved in the freshly prepared NH_3 (sat)/THF (10 mL) solution and stirred at room temperature. To this solution, DABCO (27 mg, 0.24 mmol) and DIEPA (0.04 mL, 0.22 mmol) were added. After stirring the mixture at room temperature for 2 days, the solvent was evaporated under reduced pressure, and the crude was purified by column chromatography (SiO_2 0 – 1 % MeOH / DCM) to provide compound **13** as a yellowish solid ($C_{23}H_{24}N_6O_3$, 48 mg, 50%). R_f = 0.5 (5 % MeOH / DCM).

Low-res ESI-MS (positive): Expected mass for $(M+H^+)/z$, 436.5. Observed, 436.6 $[(M+H^+)/z]$.

^{1}H-NMR (600 MHz, $CDCl_3$) δ (ppm): 9.86 ($C_{14}H$), 8.49 (C_6H, sharp s, 1H), 7.49-7.36 ($C_{9\text{-}11}H$, m, 5H), 6.05-5.96 (C_7H, m, 1H), 5.56 ($C_{15}H$, s, 2H), 5.22 ($C_{12}H$, dd, J = 17.4 Hz, 1.8 Hz, 1H), 5.09 ($C_{12}H$, dd, J = 10.2 Hz, 1.2 Hz, 1H), 4.68-4.67 ($C_{16}H$, m, 2H), 1.53 ($C_{19}H$, s, 9H).

^{13}C-NMR (150 MHz, $CDCl_3$) δ (ppm): 191.2 (C_{14}), 167.6 163.4 162.3 160.7 (C_1) (C_2) (C_3) (C_4), 153.1 (C_{17}), 144.2 135.7 134.1 (C_5) (C_6) (C_7), 128.8 128.7 128.7 (C_9) (C_{10}) (C_{11}), 116.2 115.2 101.2 (C_8) (C_{12}) (C_{13}), 82.1 (C_{18}), 69.4 (C_{15}), 49.9 (C_{16}), 28.2 (C_{19}).

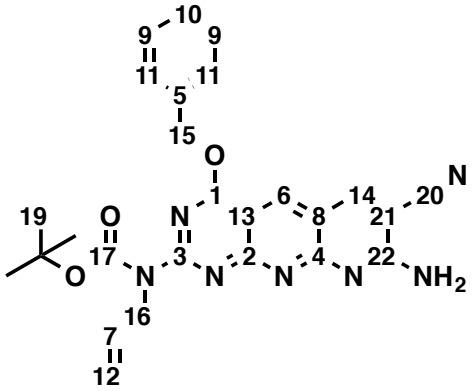

Synthesis of compound **18**. Compound **13** (500 mg, 1.2 mmol) was dissolved in anhydrous pyridine (12 mL), then malononitrile (129 mg, 1.95 mmol) was added and the solution was stirred at room temperature for 24 h under argon. Pyridine was then removed under vacuum (rotavap), and the crude was purified by column chromatography (SiO_2 20 – 30 % EtOAc / DCM) to provide compound **18** as a yellow glassy solid ($C_{26}H_{25}N_7O_3$, 493 mg, 85 %). R_f = 0.3 (5 % MeOH / DCM).

Low-res ESI-MS (positive): Expected mass for $(M+H^+)/z$, 484.1. Observed, 484.4 $[(M+H^+)/z]$.

^{1}H-NMR (600 MHz, CD_2Cl_2) δ (ppm): 8.81 (C_6H, sharp s, 1H), 8.42 (C_{14}H, sharp s, 1H), 7.56-7.39 ($C_{9\text{-}11}$H, m, 5H), 6.15 (NH, brs, 2H), 6.08-6.03 (C_7H, m, 1H), 5.66 (C_{15}H, s, 2H), 5.31 (C_{12}H, dd, J = 17.4 Hz, 1.2 Hz, 1H), 5.15 (C_{12}H, dd, J = 10.2, 1.2 Hz, 1H), 4.73-4.72 (C_{16}H, m, 2H), 1.55 (C_{19}H, s, 9H).

^{13}C-NMR (150 MHz, CD_2Cl_2) δ (ppm): 168.7 163.0 161.8 160.5 (C_1) (C_2) (C_3) (C_4), 159.5 (C_{22}), 153.7 (C_{17}), 147.0 (C_{14}), 137.8 136.1 134.8 (C_5) (C_6) (C_7), 129.3 129.24 129.23 (C_9) (C_{10}) (C_{11}), 116.6 115.8, 115.4, 107.5, 97.8 (C_8) (C_{12}) (C_{13}) (C_{20}) (C_{21}), 82.8 (C_{18}), 70.4 (C_{15}), 50.5 (C_{16}), 28.5 (C_{19}).

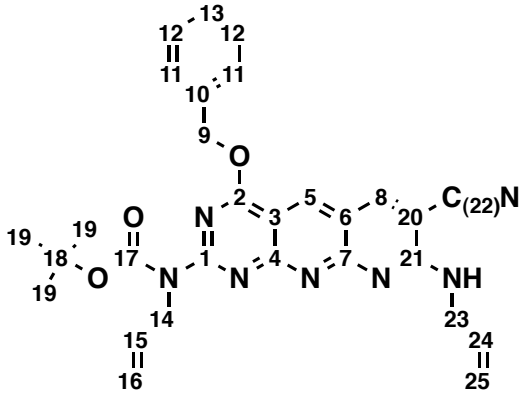

Synthesis of compound **19**. To a solution of compound **18** (300 mg, 0.62 mmol) in anhydrous THF (50 mL) added allyl iodide (0.4 ml, 4.4 mmol) and DIEPA (0.43 ml, 2.5 mmol), and the mixture was stirred in dark at room temperature for 24 h. dH_2O (25 mL) was then added, and THF was removed under vacuum. The aqueous layer was then extracted with DCM (3x) and the organic extracts were dried over Na_2SO_4. After removing DCM (rotavap), the crude oil was purified by column chromatography (SiO_2 0 – 1 % MeOH / DCM) to provide compound **19** as an orange oil ($C_{29}H_{29}N_7O_3$, 211 mg, 65 %). R_f = 0.4 (5 % MeOH / DCM).

High-resolution Positive ESI-MS: Expected mass for $(M+H^+)/z$, 524.2410. Observed, 524.2396 $[(M+H^+)/z]$.

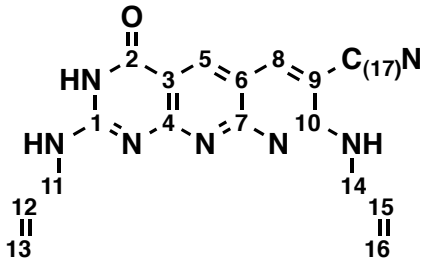

Synthesis of compound **20**. Compound **19** (25 mg, 0.048 mmol) was dissolved in a mixture containing TFA:TIS:H_2O (95:2.5:2.5 volume ratio). After stirring 1 h at

40°C, TFA was removed under vacuum. The residual solid was then subjected to repeated cycle (5x) of washing with diethyl ether, sonicating and centrifuging. After drying 2 days under high vacuum, compound **20** was obtained as an orange solid ($C_{17}H_{15}N_7O$, 15.1 mg, 95 %). Decomposed >400°C.

High-resolution Positive ESI-MS: Expected mass for $(M+H^+)/z$, 334.1416. Observed, 334.1408 $[(M+H^+)/z]$.

^{1}H-NMR (600 MHz, DMSO-d_6 + 10% TFA-d) δ (ppm): 8.96 (C_5H, sharp s, 1H), 8.80 (C_8H, sharp s, 1H), 5.80-6.0 (C_{11}H, C_{14}H, m, 2H), 5.35 (C_{14}H, d, J = 6.0 Hz, 2H), 5.28-5.10 (C_{16}H, C_{13}H, m, 4H), 4.11 (C_{11}H, d, J = 5.4 Hz, 2H).

^{13}C-NMR (600 MHz, DMSO-d_6 + 10% TFA-d) δ (ppm): 160.7 (C_{10}), 159.6 (C_2), 159.4 (C_7), 157.7 (C_1), 157.6 155.7 152.1 148.5 143.0 (C_{12}) (C_{15}) (C_5) (C_8) (C_4), 133.3 130.8 129.2 119.2 (C_6) (C_{16}) (C_{11}) (C_{13}), 111.1 110.3 94.9 (C_3) (C_{17}) (C_9), 40.6 (C_{14}), 43.7 (C_{11}).

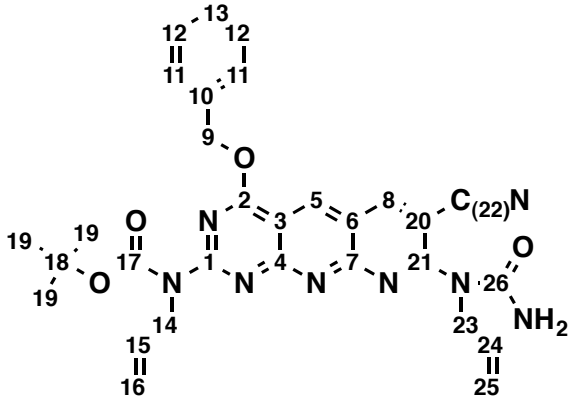

Synthesis of compound **23**. Compound **20** (100 mg, 0.19 mmol) was dissolved in DCM (25 mL), then di(n-succinimydal) carbonate (340 mg, 1.33 mmol) was added and the mixture was stirred at 40°C for 4 h. Preprepared NH_3 (sat)/DCM solution was then added, and the mixture was stirred for 5 min at room temperature. The solution was then loaded on silica gel column for purification

(SiO_2 0.5 – 1 % MeOH / DCM), which provided compound **23** as an orange oil ($C_{30}H_{30}N_8O_4$, 83 mg, 77%). R_f = 0.6 (5 % MeOH / DCM).

High-resolution Positive ESI-MS: Expected mass for $(M+H^+)/z$, 567.2468. Observed, 567.2460 $[(M+H^+)/z]$.

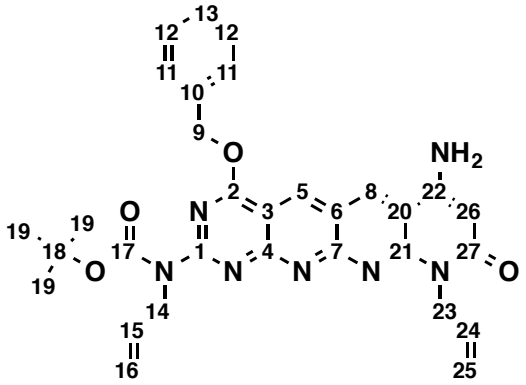

Synthesis of compound **29**. To a solution of compound **23** (375 mg, 0.66 mmol) in anhydrous THF (75 mL) added t-BuONa (444 mg, 4.6 mmol) and stirred at room temperature for overnight. NH_4Cl (sat) aqueous solution (50 mL) was added, then THF was removed under vacuum. The aqueous layer was then extracted with DCM (3x), and the organic layers were combined and dried over Na_2SO_4. Column purification of the crude (SiO_2 10 – 20 % MeOH / DCM) provided compound **29** ($C_{30}H_{30}N_8O_4$, 230 mg, 62%) as yellow oil. R_f = 0.3 (15 % MeOH / DCM).

High-resolution Positive ESI-MS: Expected mass for $(M+H^+)/z$, 567.2468. Observed, 567.2460 $[(M+H^+)/z]$.

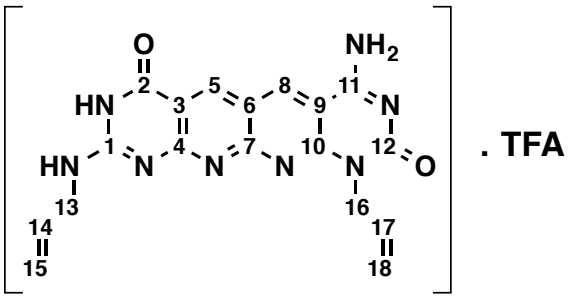

Synthesis of compound **30**. Compound **29** (33 mg, 0.058 mmol) was dissolved in a solution of TFA:thioanisole (95:5 volume ratio), and the mixture was stirred at 40°C for 1 h. TFA was then removed under vacuum, and the residual solid was subjected to repeated cycles (5x) of washing with diethyl ether, sonicating and centrifuging. After drying 2 days under high vacuum, compound **30** was obtained as an orange solid ($C_{18}H_{16}N_8O_2$, 30 mg, 93%). Decomposed >400°C.

High-resolution Positive ESI-MS: Expected mass for $(M+H^+)/z$, 377.1474. Observed, 377.1463 $[(M+H^+)/z]$.

^{1}H-NMR (600 MHz, TFA-d) δ (ppm): 9.82 (C_5H, sharp s, 1H), 9.39 (C_8H, sharp s, 1H), 5.80-6.10 (C_{14}H, C_{17}H, m, 2H), 5.69 (C_{16}H, m, 2H), 5.51-5.20 (C_{18}H, C_{15}H, m, 4H), 4.40 (C_{13}H, 2H).

^{13}C-NMR (600 MHz, TFA-d) δ (ppm): 160.7 (C_2), 158.8 (C_7), 158.6 (C_{11}), 155.1 153.4 153.3 (C_1) (C_4) (C_{12}), 148.4 (C_{10}), 145.9 144.2 129.3 127.6 (C_5) (C_8) (C_{17}) (C_{14}), 124.9 121.0 119.2 115.6 103.3 (C_{15}) (C_{18}) (C_3) (C_6) (C_9), 48.6 (C_{16}), 42.3 (C_{13}).

Elemental analysis: calculated for $((C_{18}H_{16}N_8O_2)(H_2O)_{0.4}(CF_3COOH)_{1.2}(MeOH))$ (MW = 552.16): C 46.53, H 4.01, N 20.28. Found: C 46.67, H 3.87, N 19.98.

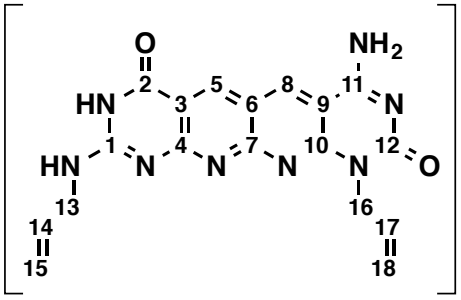

Synthesis of compound **31**. Compound **29** (10 mg, 0.018 mmol) was dissolved in a solution of 4N HCl/dioxane, and the mixture was stirred at 70°C for 3h. Dioxane was then removed under vacuum, and the residual solid was subjected to repeated cycle (5x) of washing with diethyl ether, sonicating and centrifuging. The solid was then dried for 2 days under high vacuum, and compound **31** was obtained as an orange solid ($C_{18}H_{16}N_8O_2$, 11.1 mg, 95%). Decomposed >400°C.

High-resolution Positive ESI-MS: Expected mass for $(M+H^+)/z$, 377.1474. Observed, 377.1463 $[(M+H^+)/z]$.

^{1}H-NMR (600 MHz, TFA-d) δ (ppm): 9.82 (C_5H, sharp s, 1H), 9.39 (C_8H, sharp s, 1H), 5.80-6.10 ($C_{14}H$, $C_{17}H$, m, 2H), 5.69 ($C_{16}H$, m, 2H), 5.51-5.20 ($C_{18}H$, $C_{15}H$, m, 4H), 4.40 ($C_{13}H$, 2H).

^{13}C-NMR (600 MHz, TFA-d) δ (ppm): 160.7 (C_2), 158.8 (C_7), 158.6 (C_{11}), 155.1 153.4 153.3 (C_1) (C_4) (C_{12}), 148.4 (C_{10}), 145.9 144.2 129.3 127.6 (C_5) (C_8) (C_{17}) (C_{14}), 124.9 121.0 119.2 115.6 103.3 (C_{15}) (C_{18}) (C_3) (C_6) (C_9), 48.6 (C_{16}), 42.3 (C_{13}).

Elemental analysis: calculated for $((C_{18}H_{16}N_8O_2)(HCl)_{4.7}(H_2O)_{3.5}(Et_2O)_{0.5})$ (MW = 649.32): C 37.92, H 4.38, N 17.26. Found: C 38.31, H 4.50, N 17.06.

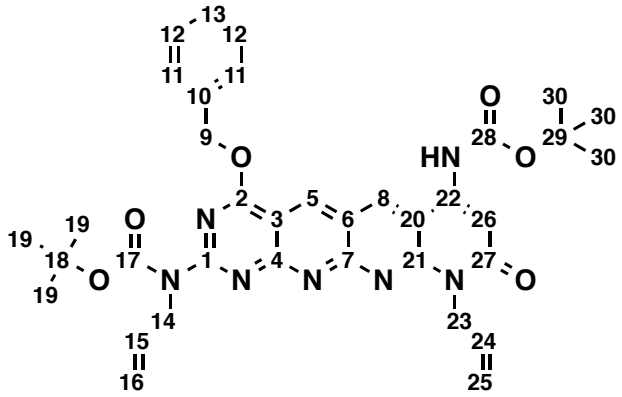

Synthesis of compound **32**. To a solution of compound **29** (50 mg, 0.09 mmol) in THF, Boc_2O (23 mg, 0.11 mmol), DMAP (11 mg, 0.09 mmol) and DIPEA (46 μL, 0.26 mmol) were added and the mixture was stirred at room temperature for 3h. Water was then added to quench the reaction, and THF was removed under vacuum. The aqueous phase was then extracted with DCM, and the organic layers were combined and dried over Na_2SO_4. Column purification of the crude (SiO_2 0.6 – 0.8 % MeOH / DCM) provided compound **32** ($C_{35}H_{38}N_8O_6$, 43 mg, 73%) as brown oil. R_f = 0.5 (5 % MeOH / DCM). MS.

High-resolution Positive ESI-MS: Expected mass for $(M+H^+)/z$, 667.7470. Observed, 667.7478 $[(M+H^+)/z]$.

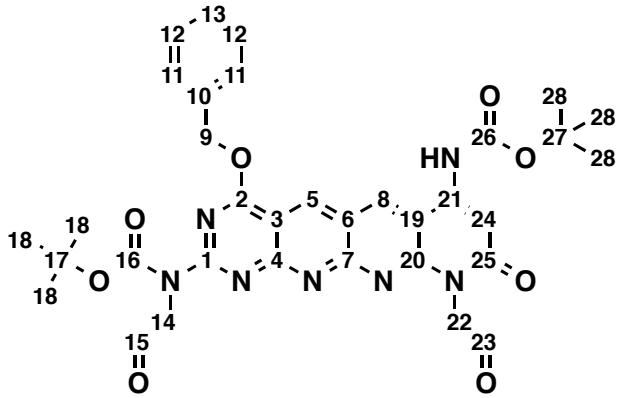

Synthesis of compound **34**. Compound **32** (40 mg, 0.06 mmol) was dissolved in THF (7 mL), then 0.1M OsO_4/t-BuOH (200 μl, 0.04 mmol) and 50% NMO/H_2O (86 μl, 0.36 mmol) were added and the mixture was stirred at room temperature for 6h. 20ml of saturated Na_2SO_3 in water was then added, and THF was removed under vacuum. The aqueous layer was then extracted with DCM, and the organic layers were dried over Na_2SO_4. After removing DCM under vacuum, the crude compound **33** was dissolved in DCM (10 ml), and then treated with $NaIO_4$ (58 mg, 0.27 mmol) in water (2 mL), and the mixture was stirred at room temperature for overnight. The DCM layer was then separated, and the compound **34** was then isolated after column chromatography (SiO_2 1 – 2 % MeOH / DCM) ($C_{35}H_{38}N_8O_6$, 23 mg, 57%) as brown oil. R_f = 0.2 (5 % MeOH / DCM). MS.

High-resolution Positive ESI-MS: Expected mass for $(M+H^+)/z$, 671.6910. Observed, 671.6913 $[(M+H^+)/z]$.

4.9 References

(1) Alsbaiee, A.; Jules, M. S.; Beingessner, R. L.; Cho, J.-Y.; Yamazaki, T.; Fenniri, H. *Tet. Lett.* **2012**, *53*, 1645–1651.

(2) Alsbaiee, A.; Bakkari, El, M.; Fenniri, H. *Mater. Res. Soc. Proc.* **2011**, *1316*, mrsf10–1316–qq12–18.

(3) Chen, Y.; Song, S.; Yan, Z.; Fenniri, H.; Webster, T. J. *Int. J. Nanomed.* **2011**, *6* 1035-1044.

(4) Song, S.; Chen, Y.; Yan, Z.; Fenniri, H.; Webster, T. J. *Int. J. Nanomed.* **2011**, *6*, 101–107.

(5) Borzsonyi, G.; Beingessner, R. L.; Yamazaki, T.; Cho, J.-Y.; Myles, A. J.; Malac, M.; Egerton, R.; Kawasaki, M.; Ishizuka, K.; Kovalenko, A.; Fenniri, H. *J. Am. Chem. Soc.* **2010**, *132*, 15136–15139.

(6) Borzsonyi, G.; Johnson, R. S.; Myles, A. J.; Cho, J.-Y.; Yamazaki, T.;

Beingessner, R. L.; Kovalenko, A.; Fenniri, H. *Chem. Commun.* **2010**, *46*, 6527.

(7) Borzsonyi, G.; Alsbaiee, A.; Beingessner, R. L.; Fenniri, H. *J. Org. Chem.* **2010**, *75*, 7233–7239.

(8) Fenniri, H.; Deng, B.-L.; Ribbe, A. E.; Hallenga, K.; Jacob, J.; Thiyagarajan, P. *Proc. Natl. Acad. Sci. U.S.A.* **2002**, *99 Suppl 2*, 6487–6492.

(9) Fenniri, H.; Deng, B.-L.; Ribbe, A. E. *J. Am. Chem. Soc.* **2002**, *124*, 11064–11072.

(10) Wiedner, S. D.; Vedejs, E. *J. Org. Chem.* **2012**, *77*, 1045–1055.

(11) Kim, M.; Vedejs, E. *J. Org. Chem.* **2004**, *69*, 7262–7265.

(12) Vedejs, E.; Klapars, A.; Naidu, B. N.; Piotrowski, D. W.; Tucci, F. C. *J. Am. Chem. Soc.* **2000**, *122*, 5401–5402.

(13) Morpurgo, M.; Bayer, E. A.; Wilchek, M. *J. Biochem. Biophys. Methods* **1999**, *38*, 17–28.

(14) Ghosh, A. K.; Hussain, K. A. *Tet. Lett.* **1998**, *39*, 1881–1884.

(15) Fenniri, H.; Mathivanan, P.; Vidale, K. L.; Sherman, D. M.; Hallenga, K.; Wood, K. V.; Stowell, J. G. *J. Am. Chem. Soc.* **2001**, *123*, 3854–3855.

Chapter 5

Significance and Future Outlook

5.1 Peptide-Functionalized RNTs

Bioinspired self-assembled nanomaterials have received tremendous attention over the past few decades for biomedical applications due to their biocompatibility, tunable physical and chemical properties, structural similarity to natural tissues, and their capacity for chemical functionalization. Included in these are nucleic acid-based nanomaterials such as rosette nanotubes (RNTs), which are obtained through the self-assembly of a biologically inspired DNA hybrid heterocycle, called the G∧C motif. Due to their bioinspired features and metal free design, several *in vitro* and *in vivo* studies have demonstrated that RNTs are biocompatible and non-toxic, and are well-suited for biomedical applications. They also have the desired dimensions and nanotopographic features that mimic the organic components of the extracellular matrix (ECM) in natural tissues such as bone and cartilage. As a result, RNTs that are surface-functionalized with amino acids and peptides such as lysine, arginine, RGD, RGDSK and KRSR, were found to dramatically enhance osteoblast cells attachment when coated on Ti implant materials or embedded in 3D hydrogels for tissue engineering applications. Moreover, RNTs can express more than one biological functional groups on their outer periphery through co-assembly, which creates a synergetic effect of the bioactive components on the outer surface.

For successful long-term treatment using Ti implant materials however, the surface coating material need to stimulate bone generation, growth, and calcium deposition in the attached cells. It was therefore necessary to develop RNTs that are functionalized with osteogenic peptides on their outer periphery to promote osteoblast cells functions on Ti surface. In order to achieve this goal, RNTs' ability to tolerate unique and multi-charged peptides longer than 5 amino acids on

their outer surface was to be investigated. In this regard, the motivation behind the first experimental chapter in this thesis (Chapter 2) was to develop three twin-G∧C constructs (named pA-TB, pB-TB, and pC-TB) functionalized with three 11-amino acid osteogenic peptides (A, B, and C, respectively) taken from the knucle (bioactive) region of the bone morphogenic protein-7, and to demonstrate their ability to self-assemble into RNTs. The three peptide-TB constructs were synthesized using a solid phase peptide synthesis strategy and then purified on large-scale by semi-preparative HPLC. Peptide controls A, B and C were also prepared along with a lysine-functionalized twin-G∧C motif called K1-TB.

The first significant achievement in Chapter 2 was the demonstration of the ability of pA-TB and pB-TB to form RNTs in physiological environment. Although the self-assembly process of the two motifs was relatively slow, I could demonstrate for the first time the exceptional ability of the RNT-system to display peptides as long as 11-amino acids. This will open the avenue to functionalize RNTs with other large bioactive peptides and therapeutic agents for biomedical applications. In addition, I elucidated the peptides' secondary structure for the first time using CD spectroscopy and demonstrated that it was maintained on the surface of RNTs, which is essential to preserve their bioactivity. I also provided evidence that the resulting pA-TB and pB-TB RNTs possess helical supramolecular chirality similar to that of K1-TB RNTs. This particularly demonstrates that the supramolecular organization of RNTs is not affected by the size and charge of the functional groups on the surface.

The second part of Chapter 2 aimed to develop three co-assembled RNT constructs consisting of 90% of K1-TB and 10% of each of the pA-TB, pB-TB, and pC-TB motifs. The goal of this co-assembly study was to provide more space for the peptides on RNT's surface for better cellular interaction and to create multi-functional RNTs that can promote bone cell adhesion and functions at the same time. Several experiments were designed and CD spectroscopy and SEM

and TEM microscopy techniques were used in order to provide physical evidence of co-assembly and to determine the spatial distribution pattern in the mixed nanotubes. For the first time, I provided evidence that co-assembled nanotubes having "random-mixed" configuration were formed upon mixing two different G∧C motifs as proof of principle. With this evidence of co-assembly, variety of multi-functionalized co-assembled RNTs having different (two or more) bio- or electro-active components will be considered in future for applications in biology and materials chemistry.

Given that different combinations of pA, pB and pC have been shown to promote bone cell proliferation and deposition of calcium-containing minerals, future efforts will be focused on the preparation of mixed RNTs that express two or more peptide groups on their outer periphery. For instance, four co-assembled RNT constructs will be prepared, having the combinations: 1) pA-TB:pB-TB:K1-TB (1:1:8), 2) pA-TB:pC-TB:K1-TB (1:1:8), 3) pB-TB:pC-TB:K1-TB (1:1:8), and 4) pA-TB:pB-TB:pC-TB:K1-TB (1:1:1:7). These combinations allow for synergy between the different peptides on the periphery, which may have an impact on the orthopedic applications of RNTs.

In addition, the expression of even larger peptide sequences on the RNT scaffold will be considered, in order to determine the electrostatic and steric limits of these functional groups on the self-assembly. For instance, the 20-amino acid peptide sequence (KIPKASSVPTELSAISTLYL) derived from BMP-2 will be considered, which was found to enhance alkaline phosphatase activity in osteoblast cells. Another peptide sequence under consideration is the 20-amino acid long (AISVLYFDDSSNVILKKYRN) peptide from BMP-7 that promotes calcium deposition and mineralization in osteoblast cells.

5.2 Radiolabeling Strategies of RNTs

Beside their outer surface functionalization, RNTs can also be loaded with hydrophobic drug molecules (such as tamoxifen (TAM) and dexamethasone (DEX)) and slowly release them into the medium. In order to investigate the potential of RNTs for drug delivery applications, it was necessary to obtain information about their bio-distribution in the biological systems and to understand their cellular uptake and pharmacological properties. Therefore, I aimed in Chapter 3 to develop two radiolabeling strategies for non-invasive imaging of RNTs using positron emission tomography (PET) and single photon emission computed tomography (SPECT) techniques.

For SPECT imaging, two twin-G∧C motifs functionalized with LGGGC pentapeptide and mercaptoacetyl triglycine (MAG_3) ligands called LGGGC-TB and MAG_3-TB, respectively were considered. The chelation reaction of the two motifs with cold rhenium (Re) metal was investigated using literature methods, but without success. However, I developed a new one-pot two-steps deprotection-chelation reaction of MAG_3-TB motif, which resulted in the formation of the corresponding TB-MAG_3-ReO complex in 30 min. Not only was the complex obtained in 95% yield, it was also very pure and did not need HPLC purification. I also demonstrated that TB-MAG_3-ReO complex successfully self-assembled into RNTs with 4.7 ± 0.4 nm outer diameter. This showed for the first time that RNTs can tolerate a transition metal complex on their outer surface. Overall, the radiolabeling strategy including chelation, purification, and self-assembly was optimized within the half-life of the radioactive $^{186/188}$Re radionuclide.

For PET imaging, a twin-G∧C motif functionalized with PEG_3-propylamine chain, called TB-PEG_3-NH_2, was developed. This motif was then successfully coupled with succinimide *p*-fluorobenzoate (SFB) in 5 min using a new coupling procedure. The self- and co-assembly of the coupled product to form RNTs was next investigated at physiological conditions. Although the coupled product did

not form RNTs due to its low solubility in water, co-assembly with 75% of TB-PEG_3-NH_2 motif gave well-dispersed co-assembled RNTs. The overall radiolabeling strategy including the coupling with SFB, purification, and the self- or co-assembly was optimized within the half-life of the radioactive ^{18}F radionuclide.

Given that the complex TB-MAG_3-ReO had low solubility in water, future efforts will be focused on incorporating one or two lysine amino acid spacers between the twin-G∧C motif and the MAG_3 ligand. The resulting complex will have $>^{+}1$ net charge, and its solubility in water will be therefore enhanced. Similarly, inserting one or more lysine spacers in TB-PEG_3-NH_2 motif will increase the solubility of the SFB coupled product in water. Alternatively, the oligo ethylene glycol chain in TB-PEG_3-NH_2 can be replaced with oligo lysine chain consisting of 3-5 lysine residues for the PET imaging strategy.

5.3 Synthesis of a Tetracyclic yG∧C Motif for Drug Delivery

Finally, in Chapter 4 I aimed to develop a tetracyclic (yG∧C) variant of the previously reported tricyclic (xG∧C) and bicyclic (G∧C) motifs. Since yG∧C motif was expected to self-assemble into RNTs with an extended inner diameter of 1.7 nm, the main motivation behind this part was to increase the RNTs' capability and potential to be loaded with larger therapeutic agents for drug delivery applications. Initially, the synthesis of organic-soluble di-allyl yG∧C motif was presented. In the corresponding synthetic strategy, a new allylation reaction using DIPEA and allyliodide was developed, which gave di-allyl tricycle **19** in 65% yield. In addition, a new reagent named N,N′-Disuccinimidyl carbonate (DSC) was used for the first time to construct the cytosine ring in 77% yield. Finally, the overall strategy included 13 steps with an overall yield of 1.6% and an average stepwise yield of 74%.

Then the self-assembly of di-allyl yG∧C was demonstrated in DMSO and MeOH to form RNTs with 4.0 ± 0.12 nm outer diameter. Unlike G∧C and xG∧C, which both form long RNTs, yG∧C formed short nanotubes under similar conditions. Nevertheless, the successful self-assembly into RNTs was an impressive demonstration of the inner diameter tunability and versatility of RNTs and their tolerance for further expansion in the G∧C core.

Having optimized the synthesis and self-assembly of di-allyl yG∧C, I also presented a mono-Boc strategy to synthesize a water-soluble di-lysine yG∧C motif. Although the first three steps of the synthesis were successful leading to the di-aldehyde yG∧C motif, the final reductive amination step to anchor two lysine amino acid residues was unsuccessful due to the decomposition of the di-aldehyde under $NaHB(OAc)_3$ reductive conditions. However, other mild reducing agents will be examined in future such as Raney-Nickel hydrogenation. Alternatively, di-Boc protection strategy could be utilized to provide more steric hindrance around the naphthyridine core, which may help to prevent the reaction of the reducing agent with the ring system. Olefin metathesis approach with allyl-functionalized lysine will also be considered. This would be a good strategy to avoid the use of reducing agents in the synthesis.